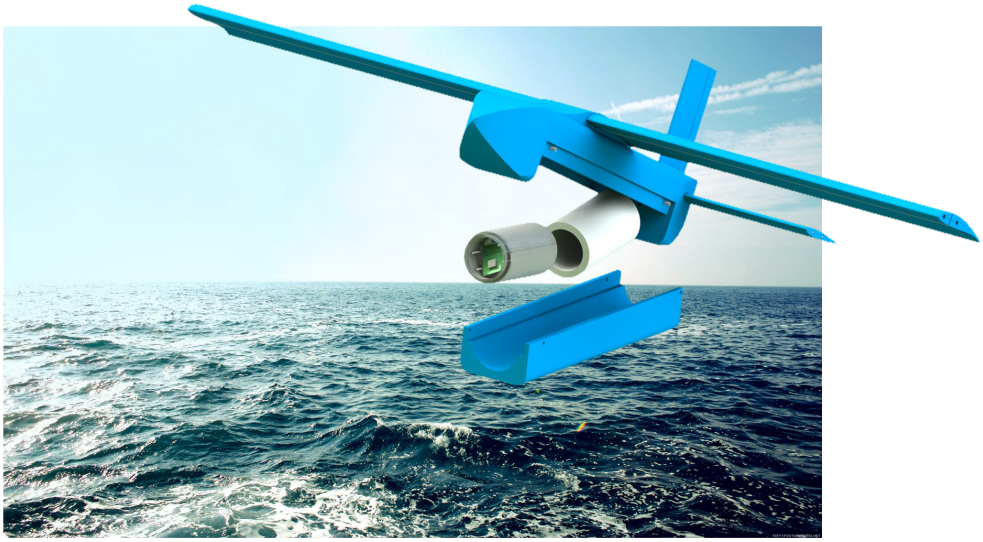

Balloon Launched Unmanned Glider

GDP 15

Summary Report

Benjamin James Oxley, Robert Gillman, Ksenija Dvurecenska, Nathan Lao, Kai Xi Tan, Mohd Izdihar Zuhdi Zulkepli, Muhammad Anas Abd Bari, Naveeyindren Thangarajah & Raja Nurul Yuhanis.

Project Supervisors: Dr András Sóbester and Professor Jim Scanlan
Second Assessor: Professor Andy Keane

April 2013

Acknowledgements

Many thanks to Dr András Sóbester, Chris Paulson, Professor Andy Keane and Professor Jim Scanlan for their input and guidance during the project. Thanks to Phil Herring and Gordon Mills for their time and help in manufacturing and thanks also to Mike Thomas and Dr David Marshall for their assistance in wind tunnel testing.

Summary Report

This project is part of the University of Southampton's Atmospheric Science Through Robotic Aircraft (ASTRA) group's study on the feasibility and development of new technologies enabling the observation of atmospheric parameters to become more affordable. The project has been split into two main aims.

Aim 1

The first aim was to expand on a UAV designed by GDP 16 (2012) in order to extend the range and/or endurance, dependent on the mission requirements of the balloon launched glider.

Objectives 1

In order to meet this aim the objectives were; to include a method of propulsion, improve the controllability through the use of additional control surfaces and revise the autopilot set up.

Scope 1

To address the aims and objectives of the first part of the project a brushless electric motor, fixed to a 3D printed motor mount, was retrofitted into the tail section. Additionally, dual elevators were installed and the autopilot system revised to an Ardupilot Mega 2.5 which enabled in-flight way point alterations. From wind tunnel and flight testing, it was concluded the powered glider is capable of climbing and the expected endurance had been extended to 10-15 minutes, limited by the Li-Po battery charge.

Aim 2

The second project aim was to provide a cost effective alternative to current Lagrangian drifters' design and deployment. In order to achieve the aim the task was broken down into a number of subsections. These subsections were drifter design, electronics development and a suitable method of transporting the drifter from the balloon to the ocean surface.

Objectives 2

The first objective was to gain an understanding on what requirements drive the design of current Lagrangian drifters and using this research develop an initial concept system. The objectives were split into two main subsections, designing a low cost drogue-buoy pair and the design of a suitable method of transporting the drifter from the balloon burst altitude to the final required position on the ocean surface.

Scope 2

Having completed the initial research and developed an understanding into the required design requirements for current Lagrangian drifters, it was apparent a significant redesign would be required in order to meet the imposed constraints, most notably a total system mass lower than $2.7kg$.

A number of conceptual designs were generated and both Excel and Visual Studio design tools were developed in order to optimise for a compact and lightweight solution. In summary, the most suitable surface buoy was a modified HDPE commercial wide-mouth chemical bottle with an internally mounted custom electronics payload. The design enabled concurrent development of both the electronics and drifter subsystems. The drogue was a 5.5m Fibermax holey-sock reinforced by aluminium welding wire which was attached to the surface buoy with a high strength nylon line. The system was not able to meet the oceanographic requirement for a drag area ratio of 40, however, a simple analysis showed a theoretical drag area ratio of 21 would provide a reasonable compromise for the slip velocity.

To address the objective for the drifter deployment from the balloon, a Styrofoam closed cell polystyrene UAV was designed manufactured and wind tunnel tested. The glider fuselage encased the drogue-buoy pair and incorporated a dual servo controlled releasable fuselage section to enable effective drifter deployment. The glider and drifter control was from the autopilot mounted within the surface buoy and

additional in-flight electronics were fitted to a custom breakout PCB. Finally a simple, lightweight balloon release hot wire cut down was developed and tested.

Resources

The group required the use of an extensive number of University resources, set out below in order of requirement, to meet the project aims. Throughout the project duration the UAV Skunk Works lab provided a central hub for the fabrication and subsystem testing of both systems.

The foam hot wire cutter and experience of Phil Herring was key to the manufacturing of both aircraft. The RJ Mitchell wind tunnel was used for three days for testing both gliders. Firstly, it provided a means of proving the range extension of the powered glider in a low risk environment to the airframe. Secondly, the RJ Mitchell wind tunnel was used for testing aerodynamic properties and static stability prior to flight testing of both aircraft.

FLUENT CFD studies were performed, requiring extensive use of the Tizard design studio and the Lyceum 2 high performance computing cluster, it is approximated that 700+ hours of Lyceum computing facilities were required in order to complete the studies. The University towing tank was used for three days to test the drogue deployment and surface buoy stability. The Celcius UAV flying test bed was required to launch the powered glider by means of a piggyback launch. The intention was to perform a glider tow for the balloon launched Lagrangian drifter system, however, due to difficult weather conditions, availability of two suitably skilled pilots and the limited roll control of the glider, it was not feasible.

Additional to the University resources, the knowledge and experience of Paul Heckles of Paul Heckles School of Model Flying, was required to pilot the aircraft during the flight testing.

Constraints

Due to the success of the Elevator Pitch early on in the project, objectives were not restricted for financial reasons. Where time implications meant that the testing plan and use of the budget had to be modified, the desire to test the systems by a balloon launch would have required further funding, which was not possible within the allocated budget.

Time constraints placed on the project were due to the high demand for the RJ Mitchell wind tunnel and the limited availability of the foam hot wire cutter due to the demand from other ongoing group design projects. Due to the project brief consisting of a large amount of oceanographic technical knowledge, it would have be beneficial for the group to have had the additional skill set of an oceanographer or ship scientist. Due to all group members being either mechanical or aeronautical undergraduates, the level of analysis completed on the drogue-buoy subsystem was limited primarily by the time to learn and implement the required skills. A further constraint was the lack of electronics knowledge within the group. The large task of electronics development for both project objectives was taken on primarily by one person. A further anticipated constraint was the availability, associated regulatory issues and logistical concerns regarding a suitable region of airspace and body of water for a complete balloon launched drifter life-cycle test.

Approaching the Task

Powered Glider

Assessment of possible solutions for incorporating the propulsion system was carried out, in which a suitable configuration was designed and implemented. It was decided to install elevators onto the powered glider to meet the requirement of increasing the aircraft controllability. The Ardupilot Mega system was

purchased and customised with bespoke autopilot code in order to increase current autopilot capabilities. A custom motor mount was designed, 3D printed and successfully implemented onto the powered glider.

Balloon Launched Lagrangian Drifter

After a rigorous design optimisation process, a final drogue-buoy pair was designed which would provide satellite uplink telemetry for up to 10 days in sea water of $5°C$, whilst having an adequate drag area ratio. A glider design was based around the drifter payload, with an integrated payload release mechanism. The electronics system development included a custom designed PCB which provided more control over power usage, thus increasing power efficiency.

Team Organisation

Where the project had two main aims, the team was split equally into sub-teams and focus primarily on one of the aims. The first aim was to be completed by the end of January 2013, where the sub-team meeting the aim then merged with the rest of the team to complete the second project aim. Each sub-team had a project manager, who organised work amongst team members. Figure 1 shows the breakdown of work completed with information on who authored and contributed to each area of work.

Results

Powered Glider

Having successfully implemented a propulsion system, elevators and an upgraded autopilot system, the powered glider was tested in the RJ Mitchell wind tunnel and performed one successful test flight at Draycott Aerodrome, via remote control. The wind tunnel results provided data which enabled confirmation that the powered glider increased its L/D ratio, provided adequate elevator effectiveness and was laterally and longitudinally stable.

Balloon Launched Lagrangian Drifter

The FEA and CFD studies carried out on sections of the glider confirmed design decisions or allowed further optimisation of the system. CFD studies were validated with data from the wind tunnel tests and showed that the studies were accurate enough to allow for further design optimisation without requiring the use of wind tunnel facilities. Wind tunnel tests confirmed designed aerodynamic performance and further tail structural improvements. The payload release mechanism was tested over a range of angles of incidence, shown in Figure 3; and operated reliably.

The flight test provided data and visual confirmation which proved the powered glider is capable of climbing to the desired testing altitude and that the endurance has been significantly increased, to approximately 10 minutes, compared to the original 90 second flight time. Figure 2 shows the first flight of the powered glider with indications of the piggyback release, the motor activation and the flight climb phase. A second flight test, which failed, highlighted issues with the autopilot system.

Conclusions

Powered Glider

The main conclusions drawn from the powered glider project are that range extension has successfully been achieved, furthermore, an added capability of allowing the aircraft to climb has been implemented. This can provide loiter capabilities of several sites of interest. Other than a few electronics reliability issues, the aircraft is stable and relatively easy to control during flight. These outcomes have been a result of efficient design and implementation of specific and measurable objectives.

Balloon Launched Lagrangian Drifter

Concluding the second aim of the project, although the desired flight tests for this system were not

Key	II	Lead
	I	Contributor
	A	Authored

Task	Name	RG	BO	KD	NL	KX	IZ	AB	NT	RY
Powered Glider										
Project management		I A	II A							
Customer requirements			I		I	II A	I	I		
Tail plane design						II A				
Motor selection & propeller size			I		II A	I				
ESC controller			I		II A	I				
Battery selection			I		II A	I				
Motor position			I		I	I	I	II A		
Design Decision Mapping						II A				
Motor mount							II A			
Servo selection			I		II A					
Controllability								II A		
Electronic design			II A							
Criticality Matrix					I	I A				
Stability calculations						II A				
Manufacturing					I		I	II A		
Wind Tunnel testing		I	I			II A	I	I A		
Piggyback release mechanism				II A						
Balloon Launched Lagrangian Drifter										
Project management		II A	I							
Literature review		II A		I					I A	I A
Design requirements		I	I	I	I	I	I	I	I A	I
Initial concepts		I A	I	I	I	I	I	I	I	I A
Drogue-Buoy Considerations		II A								I A
Concept development		II A	I	I A			I A		I A	I A
Final Concept		I A		I A					I A	I A
Buoy final design		II	I	I			I		I	I
Drifter stability		I A							II A	
Water collision simulation			II A							
Drogue final design		I		I					I A	II A
Drogue deployment testing			I	I A					I A	II A
Fuselage design		I	I					II A		
Fuselage structural analysis			I			II A			I	
Glider materials		I							II A	
Glider manufacturing		II						II		
Nose cone optimisation							II A			
Wing design		II A			I			I		
Wing tip analysis		I A			I A					
Tail design		I			II A					
Control surface sizing		I			II A					
Wing structural analysis		II A	I					I A		
Wing box analysis			I			II A				
Drag prediction					II A					
Longitudinal stability		II A			I					
Wing CFD					II A					
Wind Tunnel testing		II A	I	I		I		I	I	I
Complete Glider CFD		I			II A					
In flight electronics			II A							
Drifter electronics & manufacturing		I	II A							
PCB Manufacture			II A							
Payload release mechanism			I	II A			I		I	
Balloon hot wire cut down			I							II A
Overlapping sections										
MATLAB flight prediction							II A			
CAD Modelling			I	I				II		
Budget					II A					
Meeting Minutes		I	I						II	
Flight testing		II	II A	I	I	I				I
Health and Safety		I		I						
Report compilation		I	II		I				I	
Wind Tunnel testing mounts								II A	I	I
Lead		11	8	2	10	8	3	6	3	3
Contribute		15	22	12	11	9	8	6	13	10
Authored		13	7	5	11	8	4	7	8	8

Figure 1: Individual Roles

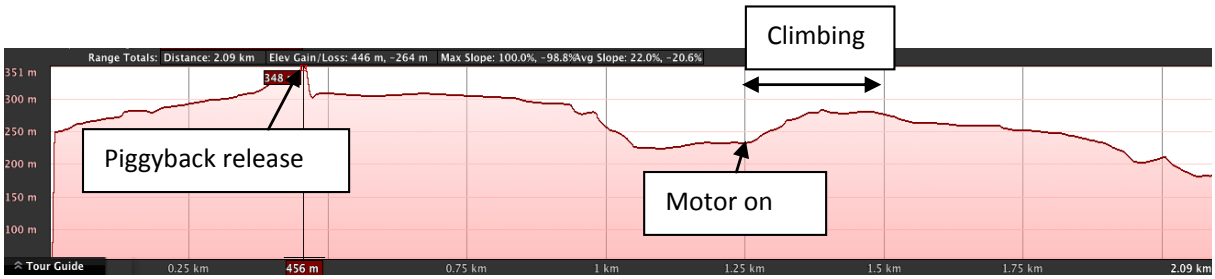

Figure 2: Flight one of the powered glider with a climb flight phase

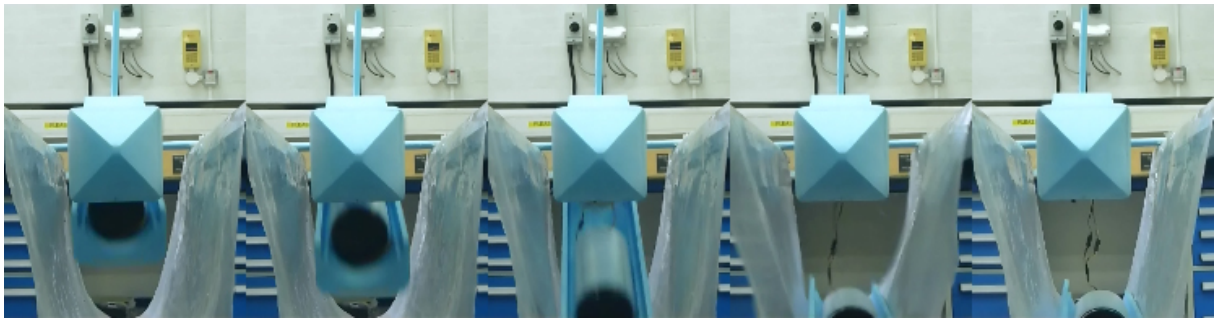

Figure 3: Time lapse of payload release mechanism static testing

successful partially due to inclement weather conditions during flight testing, visual confirmation and pilot feedback was provided that the glider performed suitably from a kite-launch, despite only having achieved a maximum height of approximately $20m$. Full operational capability of the balloon launched Lagrangian drifter system was not assessed due to constraints on time, a suitable test site and testing authorisation.

Recommendations

Powered Glider

Further work can be completed on the powered glider autopilot and the ESC prior to additional flight testing to address the issues discovered from second flight test. A further optimisation of the motor mount design can be carried out to reduce the mass, which would provide a more favourable stability due to the more forward COG. Relocation of the pitot tube into the nose cone may provide better protection upon impact. Addressing the recommendations above and further development of the system may provide a cost effective and efficient atmospheric research UAV, which can perform several loitering missions, collect atmospheric data and provide first-look images of areas of interest.

Balloon Launched Lagrangian Drifter

It is recommended that further work be undertaken to improve the fabrication of the control surfaces on the glider, to enable improved response, longevity and resistance to aerodynamic redundancy. A reduction in mass can be achieved by designing a hollowed tail section, whilst recognising the complexity of the manufacturing process; this would allow for a more forward COG position. The cavities for the payload release mechanism can be made more reliable by installing nylon inserts. The drifter design could be further optimised to reduce both the drogue packing size and the slip velocity; this would enable a more efficient fabrication of the system as well as an improved accuracy of the required current velocity over a wider range of sea conditions. The system could also be modified to provide a reliable surface drifter where there is no requirement for a drogue.

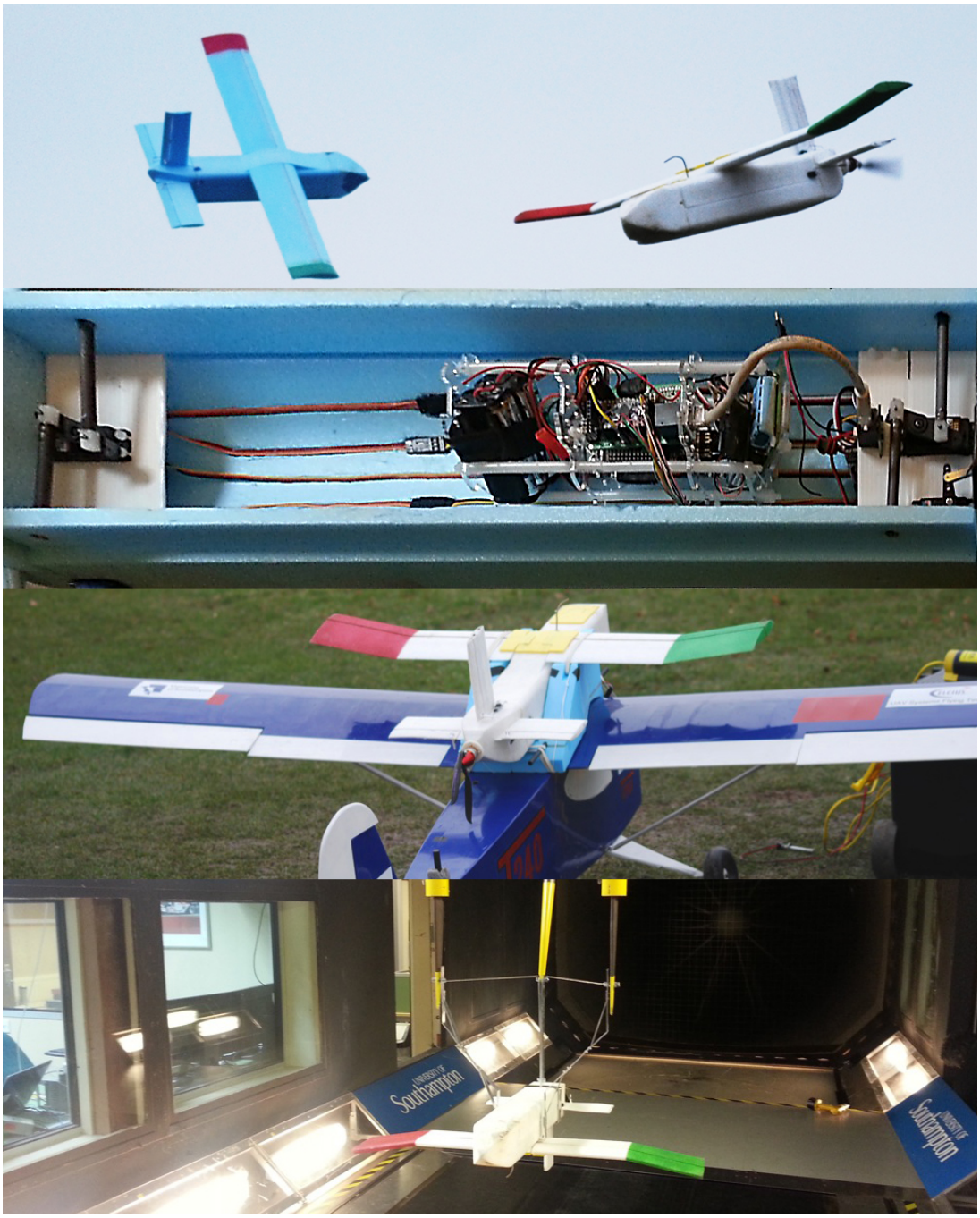

Figure 4: A summary of progress through the project, from top to bottom: The two planes in flight, The internal electronics for the drifter deployment glider, The powered glider attached with the piggyback mechanism, The powered glider in the wind tunnel.

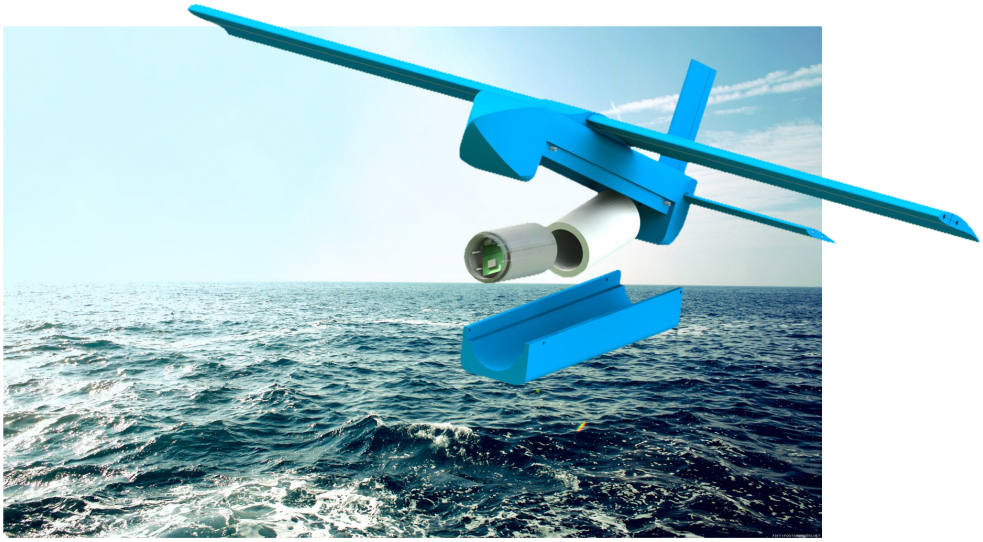

Balloon Launched Unmanned Glider

GDP 15

Main Report

Benjamin James Oxley, Robert Gillman, Ksenija Dvurecenska, Nathan Lao, Kai Xi Tan, Mohd Izdihar Zuhdi Zulkepli, Muhammad Anas Abd Bari, Naveeyindren Thangarajah & Raja Nurul Yuhanis.

Project Supervisors: Dr András Sóbester and Professor Jim Scanlan
Second Assessor: Professor Andy Keane

April 2013

Acknowledgements

Many thanks to Dr András Sóbester, Chris Paulson, Professor Andy Keane and Professor Jim Scanlan for their input and guidance during the project. Thanks to Phil Herring and Gordon Mills for their time and help in manufacturing and thanks also to Mike Thomas and Dr David Marshall for their assistance in wind tunnel testing.

Contents

List of Figures **2**

1 Nomenclature and Acronyms **6**

2 Introduction **10**
2.1 Project Brief . . . 10
2.2 Project Management . . . 10
2.3 Budget . . . 11

3 Powered Glider **15**
3.1 Powered Glider . . . 15
3.2 Tailplane Design . . . 16
3.3 Motor Placement . . . 17
3.4 Tailplane and Motor Configuration Summary . . . 18
3.5 Propeller and Motor Sizing . . . 19
3.6 Battery Selection . . . 22
3.7 Motor Mount . . . 23
3.8 Controllability . . . 27
3.9 Servo Selection . . . 28
3.10 Criticality Matrix . . . 29
3.11 Stability . . . 30
3.12 Wind Tunnel Testing . . . 30
3.13 Manufacturing . . . 40
3.14 MatLab Flight Prediction . . . 41
3.15 Piggyback Release Attachment . . . 47

4 Balloon Launched Lagrangian Drifter **49**
4.1 Project Brief . . . 49
4.2 Background . . . 49
4.3 Literature Review . . . 50
4.4 Requirements . . . 56
4.5 Initial Concepts . . . 58
4.6 Drogue-Buoy Considerations . . . 61
4.7 Concept Development . . . 65
4.8 Final Concept . . . 74
4.9 Buoy Design . . . 74
4.10 Drifter Stability Calculation . . . 78
4.11 Water Collision Simulation . . . 81
4.12 Drogue Final Design . . . 83

5 Drifter Deployment Glider **91**
5.1 Materials Selection . . . 91
5.2 Material Merit Index . . . 91
5.3 Fuselage Design . . . 95
5.4 Payload Release Mechanism . . . 97

5.5 Nose Cone Optimisation . . . 100
5.6 Wing Configuration . . . 101
5.7 Wing Structural Analysis . . . 108
5.8 Finite Element Analysis . . . 114
5.9 Tail Configuration . . . 121
5.10 Theoretical Drag Prediction . . . 126
5.11 Longitudinal Stability . . . 128
5.12 Wing Computational Fluid Dynamics . . . 130
5.13 Wind Tunnel Testing . . . 136
5.14 Nichrome Balloon Release Mechanism . . . 148
5.15 Glider Computational Fluid Dynamics . . . 150

6 Electronics **159**
6.1 Electronic Design . . . 159
6.2 Power Systems . . . 162
6.3 Autopilot Design . . . 164
6.4 Daughter Board . . . 166
6.5 Communications . . . 169
6.6 Testing . . . 170
6.7 Electronics Flight Testing . . . 171
6.8 Further Work . . . 171

7 Flight Testing **172**
7.1 Pre-Flight Issues . . . 172
7.2 Flight Tests . . . 173

8 Conclusions and Further Work **176**
8.1 Conclusions . . . 176
8.2 Recommendations . . . 178

Appendices **180**

A Powered Glider Gantt Chart **181**

B Balloon Launched Lagrangian Drifter Gantt Chart **182**

C Criticality Matrix **183**

D Stability Calculations **184**

E Pareto Front Optimisation of Glider Dimensions **185**

F Electronics Schematics **186**

G Bibliography **187**

List of Figures

1 Individual Roles . . . iv
2 Flight one of the powered glider with a climb flight phase . . . v
3 Time lapse of payload release mechanism static testing . . . v

2.1 Land & Sea Team Breakdown . . . 11

3.1 Powered glider design requirements . . . 15
3.8 Propulsion component selection tool . . . 24
3.9 Foamie mounting tube and plate[105] . . . 24
3.10 Plywood motor mount[106] . . . 25
3.11 Front of the L-shape motor mount . . . 25
3.12 Motor mount first prototype . . . 26
3.13 Stress plots of the motor mount assembly . . . 27
3.16 Final dimensions of the elevator . . . 28
3.17 Wind tunnel mounts designs 1 & 2 . . . 31
3.18 Wind tunnel mount: Design 3 . . . 31
3.19 Wind tunnel fuselage mount . . . 31
3.22 Maximum deflection and stress for section A . . . 33
3.23 Lift against AOA plot . . . 34
3.24 C_L against AOA plot for different motor inputs . . . 34
3.25 Drag against AOA plot . . . 34
3.26 C_D against AOA plot for different motor inputs . . . 36
3.27 $\frac{L}{D}$ against AOA plot . . . 36
3.28 Net lift against AOA plot . . . 36
3.29 Net lift against AOA plot for different motor input . . . 37
3.30 Net thrust against AOA plot . . . 37
3.31 Net thrust against AOA plot for 0% and 100% motor input . . . 37
3.32 Cm against AOA plot . . . 39
3.33 Cm against AOA plot for different motor inputs . . . 39
3.34 Cm against AOA plot for elevator inputs . . . 39
3.36 Structure of the Horizontal Tail . . . 40
3.40 Comparison between simulation data and test data . . . 44
3.41 Comparison between simulation data and test data using GDP16 2012 aircraft parameter 45
3.43 Flight profile for the balloon launched Lagrangian drifter . . . 46
3.44 Distance travelled by the balloon launched Lagrangian drifter . . . 47
3.45 Velocity profile for the balloon launched Lagrangian drifter . . . 47
3.46 Piggyback design . . . 48
3.47 Glider attachment . . . 48
3.48 Piggyback attachment . . . 48

4.1 SVP original vs. SVP mini . . . 51
4.2 SVP Surface Float . . . 51
4.3 SVP Mini - Marlin Yug . . . 51
4.5 Neptune Science -Micro Drifter . . . 52
4.6 Low cost Micro Drifter . . . 53

4.8 Holey sock and parachute drogue . . . 54
4.9 Tri-star drogue . . . 54
4.10 Michigan Flying Fish . . . 55
4.11 NOC UAV Launch . . . 55
4.12 Gull UAV . . . 55
4.13 Balloon launched Lagrangian drifter system requirements . . . 57
4.14 Balloon launched drifter design matrix . . . 58
4.15 Delta Wing Overview . . . 59
4.17 Initial Concept- Bubble Aircraft . . . 59
4.18 Initial Concept- Bubble Aircraft . . . 60
4.19 Initial Concept- Umbrella aircraft . . . 61
4.20 Initial Concept- AWAC Concept . . . 61
4.21 Surface buoy slip diagram . . . 63
4.22 Slip velocity in m/s versus drag area ratio . . . 65
4.23 Concept development flow chart . . . 66
4.24 Electronics development . . . 66
4.25 Drifter concept electronics . . . 66
4.26 Drifter electronics sizing . . . 67
4.27 Hemisphere concept: buoy 0.16m, drogue 0.5m. . . . 68
4.28 Internal payload concept: Overview . . . 69
4.29 Internal payload concept: Surface Buoy . . . 69
4.30 Buoy profile vs. unit Drogue Area . . . 70
4.32 Visual Studio Design Tool outcome window . . . 72
4.33 Final concept . . . 75
4.34 Final concept - CAD . . . 75
4.35 COTS cylindrical buoy solutions . . . 78
4.36 Metacentric height of the buoy . . . 78
4.38 Graphs of the result of water testing. . . . 82
4.39 Meshing of cylinder and Eulerian domain . . . 82
4.40 Maximum von Mises Stress on the cylinder . . . 83
4.41 Maximum von Mises Stress on the cylinder with time . . . 83
4.42 Mass Breakdown of Components . . . 85
4.43 Manufacturing drawing of the 1st piece of the drogue. . . . 86
4.44 Diagram showing the tether connection . . . 87
4.45 Deployment time for the drogue with weights . . . 89
4.46 Rate of Deployment against Weight:1 . . . 89
4.47 Rate of Deployment against Mass . . . 90

5.1 Modelling the wing spar as cantilever beam[29] . . . 92
5.2 Ashby Plot of Young's Modulus and Density for Common Engineering Materials[32] . . . 93
5.3 Cross-section of I-Beam . . . 95
5.4 Cross-section of a hollow spar . . . 95
5.5 Final concept . . . 95
5.6 Fuselage Final Dimension . . . 96
5.7 Solidworks model of the fuselage . . . 96
5.8 Fuselage Concept A with release mechanism fitted . . . 96
5.10 Solidworks model of the release mechanism . . . 98
5.11 Assembly in the fuselage: rear release mechanism . . . 98
5.16 $\frac{C_L}{C_D}$ vs.AOA - NACA 4415 . . . 102

5.17 $\frac{C_L}{C_D}$ vs.AOA: Suitable Aerofoil Sections: 10km . . . 103
5.18 $\frac{C_L}{C_D}$ vs.AOA: Suitable Aerofoil Sections: 0km . . . 103
5.19 Aerofoil Selection: FX 63-137: Standard . . . 104
5.20 Aerofoil Selection: FX 63-137: Modified . . . 104
5.21 Aerofoil Selection: Selig Donovan 7037 . . . 104
5.22 Aerofoil Selection: Eppler 387 . . . 104
5.23 Wing Sizing:Net & Gross Wing Area . . . 105
5.24 Wing Sizing: $\frac{L}{W}$ vs AOA . . . 106
5.25 Wing Sizing: $\frac{C_L}{C_D}$ vs AOA . . . 107
5.26 Wing Position: High Wing 1 [61] . . . 108
5.27 Wing Position: High Wing 2 [61] . . . 108
5.28 Wing loading diagram . . . 109
5.29 C_L & Wing Bending moment [M_{xx}] vs. distance from the wing root. . . . 110
5.30 Wing cross section . . . 112
5.31 Wing spar analysis: $8mm$ External diameter . . . 112
5.32 Wing spar analysis: $10mm$ External diameter . . . 112
5.33 Wing theoretical and wind tunnel measured deflection . . . 113
5.34 Upper fuselage stress analysis . . . 114
5.35 Upper fuselage displacement analysis . . . 114
5.36 Bottom fuselage stress analysis . . . 115
5.37 Bottom fuselage displacement analysis . . . 115
5.38 Wing-box FEA set-up . . . 117
5.39 Physical experiment set up . . . 117
5.40 Failure of the foam test specimen . . . 117
5.41 Material Properties for FEA[30, 123] . . . 118
5.42 Left:Initial wing geometry(with slot) and Right:Wing geometry for Abaqus (without slot) 119
5.43 Number of mesh elements and maximum stress for every global size . . . 119
5.44 Location of maximum stress . . . 120
5.45 Maximum deflection at the wing tip . . . 120
5.46 Graph of maximum stress versus number of mesh elements . . . 121
5.47 Results comparison . . . 121
5.48 Horizontal Tail Positioning [104] . . . 122
5.49 Tail Aerofoil Selection, XFLR Analysis . . . 123
5.50 Diagram of vortices on a slender rectangular wing [60] . . . 126
5.51 Neutral point reference dimensions . . . 128
5.52 Stability chart . . . 130
5.53 Wing CFD domain size . . . 131
5.54 Wing mesh boundary conditions . . . 134
5.55 Wing mesh sensitivity, lift coefficient . . . 135
5.56 Pressure contours over the wing at 3 degrees AOA . . . 136
5.57 Comparison of XFLR5 and the wing CFD lift coefficient versus AOA graph . . . 137
5.58 Wind Tunnel mount design . . . 137
5.59 Wind Tunnel set up . . . 137
5.60 Wind Tunnel boundaries . . . 138
5.61 Wind Tunnel Reynolds number . . . 138
5.62 Comparison of design and wind tunnel lift. . . . 139
5.63 Complete glider lift coefficient comparison . . . 140
5.64 Theoretical drag build up vs. Wind Tunnel . . . 141

5.65 Tare data comparison . . . 142
5.66 Glider aerodynamic efficiency . . . 143
5.67 Pitching moment vs. AOA . . . 143
5.68 Yaw moment v.s.side-slip . . . 144
5.69 Rolling moment vs. sideslip . . . 145
5.70 Effective wing dihedral from deflection vs. AOA . . . 145
5.71 Elevator influence on C_L . . . 146
5.72 C_M vs. AOA [Elevator] . . . 146
5.73 Rudder influence on C_n . . . 147
5.74 Wind Tunnel Testing: Density variation . . . 148
5.75 Wind Tunnel Testing: C_L repeatability . . . 148
5.76 Nichrome wire cutdown design . . . 150
5.77 Nichrome wire cutdown model . . . 150
5.78 R J Mitchell wind tunnel half domain with half glider . . . 151
5.79 C_L vs Element Count, Wind tunnel domain mesh sensitivity . . . 152
5.80 C_D vs Element Count, Wind tunnel domain mesh sensitivity . . . 153
5.81 Wind tunnel and CFD lift comparison . . . 154
5.82 Wind tunnel and CFD drag comparison . . . 154
5.83 Pressure contours on the glider and the adjacent symmetry plane . . . 155
5.84 Free flight domain dimensions . . . 155
5.85 Free flight domain with boundary conditions . . . 156
5.86 Wind tunnel CFD and free flight CFD lift comparison . . . 157
5.87 Wind tunnel CFD and free flight CFD drag comparison . . . 157
5.88 Glider in free flight with pressure contours and vortices . . . 158

6.1 A simple diagram of the layout and interconnections of the Ocean Glider . . . 160
6.3 Mounting system for drifter electronics . . . 161
6.4 Breakdown of all of the power consuming components . . . 162
6.5 Efficiency of combined switching regulator and LDO combined . . . 163
6.7 Approximate setup of Ardupilot simulated PID loops . . . 166
6.8 Flowchart to explain the basic operation of the Arduino control board . . . 167
6.9 The completed daughter board. . . . 168
6.10 The completed system in the glider without the buoy cylinder . . . 168

7.1 Powered glider mounted on Celsius . . . 173
7.2 Google Earth graph of flight altitude and path . . . 173
7.3 Powered glider coming in to land . . . 174
7.4 Glider in flight . . . 175

A.1 Powered Glider Gantt Chart . . . 181

B.1 Balloon Launched Lagrangian Drifter Gantt Chart . . . 182

C.1 Criticality matrix . . . 183

D.1 Stability table . . . 184

E.1 Pareto front with respective glider dimension . . . 185

F.1 The schematic for the power systems board . . . 186

1 | Nomenclature and Acronyms

Symbol	Definition	Units	Symbol	Definition	Units
m	Mass	kg	g	Gravitational Acceleration	ms^{-2}
V	Velocity / Voltage	ms^{-1} / V	L	Lift / Rolling Moment	N / Nm
D	Drag	N	W	Weight / Wind Velocity	N / ms^{-1}
ρ	Density / resistivity	kgm^{-3} / -	S_{ref}	Reference Area	m^2
C_L	Coefficient of Lift		C_D	Coefficient of Drag	
V_e	Exit Velocity	ms^{-1}	$\dot{m}$	Mass Flow Rate	kgs^{-1}
A_{prop}	Propeller Area	m^2	P	Power / Electrical Power	W / W
$P_{minimum}$	Minimum Required Power	W	η_{prop}	Propeller Efficiency	
η_{motor}	Motor Efficiency		η_{tm}	Transmission Efficiency	
RPM_{max}	Maximum Revolutions per Minute		kv	1000 RPM per Volt	
C_E	Elevator Chord	m	b_E	Elevator Span	m
C_h	Horizontal Tail Chord	m	b_h	Horizontal Tail Span	m
S_E	Elevator Planform Area	m^2	S_h	Horizontal Tail Planform Area	m^2
$\delta_{E_{max}}$	Maximum Deflection	m	$l_{n.p}$	Neutral Point / Distance from the wing aerodynamic centre to neutral point normalised by wing chord	m / -
l_{cog}	Point of Centre of Gravity	m	l_o	Aerodynamic Centre of the Wing	m
S	Net wing area	m^2	S_w	Gross wing area	m^2
S_t	Horizontal tail area	m^2	S_T	Tail Area	m^2
C_{L_α}	Coefficient of Lift with respect to Angle of Attack		C_{D_α}	Coefficient of Drag with respect to Angle of Attack	
$\frac{L}{D}$	Lift over Drag Ratio		C_M	Pitching Moment Coefficient	
x	Horizontal Position	m	y	Vertical Position	m
$\dot{x}$	Horizontal Velocity	ms^{-1}	$\dot{y}$	Vertical Velocity	ms^{-1}
$\ddot{x}$	Horizontal Acceleration	ms^{-2}	$\ddot{y}$	Vertical Acceleration	ms^{-2}
θ	Angle	Deg Rad	t	Time	s
T	Thrust	N	D_{AR}	Drag Area Ratio	
U_s	Induced Subsurface Velocity	ms^{-1}	ρ_a	Density of Air	kgm^{-3}

ρ_w	Density of Water	kgm^{-3}	A_f	Profile Area of float	m^2
W	Wind Velocity	ms^{-1}	$U_{\Delta s}$	Slip Velocity	ms^{-1}
B_f	Buoyancy Force	N	$V_{S.B}$	Surface Buoy Volume	m^3
$d_{S.B}$	Surface Buoy Diameter	m	l	Surface Buoy Length	m
ϕ	Surface Buoy Waterline / Shape Factor		n_{bf}	Ratio of Required Buoyancy	
n_m	Ratio of Maximum Payload		$n_{D_{AR}}$	Ratio of Required drag area ratio	
GZ	Righting Moment	Nm	$\overline{GZ}$	Righting Lever	m
$\overline{GM}$	Metacentric Height	m	I_{00}	Second Moment of Area of Waterline above Axis of Disturbance	m^4
u	Initial Velocity	ms^{-1}	v	Final Velocity / Deflection Along Wing	ms^{-1}/ m
s	Displacement	m	a	Acceleration	ms^{-2}
δ	Deflection	m	E	Young's Modulus	GPa
b	Wing span	m	$C_{m\alpha}$	Coefficient of pitching moment with respect to Angle of Attack	
$\bar{c}$	Mean Wing Chord	m	A_R	Aspect Ratio	
$C(x)$	Wing Loading Profile		m_t	Total Mass	kg
n	Load Factor		L_w	Lift Per Wing	N
M_{xx_a}	Bending Moment - Aerodynamic Forces.	Nm	M_{xx_m}	Bending Moment - Weight.	Nm
M_{xx_T}	Total Bending Moment.	Nm	S_f	Safety Factor	
UFS	Ultimate Flexural Strength	MPa	D_o	Outer Diameter	m
D_i	Internal Diameter	m	D_A	Drag Area	m^2
λ	Taper Ratio		A_i	Elemental area	m^2
$D_{A_{drogue}}$	Drag Area-Drogue	m^2	$D_{A_{sb}}$	Drag Area - Surface Buoy	m^2
$D_{A_{Tether}}$	Drag Area - Tether	m^2	C_{L_w}	Wing Coefficient of Lift	
$C_{L_{wo}}$	Wing Lift Coefficient at 0 Incidence		$C_{L_{w_{2D\alpha}}}$	Wing 2D Lift Curve Slope	
$C_{L_{w_\alpha}}$	Wing 3D Lift Curve Slope		C_{L_t}	Horizontal Tail Coefficient of Lift	
$C_{L_{to}}$	Horizontal Tail Coefficient at 0 Incidence		α	Angle of Attack	deg
α_{0w}	Wing Installation Angle	deg	α_{0t}	Tail Installation Angle	deg
ϵ	Down-wash		$L_{aircraft}$	Lift - Aircraft Axes	N
L_{wt}	Lift - Wind Tunnel Axes	N	$D_{aircraft}$	Drag - Aircraft Axes	N
$D_{aircraft}$	Drag - Wind Tunnel Axes	N	M	Pitching Moment Coefficient	Nm
q	Dynamic Pressure	Pa	ψ	Yaw Angle	deg
N	Yawing Moment	Nm	F_s	Side Force due to skin friction drag	N
S_f	Safety factor		C	Elliptic loading profile	

m_T	Total system mass estimation	kg	σ	Stress	Pa
D	Diameter	m	$C_{m\delta e}$	Elevator deflection	deg
I_{xx}	Second Moment of Area	m^4	Y	Spanwise distance	m^4
C_{HT}	Horizontal tail volume coefficient		c_W	Mean chord of the wing	m
S_W	Wing planform area	m^2	L_{HT}	Moment arm from the horizontal tail quarter chord to the wing quarter chord	m
C_{VT}	Vertical tail volume coefficient		b_w	Wing span	m
L_{VT}	Moment arm from the vertical tail quarter chord to the wing quarter chord	m	S_{VT}	Vertical tail planform area	m^2
S_{HT}	Horizontal tail planform area	m^2	$\bar{K_n}$	Normalised static margin	m
C_{D0}	Coefficient of profile drag		C_{Di}	Coefficient of induced drag	
C_{DW}	Coefficient of wave drag		C_f	Skin friction coefficient	
Q	Interference factor		S_{wet}	Component wetted area	m^2
S_{ref}	Reference area	m^2	Re_{cutoff}	Cutoff Reynolds number	
l	Characteristic length / Surface buoy length	m / m	k	Skin roughness value / Kinetic energy	- / J
e	Oswald span efficiency		$C_{Mn.p}$	Coefficient of pitching moment with respect to neutral point	
ω	Turbulent frequency	Hz	R	Electrical resistance	Ω
U_*	Friction velocity	ms^-1	ν	Kinematic viscosity	m^2s^{-1}
C_n	Yawing moment(Non-dimensional)		I	Electrical current	A

Please note: the Powered glider and Balloon launched Lagrangian drifter may be referred to as the land and sea systems respectively throughout the report.

Acronyms	Definition
ABS	Acrylonitrile-Butadiene-Styrene
AOML	Atlantic Oceanographic and Meteorological Laboratory
ArduPilot	A brand of autopilot system
ASTRA	Atmospheric Science Through Robotic Aircraft
AWG	American Wire Gauge
BNUC-S	Basic National UAS Certificate
CAA	Civil Aviation Authority
CAM	Computer Aided Machining
CFD	Computational Fluid Dynamics
COG	Centre of Gravity
DARPA	Defence Advanced Research Project Agency
DOF	Degree of Freedom
EPP	Expanded Polypropylene
ESC	Electronic Speed Controller
FEA	Finite Element Analysis
GDP	Group Design Project
GPS	Global Positioning System
HDPE	High Density Polyethylene
HWIL	Hardware in the Loop
ISM	Industrial, Scientific and Medical
LED	Light Emitting Diode
Li-Po	Lithium-Polymer
NACA	National Advisory Committee for Aeronautics
Ni-Cd	Nickel-Cadmium
NIMBUS	A US Satellite Program
PC	Polycarbonate
PID	Proportional Integral Derivative Control
PMMA	Polymethyl methacrylate
PPSF	Polyphenylsulfone
PWM	Pulse Width Modulation
RC	Remote Control
RPM	Revolutions Per Minute
RTTY	Radio Teletype
SVP	Surface Velocity Programme
S-A	Spalart-Allmaras
S8R	Quadratic 8-Node Shell Elements
UAS	Unmanned Aircraft System
UHF	Ultra High Frequency
VLM	Vortex Lattice Method
WOCE	World Ocean Circulation Experiment

Acronyms	Definition
AOA	Angle of Attack
AR	Aspect Ratio
ARGOS	Advanced Research and Global Observation Satellite
AWAC	Airborne Warning and Control
BEC	Battery Eliminator Circuit
BST	Breakaway Support Technology
CAD	Computer Aided Design
CD	Compact Disc
CNC	Computer Numerically Controlled
COTS	Commercial of the Shelf
DBCP	Data Buoy Cooperation Panel
EC3D8E	Eulerian 3D 8 Node Elements
EPS	Expanded Polystyrene
FDM	Fused Deposition Modelling
FSPL	Free Space Path Loss
Globalstar	A type of satellite communications technology
GFRP	Glass-fibre Reinforced Polymer
HPC	High Performance Computing
Iridium	A type of satellite communications technology
LDO	Low Drop-out Regulator
LDPE	Low Density Polythylene
MOSFET	Metal Oxide Semiconductor Field Effect Transistor
NERC	National Environment Research Council
Ni-MH	Nickel Metal-Hydride
NMEA	National Marine Electronics Association
PCB	Printed Circuit Board
PLA	Polylactic Acid
PP	Polypropylene
PVC	Polyvinyl Chloride
RANS	Reynolds Averaged Numerical Simulation
RF	Radio Frequency
RPN	Risk Priority Number
SST	Shear Stress Transport
SVBP	A buoy type
S4R	Linear 4-Node Shell Elements
TOGA	Tropical Ocean-Global Atmosphere
UAV	Unmanned Aerial Vehicle
VHF	Very High Frequency
WCRP	World Climate Research Programme

2 Introduction

2.1 Project Brief

This project is part of the University of Southampton's Atmospheric Science Through Robotic Aircraft (ASTRA) group's study on the feasibility and development of new technologies enabling the observation of atmospheric parameters to become more affordable. The project has been split into two main aims.

The first project aim was to extend the range of an Unmanned Aerial Vehicle (UAV), following on from the work of the previous year GDP 16 (2012). The UAV had previously been designed to be released from an altitude approximately $30km$, gliding a predefined flight path and obtaining user-defined atmospheric data.

The second aim was the design, manufacture and test of a balloon launched Lagrangian ocean drifter. This required a suitable method of transporting the drifter from the balloon to the ocean surface and gave rise to the development of a separate UAV. The UAV was to be released from a weather balloon at an altitude of $10km$ and glide a suitable path to a predefined location whereupon the ocean drifter would be released.

Please note: the Powered glider and Balloon launched Lagrangian drifter may be referred to as the land and sea systems respectively throughout the report.

2.1.1 Powered Glider Development

With the ASTRA initiative in mind, the existing balloon launched glider does not allow for a prolonged period of data collection due to the limited glide time. Thus, the main objective was to implement additional control surfaces and a propulsion system to provide an improved range or endurance, dependent on the mission requirement.

2.1.2 Balloon Launched Lagrangian Drifter

Currently, Lagrangian drifters are deployed either by ship or air-drop. This is an expensive process and thus the feasibility of a balloon-launched system was investigated, this would help to reduce the life-cycle costs of a Lagrangian drifter. The system is to be released from a meteorological balloon, with a 2.7kg payload limit, at an altitude of $10km$ then descends along a predefined path to a fixed deployment location. The drifter should measure the ocean current velocity at a depth of $10m$ for a duration of approximately 3 weeks and transmit the data via satellite uplink for oceanographic research.

2.2 Project Management - Robert Gillman & Ben Oxley

GDP 15 consists of 9 team members and two main project aims. In order to effectively manage such a large group the team was split into sub teams within the first week of the project. The sub-teams were named, and shall be referred to throughout this report as, "Land" and "Sea". The land group focused on the first project aim, to provide range extension of the 2012 GDP 16 "balloon launched glider". The "Sea" group focused on the initial research, design and build of the balloon launched Lagrangian drifter. It was expected that all "Land" work would be completed by the end of January, 2013. Once the first project aim had been completed both teams merged to concentrate on the balloon launched Lagrangian drifter system in order to complete both project aims within the deadline of April, 2013. Due to the

diverse range of project requirements the sub team break down was an equal balance of mechanical and aeronautical students with each member allocated a role specific to their skill sets.

Oct- Dec Team Roles		
Team	**Name**	**Role/Responsibility**
Land	Benjamin Oxley	Land Project Manager + Electronic Design
Land	Nathan Lao	Motor & Prop Selection + Flight Testing
Land	Kai Xi Tan	Motor & Prop Selection + Stability+ Wind Tunnel testing
Land	Muhammad Anas Abd Bari	CAD Design Manager + Motor Position + Control Surface Design
Land /Sea	Mohd Izdihar Zuhdi Zulkepli	Motor Mount Design & Manufacture / Drifter Optimisation
Sea	Robert Gillman	Sea Project Manager + Drifter & Drogue Research & Design
Sea	Ksenjia Dvurecenska	Drifter & Drogue Research,Design & Testing
Sea	Raja Nurul Yuhanis	Drifter & Drogue Research, Design, Manufacture & Testing
Sea	Naveeyindren Thagarajah	Drifter & Drogue Research, Design, Testing + Material Selection

Dec- Apr Team Plan		
Team	**Name**	**Role/Responsibility**
Sea	Robert Gillman	Sea Project Manager + Glider Aerodynamic Design + Wind/Flight Testing + Manufacturing
Land/Sea	Benjamin Oxley	Project Manager + Electronics Manufacturing & Testing
Land /Sea	Nathan Lao	Glider Aerodynamic Design(CFD) + Flight Testing
Sea	Kai Xi Tan	Glider Design + FEA +Flight Testing
Sea	Muhammad Anas Abd Bari	CAD Design Manager + Glider Design & Manufacturing + Wing FEA
Sea	Mohd Izdihar Zuhdi Zulkepli	Drifter & Drogue Optimisation + MATLAB flight Predictor + Nose cone optimisation
Sea	Ksenjia Dvurecenska	Drifter & Drogue Design +Testing + Piggyback & Payload Release Mechanism Design
Sea	Raja Nurul Yuhanis	Drifter & Drogue Design + Manufacture + Testing
Sea	Naveeyindren Thagarajah	Drifter & Drogue Design + Material Testing + Buoy stability calculations.

Figure 2.1: Land & Sea Team Breakdown

2.2.1 Group Communication

For a project of such scale and complexity it is vital to have regular communication between all the group members and project supervisors. Firstly, for inter-group communication, a “Facebook” group was created where meeting schedules, documents and ideas could easily be shared and discussed. Additionally, a “Google Calendar” was created to help long term planning and keep track of deadlines. A lower level of instant message communication was used, this proved to be a reliable tool for ensuring members were up to date with the latest meetings times and locations. Bi-weekly meetings were established for each sub team and a weekly meeting for the entire group with the project supervisor. Frequent supervisor meetings ensured constant progress and regular feedback with meeting minutes produced and distributed by the project secretary. Delegated work was assigned through the meeting minutes and early on in the project through DOCEAR mind maps which would be uploaded to the group “Facebook" page. A cloud file storage system, “Dropbox”, was used by all group members which enabled multiple user access and automatically updated files with the most recent addition.

2.2.2 Time Management

Time management was controlled, on a weekly time frame, through regular meetings and self imposed deadlines. For a longer term overview of key dates the Google Calendar was used in conjunction with Gantt charts to ensure the Land and Sea project progress remained on track. Gantt charts are in fig. A.1 and fig. B.1 for Land and Sea projects respectively.

2.3 Budget - Nathan Lao

2.3.1 Elevator Pitch

The initial budget allocated to the project was $£1,020$; this was calculated from the base budget of $£300$ and then the addition of $£80$ per group member, where there are nine members in the project. Having reviewed the objectives of the project, this funding did not seem adequate in achieving the project

objectives to the desired high standard. It was decided that extra funding would allow greater scope, flexibility and product maturity to be built into the project.

The elevator pitch was an opportunity to gain this valuable extra funding, where a project budget proposal is required to explain how the extra funding will add value to the project. The requested extra funding from the elevator pitch was £990. The main reasons for this request came from the desire for electronic development throughout the project, where both a commercial off-the-shelf (COTS) autopilot and a custom built autopilot would be designed specifically for each part of the project. Greater flexibility would be available in aircraft design due to the more flexible PCB dimensions. This would require approximately £317 of the requested £990 elevator pitch funding. Additionally, the extra funding would allow the testing of both systems under realistic operational conditions and deployment. Testing of the designed systems would provide project maturity and reliable data for future work. It would require the remaining £672 from the elevator pitch request. These requirements for additional funding were prioritised to improve the quality of the designed systems.

After a successful outcome, where an additional £740 were granted to the project, the total budget available for the project was £1,760. The budget deficit meant that a custom autopilot would not be developed in conjunction with the COTS autopilot but instead the COTS autopilot would be developed so that it is transferable between the two systems with minor changes; however, the budget granted was sufficient to achieve the main objectives of the project.

2.3.2 Powered Glider Project Budget

Predicted Budget
Prior to commencing the powered glider project, an analysis of the predicted budget required to achieve the aims of the project was created. This predicted budget accounted for essential components to the improved aircraft as well as components that would enhance the characteristics of the aircraft. A significant proportion of this predicted budget consisted of the readily available autopilot system, Ardupilot Mega, which is capable of an impressive set of functionality and supports hardware-in-the-loop (HWIL) testing. This was seen as an essential component as it allowed the project to focus on the integration and develop the coding of the autopilot, rather than the manufacturing of a bespoke autopilot. The predicted cost of the Ardupilot Mega was £274. Other essential components included the aircraft motor and battery, which were predicted at approximately £35 and £43, respectively. The total predicted budget for the land project was £463.

Budget Alterations
During the project a few required components were found to be overlooked in the prediction of the budget and some components were no longer required for the project as the design of the aircraft was modified for improved usability and performance.

There were several items which were cheaper than predicted, such as the Ardupilot Mega system and the aircraft motor, due mainly to sourcing from cheaper retailers and alternative components with similar or better characteristics.

Due to changes in the design and implementation of the aircraft, components such as extra servos for elevators and rudders were required in order to build in controllability redundancy to the aircraft. The requirement of extra extension cables, nylon hinges and compatible plugs also contributed to unforeseen costs. A lithium-polymer battery charger was also a significant unforeseen cost which was necessary in allowing the continual testing of the electronic system.

Components were also purchased in preparation for testing of the aircraft and its system. The aircraft was being planned for a catapult launch test flight which then required the purchase of a larger propeller in order for the aircraft to be able to climb to a desired altitude, however, due to several reasons, it was

decided catapult launching was no longer required. A spare flight battery and spare aircraft parts was also required to ensure the flight testing day would be as efficient and productive as possible. Overall, the powered glider project budget was £68 over the predicted budget, totalling £531. This was due to changes in the design and unforeseen costs.

2.3.3 Sea Glider Project

Predicted Budget
A predicted budget for the sea project was estimated to be £474. The main contributions to this were from the lithium polymer battery pack which was intended for flight and oceanographic operation, EPS foam for the manufacture of the glider and the carbon fibre rods which were to be used as wing and tail spars. In addition, the predicted budget accounted for oceanographic drogue and drifter manufacture, the balloon release mechanism and aircraft fuselage release mechanism.

Budget Alterations
This project also saw alterations to the predicted budget, where certain items were not forecasted and a change in project design meant that there were several purchases which were not originally accounted for; however, they were necessary in achieving a successful project.

On the other hand, there was over-expenditure on several other items. The original costing on carbon fibre rods was underestimated, this is because a higher quality grade of carbon fibre was used and further to this, the diameter of the tail spars were increased due to observations of the tail aerodynamic performance from wind tunnel testing.

Nearer the end of the project, a review of the budget and testing plans resulted in availability of funding to the project from balloon testing costs. Taking into account the amount of available budget and the project deadline, it was decided the spare funding could now be utilised to produce an increase in system development turnaround time by paying for faster manufacture. An extra Ardupilot Mega was purchased so that simultaneous development of both projects could be performed, thus saving development time. External manufacturing of the designed PCB and the electronic mount allowed for faster manufacturing time and a higher quality components, which proved valuable in obtaining a working electronic system in time for testing.

Overall, the sea project totalled £864, which was over the predicted cost by £390. The reason for this significant over-expenditure was due to funding made available through a change in the testing plans.

2.3.4 Testing Budget

Predicted Budget
The predicted budget allocated to the testing of each system amounted to £790. The majority of this sum belongs to the cost associated with a balloon launching, where the desire was to test fly each aircraft and payload at operational conditions; two balloon launches were budgeted for, costing £250 each. The remaining amount was accounted for by transport, local testing and Iridium data rates.

Budget Alterations
A significant change in testing plans meant that funding was made available for the design and manufacturing of the projects. Though the original plan of testing the projects was from launching each aircraft from a weather balloon, this method of testing did not was not possible due to the aircrafts' maturity levels not being adequate for balloon launches, as well as the time restrictions of the project. The cancellation of the two balloon launches meant that £500 was then available for use in the projects.

Testing costs incurred were mainly from transport and fuel costs to and from the testing site as well as material collection from retailer locations. The design and manufacture of the piggyback release

mechanism needed for flight testing was also associated with testing costs, which came under the predicted cost. Overall the budget spent on testing was £174, which was a saving of £616.

2.3.5 Final Expenditure

In total, the project used 96% of the available budget where the final expenditure of the whole project came to £1,685, this included printing and binding of three reports. This means that the project has been completed under-budget by £75, this can be attributed to alterations to the budget during the course of the project.

Overall, the project budget has been used wisely and effectively, where several alterations to the project design and testing plans meant that the budget had to adapt in order to maintain a structured budget plan.

3 | Powered Glider

3.1 Powered Glider

To achieve the first aim of the project, increasing the range of the existing glider, the following objectives were identified in order to complete this aim:

Objectives

- To increase the range of the glider by addition of a propulsion system.
- To increase controllability via the addition of extra control surfaces.
- To develop a suitable autopilot to control and monitor the upgraded system.
- To design the system to carry an array of sensors for atmospheric measurement.
- To test the modified aircraft and assess its capability.
- To complete the above within a mass restriction of $1.25kg$ due to the limitations of the current design.

3.1.1 Powered Glider Design Requirements - Kai Xi Tan

To understand the additional requirements for glider range extension, all the possible requirements were reviewed and updated. Each group member reviewed the requirements and individually ranked them in order of relative merit, where the results were averaged to provide a comprehensive overview. The ranked requirements provided guidance to aid design decisions throughout the project.

The results in fig. 3.1 showed that CAA governing regulations and safety considerations were, as expected, the primary requirements in order to allow safe flight testing. Second to the fixed regulatory requirements

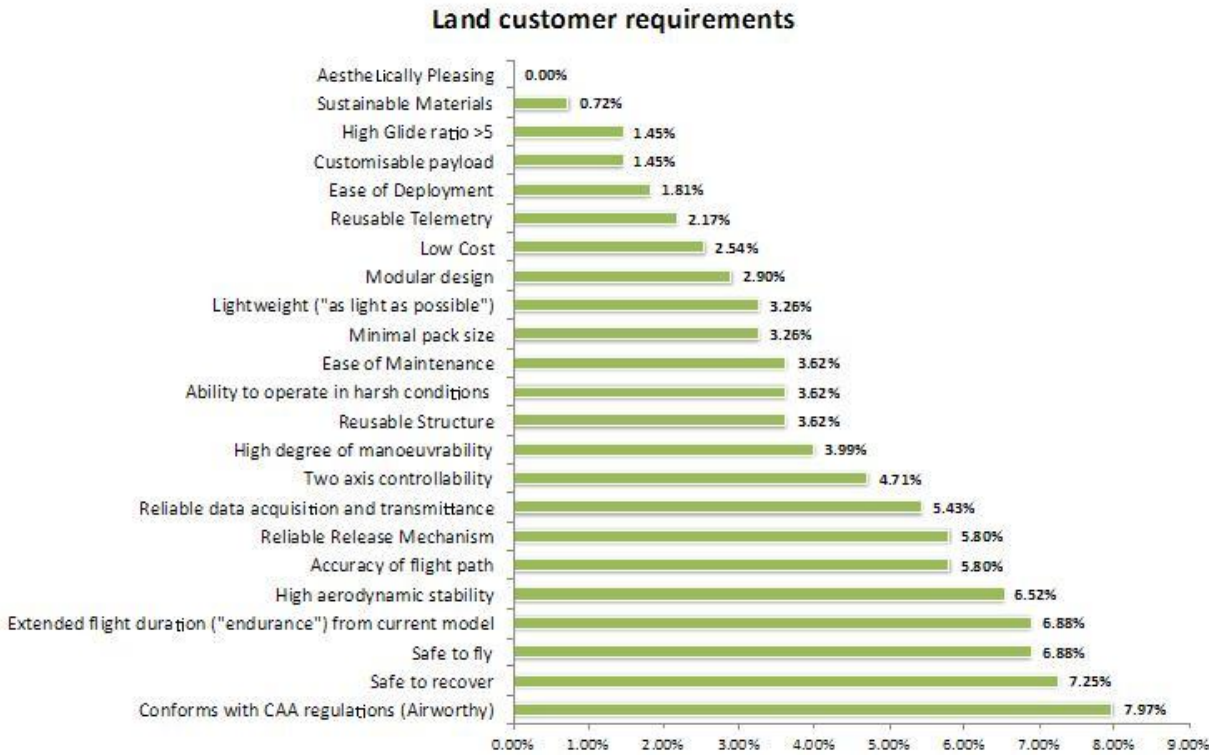

Figure 3.1: Powered glider design requirements

came the need to fulfil the project aims by ensuring the range and/or endurance, dependent on mission requirement, were extended beyond the current glider performance. The lower ranked requirements included an aesthetically pleasing design and the use of sustainable materials due to the glider remaining out of sight during the majority of its flight and reusable nature of its design.

Although an increase in glide ratio may appear to have come out as a low requirement because the requirement was written in the context of the propulsion system not operating. If an increase in glide ratio was a higher requirement a significant redesign in the aerodynamic properties of the current glider would have been required.

3.2 Tailplane Design - Kai Xi Tan

In order to select the optimum tailplane configuration research was completed to obtain the advantages and disadvantages of a wide variety of possible tailplanes.

Conventional Tail
The advantage of the conventional tail is that it has a simplistic design therefore it is not complicated to manufacture. Furthermore, the wing will stall prior to the tailplane thus the tailplane is able to provide longitudinal control during stall. However, other than the two advantages, the conventional tailplane does not excel in performance in any other area [110, 80].

T-Tail
The advantage of a T-tail is that the horizontal tail has a larger moment arm to reduce the trim drag. Moreover, by having the horizontal tail above the vertical tail, the horizontal and vertical tail would help each other to maintain both longitudinal and lateral stability. Thus requiring a smaller horizontal and vertical tail area. With the T-tail, the tailplane would undergo stall first before the aircraft would enter a spin. On the other hand, having the horizontal tail above the vertical tail required additional structural considerations to support the extra weight and aerodynamic loading, thus,ultimately resulting in a heavier tail. The most significant disadvantage is the possibility of deep stall occurring. Deep stall is when the horizontal tail is in the wake of the wing and so the horizontal tail becomes redundant and the aircraft loses stability [11].

V-Tail
The advantage of a V-tail is that it is more structurally efficient, as the rudder and elevator are combined. Furthermore, by combining the control surfaces, the aircraft will have better turning capabilities and the overall drag of the aircraft will also be reduced resulting in an improved endurance. As the control surfaces are not conventional, the control requirements will be more complex due to the adverse yaw-to-roll coupling associated with combined control surfaces. Additionally the placement of servos and control rods would be more difficult in the current glider design. Furthermore, the control authority of the control surfaces would be reduced [107].

Twin Tail
The advantage of the twin-tail is that the vertical tail is not affected by the turbulence from the fuselage at high angles of attack(AOA). The two vertical tails also improve the horizontal tail effectiveness as they act as end-plates which reduce the horizontal tail tip vortices. As there are two vertical tails, the height of the vertical tails can be reduced. In this configuration the tailplane would be heavier due to the additional structural requirements imposed by mounting the vertical tails at the tips of the horizontal tail [110].

Cruciform Tail
The cruciform tail is a trade off between the conventional tail and the T-tail. This tail configuration will have the advantages and disadvantages of both types of tailplane. By carefully analysing the design, the tailplane can be optimized such that the advantages are kept and the disadvantages reduced to a

minimum. For example, the horizontal tail should be placed in a position such that deep stall would not occur and the vertical tail is not excessively heavy [110].

Twin Boom Tail Variations
Instead of the conventional single boom connected to the tailplane there can also be twin boom-mounted variations. The twin boom mounted variations can include inverse V-tails and T-tails. The twin boom-mounted variations produce better efficiency when a pusher configuration is required. Furthermore, the fuselage length can also be reduced however, the weight would increase due to the requirement of the aircraft having to be structurally stronger in order to support the bending moment, due to the extended tail moment arm. [110].

Figure 3.4: Inverted V-Tail [14] (Left) and Twin Boom T-Tail [86](Right)

3.3 Motor Placement - Anas Bari

Location of the motor gives several impacts to the glider such as amount of drag generated, it's maintainability, controllability, structural implications and weight. The motor may be mounted on the wings, front of fuselage (tractor) or aft of fuselage (pusher). In this section, the advantages and disadvantages of suitable configurations will be discussed in table 3.1 and evaluated in order to decide which configuration is the most appropriate for the glider.

Figure 3.2: Twin Tail [52]

Figure 3.3: Cruciform Tail [97]

Engine configuration	Advantages	Disadvantages
Wing mounted [87, 46]	• Can improve inertia relief on the wing • Closer to centre of gravity (COG) hence stabilise the glider	• Causes higher drag • Lack of ground clearance for small aircraft upon take-off/landing
Pusher [87, 46]	• No prop-wash over the wing • Less likely to cause injury on landing	• Heavier wing structure needed for lost of bending relief • COG position moves aft thus requires larger tail to balance moments
Tractor [108]	• High propeller efficiency due to clean airflow • Positive dynamic stability • Good centre line thrust	• Complex structure, additional weight for a mounting system • Bad airflow to the wing due to the propwash • Induces side force due to propwash

Table 3.1: Advantages and disadvantages of different motor placements

Figure 3.5: Engine Configurations: Pusher(top-left)[39], Tractor(top-right)[21] and Wing Mounted(bottom)[125]

3.4 Configuration Summary - **Anas Bari & Kai Xi Tan**

After listing the advantages and disadvantages of the most suitable tail and motor configurations, several key factors were considered in greater detail in order to decide which configurations were the most suitable for the glider. In summary the most suitable tail configuration was considered to be the conventional tail. The reasons for this included the time and cost involved in significantly changing the current tail

configuration. Additionally the current solid tail design was suitable for housing a motor in a pusher configuration.

The wing mounted and tractor motor configuration were eliminated due to the several reasons. A wing mounted motor would require significant redesign for the wing and wing-box. Due to the wing box being manufactured from foam, the effect of motor vibrations leading to failure would have needed to be considered. A tractor configuration would have required fuselage redesign in order to maintain sufficient longitudinal stability due to the forward position of the electronics payload. Therefore, it was decided that the glider should be designed to incorporate a motor in a pusher configuration based on the following reasons. Firstly a pusher configuration required minimal redesign as the motor could be mounted in the solid foam tail section. Secondly by mounting the motor in a pusher configuration, the powered glider posed a significantly lower risk to the user during flight testing. Finally through the addition of elevators longitudinal control would gained meanwhile, suitable longitudinal stability could be achieved by moving the electronics forward into the aircraft nose [63].

3.5 Propeller and Motor Sizing - Nathan Lao

Thrust

For glider flight extension, it has been proposed to retro-fit the existing glider with a propulsion system; where the design is to fit a single motor and propeller in a pusher configuration to the glider.

Assuming, while the propulsion system is in operation, the glider maintains steady, equilibrium flight. Therefore, the thrust required to maintain level flight can be calculated, which enables suitable motor and propeller sizing and selection.

In level flight, lift is equal to the glider weight and thrust is equal to the drag; therefore, it is possible to calculate glider velocity at varying altitudes and thus densities. As the glider has a mass limit of $1.25kg$, the lift is equal to this mass multiplied by the gravitational acceleration, $9.81ms^{-2}$. Values for the wing reference area, the drag coefficient and the lift coefficient at the maximum lift-to-drag ratio have been extracted from the calculation spreadsheets from last year's design group [47].

$$L = W = mg = 1.25kg \times 9.81ms^{-2} \tag{3.1}$$

$$L = \frac{1}{2}\rho V^2 S_{ref} C_L \tag{3.2}$$

Using the above equations, rearranging and inserting known values; the velocity of the glider operating at an air density of $1.225kgm^{-3}$ is evaluated to be $19.53ms^{-1}$.

Using this cruising velocity together with values for the coefficient of drag and the reference area, the drag equation can be evaluated. Values for the coefficient of total drag and the reference area have been extracted from last year's design group calculations spreadsheet to be 0.068 and $0.134m^2$, respectively.

$$D = \frac{1}{2}\rho V^2 S_{ref} C_D \tag{3.3}$$

The drag force for the existing glider is $2.14N$, which in steady, level flight is equal to thrust; thus thrust equals $2.14N$.

Power
The exit velocity from the propeller can be evaluated using the change in kinetic energy equation as the air passes through the propeller disc, where the work done is the thrust required, $2.14N$.

$$WorkDone = \frac{1}{2}mV^2 - \frac{1}{2}m{V_e}^2 \tag{3.4}$$

$$\therefore V_e = 24.68ms^{-1}$$

The power required to supply the thrust of $2.14N$ can now be calculated using equations 3.5:

$$\begin{aligned} \dot{m} &= \rho A_{prop} V \\ Power &= \frac{1}{2}\rho A_{prop}({V_e}^2 - V^2)V_e \end{aligned} \tag{3.5}$$

These evaluate the required power to be $52.8W$. The area of the propeller is based upon a 5.5 inch diameter propeller (explained in section 3.5.1), thus $A_{prop} = 0.0153m^2$.

Efficiencies
To obtain the required power to be supplied by the motor, efficiencies of the propeller, motor and transmission need to be considered. Propeller, motor and transmission efficiencies have been estimated to be 0.75, 0.75 and 1, respectively. These values have been estimated from a range of typical values of model aircraft with motor/propeller pusher configurations. Therefore, equation 3.6 can be applied:

$$P_{minimum,required} = \frac{P}{\eta_{prop} \cdot \eta_{motor} \cdot \eta_{tm}} = 93.87W \tag{3.6}$$

The above calculations related to altitudes up to one kilometre and an air density of 1.225 kgm^{-3}. These calculations were repeated for a range of altitudes from 0 kilometres to 30 kilometres and the corresponding air densities, using the International Standard Atmosphere table [124].

3.5.1 Propeller Size and Selection

A wide scope of suitable, available propeller research was carried out to identify possible solutions for the glider. There are a few factors which narrowed the search criteria; for the chosen glider pusher configuration, a pusher propeller was required to provide optimal efficiency and direction of thrust. Furthermore, for protection of the propeller and motor mount upon impact (e.g. landing) it was decided to select a folding propeller.

There were three propeller sizes identified that would be suitable for the glider configuration in level flight; figure 3.6 provides the physical attributes of each and their corresponding maximum RPM, beyond which the propeller blades may rupture.

Propeller Name	Diameter (Inches)	Pitch (Inches)	Maximum RPM
Graupner CAM folding push prop 4.7x2.3	4.7	2.3	30851
Graupner CAM folding push prop 5.1x3.1	5.1	3.1	28431
Graupner CAM folding push prop 5.5x4	5.5	4	26363

Figure 3.6: Available propeller characteristics

The maximum RPM was calculated using the suggested RPM limits for folding electric propellers by

APC propellers[102].

$$RPM_{maximum} = \frac{145000}{\text{Propeller diameter (inches)}} \tag{3.7}$$

The motor selection was constrained by the maximum propeller RPM, where the maximum unloaded RPM of the motor should not exceed the maximum propeller RPM due to safety considerations.

A smaller propeller would require a higher powered motor to produce equivalent thrust to a larger diameter propeller operating with a lower powered motor. Another factor to consider, is that of the RPM per volt (often expressed as kv) attribute of motors, where a smaller diameter propeller requires a higher kv motor to provide the desired thrust; higher kv motors are therefore more powerful and heavier.

Since higher powered motors, for a smaller propeller, are significantly heavier than the lower powered motors, for a larger propeller option, the relative mass differences are in favour of a larger propeller, lower power and kv motor.

For these reasons, the 5.5 $\times$ 4 folding pusher propeller was selected for the aircraft to achieve level flight upon a release velocity of approximately 19 ms^{-1}.

3.5.2 Motor Size and Selection

Brushless DC motors, also known as electronically commutated motors, are synchronous electric motors with DC currents powering magnets that displace the rotor around within the stator. Brushless motors use a step motor controller to create the rotation that turns electrical energy into mechanical energy [78]. The main advantages of using a brushless motor over brushed motors are that they provide increased reliability, better efficiency, reduced noise and are more durable as there are no brushed commutators.

Brushless motors are available in two different configurations, outrunner brushless motors and inrunner brushless motors. Outrunners have the outer case rotating around the internal windings, whereas inrunner rotational cores are within the motor with windings around it. Outrunners tend to spin slower than inrunners and produce more torque; thus being suitable for direct drive of a propeller and eliminating the need for a gearbox, which introduces extra weight, noise and inefficiency.

Taking into account the minimum power required (approx. 94 W) to achieve steady level flight at an altitude up to one kilometre and the maximum RPM the 5.5 inch propeller can withstand (approx. 26,000 RPM), a suitable brushless outrunner motor was chosen which met the above criteria. Consideration of the cost with respect to the motor performance was also taken into account. The selected motor was the Turnigy D2826-6 2200kv Outrunner Motor.

3.5.3 Electronic Speed Controller Selection

An electronic speed controller (ESC) varies the speed of an electric motor and its direction, this is done through applying voltage to the motor by switching it on and off rapidly. Thus, by varying the ratio of on to off time, the ESC can vary the average voltage seen by the motor and therefore vary the speed at which the motor spins.

The selection of the electronic speed controller (ESC) was mainly governed by the recommended ESC ampage of the brushless motor, which in this case was 40A. The chosen ESC was a Turnigy Plush 40 Amp Speed Controller.

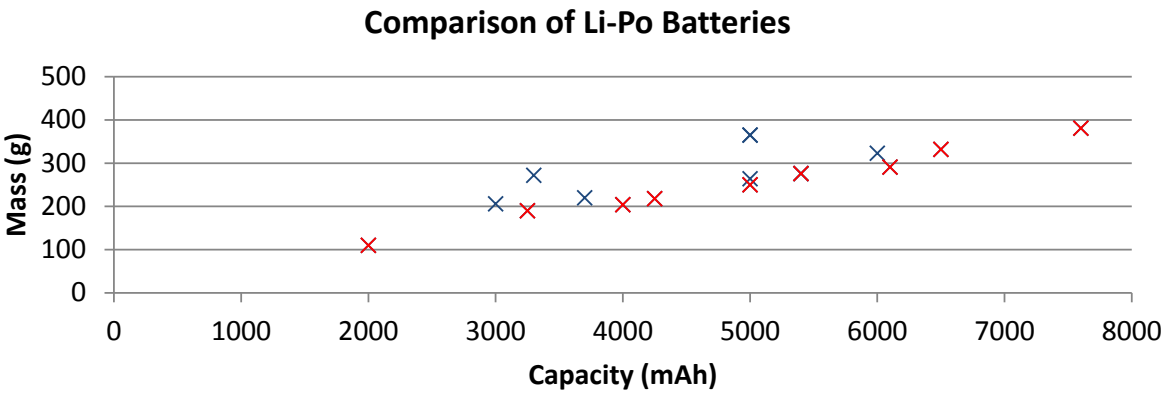

Figure 3.7: A Pareto chart of a range of Li-Po batteries enabling a mass/capacity trade-off

3.6 Battery Selection - Nathan Lao

A lithium-polymer (Li-Po) battery has a flexible polymer laminate case which encloses the electrode sheets inside, rather than a cylindrical rigid metal case which surrounds a lithium-ion battery.

Li-Po batteries are more lightweight than Li-ion, Ni-Cad or Ni-MH due to the lower density and not being bound by a rigid metal casing. Additionally, they are more resistant to overcharging than Li-ion batteries, meaning improved safety [126]. These advantages of a Li-Po battery translate to longer endurance of a powered aircraft.

The decision to use a two cell (2s) Li-Po battery was largely based on the power and voltage requirements of the selected motor and ESC; where either two cells or three cells in series would suffice the requirements of the motor and ESC. A three cell battery would be able to supply up to $11.1V$, though this will mean that the throttle on the remote control would have to be used delicately so as not to burn out the motor and ESC. Therefore, a battery with two cells in series has been selected as this would provide a voltage of up to $7.4V$ which is sufficient to allow the motor to provide the aircraft with the desired flight speed.

The mass of the battery is an important factor in the selection process due to the whole aircraft mass being limited to $1.25kg$. The battery mass limit is set to $300g$ to allow for as much aircraft powered flight endurance as possible but also so that the overall aircraft mass is not exceeded.

A battery pareto chart was constructed to assist in the selection of a suitable battery, shown in figure 3.7, where it allowed valuations and trade offs to be considered within the set of considered batteries.

The chosen battery was an Overlander SuperSport $7.4V$ $6100mAh$ $30C$ LiPo stick pack. This component was chosen due to the high capacity and the relative mass and the cost. The large capacity of this battery will allow the best endurance possible within the remaining mass from the glider limit of $1.25kg$, being $300g$. The mass of the selected battery was $291g$ which falls suitably within the limit set. The cost of this battery provided the most economic saving in terms of attributes of the battery, where batteries of lower capacity had higher purchase costs.

Endurance
Having selected the above components for the propulsion system of the aircraft, a minimum endurance required can be calculated for the particular mission intended. This minimum required endurance relates both the battery capacity and the maximum current required by the motor to determine the powered flight endurance of the aircraft.

With the combined selected components in the above sections, it has been calculated that the minimum powered flight endurance of the powered glider is approximately 10.5 *minutes*.

3.6.1 Design Decision Mapping

The different design options available for the modification of the current glider were broad with many viable solutions. However, due to both the constraints on time and finance, a design process was thought through with these constraints considered. Compendium 2.0 was utilised to map this design process into a visual format to clearly identify the decisions made and the options explored. Using this tool, analysis of the benefits and downfalls of each option were performed, where a rational decision was made to either move forward with the idea or close off that avenue of exploration.

The mapping of the design decisions made will allow easier traceability for any party interested in further developing this project, with a clear visual aid to understand the decisions made.

3.6.2 Component Alterations

Propeller for Climb
Though the selected propeller is sufficient for the powered aircraft when launching from a balloon at an altitude of approximately $10km$, it will not produce the required power to allow the powered aircraft to climb due to the relatively small propeller diameter of 5.5 *inches*.

The possibility of testing the designed aircraft from ground level on a catapult required the aircraft to climb to a suitable testing altitude to perform the desired tests. In order for the aircraft to climb it was decided to use a larger propeller for the purpose of testing, where it will extend the duration of test flights.

Although the available propeller sizes specifically made for pusher folding purposes was limited to $5.5inches$, it was discovered that tractor blades could be used in reverse to allow for a larger pusher folding propeller; though the affect on efficiency is unknown. Therefore a larger propeller was selected to enable the aircraft to climb.

A propeller of size 11 $\times$ 5.5 inches was selected, due to the suggested propeller size from the motor selection and its power output, obtained through tests.

Optimisation Excel Page

During the selection of the propulsion components for the aircraft, a propulsion selection tool was developed to assist in the selection of components, shown in Figure 3.8. The tool allows the user to firstly select a propeller of particular diameter, secondly, a motor which meets the criteria of minimum power and maximum RPM for the selected propeller and finally, the required endurance of the aircraft. The tool then calculates and selects the most appropriate ESC and battery from a range of products. With the components selected, the user is then able to visualise the characteristics of both the motor and the aircraft, along with the total mass of the combined components.

3.7 Motor Mount - Izdihar Zuhdi

The motor mount is used to hold the motor to the main body frame. The motor will be attached to an X-mount and then attached to the motor mount using screws. Normally, motor mounts are made of rubber or wood. There are 3 typical designs available on the market today.

The Foamie Mount
The foamie mount is typically built in two parts; the mounting tube and the plate. The mounting tube is glued into the tail plane, where the motor is mounted on the plate. The mounting plate is then clamped to the mount tube as shown in figure 3.9.[105] In most ground strike cases, only the mounting plate suffers

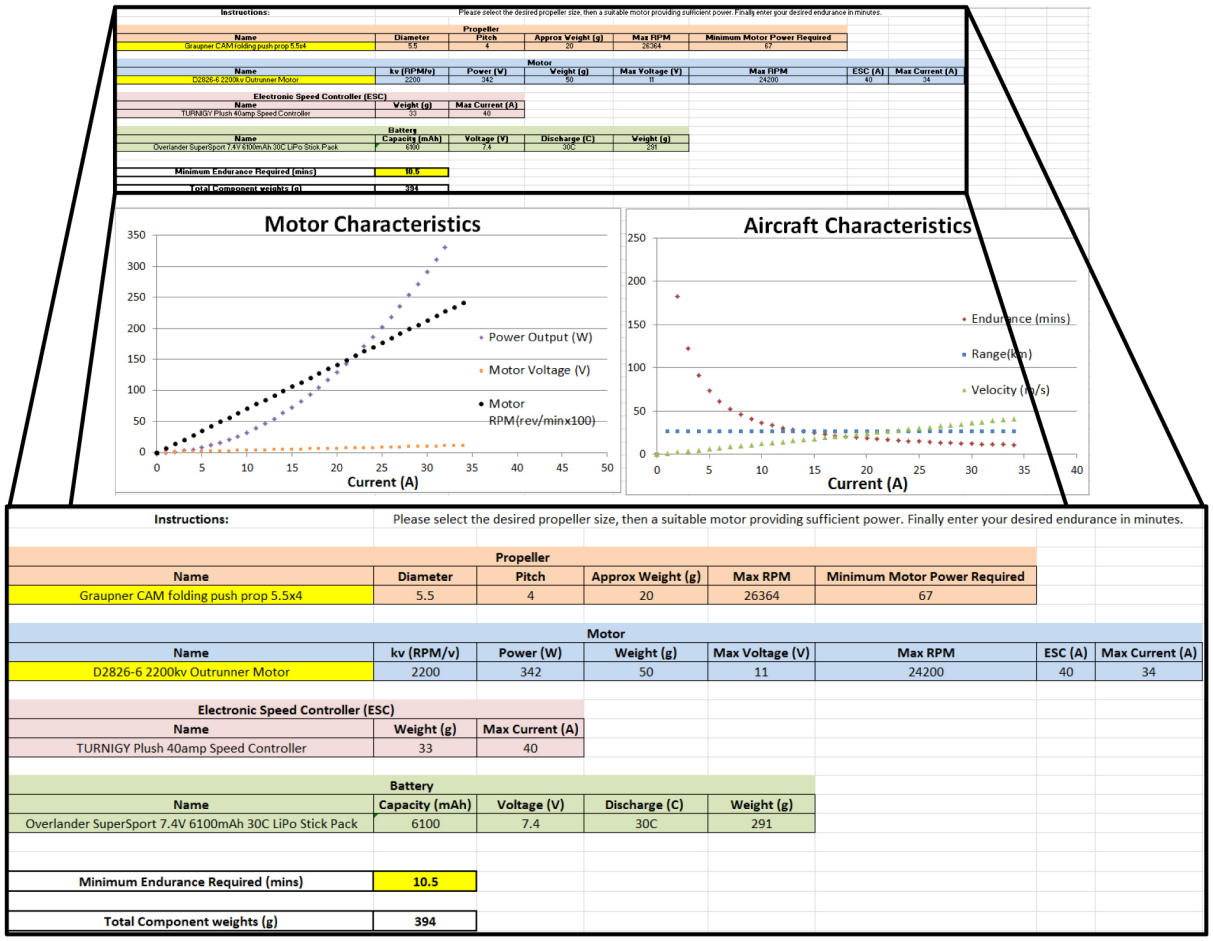

Instructions:	Please select the desired propeller size, then a suitable motor providing sufficient power. Finally enter your desired endurance in minutes.

Propeller

Name	Diameter	Pitch	Approx Weight (g)	Max RPM	Minimum Motor Power Required
Graupner CAM folding push prop 5.5x4	5.5	4	20	26364	67

Motor

Name	kv (RPM/v)	Power (W)	Weight (g)	Max Voltage (V)	Max RPM	ESC (A)	Max Current (A)
D2826-6 2200kv Outrunner Motor	2200	342	50	11	24200	40	34

Electronic Speed Controller (ESC)

Name	Weight (g)	Max Current (A)
TURNIGY Plush 40amp Speed Controller	33	40

Battery

Name	Capacity (mAh)	Voltage (V)	Discharge (C)	Weight (g)
Overlander SuperSport 7.4V 6100mAh 30C LiPo Stick Pack	6100	7.4	30C	291

Minimum Endurance Required (mins)	10.5
Total Component weights (g)	394

Figure 3.8: Propulsion component selection tool

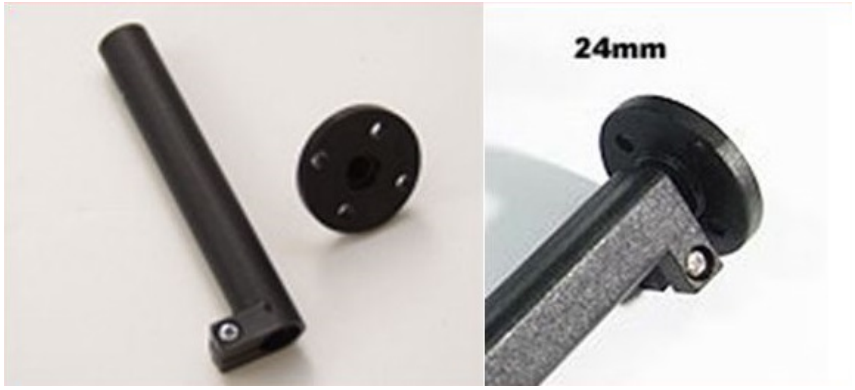

Figure 3.9: Foamie mounting tube and plate[105]

damage. Therefore, only the mount plate requires replacement, thus modularity of this design reduces maintenance costs.

Plywood Motor Mount
Normally, this type of mount is built from the highest quality aircraft grade birch plywood as shown in figure 3.10.[106] The mount is pre-cut with the hole in the centre and an E-clip clearance which is needed for the motor. A relief hole is also pre-cut into the side to relieve strain on wires.[106]

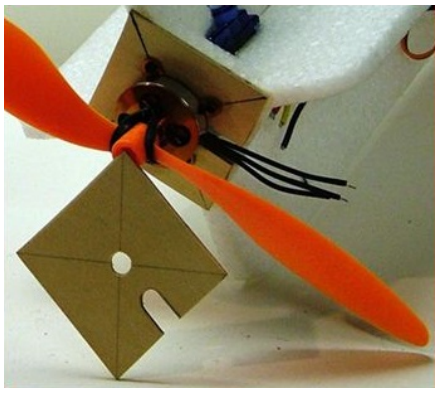

Figure 3.10: Plywood motor mount[106]

Figure 3.11: Front of the L-shape motor mount

L-shape motor mount
The L-shape motor(as shown in figure 3.11) mount is most commonly used on Styrofoam aeroplanes. It can be produced by bending a metal sheet, whether aluminium, steel or titanium into an L-shape. Holes are drilled to place the screw that connects the motor and the mount. The idea is to use the piece of metal and mount it onto the airframe whether it is the fuselage or the wing where the motor is going to be placed. Problems might arise through excessive vibrations from the motor, where the mount could be torn off from the aircraft. Heat transfer from the motor to the mount might also melt the foam and loosen the connection between them during service.

Design Decision
From these designs, the foamie mount has been chosen to be equipped onto the current glider. This is mainly due to the fact that only the mounting plate needs to be changed on the event of ground strike. By using this type of mount, we are also avoiding any use of the motor heat sink as the motor is placed outside of the airframe. The motor mount was printed using a 3D printer mainly due to quick production turnaround. The design of the mount can also be tailored according to the size of the motor and the dimensions of the X-mount. This translates to lower costs of the whole unit.

3.7.1 Motor Mount First Prototype

The first prototype was inspired by the foamie mount design. It has the same geometry as the one which is available on the on-line store; it consists of the mounting plate and the tube. A $3mm$ hole is placed at the bottom end of the mounting tube to enable the plate to be tightened to the tube using a $3mm$ screw. The length of the tube has been set to $80mm$ because it is the maximum length that a hole can be drilled into the current tail before it touches the vertical tail spars inside the tail section. A Solidworks model has been built prior to printing the motor mount, this can be seen in figure 3.12.

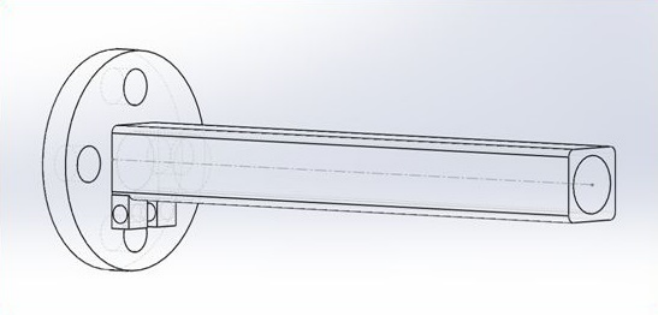

Figure 3.12: Motor mount first prototype

A few problems arose from the 3D printed motor mount design. Firstly, the mount plate does not match the size of the X-mount making it impossible to use. The section around the screw hole also seems to be very thin thus making it very fragile once a screw is used to hold the mounting plate to the tube. The problem leads to a high probability for rotation of the mount plate once the motor is in operation due to the torque from the motor. Therefore, a second prototype was designed and manufactured.

3.7.2 Motor Mount Second Prototype

A second prototype was produced to improve the problem faced from the first prototype. Basically, there are 3 major improvements in this model. The inner hole of the tube is designed as a square instead of a circle to prevent the rotation of the mount plate once the motor is in operation. The screw hole at the bottom end of the mount tube was replaced with a pin hole at the top of the end of the mount tube. This hole is to insert a pin to prevent the mount plate from falling off the tail. The face of the mount plate was also redesigned to replicate the X-mount shape and resized according to dimensions of the X-mount.

Since a hole is going to be drilled in the tail, the mount tube has been changed to have a rod shape so that it is easier to push-fit the mount tube into the tail. This design was used on the glider.

3.7.3 Finite Element Analysis

The inbuilt FEA software in Solidworks was used to analyse the capability of the motor mount under loading from the motor. Both the mounting plate and tube material have been set to ABS-PC plastics. The mount tube is set as a fixed geometry because it is assumed to be fixed to the airframe. Three forces were applied on the structure - the maximum torque applied from the motor which is $0.002Nm^{-1}$, $10N$ for the maximum thrust provided by the motor and the motor weight of $0.4905N$.

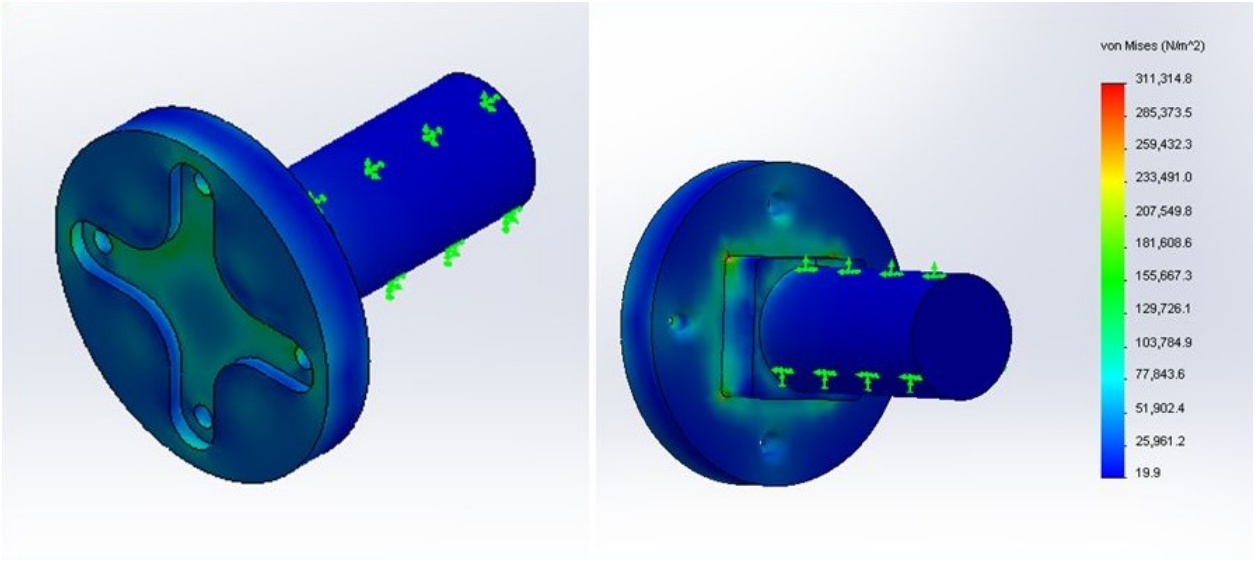

Figure 3.13: Stress plots of the motor mount assembly

From the results obtained, the maximum stress on the motor mount is $311KPa$ which occurs at the edge of the contact point between the mounting plate and tube. The maximum deflection of 2.109 μm occurs on the circumference of the mounting plate. Overall, the motor mount works perfectly fine under the required loading condition.

3.8 Controllability - Anas Bari

3.8.1 Elevator Sizing

Longitudinal control is required in order to ensure safe flight which is one of the main roles of an elevator. For a conventional aircraft, longitudinal controllability is achieved by deflections of the elevator. The tail lift is generated by deflecting the elevator, since it is located at some distance from the COG, the incremental tail lift force generates a pitching moment about the COG. This means that pitch control is achievable by varying the lift on the horizontal tail where the elevator is mounted. The design of the elevator is completely independent of the design of the rudder and aileron due to the reason that lateral-directional control does not have any effect on the longitudinal control. According to Sadraey [110] there are four main parameters which should be determined to design the elevator, which are shown in figure 3.14 and figure 3.15.

PARAMETERS	TYPICAL VALUES
Elevator chord,C_E	20%-40% of horizontal tail chord,C_h
Elevator span,b_E	80%-100% of horizontal tail span,b_h
Elevator planform area,S_E	15%-40% of horizontal tail planform area,S_h
Maximum deflection, $\pm\delta_{Emax}$	$\delta_{Emax\ up}$= -25 degrees, $\delta_{Emax\ down}$= +20 degrees

Figure 3.14: Elevator Design main parameters and its typical values.

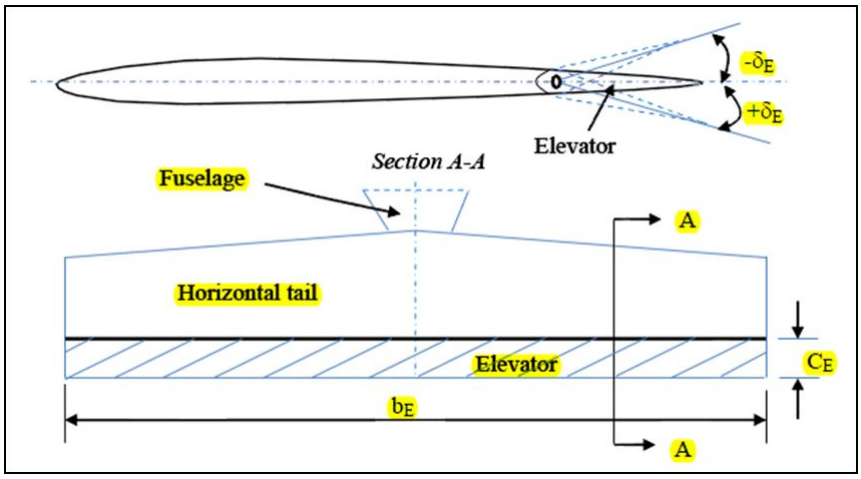

Figure 3.15: Plan view of elevator and horizontal tail [110]

Conventionally, a deflection upwards by the elevator is denoted as a negative pitch and vice versa.

3.8.2 Final Sizing

The precise elevator sizing process involves many complex equations and steps. Therefore, the precise sizing of the elevators were not performed due to limited technical data available and the limited time. The sizing of the elevators were based on the typical values shown in figure 3.14. The final design dimensions are tabulated in figure 3.16.

Parameter	Dimension	Description
Chord	30mm	30% of tail's chord
Span	150mm	90% of tail's span
Area	4500mm^2	29% of tail's area

Figure 3.16: Final dimensions of the elevator

Although the the elevator produced adequate effectiveness, further optimisation could be conducted for improvement. However, due to the time and material constraint, the elevator was not optimised further in the current project.

3.9 Servo Selection - Nathan Lao

The selection of the rudder servo by the previous group (GDP16) was based on the servo used on the Maja aircraft. The Maja aircraft is an electric UAV with the potential to carry a payload of $1.5kg$ [23]; this aircraft has the potential to be fitted out with meteorological equipment for weather research at low altitudes (up to $2{,}000ft$). The Maja aircraft uses a Futaba S3114 High Torque micro servo to operate its single elevator the span of the horizontal tailplane. Due to GDP16 unable to source the same servo for the rudder servo, they implemented a Futaba S3117 micro servo as this provided the exact same torque and speed values as the original Futaba S3114 servo [47].

The selection of the servos for the two elevators on the current design was also based on the original servos of the Maja aircraft. The reason for this was to keep servo variations to a minimum due to ease of maintenance and synchronisation; furthermore, the designed powered glider has similar dimensions as the Maja aircraft and so should see similar aerodynamic forces. Futaba S3114 High Torque servos were unavailable from all UK based sellers due to various reasons, however, Futaba S3114M High Torque servos were purchased as they were readily available, provided the same dimensions and performance as

the Futaba S3114 High Torque servos and were sourced from a UK based seller, meaning a faster delivery time. The only difference was that the Futaba S3114M High Torque servos had a micro plug (Molex connector) instead of a standard plug; this meant that conversion plugs were required for compatibility with the selected autopilot.

The selected servos' specification are shown in figure 3.2.

Weight	Dimensions	Speed	Torque	Voltage
7.8 g	22.9 x 10.9 x 20.1mm	0.09 sec/60 deg (6.0V)	1.73 kg/cm (6.0V)	4.8V/6.0V

Table 3.2: Futaba S3114M and S3114 High Torque micro servo specification [35]

3.10 Criticality Matrix - Kai Xi Tan

In order to identify and address likely modes of failure, a criticality matrix was made. The criticality matrix lists all the possible failures that may happen during flight as a result of a design decision. The failures are then measured by calculating their respective Risk Priority Number (RPN). The RPN is a measure to figure out the severity and detectability of the failure. The failures that result in high RPNs will have to be rechecked to see if the design decisions that result in those failures can be modified.

The matrix has 7 columns. The first column is a list of all possible failures. The second column explains possible effects on the glider that may arise when the failures occur. The third column gives possible precautions for early detection or to avoid the possible outcome of failure. The next 3 columns provide a ranking system that ranks the failure's severity, probability and detection. These 3 columns are of a scale from 1-10 with 1 being the least and 10 being the most. Severity means how severe the damage to the glider will be when the failure occurs. Probability means how likely it is that the failure is going to occur and detection means how easily the failures can be detected.

These 3 values are used to find out the RPN, which is the last column. The RPN is a multiplication of the scaled values from the previous 3 columns. The criticality matrix is shown in Appendix fig. C.1.

The two failures with the highest RPN are that the motor mount fails structurally due to fatigue, etc and servo linkages breaks. The first failure might cause the motor to break off the glider during flight. Furthermore, the detached motor might damage the body of the glider as the propeller may cut the body. This failure has a high RPN because the probability of the failure occurring is very high. However, it is also easily detected. Therefore, it is important to take note of this failure so that it will not occur. Thus, the glider should be constantly checked for any defects that may have started to form so that the part can be replaced or fixed. The second failure with a high RPN causes the glider to lose its pitch authority, as the elevators would stop working. In addition, push rods have no more control over the elevator. The elevator will start to flap, which will cause adverse effects on the gliders stability. This failure has a very high severity as if the failure occurs, the glider may possibly crash land and injure a person. Having said so, the failure can be easily prevented by checking that the linkages are secure before every flight. This will reduce the probability of the failure happening during flight.

In contrast, there are two failures with very low RPN. They are battery exploding and loss of power to electronics. Battery exploding is a serious failure, as it will not only cause harm to its surroundings but also towards the environment. Sadly, there is no actual way of preventing the failure from happening, as it is sudden and unpredictable. The only possible prevention would be to avoid placing the battery in too high temperatures. As the probability and detection of the failure is very low, its RPN becomes really low even though its effects are very severe. The failure where the electronics lose their power has a low RPN due to the fact that generally all three of severity, probability and detection are low. This is because having loss of power to the electronics would still allow the glider to glide down. Although there

is no more control over its yaw and pitch, the glider would still not take any severe damage. Furthermore, as long as the battery has been checked before flight that it is at full capacity, the chances of an in flight failure are reduced.

In addition, by listing down ways to detect the failures, it complies to a procedure of initial flight checks. The procedure will help as a precaution such that those failures with high RPN can be detected early and prevented.

3.11 Stability - **Kai Xi Tan**

As the powered glider is being modified in order that its range can be increased, the stability calculations have to be recalculated. In summary, the few changes that are being made to the glider are the addition of elevators and motor as well as upgrading the autopilot. The excel chart in fig. D.1 shows the updated list of components and their moment arms.

After obtaining the centre of gravity of the glider, the static margin was then calculated to determine its stability. The static margin was calculated by finding the difference between the position of neutral point and the centre of gravity on the wing [61]:

$$\text{Static margin} \quad = l_{n.p} - l_{cog}$$

The neutral point of the glider was found using:

$$l_{n.p} = l_o \quad + \frac{Sc}{(S_t l)} \frac{C_{Lt_\alpha}}{C^*_{L_\alpha}}$$

where l_o is the aerodynamic centre of the wing.

The aerodynamic centre of the glider is at quarter chord of the wing. C_{Lt_α} was taken from the last year's wind tunnel results and used as an estimation. $C^*_{L_\alpha}$ was taken from wind tunnel testing results. If the static margin is calculated to be positive then the glider is said to be stable [47].

Due to the decision of going with a pusher motor configuration, a large moment arm due to the motor and its required components pushes the center of gravity far backwards on the wing. Furthermore, with the addition of elevators, 2 extra servos have also been placed near the end of the glider which further increases the problem. In order to maintain the stability of the glider, the battery, which is the heaviest object has been placed as far forwards as possible in the glider.

Currently, the total weight of the glider is at $0.898kg$ including all the internal components. Its center of gravity is at $343mm$ from the front of the nosecone. It also has a static margin of $5.7mm$ which is positive and therefore stable.

3.12 Wind Tunnel Testing

3.12.1 Wing and Fuselage Mount - **Anas Bari**

The wind tunnel mount for the glider is required for the wind tunnel tests. The wind tunnel mount comprised of three struts, two main wing struts and a tail strut. The purpose of the main wing struts are to allow for yaw movement of the model whereas the tail strut is responsible to pitch the model about the axis of the main struts. In order to minimize the turbulence caused by the struts on the airflow over the aerodynamic surfaces, and also to avoid damaging the vertical tail during pitching, the model needs to be mounted upside down. Due to a large wing span of the glider, about 1.7 metres, it not possible to attach the mounts at the wing tips since the maximum allowable distance between the two main struts

is 0.9 metres. Therefore several designs of the main mounts have been developed as shown in figures 3.17 and 3.18.

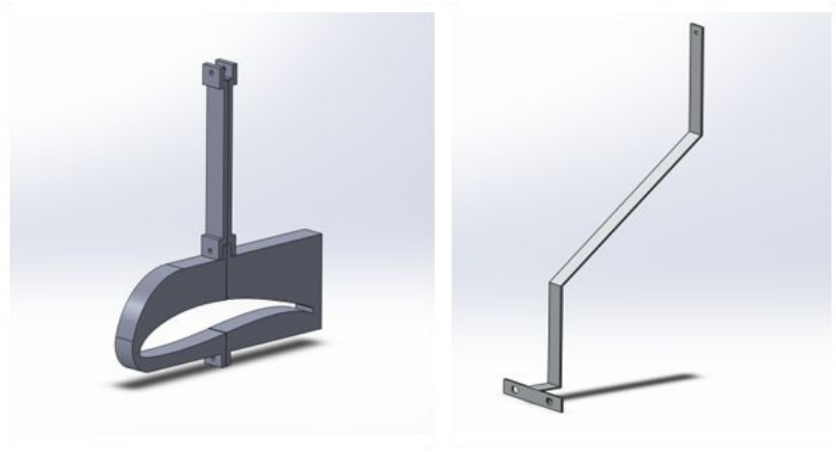

Figure 3.17: Wind tunnel mounts designs 1 & 2

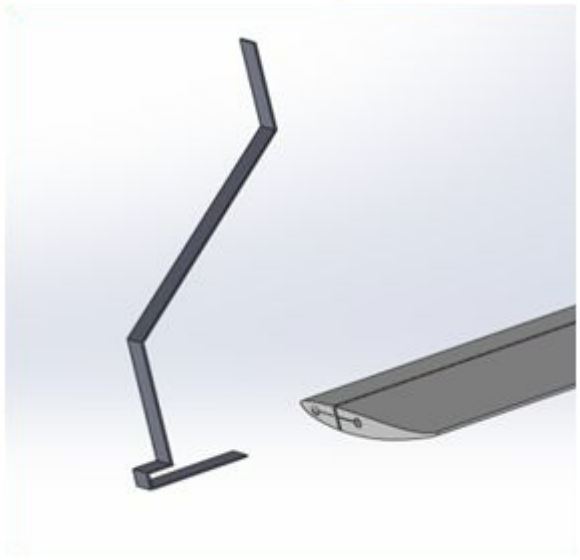

Figure 3.18: Wind tunnel mount: Design 3

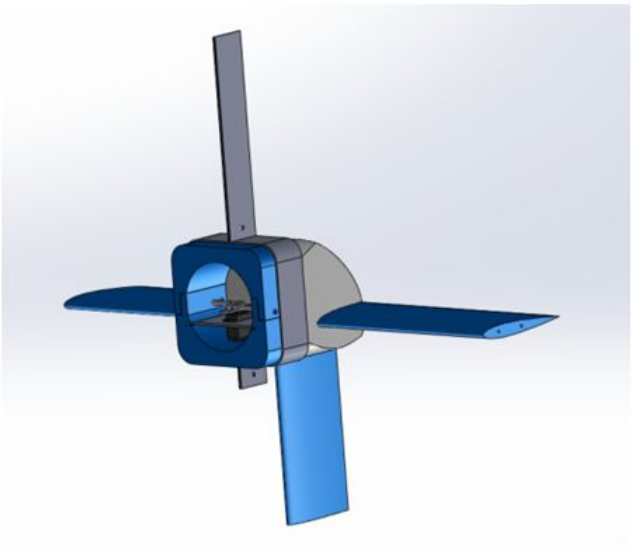

Figure 3.19: Wind tunnel fuselage mount

Due to material limitations and time constraints for manufacturing, designs 1 and 2 were neglected and design 3 has been further developed. Design 3 is a combination of L-shaped brackets made from aluminium and was inserted in the wings gap created by the foam cutter during manufacturing. In addition, it is a more effective design compared to design 1 since it helped to prevent any turbulence caused by the mount itself. For the tail mount, a simple square shaped bracket was manufactured and can rigidly hold the fuselage during the test. This is shown in figure 3.19.

As mentioned earlier, the main struts are manufactured by using aluminium strips with $3mm$ thickness, therefore they are quite flexible. Although this design requires the least amount of material and time to manufacture, it still has its own limitations because of the 90 degree bends which cause the mount to be highly flexible. At 0 degree pitch, it may not cause a problem but as the angle increases or decreases, flutter may occur due to the airflow. Therefore, FEA was conducted by using Solidworks software in order to investigate the best possible strengthener option to avoid such problem.

Finite Element Analysis

Without any strengtheners, FEA was conducted on the wing mount solely with distributed downward force at $10N$ acting on section B; section B is shown in figure 3.20(left). Since the maximum weight of the glider system is $2.7kg$ and the glider is mounted at 3 different points, this means that each point

should hold a force of:

$$\begin{aligned} 2.7kg &= 26.5N \\ \frac{26.5N}{3} &= 8.83N \\ \text{Factor of safety} &= \frac{10.00N}{8.83N} \\ &= 1.1 \end{aligned}$$

The FEA results show that without the strengtheners, the maximum displacement of the wing mount will be $15.33mm$ (the purple arrows in figure 3.20 show the original position of the mount without any load) and maximum stress of $159MPa$ located at the hole which connects the mount to the strut. It has been decided that two strengtheners need to be installed to reduce this effect as shown in 3.20(left).

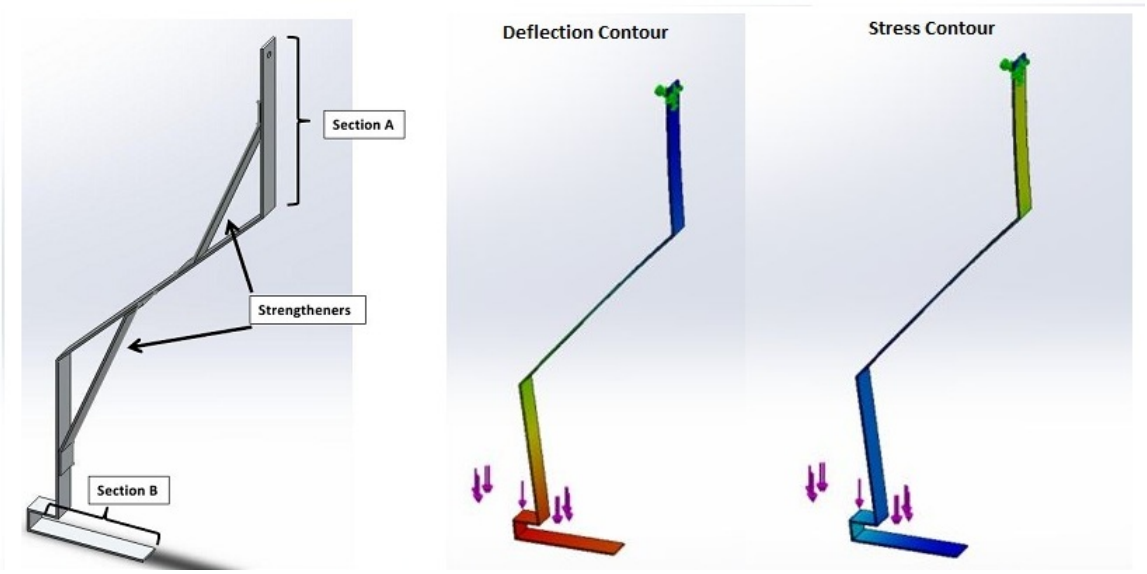

Figure 3.20: Final wing mount design(left), FEA Results- Maximum deflection (Centre) and Maximum stress (Right)

It is found from the analysis that the length of the strengthener did influence this property of the mount. To reduce the maximum displacement as much as possible, it is preferred to have the strengtheners as long as possible, as shown in figure 3.21. The resulting length used is $150mm$. By having this strengthener, the maximum displacement can be reduced by 70.12 % from $15.33mm$ to $4.575mm$ (with length of section $A = 150mm$). Another reason that drove this decision is the value of the maximum stress, with the strengthener, this value decreases from $159MPa$ to $131MPa$ which would reduce the probability of structure failure for the mount, seen in figure 3.21.

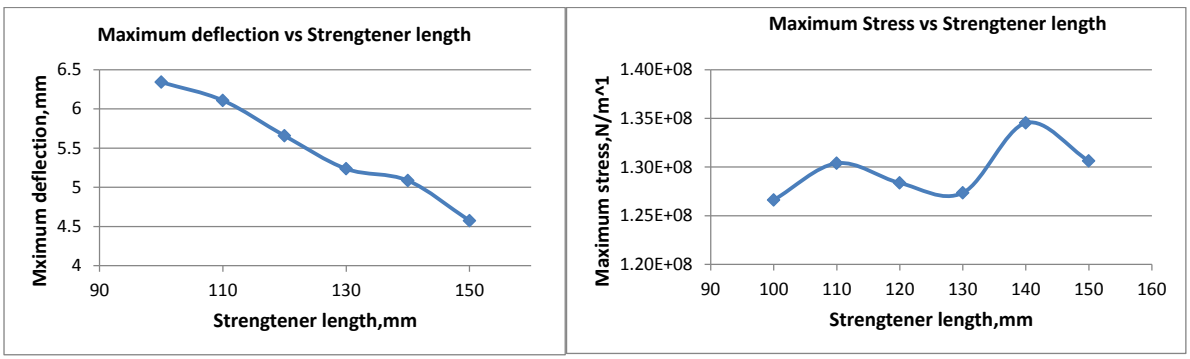

Figure 3.21: Variation of maximum deflection and stress with strengthener length (length of section $A = 150mm$)

Further investigation has been conducted to modify the strut to obtain the lowest maximum displacement as possible. The result shows that reducing the length of section A will reduce the maximum displacement as well. The length of section A equals to $125mm$, the maximum displacement is reduced to $3.084mm$, seen in figure 3.22. However, although the maximum stress increases to $135MPa$, no structure failure occurs.

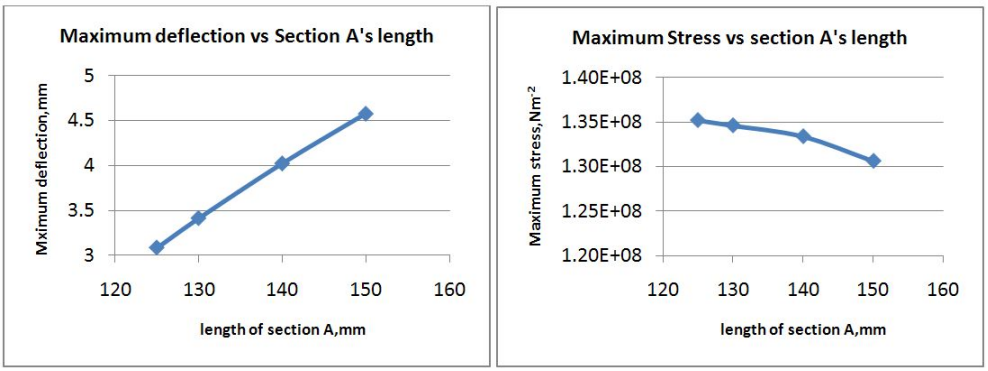

Figure 3.22: Maximum deflection and stress for section A

In conclusion, the final dimension for the investigated features of the wing mount that will give least possible maximum deflection is as follows:

- Length of strengthener = $150mm$
- Length of section A = $125mm$

3.12.2 Wind Tunnel Analysis - Kai Xi Tan

Introduction

Wind tunnel testing was done on the land glider in order to verify the theoretical values as well as improving the accuracy of theoretical calculations. A series of tests were undertaken to determine the stability of the glider, its coefficient of lift (C_{L_α}) and coefficient of drag equation(C_{D_α}) with respect to angle of attack (AOA), the net lift and thrust produces and max $\frac{L}{D}$ at different velocities. The tests were done over air velocities of $5ms^{-1}$, $10ms^{-1}$, $15ms^{-1}$ and $20ms^{-1}$. At $5ms^{-1}$ and $20ms^{-1}$, a basic test to vary the AOA of the glider was undertaken. The same basic tests were done for air velocities of $10ms^{-1}$ and $15ms^{-1}$, but also with varying motor levels 0%, 50% and 100%. At $10ms^{-1}$, tests elevator input against AOA was also done.

Lift

Based on Figure 3.23, there is a visible increase in lift as the air velocity increases. However, the plots do not provide any more additional interesting information. Therefore, the results are normalized to C_L and plotted against AOA in degrees. Based on the results, despite the increase in lift, the C_L values are independent of air velocity and only vary with AOA. From the plot, an average C_{L_α} can be obtained. The C_{L_α} is 0.0076. Furthermore, Figure 3.24 shows that the lift does not change significantly as the motor input changes and therefore can be ignored in the lift analysis.

Drag

Based on figure 3.25, the drag increases as the velocity increases. Similarly to the lift plots, the C_D remains similar despite the change in air velocities. However, in comparison to the lift case, when the motor is turned on, the resultant drag become negative, which means thrust is produced. Even so, the thrust curve gradient is still similar to the no motor case. This is shown in figure 3.26. At higher velocities, the motor appears to become less efficient as more drag is produced. The C_{D_α} for different conditions are shown in Table 3.3.

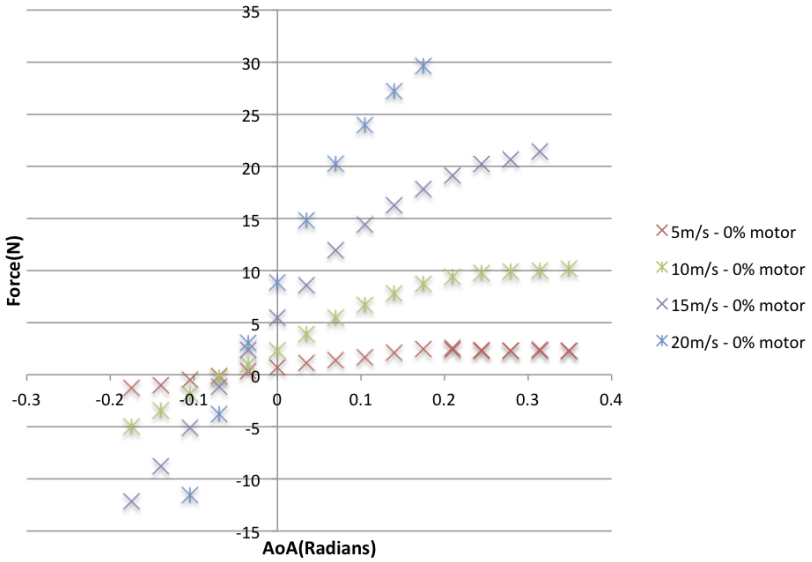

Figure 3.23: Lift against AOA plot

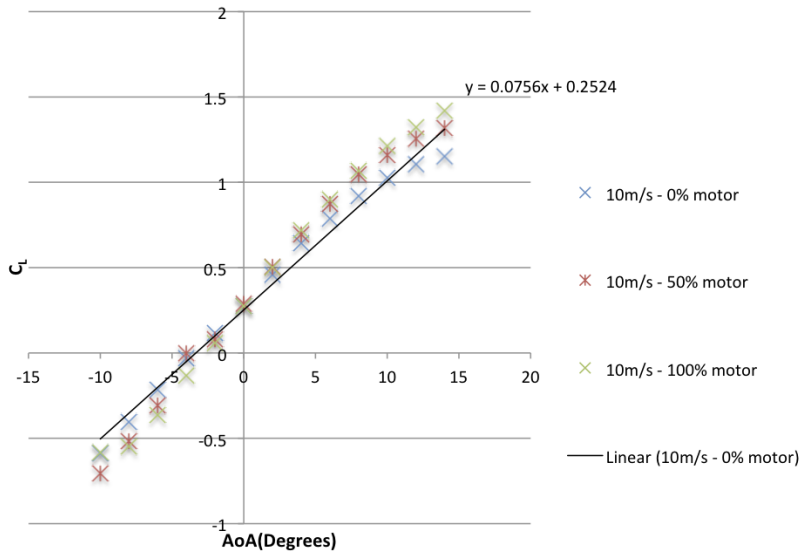

Figure 3.24: C_L against AOA plot for different motor inputs

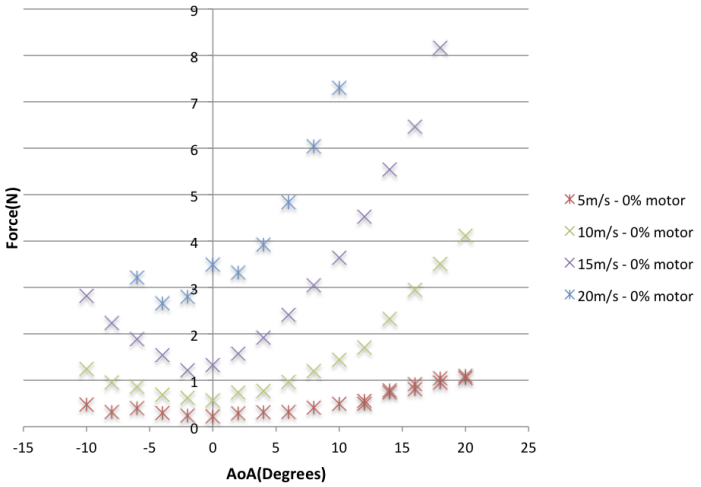

Figure 3.25: Drag against AOA plot

Air velocity(ms^{-1})	Motor input(%)	C_{D_α}	
		x	1
5	0	0.002	0.001
10	0	0.002	0.0013
10	50	0.0026	-0.0012
10	100	0.0034	-0.0102
15	0	0.0018	0.0022
15	100	0.0024	-0.0008
20	0	0.0016	0.0044

Table 3.3: C_{D_α} at different air velocities and motor inputs

Glide Ratio
The glide ratio is determined by the $\frac{L}{D}$ ratio of the glider. The higher the ratio, the better the glider's ability to glide. As turning on the motor would change resultant drag reading in the wind tunnel test to thrust, the $\frac{L}{D}$ curve is not a suitable analysis and provides no useful information. Furthermore, there is no significant increase in the lift with varying motor inputs, the $\frac{L}{D}$ curve would not change significantly if the no motor case's drag was used. However, based on Figure 3.27, the $\frac{L}{D}$ of the glider changes as the velocity changes. The main variable that is analysed is the maximum $\frac{L}{D}$ at certain air velocities and its respective AOA. This variable will show the best glide ratio that the glider can maintain at that velocity. The table 3.4 shows the maximum $\frac{L}{D}$ and its respective AOA for different air velocities.

Air velocity(ms^{-1})	AOA(°)	$\frac{L}{D}$ max
5	8.7	4.7
10	7.6	7.9
15	6.5	6.2
20	5.9	5

Table 3.4: Maximum $\frac{L}{D}$ at different air velocities

Net Lift
The net lift and net thrust with respect to the glider were calculated to determine if the glider is able to climb. The lift was calculated using the following formula:

$$L_{aircraft} = L\cos(\alpha) - D\sin(\alpha) \tag{3.8}$$

The net lift is:

$$\text{Net Lift} = L_{aircraft} - W\cos(\alpha) \tag{3.9}$$

The results are then plotted onto a graph as shown in Figure 3.28. Based on the graph, it can be seen that the net lift increases as the air velocity increases. Moreover, positive lift at positive AOA can be seen at $15ms^{-1}$ which means that the glider is able to climb if it can maintain its velocity during the climb. As expected, there is no significant difference in net lift when varying the motor input as shown in Figure 3.29.

Net Thrust
Similarly to the net lift, the net thrust is calculated by:

$$D_{aircraft} = D\cos(\alpha) - L\sin(\alpha) \tag{3.10}$$

$$\text{Net thrust} = -(D_{aircraft} + W\sin(\alpha)) \tag{3.11}$$

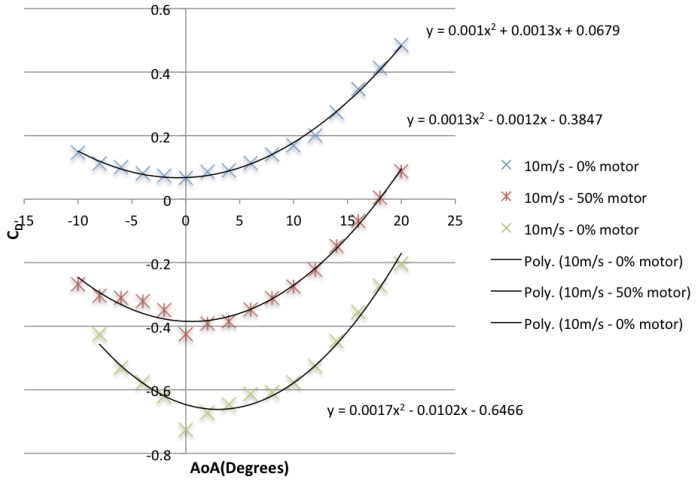

Figure 3.26: C_D against AOA plot for different motor inputs

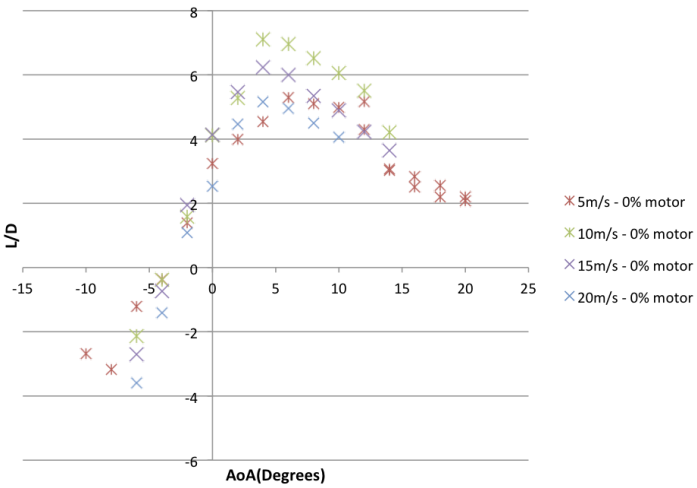

Figure 3.27: $\frac{L}{D}$ against AOA plot

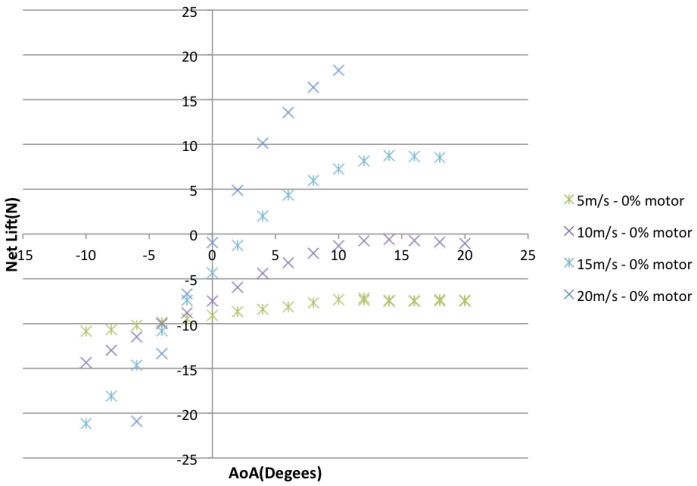

Figure 3.28: Net lift against AOA plot

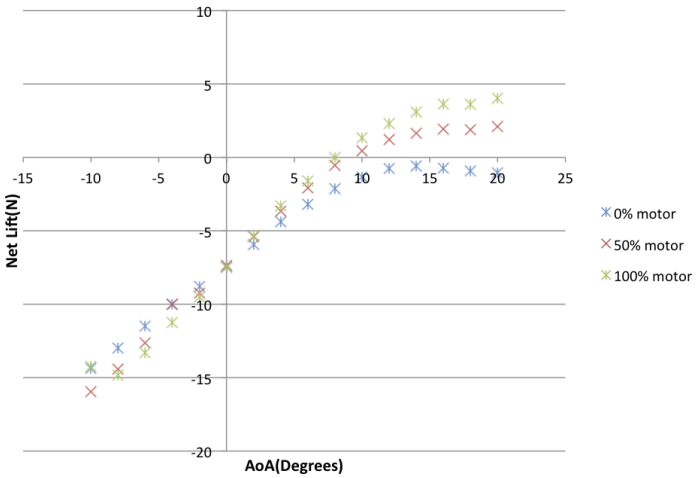

Figure 3.29: Net lift against AOA plot for different motor input

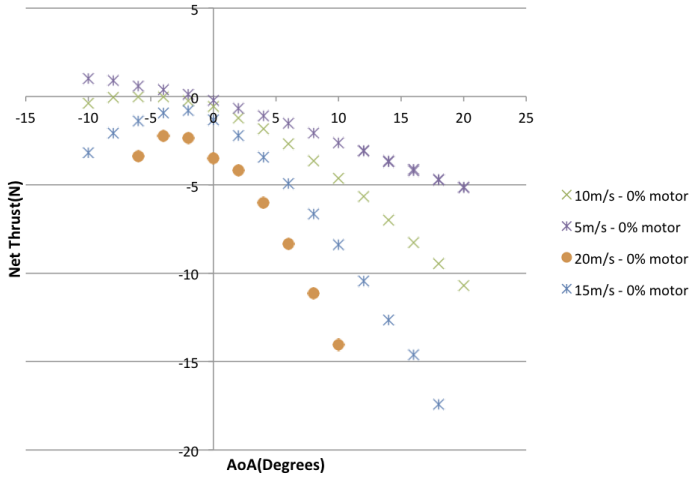

Figure 3.30: Net thrust against AOA plot

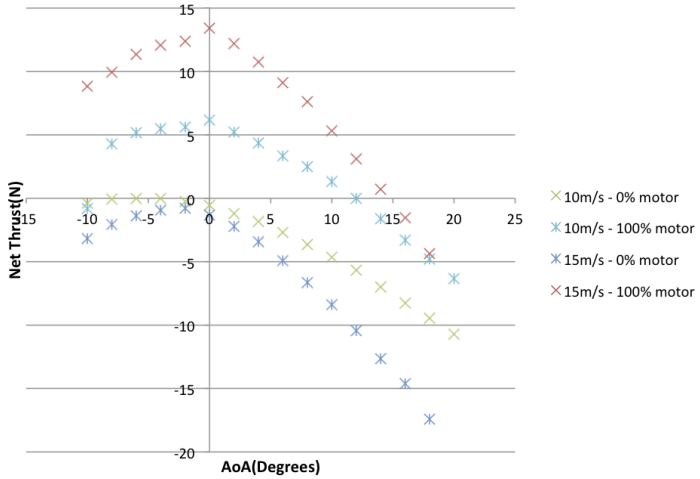

Figure 3.31: Net thrust against AOA plot for 0% and 100% motor input

The results are then plotted onto a graph as shown in Figure 3.30. The graph shows that without motor input, a high velocity ($\geq 20ms^{-1}$) is required to produce positive net thrust at positive AOA. As shown in Figure 3.31, with motor inputs however, the net thrust curve is displaced upwards significantly and positive thrust is achievable at positive AOAs. Based on the results obtained from the wind tunnel, it is estimated that the glider is able to glide at $12ms^{-1}$ with at least 50% motor input. This estimation however, is just an interpolation estimate.

Stability
Another aspect that was analysed was the stability of the glider. In order to determine if the glider is stable, a graph of C_M against AOA is plotted. If the gradient of the plot is negative, then the glider is said to be stable. The plotted graphs at varying air velocities as well as different motor inputs are shown in Figure 3.32 and Figure 3.33. The gradient of the C_M slope does not change significantly with increasing motor input, but the plotted line is displaced lower down the graph as the motor input increases. This means that as the motor input increases, the glider is more likely to want to pitch upwards and climb. Having said so, the C_M line is still negative. Therefore, the glider is still stable when the motor is in use.

Control Surfaces
As elevators have been added to the glider, it is important to determine if the size of the elevators are sufficient to pitch the glider. Similar to determining the stability, the C_M is calculated and plotted against AOA at no elevator input, 100% upwards elevator input and 100% downwards elevator input. The plotted graph is as shown in Figure 3.34. Based on the graph, there is a displacement in the C_M line between no elevator input and with elevator input. As an upwards elevator input results in displacing the C_M line upwards and vice versa, it proves that the elevators are sized sufficiently to produce a moment force to pitch the glider.

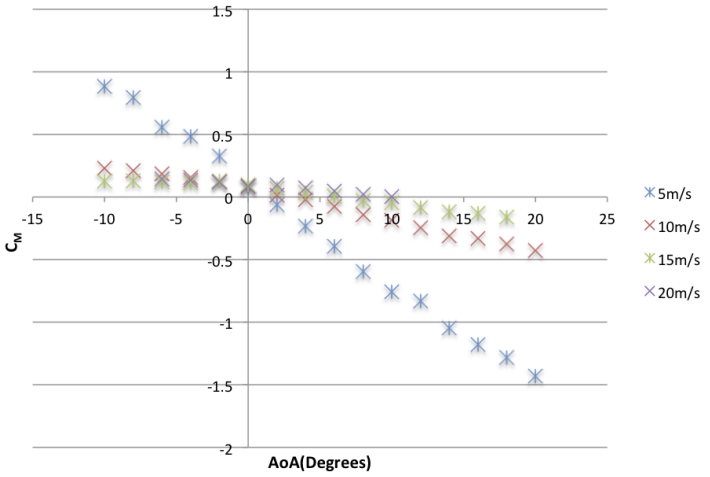

Figure 3.32: Cm against AOA plot

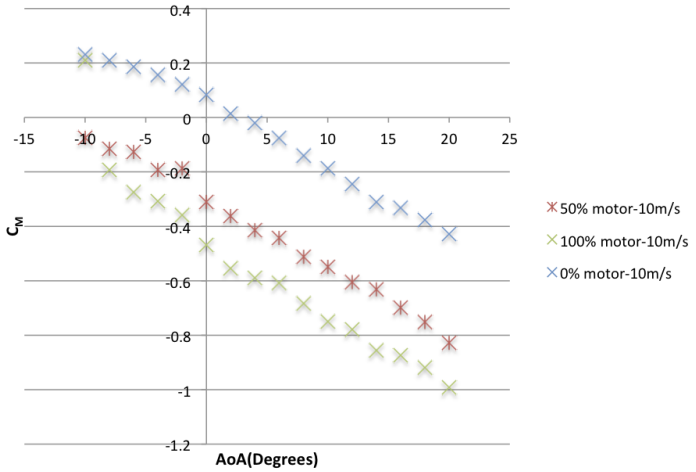

Figure 3.33: Cm against AOA plot for different motor inputs

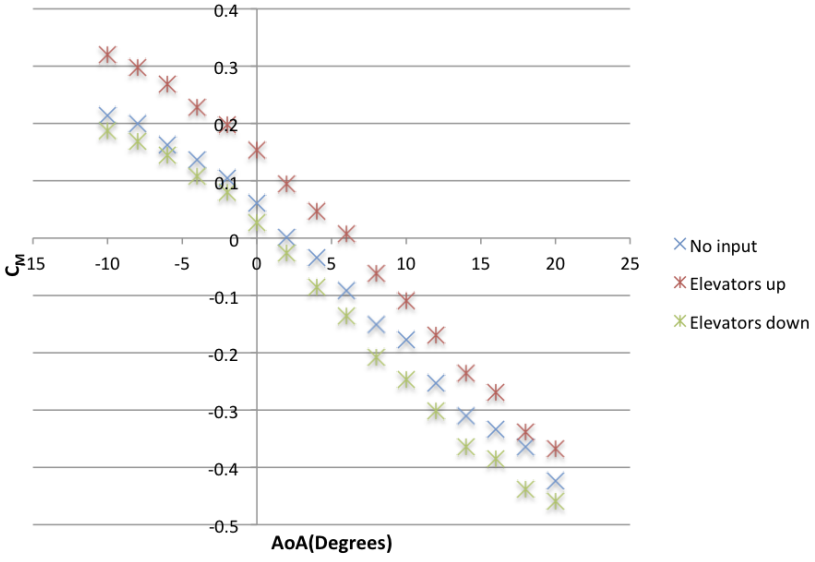

Figure 3.34: Cm against AOA plot for elevator inputs

3.13 Manufacturing - Anas Bari

The major modification works on the existing glider model include: making a new horizontal tail section, adding elevators, drilling holes for motor mounting, wires and servos.

Horizontal Tail Section and Elevator
The horizontal tail and elevators were fabricated with the same aerofoil section and foam as the existing glider which are NACA 0012 and EPP foam respectively. The choice of NACA 0012 was the same as last year as the hole in the tail at the fuselage was cut based on NACA 0012 profile shown in Figure 3.35.

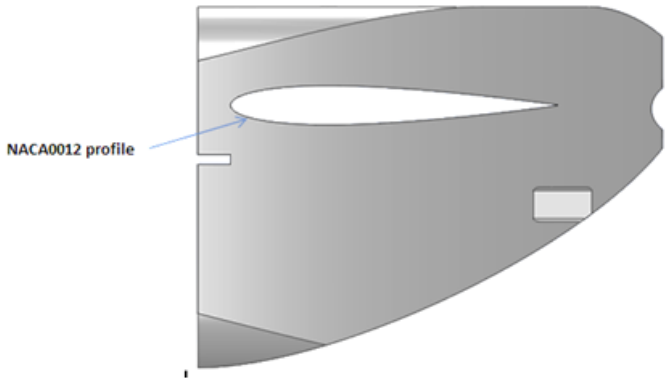

Figure 3.35: Hole to mount the horizontal tail with NACA 0012 cutting profile

The horizontal tail and the elevators are made of EPP foam which has been cut using hot wire CNC foam cutting machine. Both of these sections are made by sandwiching two half-aerofoil sections together. For the tail section, a carbon rod was glued between the sections as a spar to increase the structural integrity. Then the trailing edge was cut in order to provide a section for the elevator installation. At the trailing edge, a thin layer of balsa wood was glued in order to reinforce this section so that it can withstand the elevator loading and hence avoid structural failure (Figure 3.36).

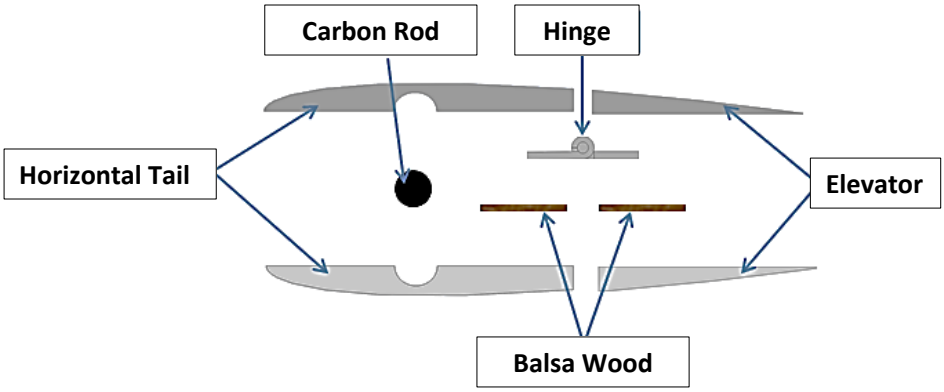

Figure 3.36: Structure of the Horizontal Tail

The main issue encountered during the process of cutting was the very thin aerofoil section at the trailing edge. This was because it is difficult to predict how much the foam will melt around the wire. Due to this reason, the initial aerofoil was scaled by a factor of 1.1 in order to avoid this problem.

Hole Drilling
The holes for the servos, wires and motor mount are drilled using a pillar drill. The dimension for the motor mount hole is 35mm deep and 11mm in diameter. Once completed, the motor mount was glued in the cavity. The servo holes are cut mainly by knife in order to get clean edges. The holes are cut based on the dimension of the servo which is $22.1mm$ X $10.9mm$.

3.14 MatLab Flight Prediction - Izdihar Zuhdi

The main objective of this part is to develop a mechanism that predicts how the glider would fly when released from different starting conditions and altitudes. This information was needed to predict the forces experienced by the glider so that the airframe could be engineered to the required specifications [47]. The script is useful to predict the range that can be achieved from the designed glider. It was also important to gather data such as the velocity profile to size the aerodynamic surfaces to determine the required lift of the glider [47]. A time stepping method using the implicit Euler integration method was implemented throughout the solution from initial conditions.

3.14.1 Simulation Setup

The problem was approached in the same way as in the previous year's (GDP16 2012) flight predictor. A model of the sea glider and the forces acting upon it, shown in fig. 3.37, was used to derive the dynamic equations.

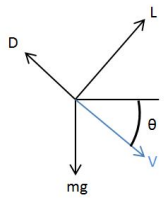

Figure 3.37: Force balance model of sea glider[47]

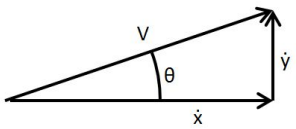

Figure 3.38: Resolving the velocity into components[47]

From figure 3.37, the horizontal and vertical force balances are as below:

$$m\ddot{x} = Lsin\theta - Dcos\theta \tag{3.12}$$

$$m\ddot{y} = Lcos\theta - Dsin\theta - mg \tag{3.13}$$

The lift, L and the drag forces, D are found using eq. (3.14) and eq. (3.15)

$$L = \frac{1}{2}\rho V^2 S C_L \tag{3.14}$$

$$D = \frac{1}{2}\rho V^2 S C_D \tag{3.15}$$

By substituting eq. (3.14) and eq. (3.15) into eq. (3.12) and eq. (3.13), the equation becomes:

$$\ddot{x} = \frac{1}{2m}\rho V^2 S(C_L sin\theta - C_D cos\theta) \tag{3.16}$$

$$\ddot{y} = \frac{1}{2m}\rho V^2 S(C_L cos\theta + C_D sin\theta) - g \tag{3.17}$$

Equations 3.16 and 3.17 are the main dynamic equations in this simulation. Both V and θ are calculated by resolving both the vertical and horizontal velocities as shown in fig. 3.38.

As for the powered glider system, the thrust from the motor will give an additional force. The forces for the powered glider are depicted in fig. 3.39.

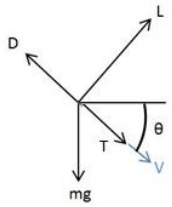

Figure 3.39: Force balance model of land glider[47]

With the thrust, the dynamic equations for the powered glider system becomes:

$$\ddot{x} = \frac{1}{2m}\rho V^2 S(C_L sin\theta - C_D cos\theta) + \frac{T}{m}cos\theta \tag{3.18}$$

$$\ddot{y} = \frac{1}{2m}\rho V^2 S(C_L cos\theta + C_D sin\theta) - \frac{T}{m}sin\theta - g \tag{3.19}$$

The Process of Time Stepping
A time stepping process using implicit Euler integration method was used to solve these equations during the entire flight [47]. This method approximates that the velocities and the positions are linear between the individual time steps and so the errors decrease as a smaller time step is used. For this simulation a timestep of 0.1 seconds is used.
The first calculation performed in each time step is to estimate the glide angle from the current step velocities. This was done using eq. (3.20) which can be derived from fig. 3.38. The inverse of vertical velocity was used because the vertical position is defined relative to the ground while the glider glides in the opposite direction.

$$\left[\theta = tan^{-1}\frac{-\dot{y}}{\dot{x}}\right]_n \tag{3.20}$$

In the event that the horizontal or vertical speed is zero the following equations are resorted to preventing trigonometric errors.

$$\left[\theta = sin^{-1}\frac{-\dot{y}}{\sqrt{\dot{y}^2}}\right]_n \tag{3.21}$$

$$\left[\theta = cos^{-1}\frac{\dot{x}}{\sqrt{\dot{x}^2}}\right]_n \tag{3.22}$$

The next stage is using the current time step's velocity and glide angle derived from it's components to calculate the acceleration they would produce from the dynamic equations.

$$\left[\ddot{x} = \frac{1}{2m}\rho V^2 S(C_L sin\theta - C_D cos\theta)\right]_n \tag{3.23}$$

$$\left[\ddot{y} = \frac{1}{2m}\rho V^2 S(C_L cos\theta + C_D sin\theta) - g\right]_n \tag{3.24}$$

For the land system, these equations can be written as

$$\left[\ddot{x} = \frac{1}{2m}\rho V^2 S(C_L sin\theta - C_D cos\theta) + \frac{T}{m}cos\theta\right]_n \tag{3.25}$$

$$\left[\ddot{y} = \frac{1}{2m}\rho V^2 S(C_L cos\theta + C_D sin\theta) - \frac{T}{m}sin\theta - g\right]_n \tag{3.26}$$

With these accelerations, the next time step's velocities, positions and thus glide angles can be calculated.

$$[\dot{x}]_{n+1} = [\dot{x}]_n + dt\,[\ddot{x}]_n \tag{3.27}$$

$$[\dot{y}]_{n+1} = [\dot{y}]_n + dt\,[\ddot{y}]_n \tag{3.28}$$

$$[V]_{n+1} = \left[\sqrt{\dot{x}^2 + \dot{y}^2}\right]_{n+1} \tag{3.29}$$

$$[x]_{n+1} = [x]_n + dt\,[\dot{x}]_n + dt^2\,[\ddot{x}]_n \tag{3.30}$$

$$[y]_{n+1} = [y]_n + dt\,[\dot{y}]_n + dt^2\,[\ddot{y}]_n \tag{3.31}$$

Atmospheric Changes with Altitude
The standard atmosphere of the Earth does not remain constant in composition at different altitudes due to factors such as gravity and weather systems [47]. These variables will influence the density of the air at different altitudes thus give an aerodynamic impact on the flight which influences the dynamic simulation. In order to consider this, it was necessary to develop approximate equations relating the density to the altitude. A 6^{th} order polynomial fit was applied to the International Standard Atmosphere 1967 data [9] to produce the density equation.

$$\rho = -3.0\times10^{-28}y^6 + 5.2\times10^{-23}y^5 - 3.0\times10^{-18}y^4 + 3.4\times10^{-14}y^3 + 2.8\times10^{-9}y^2 - 0.0001y + 1.225 \tag{3.32}$$

After the glide angle and before the accelerations are calculated, the density for the current altitude is calculated and used in eq. (3.23) and eq. (3.24). This step is important because density affects the lift and drag force that the glider produces thus affecting the horizontal and vertical acceleration at each time step.

3.14.2 Aircraft Parameters

The simulation also requires various parameters from the aircraft. These need to be accurately gathered as they have a large influence on the outcome of the simulation.
The aerodynamic properties of a surface or object can be summarised in coefficients relating flow conditions and scale to the objects performance of generating forces[47]. The coefficient of lift, C_L was required to determine its capability of generating a force perpendicular to the flow and likewise the coefficient of drag, C_D determines the drag produced [47]. Due to these coefficients having a significant impact on the solution, they needed to be determined very accurately [47]. These were obtained via wind tunnel experiments on the whole aircraft. The results was then curve fitted to get an equation that relates the values of C_L and C_D at a specific angle of attack.
There are a few assumptions made for the powered glider in simulating the thrust from the motor. The motor was assumed to provide a constant thrust throughout the entire flight until the battery runs out. For simplicity, the battery was assumed to have a constant discharge rate until it runs out. The speed of the wind was assumed to have no effect on the performance of the propeller.

3.14.3 Validation

In order to validate the reliability of the MATLAB script, the simulation data was compared to the test data obtained from Draycott flight test. Ideally, the simulation data should be compared to data obtained from full autopilot mode during the test to ensure that all the commands that have been programmed into the autopilot can to be included in the script. However, this was not possible due to the constraints of the flight test and the reasons discussed in section 7.2.4. As a result, the simulation result was compared to manual flight test data.

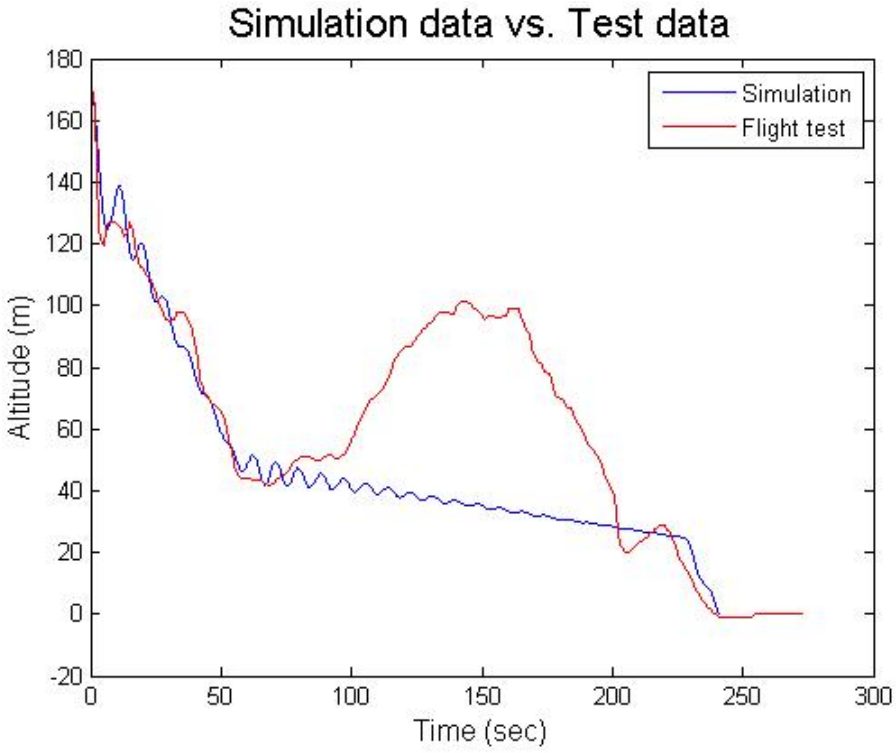

Figure 3.40: Comparison between simulation data and test data

The graph shows that there is a good agreement between the simulation and the test data from the initial release until it recovers from the dive. The glider climbs from $45m$ to $100m$ at t = $100s$ to t =$150s$. The large lift experienced by the glider was due to high wind speed at the test field. In addition, the test flight was testing the use of the motor and the ability of the aeroplane to climb during flight. In the simulation, the glider is modelled to be in still air because the wind factor was not considered. This contributes to the huge difference between these two data sets during the later phase of the flight.

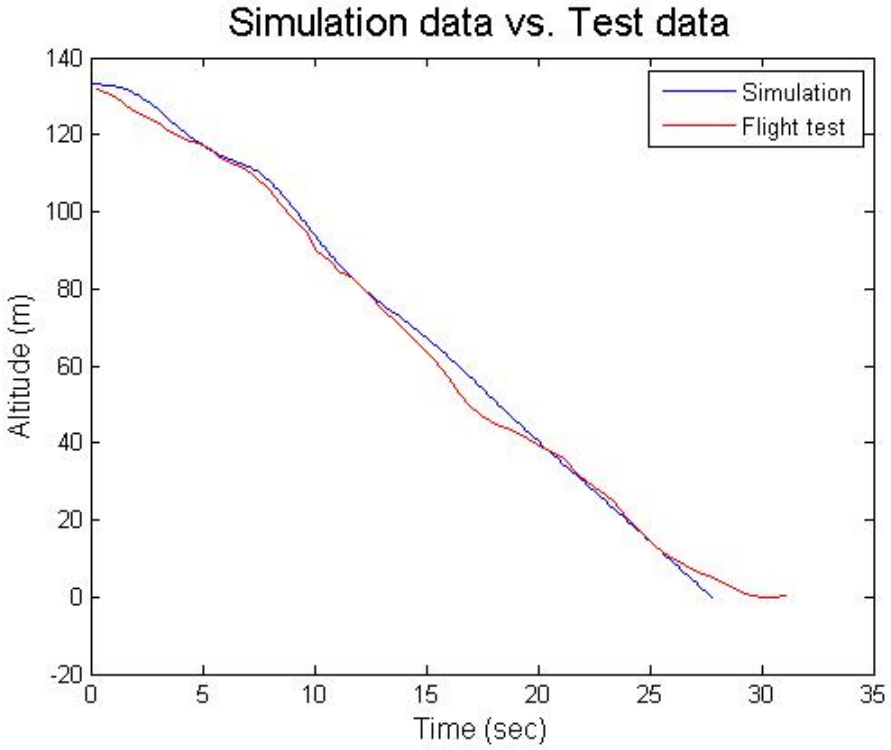

Figure 3.41: Comparison between simulation data and test data using GDP16 2012 aircraft parameter

Since there were uncertainties during the test, the MATLAB script was compared with flight data obtained from GDP16, 2012 to further prove the reliability of the code. The aircraft parameters and the initial conditions obtained from the GDP16 2012 project report were used as the input for the code.The graph (fig. 3.41) shows a good agreement between the test and simulation data. This proves the reliability of the code.

3.14.4 Data Analysis

Powered Glider
The MATLAB script was also used to compare the performance between powered glider and GDP16 2012's glider. Both of the flights were set to start at $170m$ from the ground with zero initial velocity and the gliders were placed in nose down position.The graph(fig. 3.42) predicts that the modification done to the GDP16 2012 glider will extend the flight time by around 300%. It also predicts that the powered glider is able to climb.

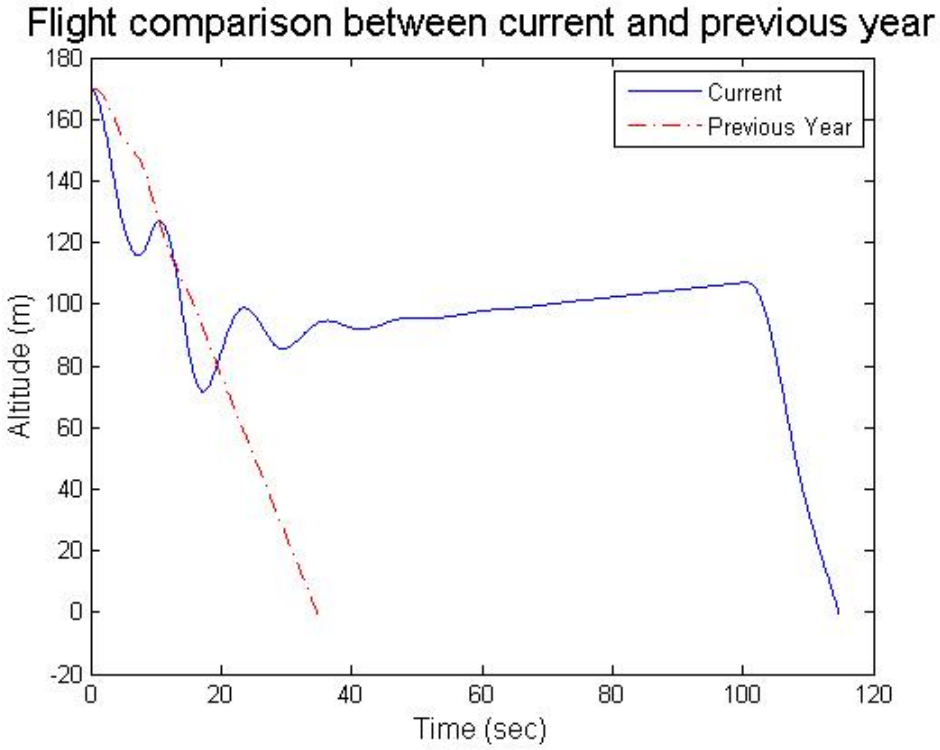

Figure 3.42: Comparison between simulation data and test data using GDP16 2012 aircraft parameter

Balloon Launched Lagrangian Drifter

The MATLAB script was also used to predict the flight profile, distance travelled and velocity profile for the balloon launched Lagrangian drifter. The glider was set to be in vertical position with nose pointing to the ground at 10,000m from the ground during release. It was also assumed to be launched from a stationary position.

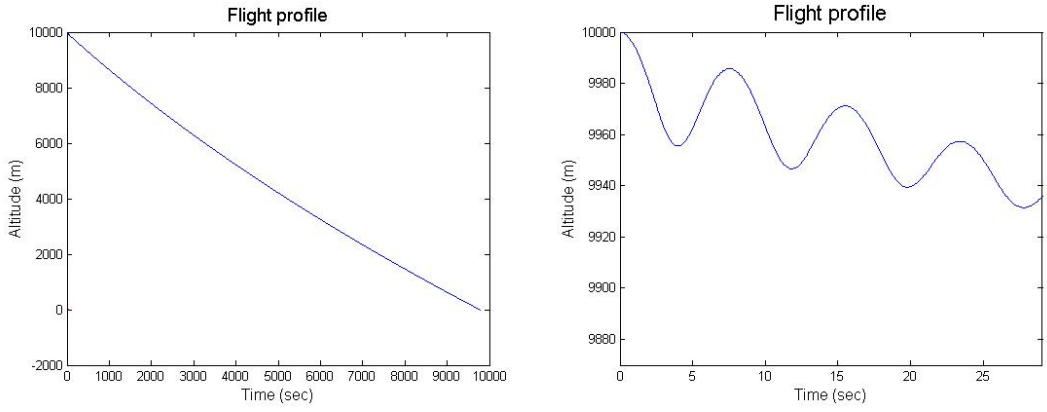

Figure 3.43: Flight profile for the balloon launched Lagrangian drifter

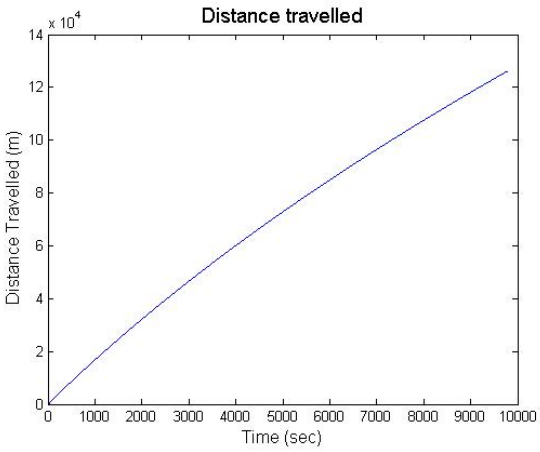

Figure 3.44: Distance travelled by the balloon launched Lagrangian drifter

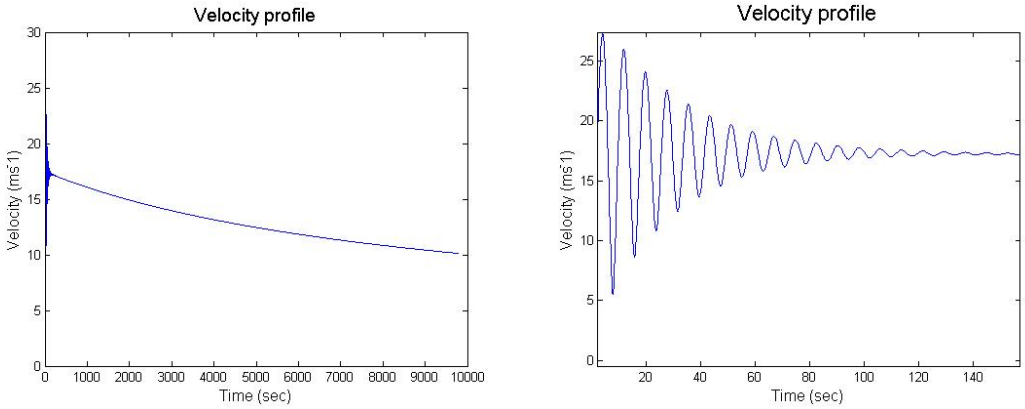

Figure 3.45: Velocity profile for the balloon launched Lagrangian drifter

The simulation predicts that the average glide ratio that can be achieved by the glider is around 13 as seen in fig. 3.44. It can be seen that there are oscillations in the flight profile and velocity profile during the initial stage of the flight. This was mainly due to a constant step size used during the integration process. A larger step size can reduce the frequency of the oscillation but results larger errors. The graph also proves that the glider is dynamically stable, as eventually the oscillation is damped, allowing the glider to enter a steady flight state.

Further Improvements
As mentioned earlier, the simulation developed has a small anomaly. The oscillation in the flight and velocity profile can be eliminated using adaptive step sizing control in the integration scheme. A few integration scheme such as the fourth order Runge-Kutta integrator and time adjusted Verlet integrator has been considered to eliminate this error. However, due to time constraints, the simulation was not further developed in this project.

3.15 Piggyback Release Attachment - Ksenjia Dvurecenska

Based on the positive experience of the previous year's project, the piggyback attachment was used to release the glider from the carrier plane during flight tests. The attachment was redesigned to be more flexible in regard to the width of glider, as initially it was planned to use one piggyback mechanism for both gliders in this project to avoid having two separate release methods. The design is shown in fig. 3.46.

The piggyback attachment was made out of Styrofoam-LB and was cut using the hot wire CNC cutter. To make it adjustable in width, it is made out of two halves connected by rubber bands. This allows it

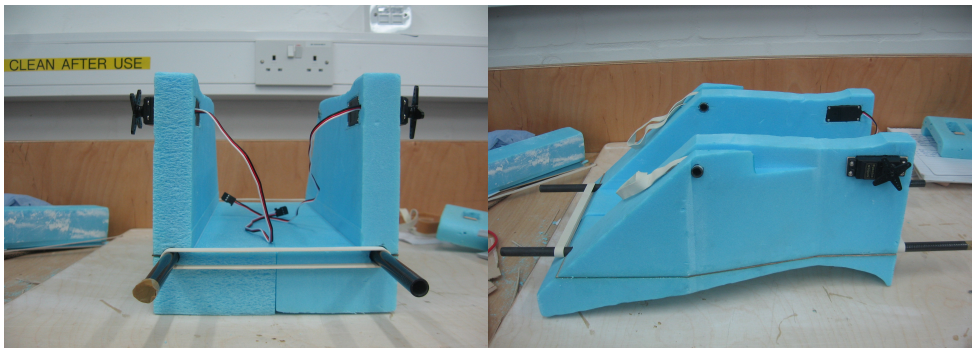

Figure 3.46: Piggyback design

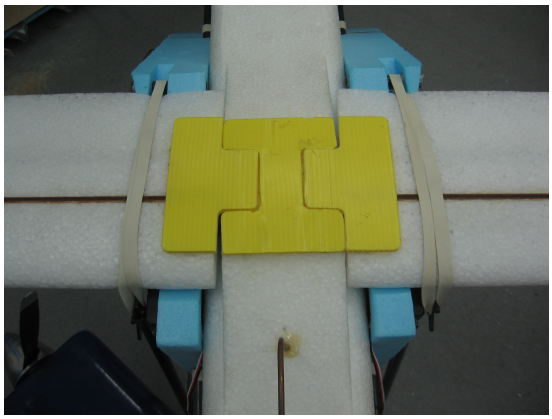

Figure 3.47: Glider attachment

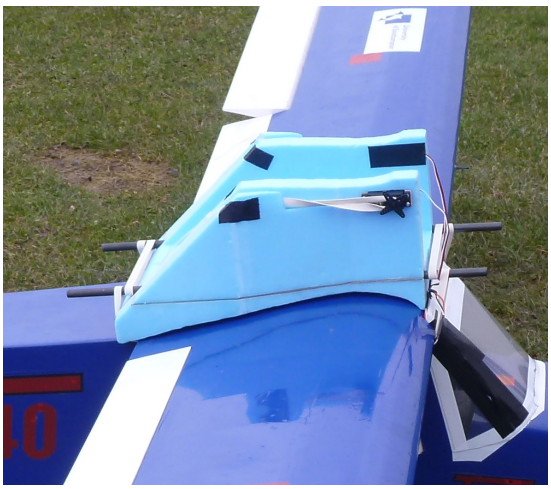

Figure 3.48: Piggyback attachment

to accommodate gliders with wider fuselages by simply adding a block of foam of required size between the two halves.

Rubber bands are used to hold both, the piggyback mechanism in place on the wing of the carrier plane and to hold the glider down during ascent as shown in fig. 3.47. Once the carrier plane reaches the required height and maintains level flight, the servo horns are rotated to release rubber bands that hold the glider. To account for a stress generated by rubber bands counteracting the lift generated by the glider wing, servos are securely screwed in place. Servos are controlled by the same controller as the carrier plane so that the pilot can release it when ready.

Figure 3.49: In-flight

4 | Balloon Launched Lagrangian Drifter

4.1 Project Brief

The aim of this section of the project is to design, manufacture and test a balloon launched Lagrangian ocean drifter capable of measuring the ocean current velocity at a depth of $10m$ and relaying the data by satellite uplink for a duration of up to three weeks. The system should be launched from a "standard" weather balloon with a maximum payload of $2.7kg$[103]. It should deploy and descend in a controlled manner, landing within a $20km$ range from a predefined target. The purpose of the balloon launched Lagrangian drifter is to offer an alternative low cost system to current methods of deployment for Lagrangian drifters.

4.2 Background - Robert Gillman

4.2.1 General Overview of Current Drifters

For many hundreds of years the ocean has played a vital part in the transportation of key resources. Since the start of ocean shipping, crude drifting observations have been conducted in the simplest of forms with the aims of tracking ocean currents. In the 19th century weighted bottles were launched with a message inside stating the launch position, time and date and relying on communication from where it was found washed up. This evolved to measurement of subsurface currents by attaching a sea anchor(drogue) to the bottle at the required depth and triangulating its position relative to a fixed point. With the birth of radio communications drifters were fitted with small above water antennas and their positions triangulated from onshore listening stations. In the 1970's with the early use of GPS navigation; NIMBUS and ARGOS satellites were used to relay drifter data. In 1982 the World Climate Research Program (WCRP) recognised the potential for a global deployment of multiple ocean drifters to aid oceanographic and climatic research. The Atlantic Oceanographic & Meteorological Laboratory (AOML) set about, under the Surface Velocity Program (SVP), designing a "lightweight, low cost" standardised drifter. The "lightweight" solution had a fibreglass surface float and cylindrical, nylon cloth drogue with diameters of $40cm$ and $100cm$ respectively with a mass of $45kg$. In 2003 the SVP mini was designed which reduced the float diameter to $32cm$, drogue diameter to $61cm$ and mass to $15kg$. Currently this is the most common SVP Lagrangian Drifter with a number of companies offering similar variants. Drifters are deployed either by launching from a ship or release from a C-130 Hercules. [68]

What are Lagrangian Drifters?
A Lagrangian Drifter is a means of measuring ocean current data at a specified depth in a Lagrangian co-ordinate system. This means the drifter moves under the motion of the water particles in time and space, i.e. at the same velocity of the water at the depth being measured. The alternative to a Lagrangian approach would be an Eulerian co-ordinate system which would involve measuring the drift from a fixed reference point, as was done historically.

In general, drifters consist of three main parts; the surface float, tether and the drogue. The surface float contains; batteries, transmitter, thermistor and a custom sensor payload. The payload often includes instruments for measuring: barometric pressure, wind speed and direction, salinity, water line and tether strain to verify the presence of the drogue.

To achieve a Lagrangian approach, a drogue is attached to the surface buoy at a fixed depth. The drogue has a large surface area to prevent the wind and surface currents acting on the float from significantly

influencing the drifter direction. For the drogue to be deemed effective, an approximate frontal drag area ratio of drogue to non-drogue elements should be larger than 40. [85]

4.3 Literature Review

A literature study was completed in an attempt to establish drifter design requirements and gain an understanding of what compromises would have to be made to meet the project aims and objectives. The review provides a brief overview on current SVP Lagrangian drifters, alternative drifter designs, alternative drogue designs and current UAVs for oceanographic applications.

4.3.1 Surface Velocity Program Lagrangian Drifters

Case Study on Microstar SVP Lagrangian Drifter - Robert Gillman
The Microstar SVP Lagrangian drifter was designed and manufactured by Pacific Gyre to assist the Global Drifter Program. The aims and objectives of the global drifter program are to maintain satellite tracked surface drifting buoys in order to accurately measure; mixed layer currents, sea surface temperature, atmospheric pressure, local wind speeds and water salinity. The global drifter program also provides a central data processing resource for national organisations such as the UK Met office. The data obtained is used to provide validation to computational studies and to aid predictions of future climatic change. [85]

The SVP Lagrangian drifter is designed to measure mean ocean currents at a pre-set depth over a duration of 1 week up to 1 year. The Pacific Gyre SVP drifter is able to measure the ocean currents by means of a drogue from $5m$ down to $100m$ below the ocean surface. The surface float provides buoyancy and houses the satellite uplink (Argos or Iridium), GPS receiver, antenna, batteries and oceanographic sensors. The GPS location and temperature data are transmitted by the Iridium or Globalstar system and made available online via the Pacific Gyre website. The drifter is designed to survive in the ocean for over one year, to be watertight and inert to UV. The limiting factor for operational duration is the power requirements and limitations in current battery capacity.[51]

The drogue is constructed in 4 sections of $1200mm$ from fray resistant Cordura fabric and spends the entire duration submerged in sea water. The drifter can be launched by two means: the most common is being thrown overboard of a research vessel from a maximum height of $10m$ and secondly by air-drop with a parachute. Both of these methods have high associated overheads contributing to the total drifter life cycle cost (the cost of the air drop is roughly $3000 [51]). The cost of the Microstar Lagrangian surface drifter is $3100.00 which includes a $20cm$ surface float, corner radar reflector drogue with 1m tether, Globalstar simplex telemetry, uBlox GPS receiver and replaceable alkaline $12V$ $15.6AH$ battery pack. Pacific Gyre offer additional Iridium Telemetry for $150.00 which provides complete global coverage, unlike the Globalstar simplex.

Marlin-Yug Drifters - Naveeyindren Thangarajah
Marlin-Yug is a Ukrainian company who manufacture slightly different SVP drifters from the Microstar by Pacific Gyre discussed above (section 4.3.1).

SVP-B
This system has a surface float of $41cm$ in diameter which results in higher volume and thus more space for electronics placement. It does not come with a GPS sensor, but can be manually added. The larger drogue diameter ($92cm$), as opposed to SVP mini and SVP-B mini, gives rise to larger drag area ratio of 41.0. The approximate lifetime for the SVP-B drifter is 37 months. [70]

SVP mini
The SVP mini has a smaller buoy diameter ($34cm$) and smaller drogue diameter ($61cm$) compared to SVP-B and similar drag area ratio of 39.7. It has no subsurface temperature or barometric pressure

sensors. The smaller, lighter design of $15kg$ means it can be launched by only one person. An alternative SVP-B mini is also available which includes above surface and sub surface temperature and barometric pressure sensors. [69].

SVP Surface Lagrangian Drifter

The SVP Surface Lagrangian Drifter has been developed to provide data for surface currents in coastal waters. Relative to other SVP drifters previously discussed the main difference is the drogue configuration. Instead of the standard cylindrical design, a tristar collapsible drogue is used (fig. 4.4). The tristar is an innovative folding solution that offers a high drag area for a small pack size for use where a long drogue is not suitable due to shallow water depth. The tristar drogue measures $15cm$ by $70cm$ when packed. The reason this drogue is not more commonly used for deeper water applications is that due to its compact size it will only measure the water current across a small vertical range where as, it is preferential to average across a few meters either side of the target measurement depth. This drifter system does not include sensors to measure subsurface temperature or barometric pressure. Additionally, it uses a GSM link to transmit the collected data as opposed to the preferred Iridium modem as GSM range is sufficient for shallow water applications.[71]

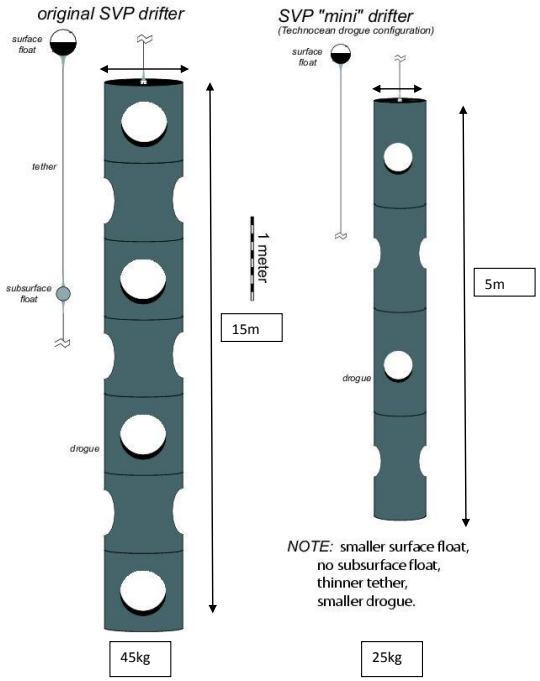

Figure 4.1: SVP original vs. SVP mini

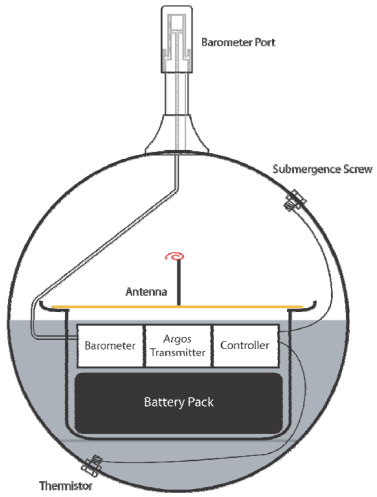

Figure 4.2: SVP Surface Float

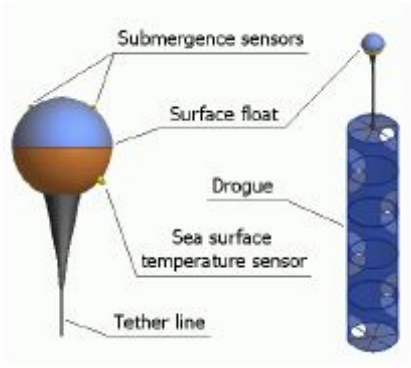

Figure 4.3: SVP Mini - Marlin Yug

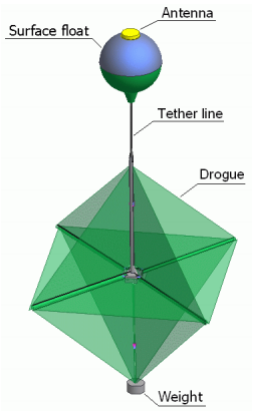

Figure 4.4: SVP Surface - Marlin Yug

4.3.2 Micro Drifters - **Robert Gillman**

Initial research has shown that SVP drifters have a common design and in their current configuration they are not suitable to form part of a balloon launched system due to their mass and dimensions. To meet the project requirements a lightweight, low cost solution was necessary. It was found that micro drifters were not commonly used for oceanographic research and instead fell into two categories; military applications and academic oceanographic projects. Additionally, the micro drifters were only used in surface or shallow water applications negating the requirement for a large drogue. The alternative design of micro drifters provided a different approach which aided the development of initial design concepts.
Neptune Sciences developed a micro sized single-use buoy, fig. 4.5 specifically designed to enable deployment from a standard countermeasure dispenser, originally designed for flares and chaff. The purpose of the design was to provide reconnaissance on surface currents close to a site of planned amphibious assault. The buoy uses a Motorola "oncore" GPS receiver to track its position and can remain operational for up to 3 weeks [77].

Figure 4.5: Neptune Science -Micro Drifter

A project by the Centre for Water Research [59] presented a compact low cost "off the shelf" GPS drifter for use in near shore shallow regions. The drifter is designed to deploy for a variable duration of a few hours up to a number of weeks dependent on the required use. It has been designed in a simplistic manner with off-the-shelf components so it can be constructed with minimal expertise in a basic workshop environment. The drifter is a $100mm$ diameter by $320mm$ long Polyvinyl chloride (PVC) drainage pipe with watertight end fittings pressure tested to a depth of $40m$. The electronics mount to an internal frame that slides into the external pipe. The GPS receiver and data logger are mounted at the top so they remain above the water line for a reliable communication link. Power is provided by seven alkaline D cell batteries which are fitted into the bottom of the casing to act as ballast and provide stability. The total cost of the unit including labour time is quoted to be $750. The micro drifter has also been modified to enable shallow $(2.5 - 8.5m)$ subsurface measurements by attaching a surf drogue (fig. 4.7). The small drogue, dimensions not provided, was stated as having a drag area ratio of 40 "due to the small scale" of the device above the water. No proof of drogue slip velocity or any design justifications were provided.

4.3.3 Existing Drogue Configurations - **Raja Nurul Yuhanis**

A drogue is a device simply used to increase the drag of an object. A common application is to deploy a drogue from a boat in order to decrease speed and keep its hull perpendicular to the waves. In an oceanographic application a drogue is weighted underwater at the required measurement depth to ensure accurate current measurements this reduces the influence of near surface current and wind shear on the surface buoy and their affect on overall drifter motion. Therefore the purpose of drogue can simply be defined as means of reducing slippage (difference) between the drifter velocity and water current of in-

terest.

Cylindrical Drogue
A cylindrical drogue is the most common design for SVP-Lagrangian drifters it is also known, and shall be referred to, as a holey-sock drogue. The holey-sock design has been a proven design for applications in the oceanographic, meteorological and oil and gas markets. The holey-sock drogue is cylindrical in shape which provides a uniform profile area from all directions, which is an advantage over a parachute drogue design. The drogue is divided into sections for ease of manufacturing, with each separated by a solid stiffening ring. Each section is designed with a pair of holes of approximately half the drogue's diameter, adjacent to each other. Adjacent sections are set at 90 degrees to the previous one, as shown in fig. 4.8. The holes serve the same design purpose as the dimples found on a golf ball and prevent the drogue from experiencing abrupt changes in the drag coefficient across the critical Reynolds number [68]. The bottom section of the drogue is reinforced and lead sink weights are attached. The weights give additional ballast to the drogue since the nylon cloth used is neutrally buoyant. The sink weights ensure the drogue remains vertical in the water even under the action on non uniform currents across its length.

Parachute Drogue
A parachute drogue is most commonly used in a sail boat applications to stop or slow down the vessel and is deployed in the direction of the wind. For current measurement applications the parachute drogue is not commonly used. The main disadvantages of a parachute drogue are that it requires a critical current velocity to remain deployed. Once the parachute collapses it provides little drag in comparison and hence the drag area ratio is significantly lower. [68] Additionally the drag is not equal in all directions and a change in current direction would result in the parachute drogue being required to rotate as well as rising if vertical current are present [81].

Tri-star Drogue
Another drogue design is a Tristar drogue. The tristar assembly comprises of orthogonal vanes forming eight adjoining tetrahedrons. During the design of SVP drifters it was found the tristar drogue had a better water following capability than the holey-sock drogue developed at AOML. However, the disadvantage of the tristar was the higher manufacturing and shipping costs due to the increased complexity

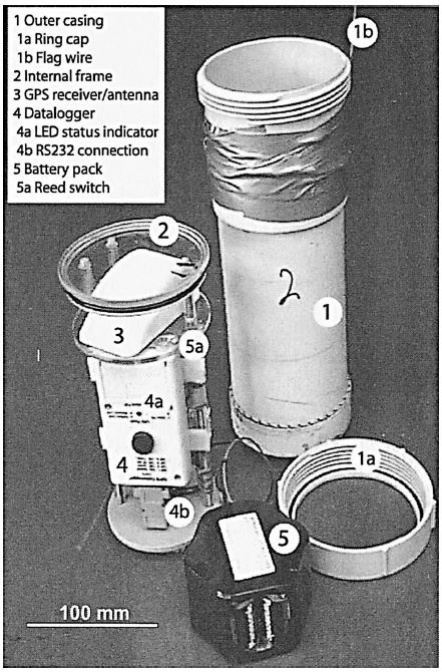

Figure 4.6: Low cost Micro Drifter (1)

Figure 4.7: Low cost Micro Drifter (2)

over a holey sock design.

Summary
Although the drogue design used was dependent on the overall delivery and drifter system specifications, it was concluded that either a tristar or holey-sock were the most likely suitable candidates for the application. The holey-sock drogue has a high packing efficiency and proven ease of deployment. This was useful as the size and weight of the UAV was constrained by the maximum balloon payload and the desire for a low cost system. The holey-sock has a high drag coefficient, good water following capability and holes to allow it to maintain a constant coefficient of drag over a wide range of sea conditions. Additionally, unlike a parachute drogue it requires no critical current velocity to sustain its shape. The nature of the holey-sock makes it simple and low-cost to manufacture. A tri-star drogue would be another choice as it has an extremely good packing ratio and is a lightweight solution. However, due to the design, it did not integrate well into some types of airframe.

4.3.4 UAVs for Oceanographic Applications - Robert Gillman

Michigan Flying Fish
A team at Michigan University in conjunction with DARPA (Defence Advanced Research Project Agency) have developed the "Flying Fish" UAV. The system is designed to act as an unanchored drifting buoy. When it drifts outside of its programmed range from a set location, determined by GPS, it will take off, fly to within the designated range and land at the defined location. The UAV samples the pressure and local temperature which is then processed with a Gumstix processor and transmitted to the ground stations using a Digi Xtend 900MHz radio modem.
The aircraft is designed to be robust and operate in moderate sea conditions (a wave height of 1.25 to $2.5m$). This is achieved using a twin boom pontoon to provide hydrodynamic stability, which although increasing weight makes the model significantly more robust to impact damage.
The propulsion is from 2 brush-less electric motors mounted on carbon fibre booms in a tractor configuration. The electric motors are located high on the UAV to prevent contact and damage with the sea upon landing. The booms extend the length of the aircraft and provide attachment for the horizontal and vertical tail sections. The vertical tail is configured in a dual stabiliser configuration which causes it act like a weather vane on the ocean surface and increases flight yaw stability.

The batteries are located in the pontoons which creates a low centre of gravity. The pontoons and central fuselage pod were designed from Kevlar with waterproof seals to prevent water ingression. The avionics,

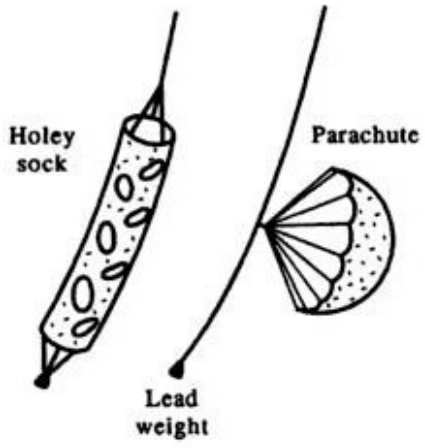

Figure 4.8: Holey sock and parachute drogue

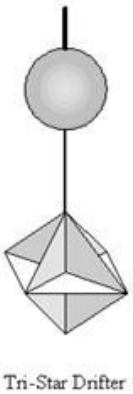

Figure 4.9: Tri-star drogue

within the fuselage, are mounted on vibration damping material and can be removed to allow development and debugging at the same time as airframe development. The control surfaces were driven using water resistant radio controlled servos and to enhance the UAV endurance solar panels were integrated onto the original design shown below.

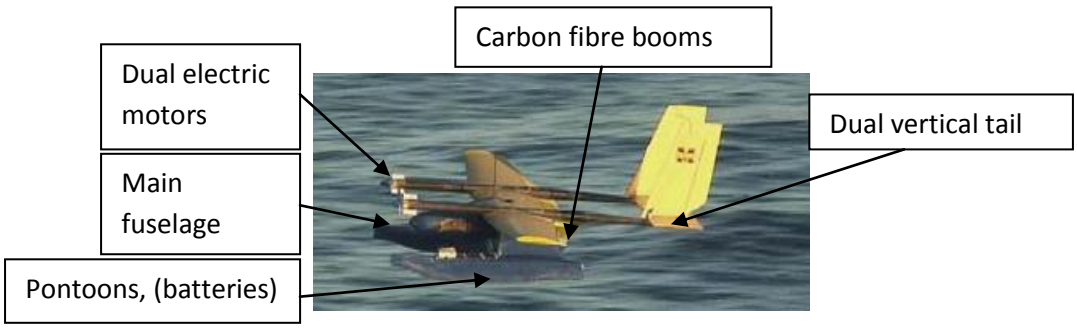

Figure 4.10: Michigan Flying Fish

NOC UAV
The University of Southampton National Oceanography Centre developed and tested a low cost oceanographic UAV for the purpose of aerial surveying large areas of ocean, collecting sea surface and meteorological data and deploying small remote devices in order to improve the efficiency of ship operations. The system is capable of launch from the National Environment Research Council (NERC) research vessels by catapult launch and can be recovered after use. The design is a pusher aircraft powered by a two stroke engine. Lateral stability is maintained with a twin boom tail section providing a large vertical stabiliser [82]. The aircraft payload is $2kg$ with total UAV mass of $15kg$ and a range of $500km$ (6hr endurance).

Gull UAV
The Gull UAV was designed by Warrior Ltd to aid the US Navy and Coastguard with unmanned maritime operations. The fuselage has a wave piercing hull design and two pontoons either side of the fuselage for additional stability. It has a high wing configuration with a wingspan of $4.0m$ to aid lateral stability and prevent the likelihood of damage from wing contact with the sea. The Gull UAV has a maximum payload mass of $2kg$ and total UAV mass of $18kg$. It has limited operational use as an oceanographic buoy as it is only able to withstand an irregular wave height of $0.3m$ [6].

Figure 4.11: NOC UAV Launch

Figure 4.12: Gull UAV

4.3.5 Regulations - Robert Gillman

When designing a new product it is vitally important to understand the legal regulations and restrictions governing its design and use. With regard to designing a balloon launched Lagrangian ocean drifter both aeronautical and maritime laws need to be considered. In the UK the airspace regulations are governed

by the Civil Aviation Authority (CAA). Meanwhile, maritime law is governed under the United Nations Convention on the law of the sea.

High Altitude Balloon Launch
The key requirement driven by the regulations for a high altitude balloon launch is for an "as lightweight as possible" payload. For this project the decision to use a standard meteorological balloon limited the maximum payload mass to $2.7kg$ [26].

Small Unmanned Aircraft
The powered glider and balloon launched Lagrangian drifter fall into the CAA category of "Small unmanned aircraft", For a UAV to operate safely it is required to have an approved method of aerial collision avoidance, which has been rigorously tested and meets CAA accreditation. Without the collision avoidance system the aircraft is required to enable manual radio controlled override. For this reason unmanned operations are not permitted in the UK outside of visual unaided line of sight of the pilot, who must hold a Basic National UAS Certificate (BNUC-S) qualification. The definition given for visual line of sight is $500m$ horizontally and $400ft$ vertically. Operations at a greater distance are possible however include the requirement for a safety case and depend if the remote radio equipment is able to maintain contact with the aircraft. The location of launch must not be within 150 metres of any congested area or within $50m$ of any person,vehicle or structure. During take-off and landing this restriction is lowered to $30m$. For an aircraft of $20kg$ or less no airworthiness approval is required by the CAA. Secondly, providing no operations take place within a congested area then operating permission is also not required. Further complications regarding regulations are added by the integration of an ocean buoy with a UAV. Article 166 of CAA 393 states "a person must not cause or permit any article or animal to be dropped from a small unmanned aircraft which could be dangerous to persons or property". This requires that the drifter payload is integrated in such a manner that there is no possibility it being released unexpectedly[27].

Maritime Law
A brief summary of relevant key points from the United Nations Convention on the law of the sea is given below:

- A mobile floating buoy cannot be deployed if it constitutes an obstacle to international shipping routes.
- Considerations should be given to the potential harm it may cause to a vessel operating under normal navigation rules.
- Owners are liable for damages against damage to another vessel or to the environment.

Potential risks can be mitigated through the careful design considerations and ensuring reliable system deployment and ultimately through a sensible remote test location. The final point regarding Maritime law is that the drifter system should not cause harm to the environment and careful consideration should be given to the materials used.

4.4 Requirements - **Naveeyindren Thangarajah**

4.4.1 System Requirements

The system requirement ranking, fig. 4.13, shows the final number of system requirements. The percentage value indicates the importance of a particular requirement over other headings. The requirements were grouped into three sections; High, Medium and Low.

HIGH (4-7%)
In order to test a UAV & drifter the CAA and maritime regulations needs to be adhered to. Hence they are given the largest emphasis compared to other aspects. Safety was considered to be the next priority and this was separated in two categories, launch and deployment safety. The former deals with safety

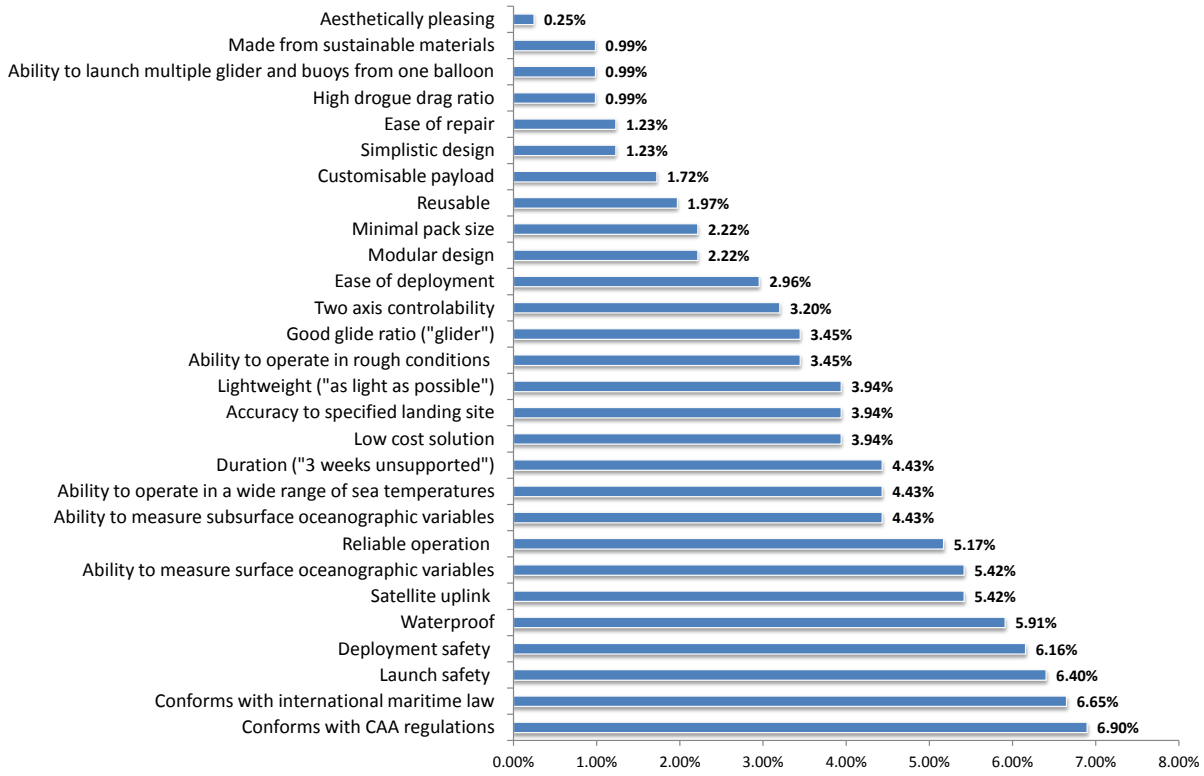

Figure 4.13: Balloon launched Lagrangian drifter system requirements

during the balloon flight whilst the latter relates to the safe deployment of the drifter from balloon to ocean surface. Measuring, collecting and transmitting data was our next priority where the drifter has to ensure reliability.

MEDIUM (2-4%)
The next batch of requirements relate to the design, accuracy and the cost of the system. The system has to be as lightweight as possible and yet operate in rough conditions. The controllability of the glider as well as its glide ratio has to be maximised. Packing and modular design of the glider is ranked as 2.22% importance as the glider can be disposed of after it has landed and deployed the ocean buoy.

LOW (0-2%)
The low end of the requirements deal with materials, design and maintenance of the glider. Since the glider can be considered redundant, maintenance is not an issue. The drogue drag ratio has to be above 40. The drifter will be on sea surface for 3 weeks and would not be recovered. Hence, usage of sustainable materials is not of primary concern here. As opposed to all other requirements, the aesthetics of the design does not carry a large importance.

4.4.2 Design Requirements

Having ranked the system requirement on relative importance a design parameters matrix was completed. The design parameters were then normalised by the ranked system of requirements to give the relative importance of specific design parameters. The normalised design matrix provides a clear representation to the key parameters that need to be considered during the conceptual design.

Figure 4.14 shows that the material impact force should be of paramount importance during material selection. The reasoning behind this stems from the fact the system will be released from a weather balloon, land in the ocean and be required to maintain full functionality. The functionality was likely to be severely restricted if the system deformed on impact. To help reduce the impact force the drive for a low mass system was also of high relative importance.

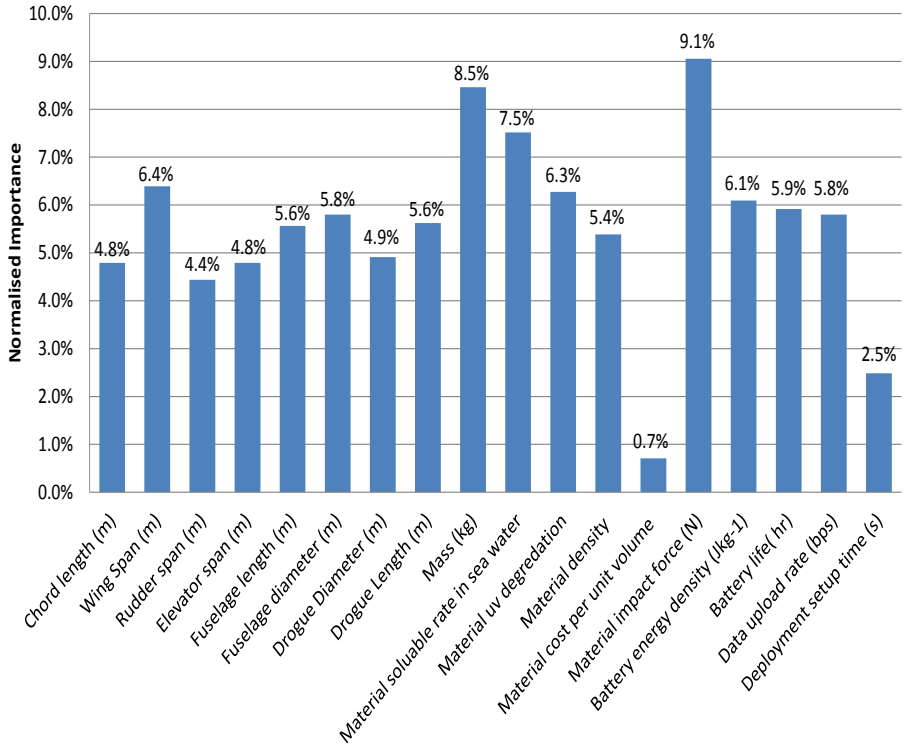

Figure 4.14: Balloon launched drifter design matrix

The battery energy density also required careful consideration. A high battery energy density enabled a lower mass buoy. A lower mass buoy required less buoyancy in order to float and could therefore be designed at a smaller scale. Small dimensions also result in a lower frontal surface area and therefore, due to the 40:1 drag area relation, the frontal area of the drogue and hence diameter could also be reduced.

On the other end of the scale of importance is the deployment set up time. With the system aiming for a deployment duration of three weeks it was not paramount that the system immediately starts to upload data on impact with the water.

4.5 Initial Concepts - Raja Nurul Yuhanis & Robert Gillman

Having completed the background research into current Lagrangian ocean drifters it was clear that a significant re-design would be required. Combing the research findings with the analysis of design requirements a range of early concepts were created.

Delta Wing
This concept (fig. 4.15 and fig. 4.16) is modelled on the idea of a delta wing planform with the drogue and buoy under slung in a cylindrical tube. The advantages of this model include a large surface area to produce lift during the glide phase as well as being simplistic to manufacture due to the modular design. Flight control would be directed by elevators alone with no vertical stabiliser or yaw control. This is a disadvantage as with close to no directional stability the possible locations of buoy deployment are limited.
The delta wing was originally intended for high speed flight as it provided a reduction in transonic and supersonic drag [104] however, at the low subsonic flight velocities that will be experienced, there are a number of key disadvantages. Due to the small wing span and associated low aspect ratio the induced drag would be high. The large surface area would also cause a high profile drag and therefore with the additional induced and profile drag the delta wing concept would have a poor glide ratio. The nose cone of the model would be weighted, which upon landing, would help drag the drogue down to the required

depth. The deployment method of the drifter considered the use of corn starch dissolvable connections or tape between the drifter system and the delta wing. Using dissolvable tape to hold the payload to the aircraft in a maritime environment is likely to be difficult to accurately and reliably design.

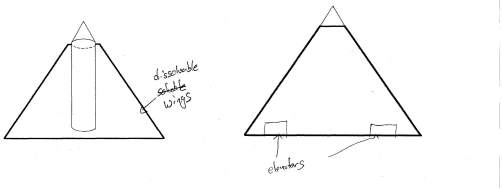

Figure 4.15: Delta Wing Overview

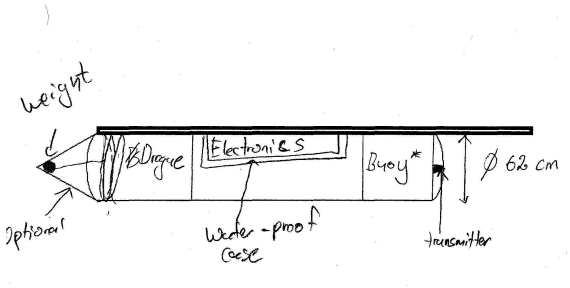

Figure 4.16: Delta Wing Body

Bubble Aircraft

The body of the bubble aircraft consists of the drogue and buoy packed together with the wings and tail section attached to the surface buoy. The system will glide down to the sea surface where the drogue will be deployed from under the buoy body. The glider body, with autopilot contained within, will act as the surface buoy. The advantage of this method is that the payload mass is central to the glider construction and would ensure a central centre of gravity. If the wings are detached from the aircraft once the payload is on the ocean surface then the design will act in the same manner as a current Lagrangian drifter however, it is likely to be difficult to design a concept that is structurally strong during flight yet simple and reliable to disassemble once in the water. The disadvantages of the bubble aircraft include the short stubby wings and thin tail section. Although the image shown (fig. 4.17) was only an initial concept it highlighted the difficultly of having a structural wing box and providing support to the rear tail boom. Secondly with the requirement of a high drogue area relative to surface buoy area it is likely that the packed drogue length would be of the order $\approx 10 - 20cm$ therefore, reducing the aerodynamic efficiency of such a design.

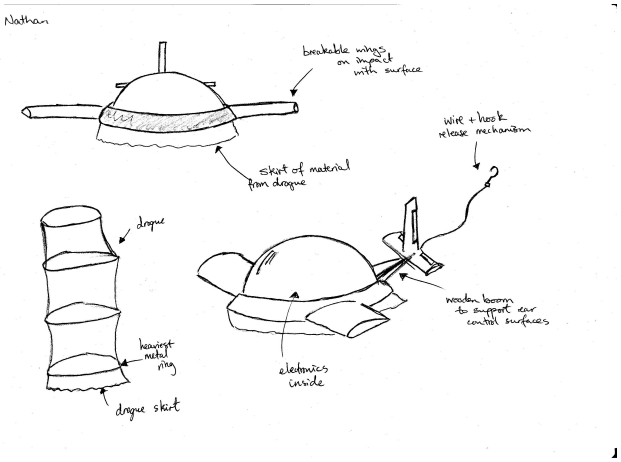

Figure 4.17: Initial Concept- Bubble Aircraft

Tilting Aircraft

The idea of this system is that a holey-sock drogue is integrated as part of the glider, instead of just sitting inside the fuselage of the glider. The weighted nose section would help to deploy the ballasted drogue. The remaining part of the aircraft would act as the surface drifter . In this design concept, the drogue is situated at the front most of the aircraft and the satellite transmitter is situated at the tail such that when deployed as a drifter the antenna would remain out of the water. The main advantage of this concept is the integration between subsystems while maintaining the ability to have a standard

glider design with a suitable glide ratio. Additional advantages include dual control surfaces, simple in concept and a compact solution.

The design poses some key areas to be addressed. Firstly, how to incorporate the drogue and the glider together as one system. The drogue, being fabric, will require additional structural support if it is to be used as a fuselage section. The nature of the concept may cause a difficulty designing specific sections to be water proof, especially for the electronics. The centre of gravity for the aircraft would also be difficult to manage. A forward mounted drogue would move the centre of gravity closer to the nose, hence reducing longitudinal stability in flight. The nose is likely to impact the water first therefore, designing a reliable release mechanism capable of sustaining the impact would add complication. Additionally, the remaining aircraft body, acting as the drifter, would present a large and non uniform profile area. The effect of this on the required drogue dimensions would need to be carefully considered.

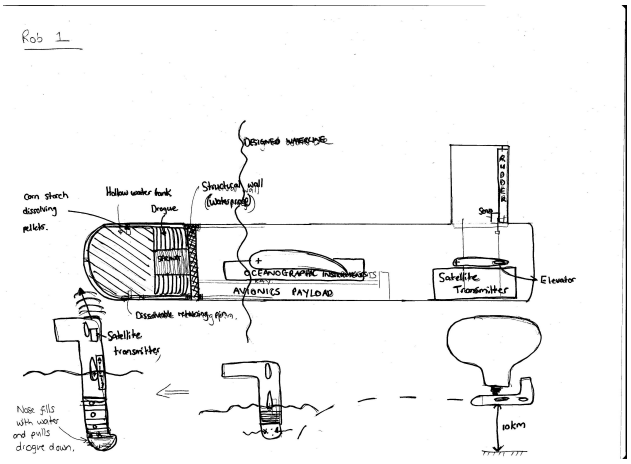

Figure 4.18: Initial Concept- Bubble Aircraft

Tri-star Drogue Concept
The idea for the tri-star drogue design was that the glider shell was a simplistic means of transporting the drifter payload. Into the bottom of the glider was mounted a drogue-buoy pair. This design offered a high packing efficiency due to the folding design of a tri-star. When the drifter is released from the glider, once it has hit the water, a release mechanism holding the compressed drogue will be released. The advantage of the tri-star drogue is that it has a good water following capability however, in current Lagrangian drifter designs is commonly used for shallow water applications. Due to the separating glider and drifter it would enable optimisation of each sub section separately.

The disadvantages include the complexity of designing a drogue to unfold underwater due to the increased water density and viscosity. It would require significant force to deploy the drogue, similar to opening an umbrella underwater and, considering the ideal lightweight construction this is likely to add unnecessary complication.

“AWAC” Concept
The final design concept was based on an airborne warning and control system (AWAC). Instead of a radar antenna mounted on top of the fuselage as in fig. 4.20 this would be replaced with a compressed drogue. Upon impact with the water the drogue would be released and self deploy with the required ballast to ensure it remained vertically orientated in the water. The advantages of this design include a “standard" fuselage design with modifications to include the drogue mounting. A further advantage to the simple fuselage design is that it would enable the attachment of rudder and elevator controls. Unfortunately, there were a number of key disadvantages. The large drogue mounted externally would, due to its large surface area, produce a significant increase in profile drag and reduce the maximum lift to drag ratio.

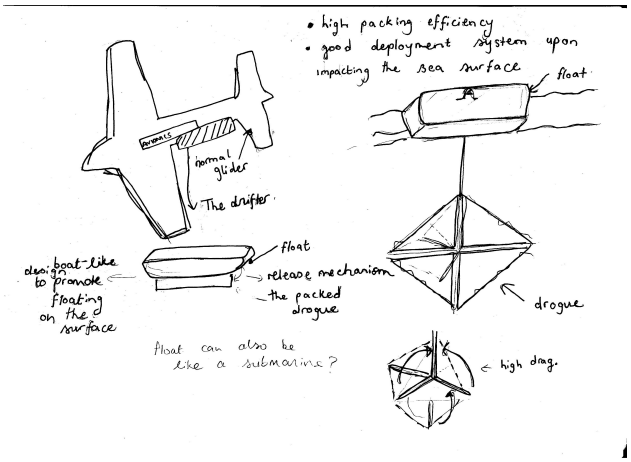

Figure 4.19: Initial Concept- Umbrella aircraft

In order to maintain a suitable drag area ratio it is expected that the drogue length would be within the region of $5 - 7m$, dependent on the buoy characteristics. The compressed drogue is likely to contribute a significant proportion of the system mass and mounting the drogue above the centreline of fuselage would produce additional rolling and potentially yawing moments increasing the required rudder and elevator authority.

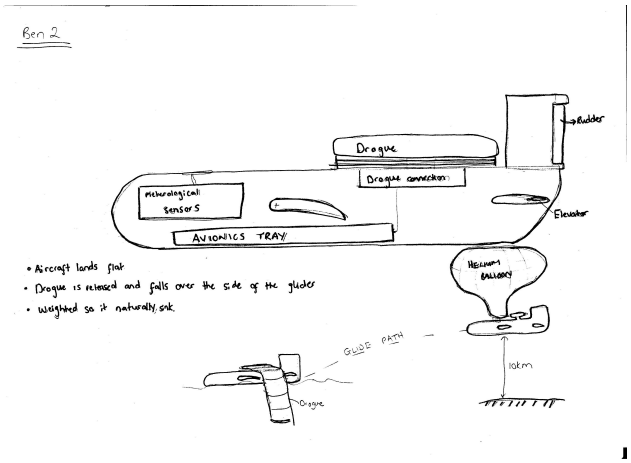

Figure 4.20: Initial Concept- AWAC Concept

Summary
In summary the AWAC, Tri-star and delta wing concepts were ruled out due to reasons stated above. One common disadvantage was the large area of non-drogue elements which will give a low D_{AR} or for a D_{AR} of 40 would require a large drogue.

The bubble aircraft and the tilting concept were considered more feasible to manufacture and were developed further in the following section. Considerations included the orientation of subsystems in order to maximise the total drag area ratio, subsystem integration, the volume required to support the electronics payload, optimising the glide ratio and maintaining a simplistic, lightweight design.

4.6 Drogue-Buoy Considerations - Robert Gillman & Raja Yuhanis

A well designed drogue-buoy pair will include a buoy large enough to house the electrical systems like the sensors, modem and batteries while provide sufficient buoyancy to offset the combined weight of the buoy, drogue and required drogue ballast.

The drogue should be designed in a manner where the total slip velocity of the drogue-buoy pair is low, current Lagrangian drifter aim for $1cms^{-1}$ slip in a $10ms^{-1}$ wind. Slip is the horizontal motion of a

drifter that differs from the lateral motion of ocean currents averaged over the drogue depth [95]. The slip of the drifter is difficult to accurately quantify due to the large number of variables, it can however be shown to be proportional to the speed of the wind and inversely proportional to the drag area ratio of the drogue-buoy pair. In other words, a very low slip would mean that the drogue-buoy pair will not be influenced by the external effect of the wind acting on the drifter. This means that the relative motion of the buoy is dependent only upon the ocean currents at the predefined drogue depth and not that of the surface wind velocity or surface currents acting upon the buoy.

4.6.1 Drag Area Ratio

The drag area ratio is defined as the ratio of the drag area of the drogue over the drag area of the non-drogue elements. Where the drag area is defined as the drag coefficient times the complete horizontal cross section. In order for the drogue-buoy pairs to follow water parcels accurately, a drag area ratio of greater than forty is suggested which enables, for a spherical buoy, a slip velocity less than $1cm/sec$ for the $10ms^{-1}$ wind [118].

$$D_{A_{(i)}} = A_{(i)} * C_{D_{(i)}} \tag{4.1}$$

$$D_{AR} = \frac{D_{A_{DROGUE}}}{\sum(D_{A_{\text{SURFACE BUOY}}} + D_{A_{TETHER}} + D_{A_{\text{SUB-SURFACE BUOY}}})} \geq 40 \tag{4.2}$$

In order to achieve accurate and predictable drift characteristics it is clear the design must attempt to minimise the effects of the wind and waves on the surface float. In the current design of SVP drifters a spherical float is used which minimises the adaptation of surface waves into net horizontal forces [101]. A low mean tension between the buoy and the drogue is suggested to reduce the aliasing of vertical forces into slip-producing horizontal forces. Some designs use a sub-surface float to achieve this; however a sub-surface float would cause a reduction in drag area ratio and increase the system weight. Finally the buoy should have sufficient stability such that it is able to maintain the position of the satellite transmitter above the waterline and the drogue should have sufficient negative buoyancy to keep the drogue upright over a wide range of current velocities.

During the initial research into drogue design it became clear that, within the realms of oceanographic research, the drogue-buoy pair was only deemed to be accurate if the drag area ratio D_{AR} was greater than forty. However it was difficult to find further information as to why this should be the case and why, for example, a drag area ratio of 20 would not provide a suitable compromise.

In an attempt to understand how the slip velocity was dependent on the key drogue-buoy design parameters a simplified analysis was completed for wind induced shear currents, the largest contributor to the slip velocity [101, 129, 49].

The atmospheric boundary layer induces a shear stress acting on the surface of the ocean, the magnitude of this stress is dependent on the boundary layer velocity profile dictated by the wind. Due to conservation of momentum, the shear force on the air-sea boundary induces a subsurface force acting on the top layer of the Ocean, the force acting on the water molecules induces a near surface current. The exact value of this induced current is difficult to calculate due to the requirement for the root mean square velocity of a turbulent boundary layer however, using a much simplified approach, an estimation of the induced velocity can be calculated and thus with further assumptions an approximate relationship between the slip velocity and drag area ratio can be derived.

The following key assumptions were required during the analysis:

- Wind induced shear was the largest contribution to slip velocity.

Beaufort Scale	Wind Velocity [m/s]	Wave Height [m]	Sea Condition
5	8.0-10.7	2-3	Rough

Table 4.1: Wave height conditions

- Wind velocity was fixed.
- The ocean surface had a constant coefficient of roughness, taken as an equivalent roughness for rough sea conditions.
- The physical presence of the waves was neglected.
- The buoy's coefficient of drag remained approximately constant above and below the surface.
- The buoy was neutrally buoyant at a water line of 50% its height.

Assuming, at a given instant, the two fluid bodies of the air above the surface and a shallow region of ocean close to the air/sea boundary are in equilibrium, the current drift velocity can be determined by applying conservation of momentum across the boundary.

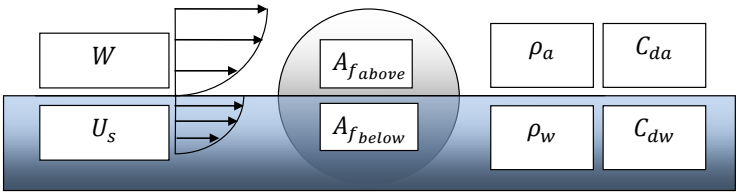

Figure 4.21: Surface buoy slip diagram

$$U_s = \sqrt{\frac{\rho_a A_{f_{above}} C_{d_a}}{\rho_w A_{f_{below}} C_{d_w}}} W = R_\rho R_a R_c W \tag{4.3}$$

R_p and R_A can be calculated easily by direct measurement however, R_C was not so simple as the coefficient of drag of an object is a function of Reynolds number. The Reynolds number was defined with respect to the buoy diameter and fluid properties above and below the waterline respectively. It was also assumed that the decrease in induced velocity from the shear layer in the air to the subsurface layer was of equivalent magnitude to the change in fluid properties, such that the buoy coefficient of drag remained approximately constant.

$$R_C = \sqrt{\frac{C_{d_a}}{C_{d_w}}} \approxeq 1 \tag{4.4}$$

Assuming the buoy to be floating at a waterline of 50 % its height, in fresh water, under standard atmospheric conditions then a worse case maximum subsurface induced velocity was calculated.

$$U_s = \sqrt{\frac{1.225 * 0.5 * 1}{1000 * 0.5 * 1}} * 10.7 = 0.3745 ms^{-1} \tag{4.5}$$

A suitable subsurface velocity should be close to the margin of 2-3% of the surface velocity [49], which given the use of fresh water and a $10.7 ms^{-1}$ wind velocity above provided a reasonable estimate. The drift current is maintained in a thin layer close to the surface and the velocity magnitude decays exponentially with depth [101]. It can be shown that the wind induced near surface force acting on the drifter will be significant, however its effect on the tether and drogue will rapidly decrease with depth. Due to the induced force acting principally on the drifter and the near surface tether the wind induced surface current is responsible for the main contribution in overall slip velocity. The vertical profile of the induced

current can be given as;

$$u(z) = U_s e^{-kz} \tag{4.6}$$

Where z is depth from the air-sea boundary and k^{-1} is known as the shear folding depth. Using a quadratic drag law derived by Hoerner (1965) the relative forces acting on the drogue and surface buoy were estimated. It was assumed the water velocity moving past the drogue to be given by the slip velocity $U_{\Delta s}$ and, for simplicity, the tether and drifter forces were combined together.

$$F_{_{BUOY}} = \frac{1}{4}\rho_w C_{d_{BUOY}} A_{_{BUOY}} (U_s - U_{\Delta s})^2 \tag{4.7}$$

Where $A_{_{BUOY}}$ is the entire frontal buoy surface area.

$$F_{_{DROGUE}} = \frac{1}{2}\rho_w C_{d_{DROGUE}} A_{_{DROGUE}} U_{\Delta s}^2 \tag{4.8}$$

For simplification a new variable r was defined such that,

$$r = \frac{C_{d_{BUOY}} A_{_{BUOY}}}{C_{d_{DROGUE}} A_{_{DROGUE}}} = \frac{1}{D_{AR}} \tag{4.9}$$

Using analysis provided in Geyer, 1989 [49] the following relationship was derived for the ratio of wind induced slip velocity acting on the drogue to the wind induced slip velocity acting on the submersed half of the buoy.

$$\frac{U_{\Delta s}}{U_s} = \frac{r^{\frac{1}{2}}}{1 + r^{\frac{1}{2}}} \approxeq r^{\frac{1}{2}} \approxeq \frac{1}{\sqrt{D_{AR}}} \tag{4.10}$$

Equating the above equations provide an approximate relationship between the physical design properties of the drogue and surface buoy with the induced near surface current velocity and the drogue slip.

$$D_{AR} = \frac{C_{d_{BUOY}} A_{_{BUOY}}}{C_{d_{DROGUE}} A_{_{DROGUE}}} \approxeq \frac{(U_s)^2}{(U_{\Delta s})^2} \tag{4.11}$$

$$U_{\Delta s} \approxeq \frac{U_s}{\sqrt{D_{AR}}} \tag{4.12}$$

The analysis so far had neglected the additional slip produced from the aerodynamic drag on the drifter from the turbulent boundary layer. It was difficult to accurately quantify the full extent of this contribution due to the turbulent nature of the wind profile and associated velocity fluctuations. The velocity was dependent on the boundary layer profile which in turn was a function of the roughness coefficient of the ocean surface and therefore a function of wave amplitude and frequency. At this point the simplification used in [Geyer 1989][49] was applied. "For a buoy extruding from the surface of the ocean by $0.1m$, a mean wind velocity of $10ms^-1$ and a ocean roughness coefficient of 1.5-3, the force produced was roughly 0.25-0.5 times the value of the force produced by the induced surface current." Using the worse case estimation of 0.5 the total induced slip velocity was approximately 1.5 times the value calculated previously for current induced slip. The outcome of this relationship meant that in order to achieve a small reduction in slip velocity there must be a large increase in the drag area ratio. In physical terms this correlated to a large increase in drogue size in order to achieve a small improvement in slip velocity. Although by no means did this analysis provide conclusive proof it suggested for designing a balloon launched Lagrangian drifter, where weight and glide ratio are important design drivers, a compromise in the drag area ratio may not be significantly detrimental to the system oceanographic accuracy and therefore should not be ruled out.

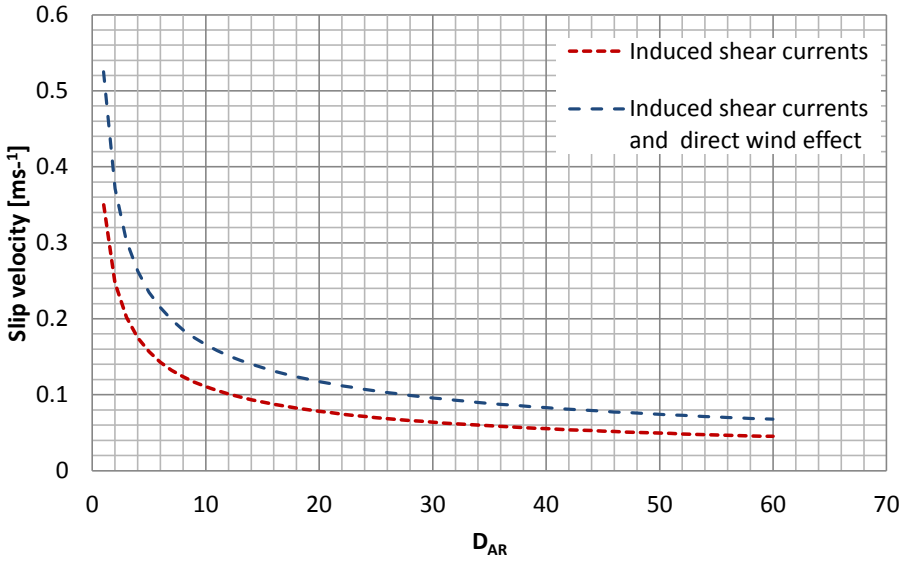

Figure 4.22: Slip velocity in m/s versus drag area ratio

4.7 Concept Development - Gillman & Thangarajah & Dvurecenska & Yuhanis

The initial concepts were analysed with respect to the project brief for their suitability as both a UAV and balloon launched drifter. The bubble concept and tilting aircraft were developed concurrently and formed the second generation concepts. In order to establish the final concept an electronics payload was sized, in terms of both power requirements and dimensions and the manufacturing methods and materials were explored in relation to each design.

Using the preliminary electronics mass, initial material properties, buoyancy calculations and preliminary design dimensions for each concept were established. An optimisation for the smallest surface buoy that met the following drogue-buoy requirements was completed. The requirements included; the surface buoy should be able to support its own weight, the weight of the drogue and tether and, if, the design included the glider and drifter staying together, the weight of the glider as well. Additionally, the drag area ratio of drogue to non drogue elements should, ideally, be greater than forty and the total payload mass should be less than $2.7kg$. Due to the coupled design variables, an iterative approach was used to establish the concept total buoyancy, mass and drag area ratio as shown by fig. 4.23.

4.7.1 Electronics Payload - Robert Gillman & Ben Oxley

Selection and understanding of the drifter and glider electronics requirements, sizing and weight were key to the design of the system as it would drive the size and layout of the glider and surface buoy. A system layout and components list were compiled for component weights, power requirements and dimensions.

The autopilot system, which was being developed concurrently for the powered glider range extension, section 3.1, would act as the drifter processor and control the frequency of satellite transmissions, fig. 4.24. Initially, an electronics concept was arranged, as shown in fig. 4.25 which enabled an approximation of the minimum dimensions for the surface buoy.

Once the required components were established, a power budget was calculated and thus the minimum surface buoy volume approximated. In order to maximise the endurance, the Ardupilot system was assumed to send one transmission of its GPS location per hour. The Ardupilot has an idle power and GPS acquisition power, along with a GPS acquisition time. Combined with the iridium modem

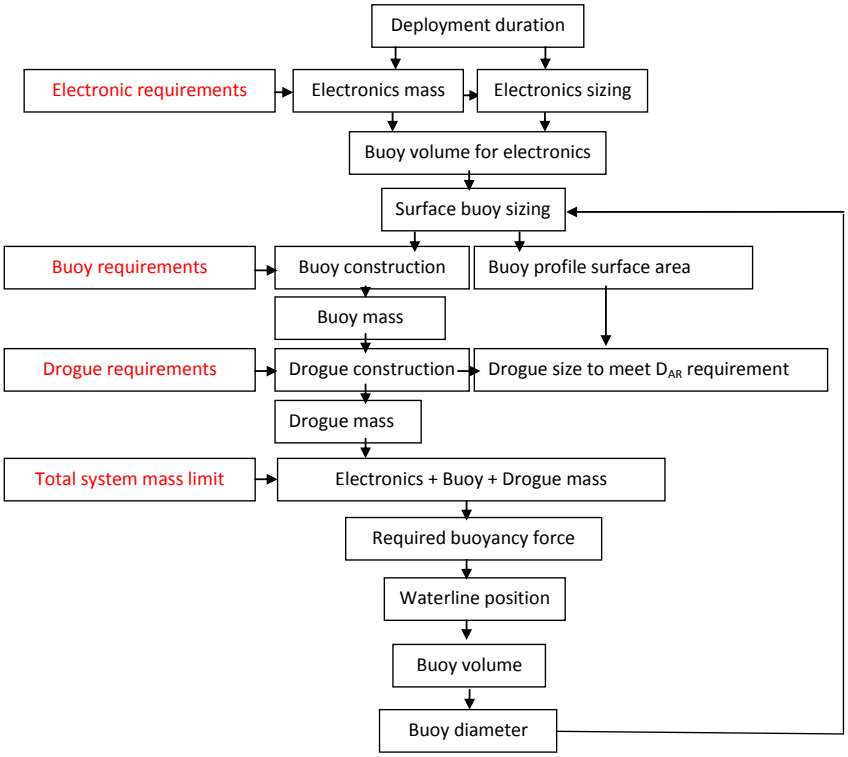

Figure 4.23: Concept development flow chart

characteristics it enabled an estimation for the total charge and battery requirements during the drifting stage of deployment. Further development of the electronics sub system is described in detail in chapter 6.

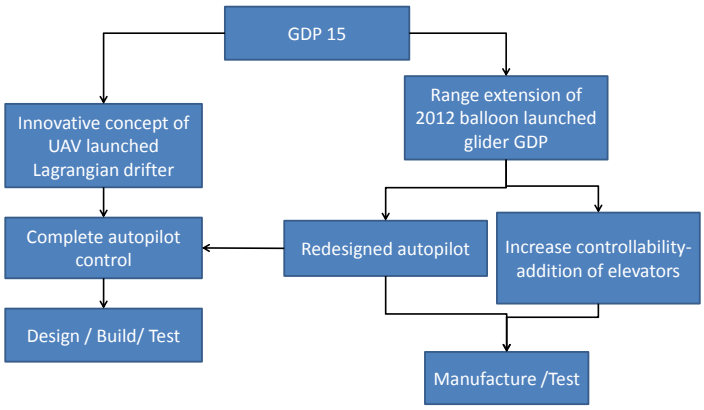

Figure 4.24: Electronics development

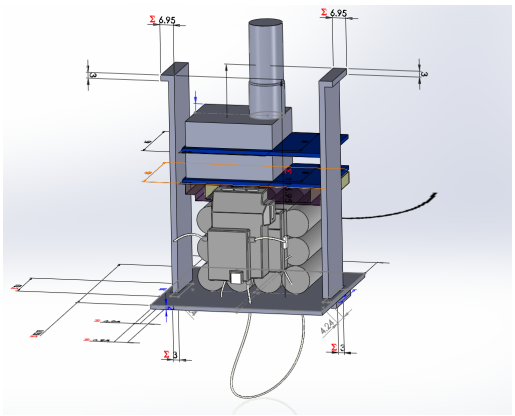

Figure 4.25: Drifter concept electronics

4.7.2 Materials & Manufacturing - **Naveeyindren Thangarajah**

As part of the concept development for the balloon launched Lagrangian drifter, the manufacturing methods for both second generation designs were considered and combined with the concept electronics payload, to provide an approximate mass build up. The manufacturing methods considered for the buoy were vacuum forming, 3D-printing or to purchase a commercial off the shelf (COTS) container. The drogue could be manufactured in-house or by purchasing a COTS solution. A foam hot wire cutter was the most suitable method for manufacturing a lightweight glider. The relative merits of each methods are discussed in section 4.8.

These steps served two purposes: Firstly, it ensured the group had considered the manufacturing im-

Component		1 Week [kg]	2 Week [kg]	3 Week [kg]
Autopilot	Ardupilot	9.0E-03	9.0E-03	9.0E-03
Satellite modem	Iridium 9602	3.0E-02	3.0E-02	3.0E-02
PCB for Sat Modem		4.0E-03	4.0E-03	4.0E-03
GPS module	On off use	7.0E-03	7.0E-03	7.0E-03
Voltage regulator	Negligible	-	-	-
Pressure sensor	Included in autopilot	5.0E-03	5.0E-03	5.0E-03
Temperature sensor	Included in autopilot	1.0E-02	1.0E-02	1.0E-02
Salinity sensor		5.0E-03	5.0E-03	5.0E-03
SD card writer		1.0E-03	1.0E-03	1.0E-03
SD card		2.0E-03	2.0E-03	2.0E-03
Satellite antenna	Iridium antenna	2.9E-02	2.9E-02	2.9E-02
Servos	EXTERNAL	7.8E-03	7.8E-03	7.8E-03
Status LEDs		-	-	-
Second processor	Arduino pro mini based	1.2E-02	1.2E-02	1.2E-02
Radio	RFM22B	7.0E-04	7.0E-04	7.0E-04
Radio Control System	Spectrum Receiver TM1000 module	5.0E-02	5.0E-02	5.0E-02
Switches		2.0E-02	2.0E-02	2.0E-02
Release mechanism	EXTERNAL	5.0E-02	5.0E-02	5.0E-02
Wires and connectors		3.6E-02	3.6E-02	3.6E-02
Battery Holder		2.0E-02	2.0E-02	2.0E-02
Batteries	Energizer lithium ultimate	5.8E-02	1.2E-01	1.7E-01
	Total mass [kg]	0.36	0.428	0.50

Figure 4.26: Drifter electronics sizing

plications such as time and expense associated with each design. Thus, ensuring the final concept was manufactured in a time and cost-efficient manner. Secondly, the system mass estimate enabled the required buoyancy and drogue dimensions to be established, which combined with further analysis enabled the final concept to be developed.

4.7.3 Bubble Concept Development - **Ksenjia Dvurecenska**

The aim at this stage was to design the buoy with the smallest possible diameter to allow for the most compact system. Overall, the bubble concept, as described in the initial concept section, incorporates a hemisphere buoy together with the drogue as the body of glider, with wings and control surfaces attached from the sides.

The advantage of this design was that there is no fuselage for the drifter to fit into thus reducing overall weight of the system. The buoy and the drifter arranged in a horizontal position act as a wing-box and provide support for the wing when it is placed in between the two. With the addition of supports for the tail plane there was not any other additional structure. The main disadvantage was the aerodynamic performance. To develop this concept further, it was re-analysed by taking into account research from drogue requirements and the buoy-drogue interaction. Taking into account these considerations, the main constraint in this design was the size of the drogue when it's packed and a suitable method of attachment and deployment.

The first issue was that even for a $0.16m$ diameter buoy, the minimum drogue length required was $10m$ assuming the drogue diameter was equal to the buoy diameter and it can be packed to approximately $0.5m$ in length. This would create a great amount of drag, leading to an unstable glider. As there was no fuselage for the drogue to fit into, it was possible to increase the diameter without influencing the buoy. The diameter and length were varied by keeping constant the drogue frontal area required by the drag area ratio of 40. Values summarised in the table 4.2.

Any diameter larger than 0.5m was decided to be infeasible. At this diameter the drogue can be packed up to approximately 0.17m and thus the body of the glider becomes a 0.5m cylinder. A schematic drawing is shown in Figure 4.27, where the system can be observed from the top and front views. For any of the options in the Table 4.2 the glider would still require a very complex flight control and a very efficient

Drifter Diameter (m)	Drogue Diameter (m)	Drogue Length (m)
0.16	0.16	10.0
	0.20	8.0
	0.25	6.4
	0.30	5.4
	0.35	4.6
	0.40	4.0
	0.45	3.6
	0.50	3.2

Table 4.2: List of possible drogue sizes and appropriate lengths

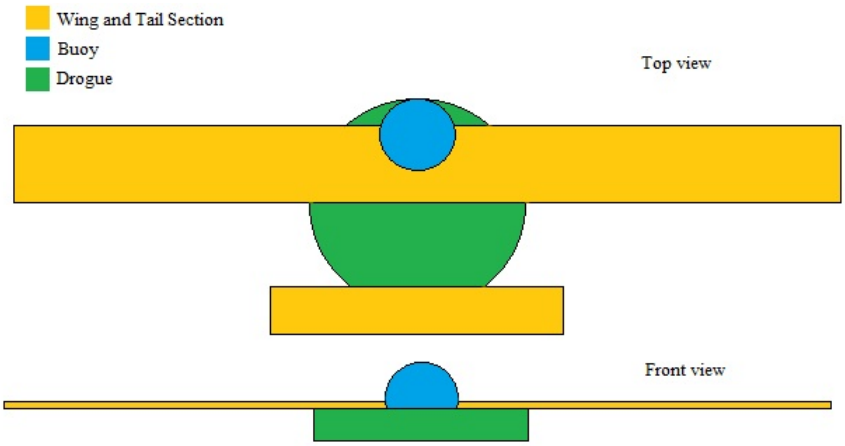

Figure 4.27: Hemisphere concept: buoy 0.16m, drogue 0.5m.

wing structure design to counteract the substantial amount of drag created by the frontal area. There is a possibility of the system being unstable and turning upside down.

The other issue is the drogue connection. It is essential to ensure a secure attachment during flight but at the same time the drogue should be able to deploy quickly once on the water surface. Designing the attachment, it is also necessary to remember that the wing and the tail sections have to detach from the drifter so as not to disturb the drag area ratio when balancing in the water. These contradictions can only be solved through a complex design and manufacturing process.

Summary
Summarising the advantages and disadvantages of the concept, the system is concluded to be unsuitable for our project. Advantages of this design are that it is a compact solution with a large circular diameter (>20cm) for the drifter and drogue, and minimal and structure and material is added to the system reducing the overall weight. However, it requires complex manufacturing and assembling processes and provides weak aerodynamic performance and unreliable safety characteristics. For the concept to satisfy the criteria, design and assembly will take much more time than currently available for this project.

4.7.4 Internal Payload Concept Development - Robert Gillman

Using the relative merits from the previously discussed concepts, and considering the manufacturing implications, a simplistic glider with internal drifter subsystem was designed. The internal payload underwent shape and size optimisation in order to find the minimum required drifter diameter that would enable a suitably sized glider, a total mass less than $2.7kg$ and a reasonable drag area ratio.

System Integration
It was clear that with the competing design requirements, discussed in more detail previously, the surface buoy was required to be as small as possible while providing sufficient buoyancy for the drifter subsystem.

The tilting aircraft concept involved the glider and drifter subsystems remaining together during deployment as a Lagrangian drifter. Therefore the tilting aircraft required greater buoyancy than a concept where the drifter and glider separated before, or on, contact with the water.

There were three main advantages gained by separating the subsystems. Firstly the surface buoy required a lower buoyancy therefore a smaller surface buoy and smaller drogue could be considered for an identical drag area ratio. Secondly, the original tilting aircraft concept had a large inhomogeneous surface area above the water, when deployed as a drifter. Hence, by separating the glider and drifter it allowed a smaller drogue design from the reduction in the drag area of non drogue elements. Finally, a system with the glider and drifter separating enabled a greater deal of flexibility for subsystem optimisation as well as reducing a number of the overall design constraints. The disadvantage was the additional complexity associated with imposed requirement of a reliable method of separating the two subsystems. The release mechanism concepts considered are discussed in section 4.7.6.

Concept Drawing

The second generation concept included the surface buoy and drogue packed into the fuselage of the glider as shown in fig. 4.28. Figure 4.29 shows the vacuum formed conceptual surface buoy with electronics payload mounted within. Upon deployment the drogue and surface buoy would leave the glider and use the autopilot system and satellite modem to transmit the drifter position. The minimum dimensions of the spherical surface buoy concept were found using an excel development tool discussed in the following section (eq. (4.17)).

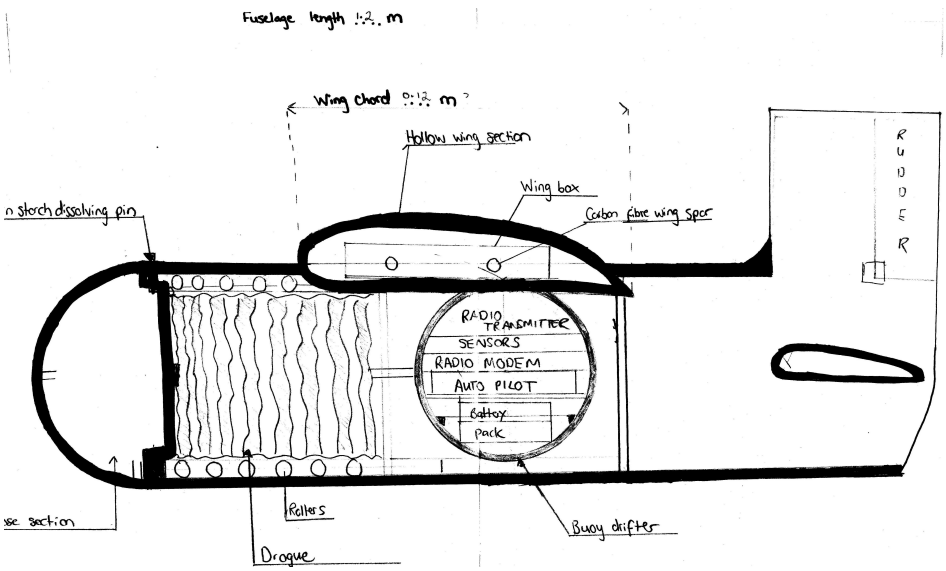

Figure 4.28: Internal payload concept: Overview

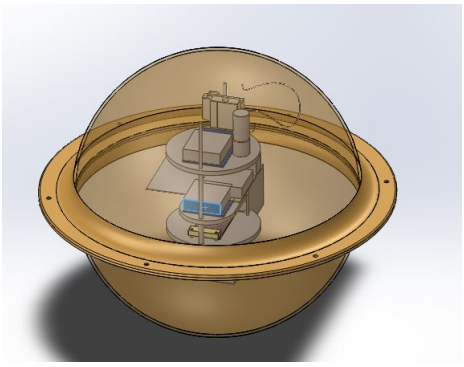

Figure 4.29: Internal payload concept: Surface Buoy

Surface Float Design

It was concluded from section 4.3 that there were two common configurations of surface buoy for drifter applications. Firstly, the spherical design as is currently used for SVP Lagrangian drifters and secondly, a cylindrical buoy which is more commonly used for lower budget applications. The merit of each was carefully considered with the steps leading up to the final configuration discussed below. Using the relationship for drag area ratio given in section 4.6; assuming a constant above and below water coefficient of drag for the float the drogue frontal area per unit profile area of surface buoy was plotted over a range of drag area ratios.

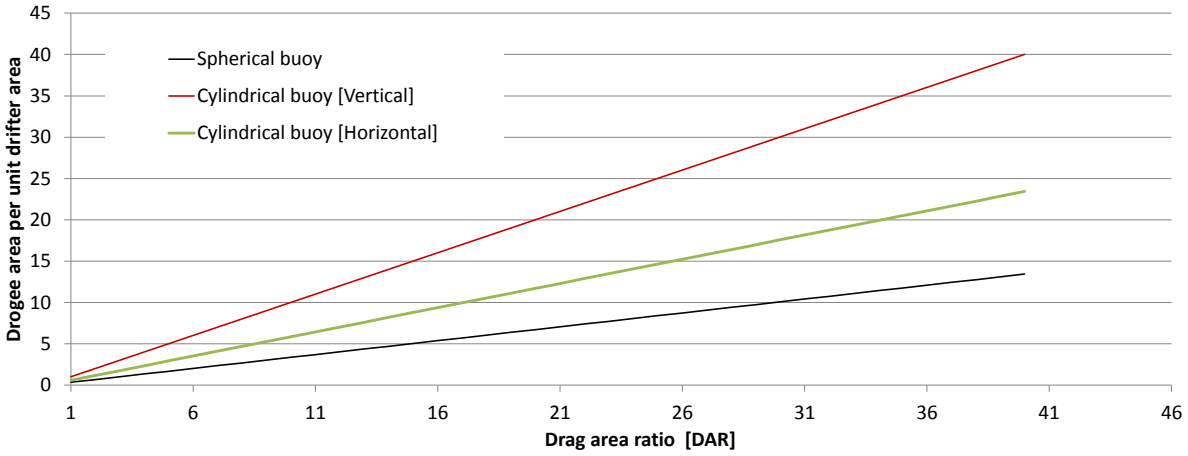

Figure 4.30: Buoy profile vs. unit Drogue Area

From fig. 4.30 a spherical buoy, due to its lower coefficient of drag, requires the smallest drogue area per unit front area of float. Therefore, to achieve the smallest drogue length a spherical buoy would be the most suitable. The disadvantage of the spherical buoy was the large diameter driven by the requirement for sufficient buoyancy to support its own weight, the electronics payload and the drogue. A cylindrical buoy in a vertical orientation was found to require the highest drogue area due to its higher coefficient of drag [81]. One advantage of a cylindrical float is that a smaller diameter, longer buoy is more suitable to fit in a conventional glider design that a spherical buoy. The long thin cylindrical design could provide sufficient buoyancy and maintain a small diameter thus allow the complete system to have an improved aerodynamic efficiency. The disadvantage of a cylindrical buoy is that the drogue length required would be higher than an equivalent spherical buoy [1].

Buoyancy Calculations

The buoyancy force is the thrust produced by displacing a volume of fluid with one of a lower density. In order for the system to float on the surface of the ocean the buoyancy force produced by the volume under the water line must be approximately equal to the combined weight. The surface float waterline, ψ_s, was taken as a percentage of the height and initially fixed to be 0.5, ensuring the antenna would remain above the surface and providing a small safety factor from initial to actual design.

$$B_f = \rho_f V_{S.B} g \psi_s \tag{4.13}$$

For the drifter

$$B_f > (m_{SURFACE.BUOY} + m_{DROGUE} + m_{TETHER})g \tag{4.14}$$

$$\rho_f V_{S.B} g \psi_s > (m_{SURFACE.BUOY} + m_{DROGUE} + m_{TETHER})g \tag{4.15}$$

With the volume for the cylindrical fuselage with semi spherical end caps and spherical concepts given

by:

$$V_{S.B} = \frac{\pi d_{S.B}^2}{4}(l - d_{S.B}) + \frac{\pi d_{S.B}^3}{6} \qquad (4.16) \qquad V_{S.B} = \frac{\pi d_{S.B}^3}{6} \qquad (4.17)$$

Excel Driven Design Development
It was apparent due to the number of design parameters, ($\cong$ 40), additional constraints were required to control the design space. Initially the following were imposed for a variation of three different durations and three differing acceptable levels of drag area ratio of 30, 35 and 40, using the analysis from section 4.6.

- The drogue diameter to be equal to the surface buoy diameter. This would produce the smallest system diameter and help drive towards a design of high aerodynamic efficiency.
- The drogue length, set as a variable, could only be in the range $0.5m$ to $7m$ in intervals of $0.5m$.
- The holey-sock eddy hole diameter was fixed to be equal to half the drogue diameter.
- The number drogue sections was limited to be in the range 2-28.
- The drogue material cloth was taken as cordura fabric with a density of $44kgm^{-3}$.
- The number of drogue strengtheners was limited in the range of 3-29.
- The diameter of the wire drogue strengthener was $1.5mm$ with a density of $2400kgm^{-3}$.
- The drogue sink mass was assumed to be $200g$.
- The glider mass was assumed to be no more than $1.2kg$, based on a scaled up approximation of the UAV Glider from GDP 16, 2012.
- The surface buoy manufacturing method of vacuum forming limited the minimum material thickness to $2mm$.
- The electronics mass was fixed dependent on the duration of deployment which was fixed between 1 & 3 weeks.

To reduce the number of potential designs three non dimensional criteria were introduced. By applying logic statements those designs which did not meet the requirements were filtered out.

- Ratio of required buoyancy

$$n_{bf} = \frac{B_{SURFACE.BUOY}}{B_{TOTAL}} \geq 1 \qquad (4.18)$$

  Which for a spherical buoy was given as;

$$n_{bf} = \frac{\rho_f g \psi_s \pi D_{SURFACE.BUOY}^3}{(m_{SURFACE.BUOY} + m_{DROGUE} + m_{TETHER})g} \leq 1 \qquad (4.19)$$

- Ratio of maximum payload

$$n_m = \frac{m_{SURFACE.BUOY} + m_{DROGUE} + m_{TETHER} + m_{GLIDER}}{2.7} \leq 1 \qquad (4.20)$$

- Relative drag area ratio

$$n_{D_{AR}} = \frac{D_{AR_{DROGUE}}}{\sum D_{AR_{NON.DROGUE.ELEMENTS}}} \geq 1 \qquad (4.21)$$

Out of the 7,560 designs considered, 7,484 were ruled out leaving only 76 potential solutions. It was clear, given these 76 possible designs were only for a spherical surface buoy a more efficient method of optimising between spherical or cylindrical would be required for the final design.

4.7.5 Visual Studio Design Tool - Izdihar Zuhdi

Due to the large number of design configurations and complex interactions between design variables the excel tool had become laborious to operate and difficult to manage. In order to progress further and analyse the advantages of a spherical and cylindrical surface buoy a C# script was written.

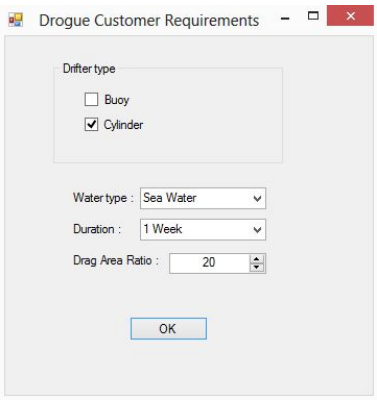

Figure 4.31: Visual Studio Design Tool main window

The tool allowed the user to define the water type, duration and minimum acceptable drag area ratio and as shown in fig. 4.31. The calculations done in this software were based on the equations defined in the Excel analysis above. The outcome showed all suitable cylindrical and spherical surface buoy options at the same time. The suitable solutions were chosen based on three characteristics defined in Excel analysis: Ratio of required buoyancy, $n_{bf} \leq 1$; Ratio of maximum payload, $n_m \leq 1$; and Relative drag area ratio $n_{D_{AR}} \geq 1$. As the result, the drogue and drifter diameter, drogue length, drogue aspect ratio, total mass fraction and total drag area ratio were presented as the outcome as shown in figure 4.32. The main advantage of this tool over Excel was that these parameters can be sorted in ascending or descending order to reduce the time required to draw suitable conclusions between the different designs. When comparing the spherical and the cylindrical results, it was noted that a larger spherical diameter was required in order to support the mass of the system. Thus, it was decided to continue with cylindrical buoy in further considerations.

Drogue & Drifter diameter	Drogue length	Cylinder Length	Drogue aspect ratio	Total mass fraction	Total drag area ratio
0.12	6.50	0.2000	54.1667	0.8589	20.3655
0.12	7.00	0.2000	58.3333	0.8629	22.2222
0.13	6.50	0.2000	50.0000	0.8721	20.9677
0.13	7.00	0.2000	53.8462	0.8765	22.8643
0.14	6.50	0.1500	46.4286	0.8698	25.9259
0.14	7.00	0.1500	50.0000	0.8746	28.3237
0.14	5.50	0.1500	39.2857	0.8601	21.3296
0.14	7.00	0.2000	50.0000	0.8903	23.4450
0.14	6.00	0.1500	42.8571	0.8649	23.5955
0.14	6.50	0.2000	46.4286	0.8855	21.5130
0.15	6.50	0.1500	43.3333	0.8822	26.6393
0.15	6.00	0.1500	40.0000	0.8769	24.2588

Figure 4.32: Visual Studio Design Tool outcome window

Pareto Front Analysis

The Pareto front is a concept that formalises the trade-off between a given set of mutually contradicting objectives.[4] A solution is Pareto optimal when it is not possible to improve one objective without

deteriorating the others.[4] A set of Pareto optimal solutions constitute the Pareto front[4].
The Pareto front was plotted based on the solutions generated by the Visual Studio Design Tool(fig. E.1). A trade-off between the drogue and the drifter diameter had to be made since these parameters affect the dimension of the balloon launched glider. From Figure in Appendix E.1, it can be seen that a longer glider was required to deliver a longer drifter while larger drogue diameter causes a bigger and bulkier glider needed to transport the whole package. It was decided to compromise the drogue length to have a smaller drifter diameter. Based on that, a cylinder buoy with $0.12m$ diameter and $0.20m$ long was chosen to be the optimal size. The corresponding shortest drogue length for this buoy was $5.5m$.

4.7.6 Payload Release Concepts - Ksenjia Dvurecenska

A release mechanism was required to deploy an oceanographic payload from the glider. During the design process discussed earlier in the report it was decided to keep two systems independent and thus the buoy and the drogue have to be separated from the glider before they can function correctly in the water.

Concept Analysis
Two main concepts were considered before developing detailed mechanism. At this stage of development the safety of the design is crucial and is the prime criteria when comparing concepts.

Payload Release on the Water Surface
The concept consists of the glider landing on the water surface before deploying the drifter and the drogue. It provides relatively safe delivery of the payload to the water surface and eliminates the risk of the drifter being damaged on direct impact with the water surface or tangling in the drogue if it unravels. However, this method prolongs the deployment process since it relies on the external environmental forces acting to remove the glider. It was established earlier in this report that it is essential for the glider not to interfere with the oceanographic payload on the water surface so it has to be removed as soon as possible. Water soluble materials were considered but appeared unfeasible to be used in the fuselage be it a complete body or number of parts. This brings the risk of premature deployment or the entire system failing in the air due to the environmental conditions such as any kind of moisture present in the atmosphere. Another parameter to be considered is the buoyancy of the fuselage to assure that it will not sink before the drifter is deployed resulting in the loss of the product.

Mid-air Deployment
This concept is based on using a mechanical or pyrotechnic mechanism to deploy the payload, specifically:

- Drogue used as a parachute that pulls the drifter out
- Detaching the rear part of the fuselage leaving the nose for the weight to pull the drogue down
- Bottom half of the fuselage falls off or opens

All concepts imply that the drifter and the drogue will be free-falling for a certain period of time before reaching the water surface. This, of course, requires significant consideration into the payloads impact resistance such as material strength and drifters contents alignment.
The first two design ideas involve large risk of the entire system being damaged and failing during or prior to the release. These designs also require intricate manufacturing and a complex assembly of the fuselage. If the nose of the fuselage is part of the oceanographic payload, then the pyrotechnic release mechanism and in-flight electronics have to be placed together in the rear part of the fuselage, bringing the glider's centre of gravity towards the tail section. This will result in unstable flight behaviour and will place electronics in an unsafe environment.
The third option is a mechanical mechanism that opens or releases the bottom of the fuselage. This can

be controlled together with the in-flight electronics and would require minimum space. The release can be performed instantly and without disturbing the rest of the glider components.
Overall, from the arguments presented above it is understood that mid-air release concept is more suitable for this project. In particular the mechanical release as it is simpler to operate and integrate, and it involves less risk for the entire system. The advantages of this design outweigh the disadvantages and those can be solved without radical changes in components design and interfering with their functionality. Further, it was decided to proceed with developing number of possible implementations of the mechanical mechanism that involves the release of the bottom of the fuselage.

4.8 Final Concept - **Raja Nurul Yuhanis**

4.8.1 System Overview

The balloon launched Lagrangian drifter final concept consisted of a number of key compromises to the drifter payload to ensure all project aims were met. Firstly, the surface buoy was a COTS container with a custom internal electronics payload with an expected deployment duration of one week. The drogue was a 5.5m holey-sock with a D_{AR} of 21 instead of the "ideal" 40. To provide a controlled descent of the drifter from the balloon burst altitude of $10km$ a simplistic foam built, single use, UAV with a releasable payload was to be designed.

4.8.2 Final Design

The glider design is based around a foam glider with an oceanographic payload, i.e. drogue and buoy, packed inside the fuselage. Both electronics for the glider and the drifter sit inside the buoy but separate batteries are placed in the nose and used for in flight control. The batteries required for the drifter deployment are placed inside the buoy. A waterproof ethernet cable connects the in-flight batteries and the control surfaces to the glider electronics inside the buoy. A cylindrical shape buoy was chosen together with a holey-sock drogue due to simple design and good packing ratio to fit inside the fuselage. The buoy is a leak proof chemical container with a metal bracket tether attached to the bottom of it. For water proofing, the lid and area around the tether connection are sealed shut with silicon to ensure the buoy remains watertight in rough sea conditions. The fuselage diameter was driven by the drogue and buoy diameter and consequently determined the size of the tail section for the aerodynamic stability. A removable bottom fuselage is incorporated into this design to deploy the oceanographic payload by a mechanical release mechanism, section 5.4.

4.9 Buoy Design

As was shown in fig. 4.30 a spherical surface buoy, due to its lower coefficient of drag, would enable (per unit buoy area), a smaller drogue. However, from the Excel design tool it was clear that due to the required electronics mass the minimum diameter of a spherical buoy could be $160mm$. The difficulty with a surface buoy of such diameter was how to design a suitable aerodynamic means of transporting it to the required location from balloon release. From previous drogue slip velocity analysis (see4.21) it was shown that by compromising the drag area ratio there would be only a small increase in slip velocity. Therefore, the decision was taken to use a cylindrical surface buoy which, for the same D_{AR} of a spherical buoy meant a longer drogue however, it enabled a simplistic solution to the transportation of the drifter. The decision for a cylindrical buoy was also influenced by the manufacturing limitations imposed (see section 4.9.1).

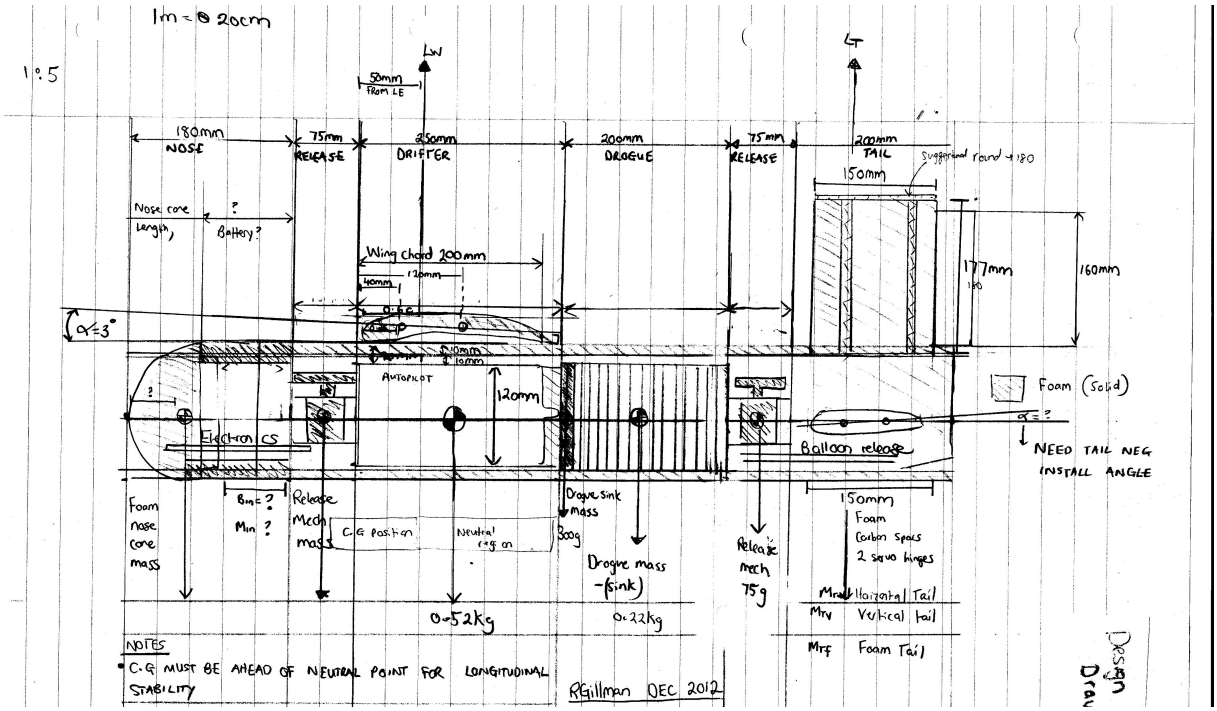

Figure 4.33: Final concept

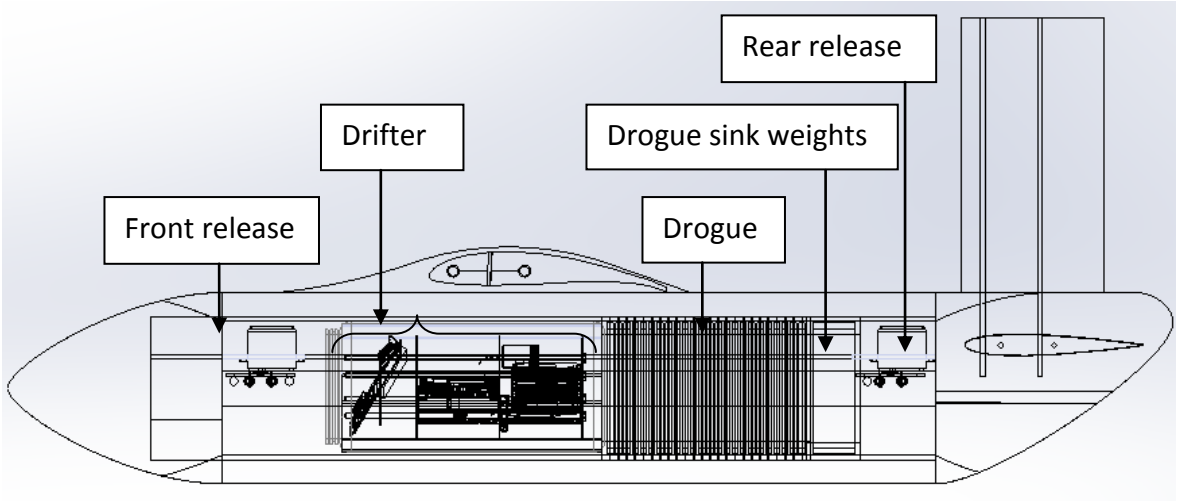

Figure 4.34: Final concept - CAD

Materials	**Density** (gcm^{-3})	**Advantages**	**Disadvantages**
Acrylonitrile Butadine Styrene, ABS[12]	1.08	Hard and rigid with good impact strength and weather resistance. UV-stabilised ready	Shrinkage due to thermal stress
Polycarbonate, PC [93]	1.2	Hard, rigid. UV-stabilised available	Expensive
Polypropylene, PP [99]	0.91	Low cost. Good impact strength and flexible	Cannot be painted on
High Density Polyethylene, HDPE[119]	0.97	Very good impact strength, Low cost and flexible	Need special ink to be painted on
Low Density Polyethylene, LDPE[120]	0.94	Lightweight yet tough, Highly flexible and easy to vacuum form	Can be fragile
Acryllic-Polymethyl methacrylate (PMMA)[121]	1.18	Hard and medium strength. Can be hand worked	Brittle and expensive

Table 4.3: Common Materials used in Vacuum Forming

4.9.1 Manufacturing - **Naveeyindren Thangarajah**

Surface drifters are generally made of light-weight polymers with good UV resistance and high impact strength. Typically, a buoy stays afloat for weeks or months, and hence it has to withstand the rough conditions of the ocean, including chemical degradation due to seawater. Currently the two most popular materials used to manufacture buoys are Acrylonitrile Butadiene Styrene (ABS) and Glass-fibre Reinforced Plastic (GFRP). To manufacture the buoy for this project, vacuum forming, 3D printing and rotational moulding manufacturing processes were considered.

Vacuum Forming
Vacuum forming is a thermoforming treatment, in which a heated thermoplastic sheet is formed over a mould and heated. The suction of air from between the sheet and the mould, allows the plastic to form around the mould taking its shape. The common thermoplastics that are shaped through vacuum forming and their relative merits are summarised in Table 4.3.

The vacuum forming machine in university is limited to manufacture products of size $20X20cm$ and it should not contain sharp corners or re-entrant angles. Moreover, the minimum wall thickness of the buoy it could produce was $2mm$ and the machine uses ABS plastic. Therefore, the weight of the surface buoy would be high and conflict with the requirement for a lightweight buoy.

3D Printing
3D printing was considered as an alternative to vacuum forming, due to geometric and time constraints. This is an additive manufacturing process which forms three dimensional objects through a layering process from a digital CAD drawing. Layers of plastic liquid or powder are set on a building tray, where, depending on printing method, the desired geometry is moulded together forming a fine layer of the final object. A new layer is then added to the current layer and the process repeats until the object is formed. 3D printing is an extremely useful rapid prototyping technology that allows structurally functional models to be built and testing in small batches. For electronic prototypes is allows single piece designs to be built with complex geometry that can save on manufacturing time, overall system mass and cost. As an example, with 3D printing it is possible to print large threads, clips and mounting posts.

The project had access to a 3D printer by Dimensions, model Breakaway Support Technology (BST) 1200es. This printer uses Fused Deposition Modelling (FDM), where a semi-liquid acrylonitrile butadiene styrene (ABSplus) is extruded through a temperature-controlled print head, building one successive layer

Materials	**Density** (gcm^{-3})	**Advantages**	**Disadvantages**
ABSplus[117]	1.04	Good toughness and strength	Shrinkage due to thermal stress
Polyphenylsulfone, PPSF [45]	1.3	Excellent heat and chemical resistance	Relatively costly
Polylactic acid, PLA[12]	1.25	Easily shaped	Water soluble under certain conditions
VeroWhite resin[94]	1.18	Sturdy and structurally stable	Need support material and incur high cost

Table 4.4: Relative merit of common materials used in 3D Printing

at a time [37]. The printer allows components to be built to maximum dimensions of 254 X 254 X 305mm and layer thickness as fine as 0.33mm [36]. Common materials that are used in 3D printings are listed in 4.4.

3D printing is high in cost and if the buoy was produced by 3D printing it would be heavy for the required volume of this project, due to the density of ABSPlus.

Rotational Moulding
Rotational moulding is also known as Rotomoulding. This process involves placing polymer powder (usually LLDPE, PP) into moulds. The mould is then heated and rotated in two axes in an oven. The powder then melts and sticks onto the inner walls of the mould in a uniform manner. Once the consolidation ends, the mould is cooled by air or water and the product is removed[98].

The University does not have a rotomoulding facility and seeking an external source to manufacture the buoy via rotamoulding would require a larger amount of cost and time. Therefore, this option was considered unfeasible.

Summary
It was shown in the pareto front,fig. E.1, that a 0.12m diameter cylinder of length 0.2m, with a drogue length of 5.5m, was the optimal solution. It had previously been shown that a cylindrical surface buoy was able to achieve a smaller diameter than a spherical equivalent. Regarding the manufacturing methods mentioned above 3D printing was viable but a costly option and vacuum forming offered a lower cost alternative. In summary the methods above would have produced a buoy with a large wall thickness and have resulted in a high buoy weight, high drogue length and large drifter diameter resulting in a reduced glider aerodynamic efficiency. Using vacuum forming to manufacture the cylinder would have been difficult due to its geometry and it would not have provided a lightweight solution therefore, the use of a COTS solution was explored. Potential surface buoys included blow moulded water bottles and chemical containers which provided a water tight seal and suitable means of inserting the electronics. The potential candidates came in a fixed range of volumes and were considered relative to the surface buoy requirement as shown in fig. 4.35.

Product	Cost	Neck diameter [m]	Volume [L]	Cylinder length [m]	Buoy external dia [m]	Buoy internal dia [m]	Buoy mass [kg]	Drogue Diameter [m]	Drogue Length [m]	Waterline [% Buoy height]	Total drag area ratio	Mass/ Total payload mass
2L Bottle	£11.66	87	2	0.235	0.11	0.108	0.2	0.12	5	0.50	19.29	0.83
1.5 L Bottle	£9.64	87	1.5	0.182	0.11	0.108	0.15	0.12	5	0.64	23.74	0.81
1L Bottle[Bulk purchase only]	£32.55	85	1	0.128	0.11	0.108	0.1	0.12	5	0.91	31.04	0.79
2L Bottle[chosen solution]	£11.66	87	2	0.235	0.11	0.108	0.2	0.12	5.5	0.51	21.34	0.83
1.5 L Bottle	£9.64	87	1.5	0.182	0.11	0.108	0.15	0.12	5.5	0.64	26.30	0.81
1L Bottle[Bulk purchase only]	£32.55	85	1	0.128	0.11	0.108	0.1	0.12	5.5	0.92	34.46	0.79
2L Bottle	£11.66	87	2	0.235	0.11	0.108	0.2	0.12	6	0.51	23.41	0.83
1.5 L Bottle	£9.64	87	1.5	0.182	0.11	0.108	0.15	0.12	6	0.65	28.89	0.81
1L Bottle[Bulk purchase only]	£32.55	85	1	0.128	0.11	0.108	0.1	0.12	6	0.93	37.93	0.80

Figure 4.35: COTS cylindrical buoy solutions

A cylindrical chemical bottle was bought from Fischer Scientific. The final selection was a Kartell $2000ml$ wide neck leak proof bottle [112] which weighed only $0.265kg$ and was made from High Density Polyethylene (HDPE). As seen from 4.4, HDPE has very good impact strength and highly flexibility, whilst having a density lower than that of ABS and PLA. The container is also highly resistant to chemical degradation as it is usually used to store chemical powders and paste. The tether bracket was made by drilling a hole in the bottom of the container, and retrofitting an L-shaped aluminium tether attachment. The bottom of the container was resealed with silicone sealant to ensure a watertight container.

4.10 Drifter Stability Calculation - Naveeyindren Thangarajah

A floating body is considered stable if it returns to its original state after experiencing small disturbance. The stability requirement for a partially floating body is explained in Figure 4.36, depicting a floating buoy in an upright stable position.

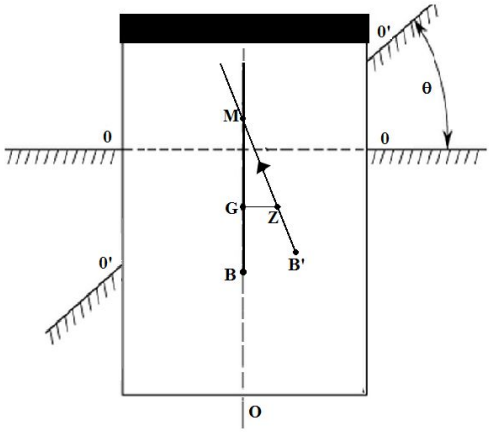

Figure 4.36: Metacentric height of the buoy

In Figure 4.36, the line **00** indicates the original water surface and the line **0'0'** refers to the new water line, after the buoy had been tilted with an angle of θ radians. **G** is the centre of gravity of the buoy and it remains the same in position, relative to the buoy after being perturbed. **B** is the initial centre of buoyancy, the centroid of the volume of fluid displaced by the buoy. After tilting, the centre of buoyancy

changes from **B** to **B'** due to the change in the shape of the submerged volume. Initially the buoy was in an equilibrium position, i.e., the points **B** and **G** lie on the same vertical line. The intersection point of the original vertical and the line connecting **G** and the new centre of buoyancy, **B'** is labelled **M**. The point **M** is known as the *metacentre* of the buoy.

Z is the foot of the normal from **G** on to the line of action of the buoyancy force, which acts along the point **B'**. A restoring moment acts to force the buoy to its initial position, from point **G**. This moment is known as the *righting moment*, **GZ** and the moment arm $\overline{GZ}$ is termed the *righting lever*[62].

For small values of θ,

$$\begin{aligned} \overline{GZ} &= \overline{GM} sin\theta \\ &\simeq \overline{GM}\ \theta \end{aligned}$$

$\overline{GM}$ is known as the *metacentric height*. The condition of stable equilibrium of a floating body can therefore be expressed in terms of metacentric height as follows [91]:

$\overline{GM} > 0$ (**M** is above **G**)	Stable equilibrium
$\overline{GM} = 0$ (**M** coincides with **G**)	Neutral equilibrium
$\overline{GM} < 0$ (**M** is below **G**)	Unstable equilibrium

Example Calculation

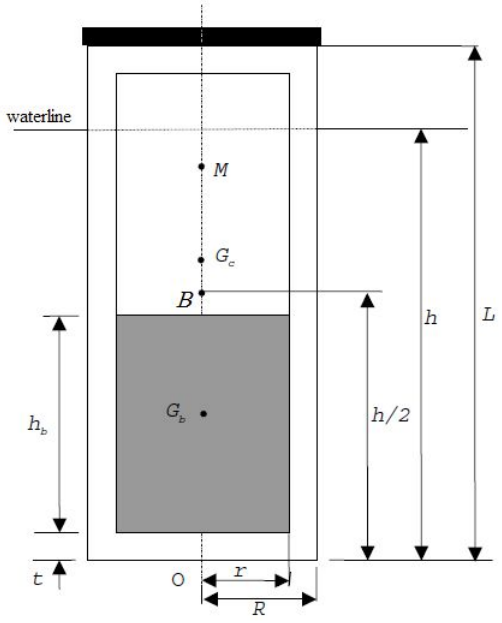

Figure 4.37: Dimensions of the buoy[89]

Figure 4.37 shows the dimensions of an arbitrary hollow cylinder, similar to the buoy used for this project. The cylinder has been made stable by placing ballast inside and floats vertically. Assuming the density of the liquid in which the cylinder floats is ρ, with a depth of immersion of h. B is the centre of buoyancy while G_c and G_b are the centres of gravity of the cylinder and ballast respectively. G refers to the centre of gravity of the cylinder/ballast pair and its metacentre is indicated as M. The mass of the cylinder is denoted as m_c and the mass of ballast is m_b.

From Archimedes' Principle:

$$\begin{aligned} F &= \rho\, V_{submerged}\, g \\ (m_c + m_b)g &= \rho\pi R^2 h g \\ h &= \frac{m_c + m_b}{\pi R^2 \rho} \end{aligned}$$

The distance of OG can be written in terms of cylinder/ ballast dimensions and masses,

$$\begin{aligned} OG &= \frac{OG_c m_c + OG_b m_b}{m_c + m_b} \\ &= \frac{m_c \frac{L}{2} + m_b(\frac{h_b}{2} + t)}{m_c + m_b} \end{aligned}$$

According to K.J Rawson and E.C. Tupper's Basic Ship Theory, page 105, metacentric height, $\overline{GM} = BM - BG$ [62] Hence:

$$\overline{GM} = BM - BG = BM - (OG - OC) \tag{4.22}$$

$$= \frac{I_{00}}{V} - \frac{m_c \frac{L}{2} + m_b(\frac{h_b}{2} + t)}{m_c + m_b} + \frac{h}{2} \tag{4.23}$$

Where I_{00} is the second moment of area of the waterline about the axis of disturbance. Since the buoy is a cylinder, the waterline area is effectively a circle and thus:

$$I_{00} = \frac{\pi R^4}{4} \tag{4.24}$$

Substituting 4.24 into 4.23 yields,

$$\overline{GM} = \frac{R^2}{4h} - \frac{m_c \frac{L}{2} + m_b(\frac{h_b}{2} + t)}{m_c + m_b} + \frac{h}{2} \tag{4.25}$$

Substituting known values, $m_c = 0.153kg$, and $m_b = 0.385kg$

$$\begin{aligned} \overline{GM} &= \frac{(0.11/2)^2}{4(0.05179)} - \frac{0.153kg\frac{0.235m}{2} + 0.385kg(\frac{0.21m}{2} + \frac{(0.11-0.108)}{2})}{0.505kg} + \frac{0.05179}{2} \\ &= \frac{605}{41432} - 0.10927 + 0.025895 \\ &= -0.068m \end{aligned}$$

As $\overline{GM}$ is less than 0 and it is 32.4% of the buoy's height, the buoy is significantly unstable on its own. From equation 4.26, to increase stability of the buoy, a higher ballast mass has to be used, since all other parameters are fixed. This would cause the centre of gravity of the cylinder / ballast to be lower and add on to its stability. In actual case, the increase in stability of the buoy is due to the fact where the extra mass effectively lowers the centre of gravity of the whole system causing the position of G to be below M, leading to a stable equilibrium of the buoy-drogue pair. The buoy would only be unstable if there were forces due to sub-surface currents which acts to cancel out the tension acting on the tether. However, as the currents subside, the whole system (buoy and drogue) will return to its stable position.

Future Work
The static stability of the drifter could be analysed in more detail through the use of commercially available software such as HydromaxPro to obtain its righting moment arm curves. These curves indicate the angle of heel and the energy that is needed to capsize the buoy as well as the angle of vanishing

stability - a critical point where exceeding this angle would capsize the buoy, indicating the start of a negative stability regime. Knowing this, one could improve the stability of the current buoy, minimising loss of functionality of the drifter should the drogue detach.

4.11 Water Collision Simulation - **Benjamin James Oxley**

When the drifter collides with the water the drifter structure is subjected to it's maximum stress. It is important to check that the drifter will not break upon impact. To do this, some simple equations can be derived to determine the forces on the drifter.

The glider aims to release the drifter near sea level, as we know the altitude of sea level exactly (as sea level is roughly constant), we know what GPS altitude it would be best to release from. However, the GPS has a margin of error of approximately one to two metres so the glider must reach a few meters above sea level.

Where we assume vertical speed to be zero when the glider is flying level near the ground. In addition, for this calculation, air resistance will be neglected. To model the worst possible crash conditions, a drop from 20 meters was simulated using $v^2 = u^2 + 2as$ we get: $\sqrt{2 * 9.81 * 20} = 20ms^{-1}$ a horizontal speed of $10m/s$ (The glider's flight speed).

The drifter mass is 0.5kg and hence the kinetic energy associated with the vertical component of motion will be 100 joules. A calculation can be done to determine how quickly the drifter is stopped by looking at force produced by buoyancy force and integrate until the drifter velocity is zero.

4.11.1 MatLab Collision Simulation

The governing equation for this system can be found in terms of a force balance between buoyancy (assumed to be constant up-thrust as a simplification), gravity and drag in water:

$$ma = -h\pi r^2\rho + mg - \frac{1}{2}\rho v^2 C_d A \tag{4.26}$$

$$\frac{dv}{dt} = \frac{-h\pi r^2\rho + mg - \frac{1}{2}\rho v^2 C_d A}{m} \tag{4.27}$$

This is then solved using MatLab's ode45 program and the results are plotted in fig. 4.38. This shows a maximum force (acceleration×mass) of 2.3 kN and if this is assumed to act directly on the bottom of the cylinder area, this relates to a pressure of $240kPa$. This approach contains a lot of assumptions and considers one of the best-case scenarios for force distribution on the structure.

4.11.2 Abaqus Finite Element Analysis Collision Simulation

To corroborate this calculation, a coupled Eulerian-Lagrangian water crash simulation was carried out in the Dassault Systeme's Abaqus FEA package using the explicit solver [34, 33]. Due to the limitations of the Abaqus package the simulation had to be low fidelity in order to remain under the licences 20,000 node limit. The cylinder model was created using 4,196 type S4R Lagrangian shell elements (better S8R elements are not available with the explicit solver). The Eulerian domain was modelled with 14,208 type EC3D8R elements and material properties for the plastic and water were defined. A close-range mesh was built around the cylinder impact region to attempt to more accurately model the interaction (in a similar way to meshing CFD domains). Zero normal velocity boundary conditions were set up around the Eulerian mesh and initial velocity and inertia properties were set up on the cylinder. The solver was validated by monitoring the initial kinetic energy determined by the solver which matched that of the calculations performed above.

Results in fig. 4.41 show a rising stress with time but only on a few nodes. It is likely, due to the low

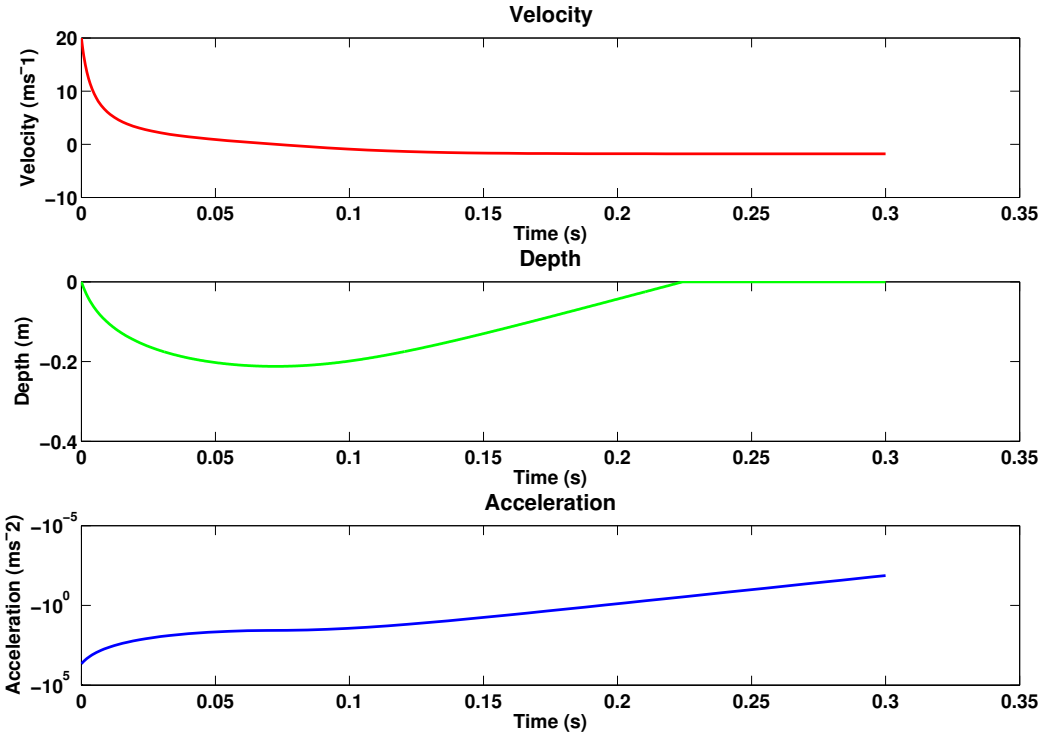

Figure 4.38: Graphs of the result of water testing.

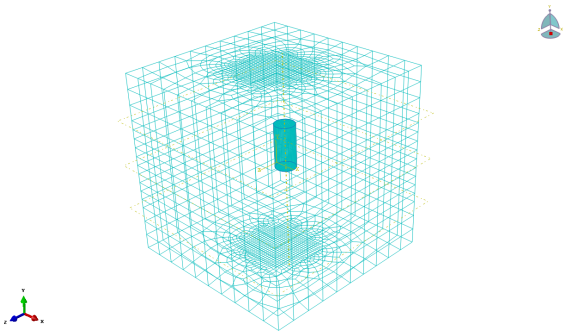

Figure 4.39: Meshing of cylinder and Eulerian domain

fidelity of the meshing and the simplified buoy shape that unrealistic buckling of these nodes. Therefore these single node stresses should be ignored. A more distributed stress of approximately 1MPa maximum can be seen to be an average of many node stresses further analysis could be taken from this data to average nodal values and remove the noise from results. As the simulation is being undertaken to ensure the safety of the cylinder on impact and the quality of the mesh is causing inaccuracies it is best to compare against the MatLab simulation to take conclusions. The FEA simulation corroborates the MatLab calculation results within one order of magnitude. The Abaqus simulation is likely to have a higher stress as it more accurately models the stress distribution likely through the cylinder. Although this stress is much lower than the ultimate properties of the material, it is extremely important to understand that failure in compression is likely to occur through buckling. However, the cylinder design with the internal electronics mount means that buckling is much harder than when simulating just the cylinder alone. It is also possible to deduce, due to the minimal deformation of the cylinder, that internal pressure is unlikely to force the cylinder lid to come off.

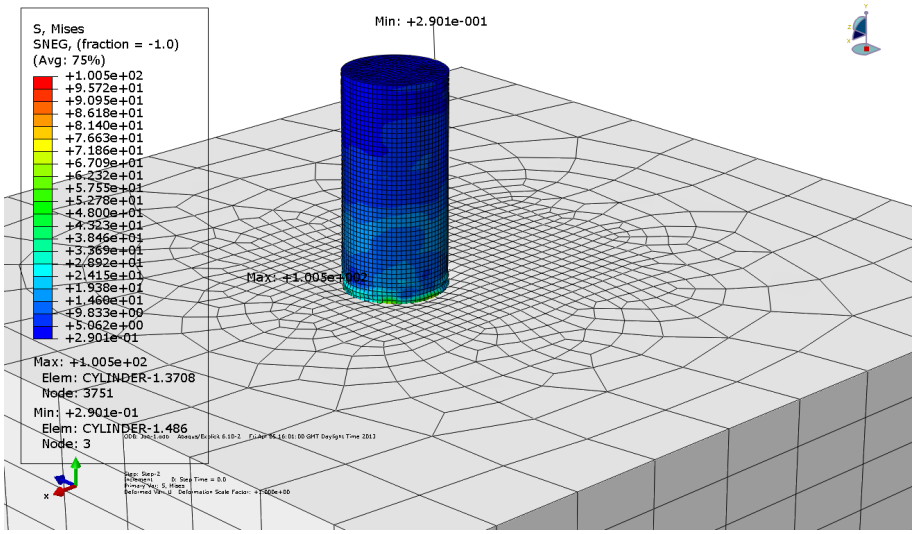

Figure 4.40: Maximum von Mises Stress on the cylinder

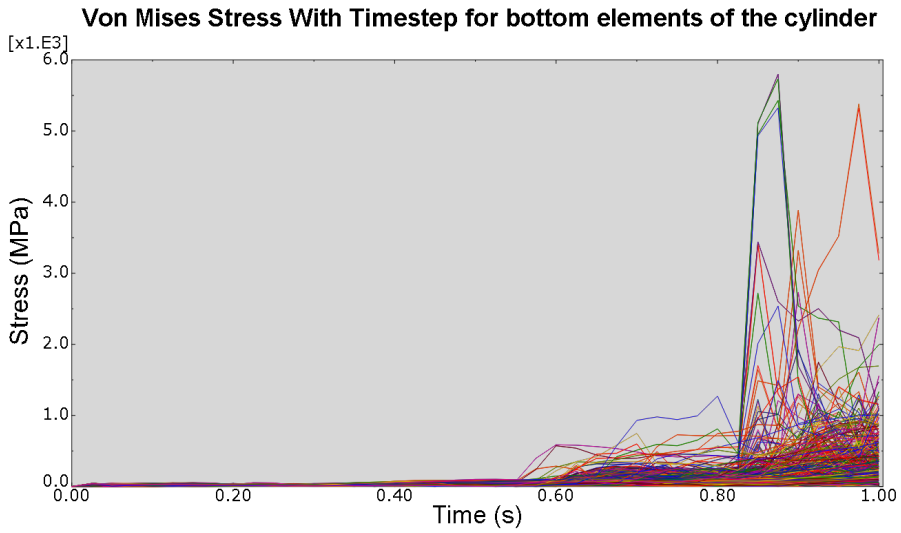

Figure 4.41: Maximum von Mises Stress on the cylinder with time

4.12 Drogue Final Design - Raja Nurul Yuhanis

In the previous section, drogue-buoy considerations, the requirements of the drogue-buoy system were discussed in detail. In short, a good drogue-buoy system should be able to support enough electronics for oceanographic purposes, provide enough buoyancy, as well as a high drag area ratio which will give a low slip velocity for the drifter.

4.12.1 Shape

One of the drogue designs that was considered in this project was the tri-star (cruciform) drogue, which is a collapsible drogue. This was considered for being easy to pack, having a high packing efficiency (high ratio of the deployed volume to packed volume), able to save space and efficient for currents in all directions. However, this type of drogue is not feasible for the design requirements of the current drifter system, as this type of drogue is only suitable for shallow water operation, as opposed to the required depth of ten meters of this project. Apart from that, the parachute type drogue was also studied. A parachute drogue is not commonly used for a drifter system, but it is predominantly used for sail boats. This type of drogue has a very high coefficient of drag but it reacts against the direction of the current, and under a very low velocity current, the parachute may collapse and will not contribute any drag,

unless a stiffener is applied to it to retain its shape.
Hence, a cylindrical shape was chosen for the design of the drogue. A cylindrical drogue is also known as a holey-sock drogue. This design is popular among ocean drifter manufacturers. A holey-sock drogue is a long hollow cylinder, with pair of holes adjacent to each other along its length. The set of holes are placed 90 degrees to the previous section's holes. Each section of the drogue is separated by a circular metal ring for structural support and rigidity underwater. The holes work in a similar manner to dimples on the golf balls, by disrupting the otherwise laminar flow which would generate organised vortices. As a consequence, the drogue does not experience abrupt changes in drag coefficient across a critical Reynolds number which would be associated with vortex shedding [42]. At the bottom of the drogue, a set of metal rings are bound together for extra weight for the drogue.

4.12.2 Size

The size of the drogue is related to the drag area ratio of the drifter system. This drag area ratio should be maintained high enough to reduce slip velocity, which was discussed in detail in the drag area ratio section. Most manufacturers of ocean drifters aim for a drag area ratio of approximately 40. For this design, after a considerable amount of work, it was decided that this particular drogue sizing needs a compromise on the drag area ratio. The compromise was to reduce the drag area ration from 40 to 20.

The drogue is 0.12 m in diameter, and 5.5 m in length. The drogue consists of sections which are separated by circular rings along the length of the drogue. Length of the section is equal to the diameter of the drogue. Hence, the number of sections was calculated by dividing total length by the diameter of the drogue, this resulted 46 sections. The diameter of the holes are taken as half of the diameter of the drogue according to the WOCE/TOGA Lagrangian drifter construction manual [85] and are $0.06m$.
The sizing of the drogue also lies behind design limitations of the UAV which was, the drogue has to be able to fit into the fuselage of the glider, which is the main limitation. A larger glider will cause worse aerodynamic efficiency due to the increase in skin friction drag. The holey-sock drogue will be packed by compressing the drogue to a shorter length of approximately 0.2 m. In this case, the diameter of the drogue is driven by the diameter of the fuselage. An optimisation was performed to determine the diameter and length that will give the best performance for the buoy-drogue pair.

4.12.3 Materials - **Naveeyindren Thangarajah**

The drogue is to be manufactured from a fray-resistant synthetic cloth or canvas. According to the SVBP Design Manual, it was recommended to use 370 gsm, 1000 denier Cordura nylon cloth as it is extremely durable, due to the fact that it has been coated to prevent fraying. The manual has also specified an alternative of 200 gsm stabilised Dacron sailcloth. This material, however requires the holes to be cut thermally to ensure fraying does not occur [85]. These materials, whilst being an excellent choice to manufacture a drogue, are relatively heavy for this project.

As the mass of the whole system, including the drogue-drifter, electronics and the actual glider should not exceed $2.7kg$, minimising the weight of the drogue is crucial but at the same time, the drogue will be able to serve its main purpose.

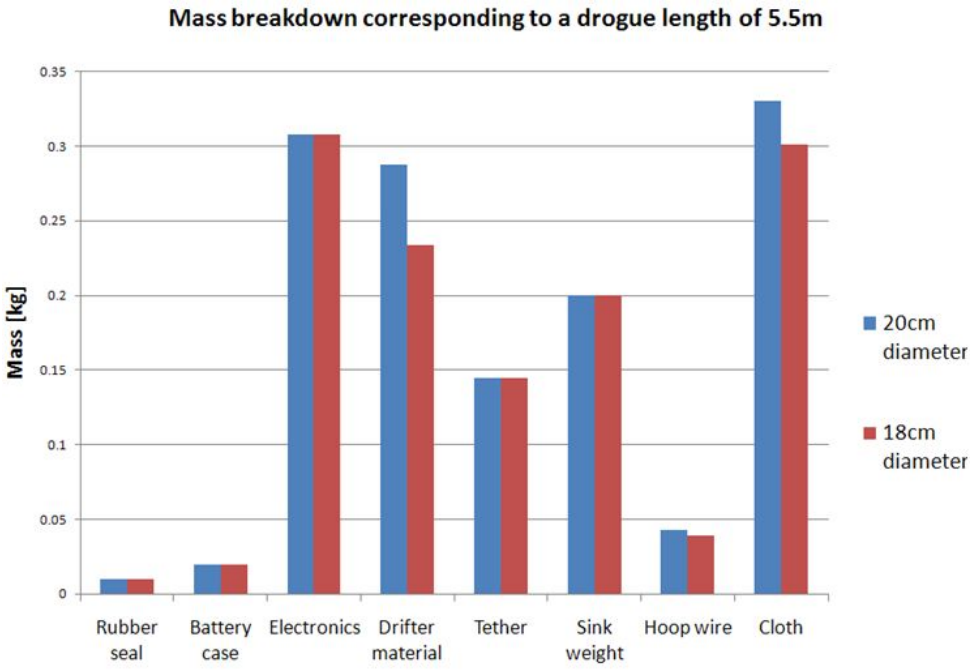

Figure 4.42: Mass Breakdown of Components

A glider is to be modelled around the buoy-drogue system. Currently, the glider diameter is too large as it is driven by the diameter of the buoy. Hence, the need for a smaller buoy arises. This can be done by reducing the required buoyancy of the drifter. The required buoyancy of the drifter depends on the mass of the drifter plus the tether and the drogue. Taking the drogue length to be 5.5m and comparing the mass of components of the whole system for 18cm and 20cm buoy diameters shows that the cloth mass is the largest contributor to the buoyancy force required by the drifter, according to figure 4.42. By reducing both the cloth mass and buoy material mass, it was possible to reduce the required buoyancy force. It was ensured that the decrease of the buoy's diameter still corresponds to the design criteria of drag area ratio greater than 40.

The alternative material sought was ripstop nylon fabrics. They are predominantly used as sail cloth as they are highly water resistant and durable. This type of material resists tearing and ripping as it is reinforced by being interwoven at a regular interval in a cross-hatch pattern. Due to this, small tears cannot easily propagate along the fabric. It was decided that a fabric with smaller density had to be used, owing to the weight constraint of the whole system. Hence, Fibremax 44 (44 gsm) was used to manufacture the drogue. Fibremax 44 is a stabilised nylon fabric, where it was dipped in a solution of dissolved resin. The resin particles are embedded in the weave as the resin is cured at high temperatures. Due to this treatment, the fabric is highly efficient it resisting stretch [111]. Although Fibremax 44 is approximately eight times lighter than the recommended material due to its durability and strength, it is concluded to be the suitable drogue material for this project. Since abiding the strict weight limit was one of the main concern, this compromise is justified.

4.12.4 Manufacturing - Raja Nurul Yuhanis

Drogue

The drogue was manufactured by sewing pieces of fabric together to form a cylinder with pockets sewn along the length for the sections of the drogue. The length of each section is equal to the diameter of the drogue i.e. $0.12m$. For the purpose of testing, a circular bottom was sewn on the drogue so that weights can be dropped from the water surface onto the bottom of the drogue, preventing the weights from sinking to the bottom of the testing water tank.

The full-scale, 5.5 m drogue, was manufactured in sections. Firstly, the cloth was cut into five large pieces. Then, small strips were cut for pockets to integrate circular rings between sections. The first four pieces included 10 sections of drogue, and the final piece comprised of the remaining six sections of the drogue including the pocket for the ballast weights. The piece is a rectangle with dimensions of $0.4m$ (circumference + $0.02m$ seam allowance) X $1.22m$ including $0.01m$ seam allowance on each side. The holes are cut on each section and positioned accordingly. The top most part of the drogue was folded up twice for the pocket for the tether connection. The bottom pocket was made relatively larger than the rest for the sink weights to be placed in. Finally, the long sides of the drogue are sewn together to form a long cylinder. For most of the parts, normal stitching was used. The bottom pocket and the upper most part required zigzag stitching so that the stitching reinforces the areas with high stress concentrations.

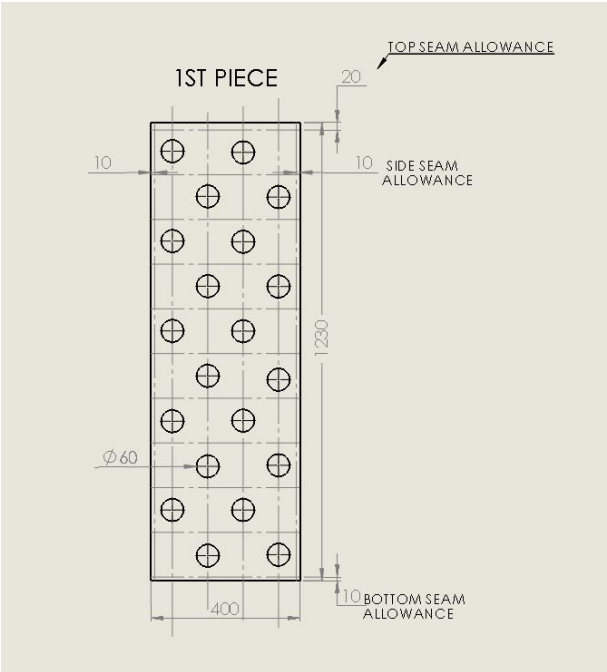

Figure 4.43: Manufacturing drawing of the 1st piece for the drogue.

Each section of the drogue was integrated with metal hoops for structural rigidity. These hoops were inserted into the sewn pockets. For this purpose, aluminium welding rods were used as they are lightweight (density $\rho = 2650\ kgm^{-3}$) and have a good corrosion resistance. Aluminium welding rods can easily be shaped into hoops as opposed to wires made from other metals, such as steel. The rods were also cheap and readily available through University workshop.

Sink Weight - Naveeyindren Thangarajah
The drogue has to be attached with sink weights at the bottom to prevent tangling and spiralling. Usually, a drogue-buoy pair consists of lead weights as sink material. From the scale model tests of the drogue (see 4.12.5, it was decided that a sink mass of $300g$ is sufficient to ensure the buoy-drogue pair is stable underwater. In order to save cost, it was decided to use materials which were easily available as sink weights as the mass needed was relatively low. Hence, the final decision was to use hoops made of galvanised steel wires as the sink weight.

Three strands of wires of length $34cm$ each were inserted into a plastic tube and the tube was bent to form a circle. The mass of a hoop (circular tube with three strands of wires) was $33g$ and 9 set of tubes were slotted into the pocket of the drogue's final section.

Tether - Naveeyindren Thangarajah
The tether connects the drogue to the drifter and thus it has to withstand high forces, because in rough sea conditions, there will be tension and shock loads transferred from the drogue to the buoy. These forces will be distributed along the length of the tether and as such, a material with good strength was required for the tether.

To reduce the shock loading on the tether, usually, subsurface floats are incorporated in a drifter system. This subsurface float absorbs some of the shock from the surface wave motion. However, having a subsurface float in this design reduces drag area ratio, as it increases the area of non-drogue components (see equation 4.2). The forces acting on the tether were highly complex to model, due to the harsh sea condition. The recommended material for the tether is wire rope, made from plow-share steel and impregnated with plastic. For this project, since the drogue-buoy pair has to fit in the fuselage of the glider, a compromise has to be made as it is unfeasible to have stiff wires in the fuselage.

The possible options included were fishing line, kite wire, and flexi wire. For this project, fishing line was chosen to be the tether as it was easily available, cheap as well as being able to withstand the weight of the drogue with sink weight. The particular fishing line chosen was Araty Superflex, made of nylon, with thickness of $0.6mm$ and a length of $7.8m$. This fishing line was was selected as it was able to withstand a force of 195N, easily wound, lightweight whilst being flexible. The kite wire, was not as strong as the fishing line and thus ruled out. The flexi wire, was too heavy and costly for the purpose of this project and it was considered unfeasible.

Tether Connection - Naveeyindren Thangarajah
The additional length of the fishing line was to compensate for the length loss due to the connection points. It was wound on a plastic spindle for ease of deployment. The configuration of the attachment is shown in Figure 4.44

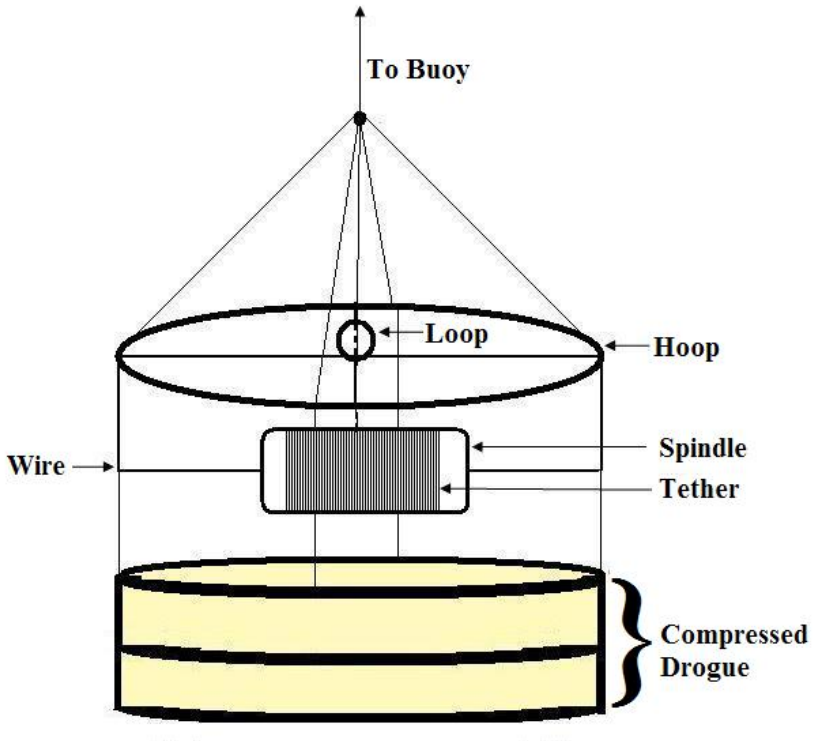

Figure 4.44: Diagram showing the tether connection

A hoop of $10cm$ diameter was made by inserting a strand of galvanised wire into plastic tube and bending it to a circular shape. Both ends of the tube were attached by waterproof tape. Two wires were bent diametrically around the hoop and a small loop was made on a wire at the centre. This was done so that

an X configuration was obtained, to maintain the rigidity of the hoop. A single wire was bent in two places to create the platform for the spindle and connected to the hoop and also ensured enough clearance for the spindle to revolve freely. One end of the fishing line the spindle was attached and secured with waterproof tape before the rest of the line was wound on the spindle. The other end of the tether was inserted into the loop and secured to the bottom of the buoy with the aid of a carabiner hook. Four strands of $15cm$ fishing line was tied on the hoop and their ends were merged with the single strand of the fishing line from the spindle. Similar strands of fishing lines were attached from the bottom half of the hoop to the first section of the drogue.

4.12.5 Water Tank Testing - Raja Nurul Yuhanis

The actual drogue is $5.5m$ in length but the model drogue was manufactured to be $1.0m$ due to the limitation of the tank's depth. The diameter was left unchanged. The aim of the tests was to record the behaviour of the drogue under water, and assess how well it sinks with and without weights attached to it. In addition, the packing efficiency of the drogue was determined.

Packing Efficiency of the Drogue
It is very important to calculate the packing efficiency of the drogue, because it has to fit within the limit length of the glider fuselage. The test piece of $1.0m$ was packed in between two planar blocks for the accuracy and the distance between was measured. The final value was $0.04m$. This value was further used to calculate the packing ratio and efficiency to determine the actual size of the packed drogue.

$$\text{Packing ratio} = \frac{\text{Length Before}}{\text{Length After}}$$

$$\text{Packing ratio} = \frac{1.0m}{0.04m} = 25$$

$$\text{Packing Efficiency} = \frac{(\text{Length before} - \text{Length after})}{(\text{Length before})}(100)$$

$$\text{Packing Efficiency} = \frac{0.96}{1.0}(100) = 96\%$$

Hence, the packing efficiency of the drogue is very high. To compute the actual packing length, the full length is multiplied by the reciprocal of the packing ratio and is $5.5 \times \frac{1}{25} = 0.22m$

For a better fit into the final design and to account for any roughness due to uneven packing, complete packed drogue is tightly wrapped into the water soluble material.

Drogue Testing
Initial testing of the drogue was required because the behaviour of the drogue under the water was uncertain. Before proceeding to the actual test, the two resulting possibilities were predicted. Firstly, the drogue will take an infinitely long time to deploy under water, so would require additional weight. Secondly, the drogue will deploy under water under its own weight. With these two possibilities, the drogue was packed and released on the surface of the water and was timed.

In this testing, the drogue was recorded to take 4min 45s to fully deploy under water. The worst case scenario was also considered, where the drogue might unpack in the air, and land on the water surface horizontally. The time taken for horizontal drogue released on the surface of the water is 1 min 11s.

From the initial testing, it can be concluded that there will be no problems with drogue deployment. The deployment in the tank was performed under static water conditions.

Weight, W (N)	Time, T (s)					Average Time, T (s)	Rate, 1/T (s^-1)
	t1	t2	t3	t4	t5		
0.005	12	22	20	17	22	18.6	0.053763
0.01	10	7	11.4	9.3	11	9.74	0.102669
0.015	7	7	6	6	7	6.6	0.151515
0.02	5	5	5.3	5	6	5.26	0.190114
0.025	5	5	5.2	4.9	5	5.02	0.199203

Figure 4.45: Deployment time for the drogue with weights

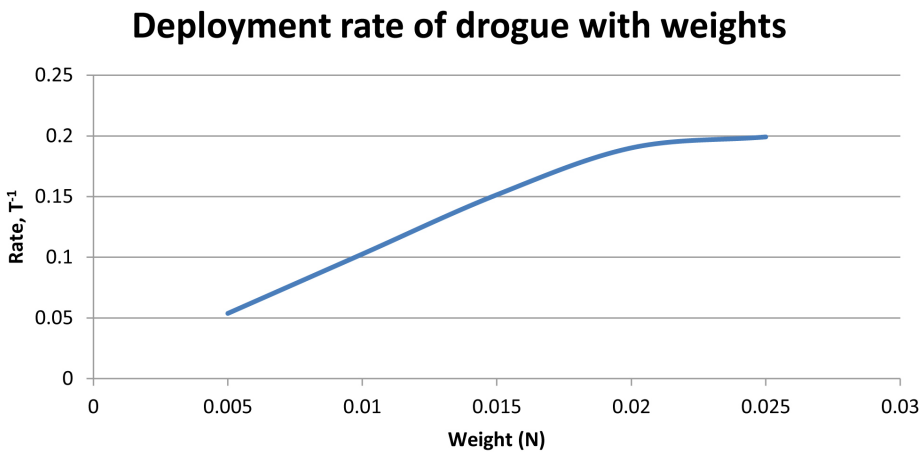

Figure 4.46: Rate of Deployment against Weight:1

Test 1
The aim of the test was to record the behaviour of deployment of the drogue under weights. Time taken for the drogue to be fully deployed under water was recorded. The maximum mass of the drogue is 300 g due to the limitation of negative buoyancy of the drifter. The masses were added from 50g to 250g in increments of 50g. A set of 5 readings were taken for each configuration and the average was calculated. For this first test, a table of results and a graph are shown in Figure 4.45 and Figure 4.46 respectively.

The results show that as the weight increases, the time taken for the drogue to fully deploy will decrease as expected.

Test 2
The bottom was then cut out and an attachment was made to hang the weight underneath of the drogue to determine if the sealed bottom was affecting deployment time.

The tests were done in a similar manner to Test 1, and the results were then recorded (See Figure 4.47), and graphs were plotted to analyse the difference between the two test results (See Figure 4.48).

It can be seen from fig. 4.48 that the circular bottom affects the deployment rate of the drogue. The deployment rate behaves linearly with the increase in weight. From the testing, it was concluded that the drogue will not suffer major issues when deploying under water.

Test 3
The aim of this test is to assess the water solubility of the fabric that was used to wrap the drogue inside the glider, as well as deployment of the full size drogue in the tank. With the limitation that the tank is only 1.2 metres deep. It was seen that the drogue seemed to deploy successfully with the weight attached at the bottom.

Weight, W (N)	Time, T (s)					Average Time, T (s)	Rate, 1/T (s^-1)
	t1	t2	t3	t4	t5		
0.005	15	18	18	29	20	20	0.05
0.01	8	9	8	9	7.5	8.3	0.120482
0.015	6	6	5.5	6	5.5	5.8	0.172414
0.02	5	4.5	4	4	4	4.3	0.232558
0.025	3	3.5	3.5	3.4	3.6	3.4	0.294118

Figure 4.47: Rate of Deployment against Mass

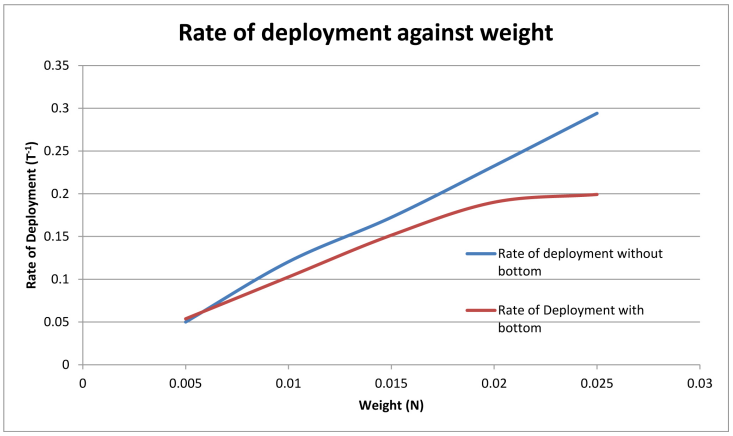

Figure 4.48: Rate of Deployment against Weight:2

4.12.6 Analysis - Naveeyindren Thangarajah

As mentioned earlier in this section, the model drogue was designed by reducing the full length due to the depth of the water tank facility in the University used for testing. To complete a more accurate test, a scaled model would be required, however it was complicated to manufacture with the equipment available. Consequently, it is suggested that a full scale test is necessary to determine the effectiveness and durability of the drogue in actual conditions. The minimum water depth would otherwise need to be $6m$ to perform a full scale deployment test and determine the drag coefficient of the drogue.

For the slip test a much deeper facility is needed because it has to include a full drifter system with tether and buoy. The drag coefficient of all components would be determined and used to obtain drag area ratio and then the slip velocity. Currently, data used in calculations is extrapolated from values found in appropriate literature, so finding actual values would allow more accurate results.

It is also important to note that data obtained from tests described above correspond to steady flow conditions. The dynamic sea conditions could be simulated for the full scale systems with more well equipped testing facilities, to observe its behaviour and component interaction.

5 | Drifter Deployment Glider

5.1 Materials Selection - Naveeyindren Thangarajah

5.1.1 Materials Selection Process

A successful engineering application or design depends highly on the correct usage of materials. In order to decide on a specific material to be used in a project, one has to scrutinise the types of material that can satisfy the job requirements, their performance as well as the cost of using them. To do this, a coherent selection process is vital.

The selection process starts with listing down all possible materials that are deemed to be useful. Secondly, a screening and ranking procedure will be carried out to eliminate materials which are unfit for the application and to indicate the materials' ability to fulfill specific roles. This is done by applying material indices (see section 5.2). The next step requires supporting information of the potential materials. This information includes the materials' behaviour in different environments, case studies of previous uses and also its environmental impact. This information were obtained through handbooks, supplier's data sheets or engineering standards. The final stage depends on local conditions such as, availability of the material, delivery speed and existing facilities to work with the material[18]. Materials selection is the foundation for any engineering design and if it is carried out incompetently, the bad decision could dramatically compromise the safety of any project.

5.2 Material Merit Index

Material Merit Index is a combination of material properties which characterises the performance of a given material in a particular application. For a structural element, its performance is decribed by a generic equation of the following form.
$Performance, p = f$[(Functional Requirements, F) $\cdot$ (Geometric Parameters, G)
When the above equation is separable, it can be written as,

$$p = f_1(F) \cdot f_2(G) \cdot f_3(M) \tag{5.1}$$

As structural equations generally are separable, the optimum choice of material is independent of the designs, therefore its geometry, G is valid for all the values of functional requirements, F. Thus, the performance of a structural element could be maximised by maximising $f_3(M)$, which is known as the materials merit index.

An example of calculation of Material Merit Index for a structural element can be seen in section 5.2.1

5.2.1 Selection Process

Fuselage
Typically, the materials that are used to manufacture the fuselage of a UAVs are metallic alloys, wood, fibreglass, plastics and foams. Since the glider is expected to land in the sea and the materials are expendable, maintenance of the glider is not a major concern (see section 4.4.2). Hence, the material needed was preferred to be of low cost. As the design requirement presents a weight limit of $2.7kg$ for

Aspect	Expanded Polypropylene, EPP	Expanded Polystyrene, EPS
Tensile Strength ($kgcm^{-2}$) [100]	2.5	3.2
Density (kgm^{-3}) [100]	20.8	20.0
Cost [44]	High	Low
Suitable for [44]	Small Wings	Small and Large Wings

Table 5.1: Comparison of EPP and EPS foams

the whole system, the main concern is to choose a light material, having low density. Since the glider design was expanded from the works of GDP16 2012, it was decided to manufacture the glider's fuselage and wings using engineering foams. The two most commonly used foams for UAVs and model planes are Expanded Polypropylene, EPP and Expanded Polystyrene, EPS. A comparison table of both foam types, of similar density is given in Table 5.1

From Table 5.1, it can be submitted that EPS has a better structural strength than EPP while being cheaper. EPP foam is commonly used as packaging material, especially for delicate electronic components as it is able to withstand rough handling. EPS foam is lighter and provides better workability. However, it is not as durable as EPP. Commonly used as insulation material, EPS requires coating with carbon fibre cloth or balsa sheeting fibreglass to increase its durability.

A study by GDP16, 2012 indicated that EPS foams offer slightly better energy absorption compared to EPP. However, during compression, EPP tends to remain in the elastic region for a larger time period and thus offer prolonged impact resistance [47]. While being an advantage for the usage of EPP, the fact that the glider is expendable upon landing indicates that the glider would only experience single impact. Moreover, reusability of the glider ranked little in the design requirement. hence, it was decided that the fuselage as well as wings were to be manufactured from the EPS foam.

Hot Wire Foam Cutting
The glider can be manufactured by cutting EPS foams via hot wire cutter. This technique of using a hot thin metal wire to melt and therefore cut the foam at the precise point of contact is an effective method of shaping foam [43]. Feeding the wire into a desired location within the foam and then turning on the heat is also possible to produce cavities within the foam. This facility would not involve any project costs.

Wing Spars
As an example of the usage of Materials Merit Index, the wing spar will be studied. A spar experiences high levels of loads during flight. It is anticipated that the spar withstands three times the mass of the glider.

The wing spar was modellled as a cantilever beam, in bending under uniform load, F as shown in Figure 5.1. The beam is square in cross section and has dimensions of length L and sides h and a uniform density ρ.

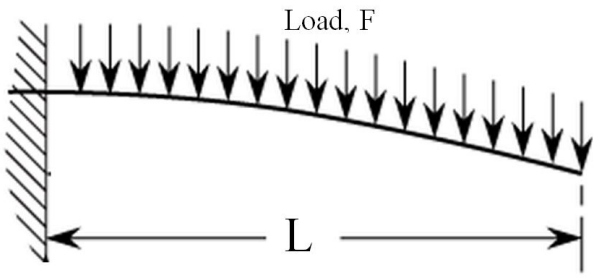

Figure 5.1: Modelling the wing spar as cantilever beam[29]

The objective of this study is to choose the lightest material which can act as a wing spar. The beam is

allowed to deflect δ units under force F. C_1 is a constant depending on the load distribution.

The beam has a square cross section of area, $A = h^2$ and second moment of area, $\mathrm{I} = \frac{bh^3}{12} = \frac{h^4}{12}$ The mass of the beam is:

$$m = A \cdot L \cdot \rho \tag{5.2}$$

Hence,

$$\frac{F}{\delta} \geq C_1 EI = \frac{C_1 E h^4}{12L^3} = \frac{C_1 E A^2}{12L^3}$$

Therefore,

$$A = \sqrt{\frac{12FL^3}{C_1 \delta E}}$$

Substituting the expression for A into equation 5.2 and further simplifications gives,

$$m = \sqrt{\frac{12F}{C_1 \delta}} \cdot \sqrt{L^5} \cdot \sqrt{\frac{\rho^2}{E}}$$

Comparing with 5.1 indicates that,

$$f_3(M) = \sqrt{\frac{\rho^2}{E}}$$

To minimise mass of the beam, $f_3(M)$ has to be minimised. This is essentially the same as maximising $\sqrt{\frac{E}{\rho^2}}$. Hence the materials merit index for this case is $\frac{E^{\frac{1}{2}}}{\rho}$ [88] Having calculated the merit index, the next step was to use property charts to indicate groups of materials that are suitable to be used as a wing spar. Since the merit index is known, an Ashby plot of Young's modulus and density was consulted.

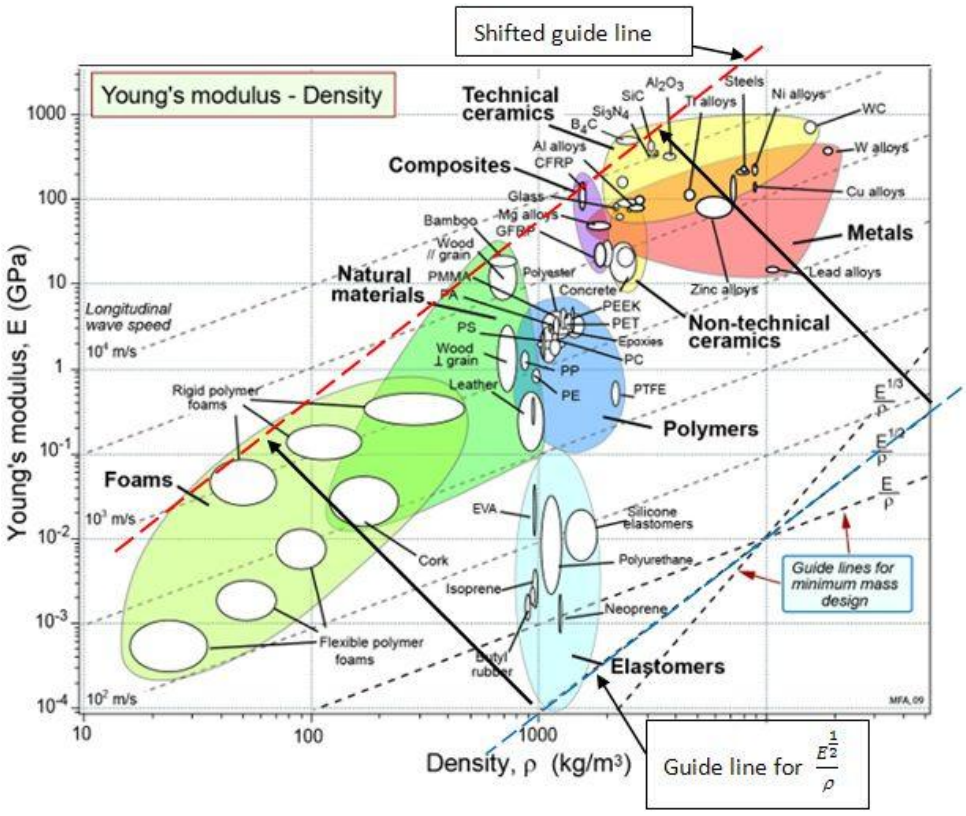

Figure 5.2: Ashby Plot of Young's Modulus and Density for Common Engineering Materials[32]

Figure 5.2 contains guidelines for minimum mass, according to merit indices. A guide line for merit index of $\frac{E^{\frac{1}{2}}}{\rho}$ is indicated in blue. This guide line will be shifted upwards along the vertical axis of the plot to indicate materials with highest $\frac{E^{\frac{1}{2}}}{\rho}$ value. The final position of the guideline is indicated in red. The red dashed line shows the regions for the materials with high merit index as wing spar. They are technical

ceramics, composites, woods and rigid foams.

Ceramics are inherently brittle and expensive hence they were not considered to be a potential spar material. As the wings are made out of foam, having a spar made of foam is not sufficient to withstand the high stresses and bending moments the wing would experience in service. A comparison of merit index for materials commonly used to manufacture wing spars is presented in Table 5.2

Material	Elastic Modulus, E (GPa)	Density, ρ (Mg/m^3)	Merit Index, M
Carbon Fibre[7]	70	1.85	4.5
Plywood[131]	6.96	0.4	6.6
Aluminium Alloy (7075 T6)[116]	71	2.82	3.0
Steel[10]	200	7.85	1.8

Table 5.2: Comparison of possible spar materials

Table 5.2 indicates that the material with the highest merit index is plywood. However, plywood had the lowest elastic modulus in comparison with other materials in Table 5.2 and its strength will be compromised if it comes into contact with water.

Using steel or aluminium alloy would lead to a large mass of the glider, due to their density being higher than plywood and carbon fibre. Therefore, the material that was chosen to be the wing spar was carbon fibre. This decision was taken considering the lightweight property and easily availability of carbon fibre.

Shape Factor
The previous analysis was done by assuming the wing spar takes the shape of a square cross sectioned beam. However, other shapes offer greater resistance to loading for a given cross section. Using shape factor, one can compare the efficiency of utilising beams with different cross sectional shape to resist bending. Shape factor values are highly dependent on manufacturing constraints, especially the formability of a material. It is vital that the material used can be formed to the most efficient shape as geometry plays a major role in shape factor as shown in the following example. Shape factor, ϕ is defined by,

$$\phi = \frac{\text{Efficiency of a shape to resist load}}{\text{Efficiency of a solid rod with same cross section to resist load}}$$

Since for a wing spar, stiffness is of concern, the shape factor is written as:

$$\phi_B^e = \frac{S}{S_0} = \frac{EI}{EI_0} = \frac{I}{I_0}$$

The superscript e denotes that this is an elastic case, the subscript B indicates that the loading is in bending, S = Stiffness of a cross-section of interest, S_0 = Stiffness of reference solid cross-section. As the reference cross section is square,

$$I_0 = \frac{h^4}{12} = \frac{(A_0)^2}{12}$$

Comparing sections of same area, $A_0 = A$ gives,

$$\phi_B^e = \frac{I}{I_0} = \frac{12I}{A^2} \tag{5.3}$$

Example
Two possible cross-sections for the wing spar were analysed. The following example shows the shape factor for an arbitrary I-shaped and a hollow circular wing spar, with similar cross-section area.

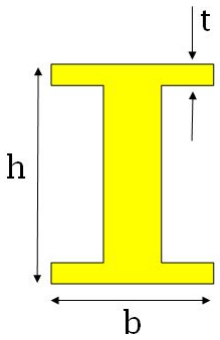

Figure 5.3: Cross-section of I-Beam

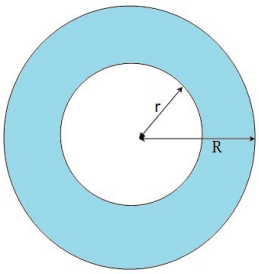

Figure 5.4: Cross-section of a hollow spar

Let b = 1, h = 3 and t = 0.175, This gives,

$$I = \frac{1}{6}h^3t\ (1 + 3\frac{b}{h}) = 1.125 \qquad (5.4)$$

$$\therefore \phi_B^e = \frac{12I}{A^2} = 13.5[90] \qquad (5.5)$$

Let r = 0.44 and R =0.8

$$I = \frac{\pi}{4}(R^4 - r^4) = 0.29 \qquad (5.6)$$

$$\therefore \phi_B^e = \frac{12I}{A^2} = 1.8 \qquad (5.7)$$

The dimensions h, b, t, R and r were arbitrarily chosen to maintain an equal cross-section area for both shapes.

The shape factor works on a materials mechanical properties and thus, it manifests itself along the material property. In this case, the optimised merit index is $\frac{(\phi E)^{\frac{1}{2}}}{\rho}$. The example above indicates that different geometry results in a different shape factor and hence a careful consideration has to be applied in selecting a structural member. For this purpose, a hollow carbon spar tube was selected, even though it has almost 8 times lesser stiffness than an I-section, whilst having the same area. This is due to greater availability of carbon fibre tubes as opposed to I-sections. Further, the shape of wing spar depends on the shape and structure of the wing. Further discussion was carried out in section section 5.7.

5.3 Fuselage Design - Muhammad Anas Abd Bari

Geometry

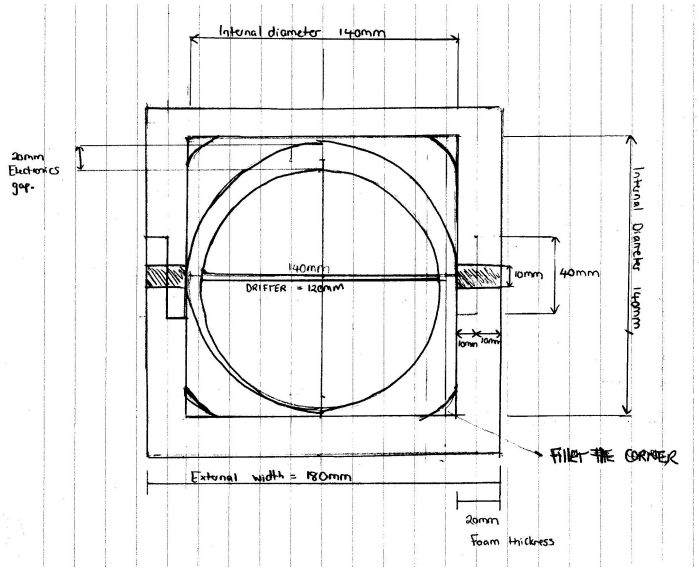

Figure 5.5: Final concept

The principle of the modular fuselage, as developed in GDP16, was integrated into the current design. Due to the requirement for the payload to release prior to contact with the water, the fuselage was

	Dimension, mm
Fuselage Thickness	20.0
Internal Diameter	120.0
Fuselage Height	160.0
Fuselage Width	160.0
Fuselage Length	600.0
Nosecone Length	180.0
Rear Fuselage Length	200.0
External Filleted Corner Radius	24.0

Figure 5.6: Fuselage Final Dimension

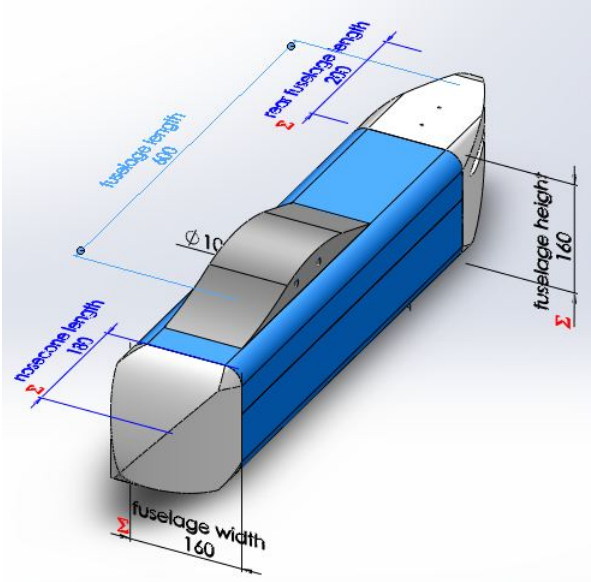

Figure 5.7: Solidworks model of the fuselage

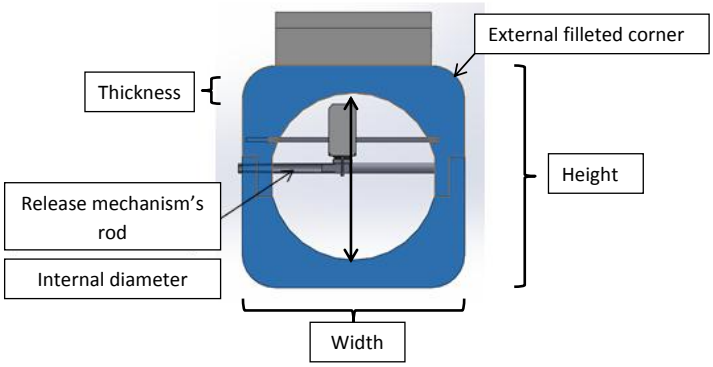

Figure 5.8: Fuselage Concept A with release mechanism fitted

designed such that the bottom fuselage section could be separated in flight. The initial design concept of a foam fuselage, with an integrated wing-box, was developed from the Powered Glider. The modular concept provided internal access to the payload and easy replacement of components. Which, although the glider was designed as a disposable UAV the ease of replacing components would most likely be beneficial during flight testing.

In GDP16 the thickness of the fuselage was $15mm$ with the internal diameter of $80mm$, it was shown to be sufficient to prevent excessive deformation and fracture [47]. Based on this result, the initial dimensions were calculated using an appropriate geometric ratio which was a function of the anticipated loading and the internal diameter required by the drifter combined with an appropriate safety factor. For a required internal diameter of $120mm$, the final dimensions are shown in figures 5.6 and 5.7. The length of the fuselage was determined by the sum of the drifter length, the length of the packed drogue and the release mechanism width. The external fuselage fillet radius, from the method described above was 20 mm, however to reduce potential stress concentrations from payload loading it was increased to 24 mm. The width, height and length of both the nose-cone and rear fuselage sections were also parametrised with respect to the internal diameter.

Instead of using a sliding fuselage a vertical tab design was developed. This enabled the bottom fuselage section to separate in a vertical manner during flight as shown in figures as below:

The release mechanism was installed at the top half of the fuselage as shown in figure 5.8 and therefore concept A was more suitable since the release mechanism rods would only go through half the fuselage

wall thickness as opposed to if the tabs were the other way around (on the outer surface of the top half). This acted to reduce the time required for release as well as reducing the potential for the failure of deployment.

Further modification was also undertaken to optimise the nose cone aerodynamic efficiency and include a suitable means of mounting the batteries and electronics close to the nose to balance the drifter mass and hence improve the longitudinal stability. The final nose cone has been manufactured with a hole inside, as shown in figure 5.9. However, the thickness of the nose cone decreases as the length of the hole increases thus, the maximum allowable value for the cavity was $100mm$.

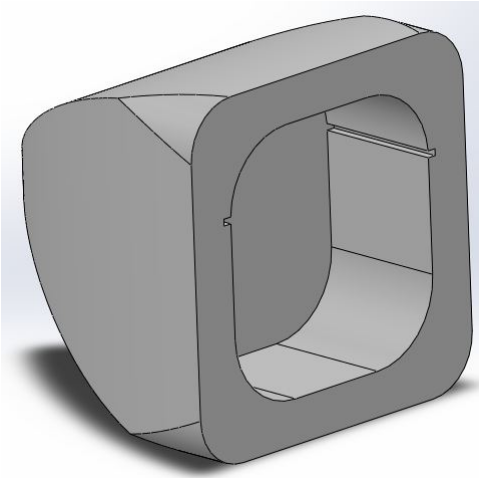

Figure 5.9: Nosecone with hole

5.4 Payload release Mechanism - Ksenjia Dvurecenska

5.4.1 Mechanical Release Mechanism

Three main design ideas were put forward and compared.

Bomb Door

This mechanism is based on the existing bomb door designs. The bottom of the fuselage will be split into two halves along its length and will be attached through hinges. Minimum of two hinges are required per side together with the detachment mechanism. Because the fuselage radius is designed to a tight fit with the oceanographic payload, the mechanism has to be placed whether in the far front and at the back of the fuselage, or inside the foam. The foam thickness is too small to accommodate the mechanism and by reducing it the glider structural strength is reduced. As a result, two detachment mechanism are required in addition to a minimum of four hinges. Overall, this design requires multiple alterations to the fuselage design in order to accommodate all the components and increases the probability of failure as there are more components to rely on.

Bottom Release: one servo and one hinge

In this design bottom of the fuselage stays attached to the glider after release by hanging on one hinge. The hinge would be placed next to the nose section and the servo in the tail section. It assumes that glider will reach level flight and then will pitch up to release. This is required to reduce the speed at which the drifter is deployed and, consequently, to reduce the speed at which it hits the water. There is a concern about the effect aerodynamic forces could have on deployment. For example, even when the servo is released the bottom fuselage can stay attached as it is pushed by the lift force acting on the fuselage. In general, this design relies on a single servo to release the bottom fuselage and on a single hinge to release the payload. This design, in comparison to the bomb door design, significantly reduces the number of components to fail and thus the possibility of failure. In addition, it is more compact and

is easy integrate into the fuselage.

Bottom Release: two servos

There is no requirement for any part of the fuselage to be recovered after the launch, so this design was developed by improving the design above and replacing the hinge with a servo. This involves a complete release of the bottom fuselage leaving no obstruction for the payload to fall out. By eliminating the disadvantage of previous designs, this design is agreed to be the most suitable and reliable and was put forward for detailed development.

Final design

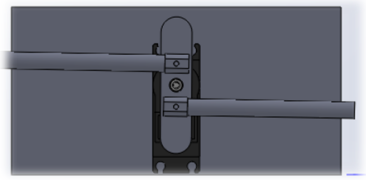

Figure 5.10: Solidworks model of the release mechanism

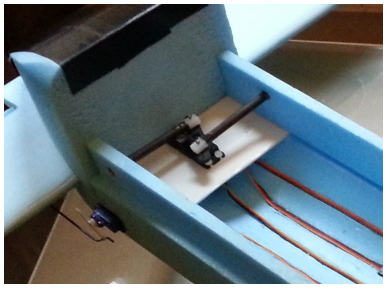

Figure 5.11: Assembly in the fuselage: rear release mechanism

The final design shown above consists of two pins and a servo motor that is controlled together with the rest of the in-flight components. The mechanism is placed horizontally in the upper half of the fuselage one near the nose section and other next to the tail section. All release pins are the same distance away from the wall and have to move by the same distance to release. Both servos move simultaneously and release the payload evenly. To release, a signal is sent to the servo motor to rotate the servo arm by a set angle.

$$\tan^{-1}\left(\frac{\text{wall thickness + tolerance}}{\text{distance from the center of rotation to the pin attachment}}\right) = \tan^{-1}\left(\frac{11.2mm}{9.5mm}\right) = 49^{\circ} \quad (5.8)$$

The angle allows the pin to move by a distance equal to the half thickness of the fuselage wall plus the 10% tolerance to ensure secure deployment with the minor disposition error.

To choose the material and size of pins, the value for a force acting as a point mass at the position of holes was estimated by (2.7 x 9.81)/4 = 6.62N. Because these estimations are based on the target mass of the complete glider, it was appropriate to add a safety factor to account for any additional mass in the final product. As a result it was decided to use 7mm Carbon Fibre coated Aluminium tubes as they are light and strong enough for the purpose. The length of each pin was calculated based on the inside fuselage radius and half of the fuselage wall thickness. To the servo arms, release pins are connected through splitting pins that allow free rotation in the horizontal plane to account for the small turning angle. Initially, it was designed to slide in the slot on the servo arm to account for the turning angle but, because the angle is relatively small, it was agreed that rotation around split pin is sufficient. This rotation prevents pins from damaging walls of the holes when sliding to release. To improve this design, it is suggested to add Nylon inserts in the holes to further protect the foam.

5.4.2 Testing

A test was conducted to check the reliability of the mechanism when assembled into the fuselage. Two main objectives were to establish breaking point of the foam around holes and deflection of pins. Below is shown the test set-up where weights were gradually added from $500g$ in steps of $500g$ and represented the weight of components inside the fuselage. The release mechanism was placed in the same manner as in the actual design but the upper half of the fuselage was fixed. As a result, holes started to deform at $3.5kg$ and final fraction took place at $8.5kg$ with no damage to release mechanism. Throughout the test pins

Figure 5.12: Foam tear and pin deflection test setup

Figure 5.13: Foam failure

deflection did not change significantly with addition of weights. At the point of foam deformation pins were deflected downwards by $10mm$ and at the foam failure by $13mm$. This behaviour was expected since no pins are pulled away from the mechanism but the force is experienced by the whole assembly. This assures that both foam and release mechanism are strong enough as the assembly holds approximately 3 times the weigh of the entire glider with the payload.
Once the mechanical testing was passed, the release test was performed. It was desired to test the mechanism in the wind tunnel to check the effect of aerodynamic forces on release but this was not possible due to safety restrictions. Instead, the static test was done where the drifter was released from the suspended glider at different pitching angles varying from $0°$ to $14°$ in steps of $2°$. 100% of releases deployed the drifter proving the reliability of the design. The lack of time and opportunity, did not allow to include in-flight release test. Though, it is necessary to assure complete reliability in realistic environment. At the current stage of the project, it is agreed that performed tests are sufficient to state that developed release design is appropriate for the purpose and is working as predicted.

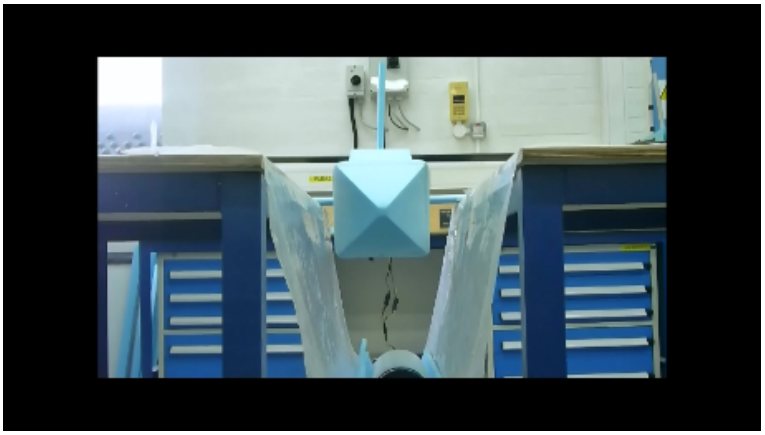

Figure 5.14: Drifter release set up

5.5 Nose Cone Optimisation - Izdihar Zuhdi

In order to achieve a higher glide ratio, the drag needs to be as low as possible. Theoretically, a lower drag can be achieved by having a longer nose. To test this claim, a study on the drag of the nose with varying length was carried out. The idea was to run a study for each of the new nose length and compare the drag, (C_D) induced by each nose to the drag with the original nose length ($150mm$).

5.5.1 Methodology

Analysis on the nose section was done using Solidworks Flow Simulation. All simulations were carried out assuming the aircraft is at sea level and travelling at $15ms^{-1}$ with 2% turbulence. The control volume used was 5 times the volume of the whole nose. This ensures that flow around the nose is fully developed. The objective of the analysis was to find the optimum length for the new nose. Any change in the length of the nose will directly influence the volume. This is due to the fact that the shape of the nose was chosen to be the scaled size of the powered glider. For convenience, the volume added to the nose was compared to coefficient of drag of the nose since the volume is directly proportional to mass. The drag coefficient C_D was calculated using:

$$C_D = \frac{2D}{\rho v^2 A} \tag{5.9}$$

where:
D is the drag force
ρ is the mass density of the fluid
v is the speed of the object relative to the fluid and
A is the planform area

5.5.2 Data Analysis

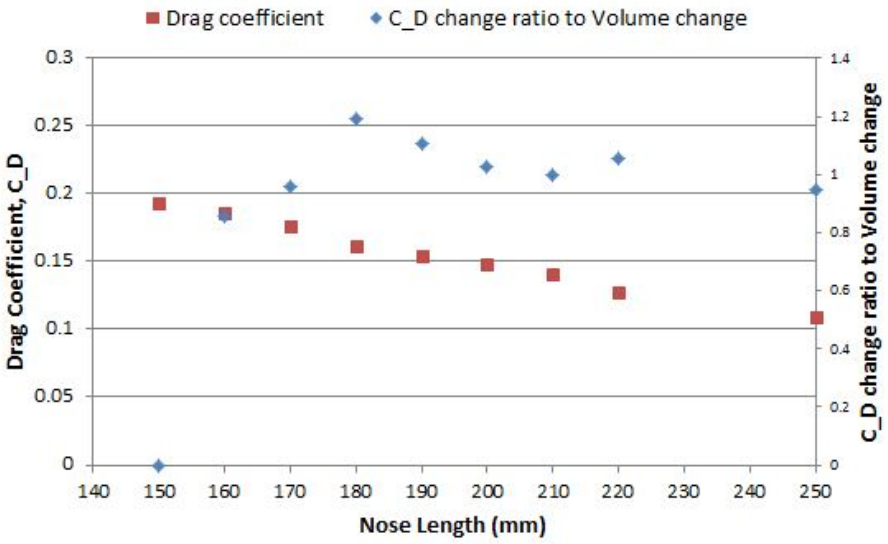

Figure 5.15: Drag coefficient, C_D vs. Nose length and ratio of C_D change to volume change vs. Nose length

Figure 5.15 shows the variation of coefficient of drag with respect to nose-cone length. As expected, it shows that the value of coefficient of drag is smaller with longer nose. It also shows the ratio of C_D change to volume change for different nose length. The highest value of the dependent variable gives the largest reduction in coefficient of drag with least volume added. Therefore, it can be deduced that the optimum

nose length is for the balloon launch Lagrangian drifter glider is $180mm$. There was a limitation in this analysis. Since the cone was to be made from blue Styrofoam, a larger nose will absorb more water in the atmosphere compared to a smaller one. However, this factor was not considered in this analysis because the amount of water absorbed by the cone is negligible compared to the mass of the cone.

5.6 Wing Configuration - Robert Gillman & Nathan Lao

5.6.1 Aerofoil Design

The glider design release altitude had previously been stipulated to be from a weather balloon at $10km$. During the descent to sea level the glider will experience a large variation in atmospheric density and pressure, resulting in a lower Reynolds number at $10km$ than at sea level. It was important to design the wing with an aerofoil section that is able to maintain suitable performance over the entire range of expected Reynolds numbers.

For an aerofoil approaching stall at low Reynolds numbers the laminar boundary layer will separate before transition to turbulence. The separated boundary layer then becomes turbulent, and as a turbulent boundary layer is able to withstand a stronger adverse pressure gradient prior to separation, the boundary layer will reattach to the aerofoil surface. This leads to a separation bubble on the aerofoil upper surface increasing the form drag. In order to achieve maximum aerodynamic efficiency it is important to minimise the size of the separation bubble and extend the region of laminar flow [38]. The aerofoil should also meet the following requirements.

- Exhibit a good lift to drag ratio and gentle stall characteristics over the expected range in Reynolds number and over a suitable range of angles of attack (AOA).
- A high AOA prior to stall at a Reynolds number for conditions at $10km$.
- Stall gradually from the trailing edge rather than a sudden loss of lift associated with leading edge stall. The maximum aerofoil thickness needs to be greater than 14% of the mean chord to meet this requirement [104].
- Ideally the aerofoil section should have a negative zero lift angle due to the UAV only operating in the glide.

The requirement for deploying a balloon launched Lagrangian drifter in a controlled descent from $10km$ led to the design of a single use disposable glider with the acting to simply transport the drifter to its predefined location. In order to prevent damage to the drifter during deployment the UAV was designed to release the oceanographic payload from the glider when it is as close as feasibly possible to the ocean surface. Taking into account the accuracy of the autopilot system and the variable nature of the wave height the design release altitude was $10m$ above the sea surface.

When the wing dimensions were calculated the method of drifter release was not finalised and its reliability remained untested therefore, the glider was sized to achieve, theoretical, level flight prior to payload release. Additionally to mitigate the risk of damage to the electronics the release velocity was designed for $10ms^{-1}$. Using these initial assumptions the wing area could be determined as a function of the chosen aerofoil characteristics. The aerofoil chord length was taken to be $0.2m$ and a constant velocity was assumed throughout the glide phase of $10ms^{-1}$ which, although not entirely accurate enabled a suitable comparison between potential aerofoil sections. The Reynolds number, based on chord length and free stream velocity, varied over the range 68000 ($10km$) to 148000 (Sea level) assuming standard atmospheric sea level conditions [28].

The first aerofoil section investigated was the NACA 4415 as was is used on the powered glider, section 3.1, and suggested as a reasonable option for homebuilt and sail-plane aircraft [104]. Using a simplistic CFD

solver,"XFLR 5" the NACA 4415 aerofoil was varied over the range $-10°$ to $+20°$ for multiple Reynolds numbers in the range given above. The 2D section aerodynamic efficiency ($\frac{C_L}{C_D}$) was plotted against AOA. Figure 5.16 clearly shows a decrease in aerodynamic efficiency as the Reynolds number decreases towards the release altitude.

At the lowest Reynolds number, equivalent to $10km$ altitude, the aerofoil exhibits a complex oscillation in aerodynamic efficiency from a low angle of attack. It is believed this is due to the separation and reattachment of the boundary layer entering into a hysteresis loop, [79], and should be avoided for optimal efficiency.

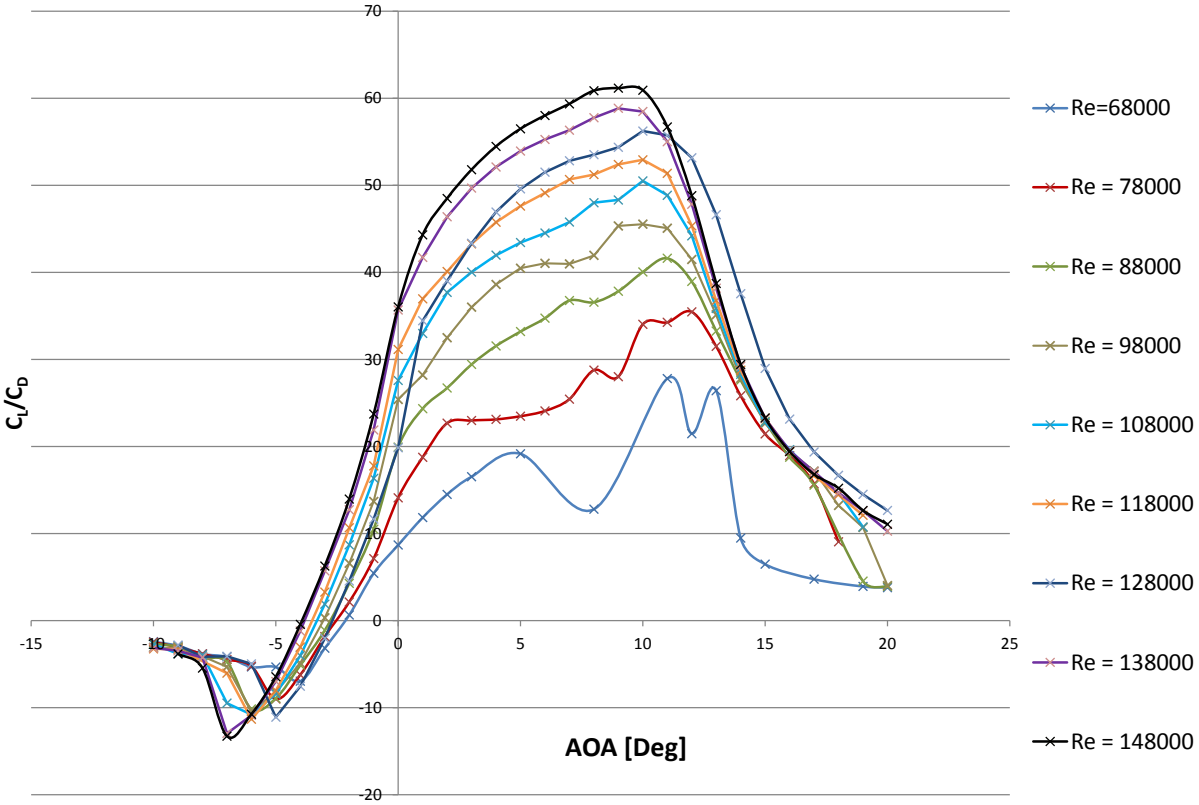

Figure 5.16: $\frac{C_L}{C_D}$ vs.AOA - NACA 4415

In "Low Reynolds Number Airfoil Design" by Selig, 2003[113] the importance of the laminar separation bubbles on low Reynolds number aerofoils was outlined and it was suggested that due to the wide variation in operating requirements for UAVs there is no suitable blanket aerofoil section. Instead the optimal aerofoil design would be custom to each aircraft requirement and involve an inverse design study working back from the ideal velocity distribution over the aerofoil surface.

However, for this project in the interest of time, this was not completed. Instead recommended low Reynolds number aerofoil sections presented by [113] were tested over the expected Reynolds number range, compared to the NACA 4415 and analysed with respect to the requirements stated above.

NACA 4415

Figure 5.17 shows oscillations in aerodynamic efficiency at high AOA. Using the coefficient of skin friction from XFLR5 the presence of a separation bubble on the aerofoil top surface was confirmed. It was clear that the NACA 4415 was not the most efficient aerofoil at an altitude of $10km$. Additionally, from fig. 5.18 it was found to perform poorly compared to the remaining sections at $0km$.

The NACA 4415 shows a gradual decrease in $\frac{C_L}{C_D}$ with increase of AOA past the stall angle in fig. 5.18 and from the XFLR5 analysis it was found the separation propagated along the aerofoil surface from the trailing edge. However, it produces a large negative C_L for negative AOA and has a relatively small zero

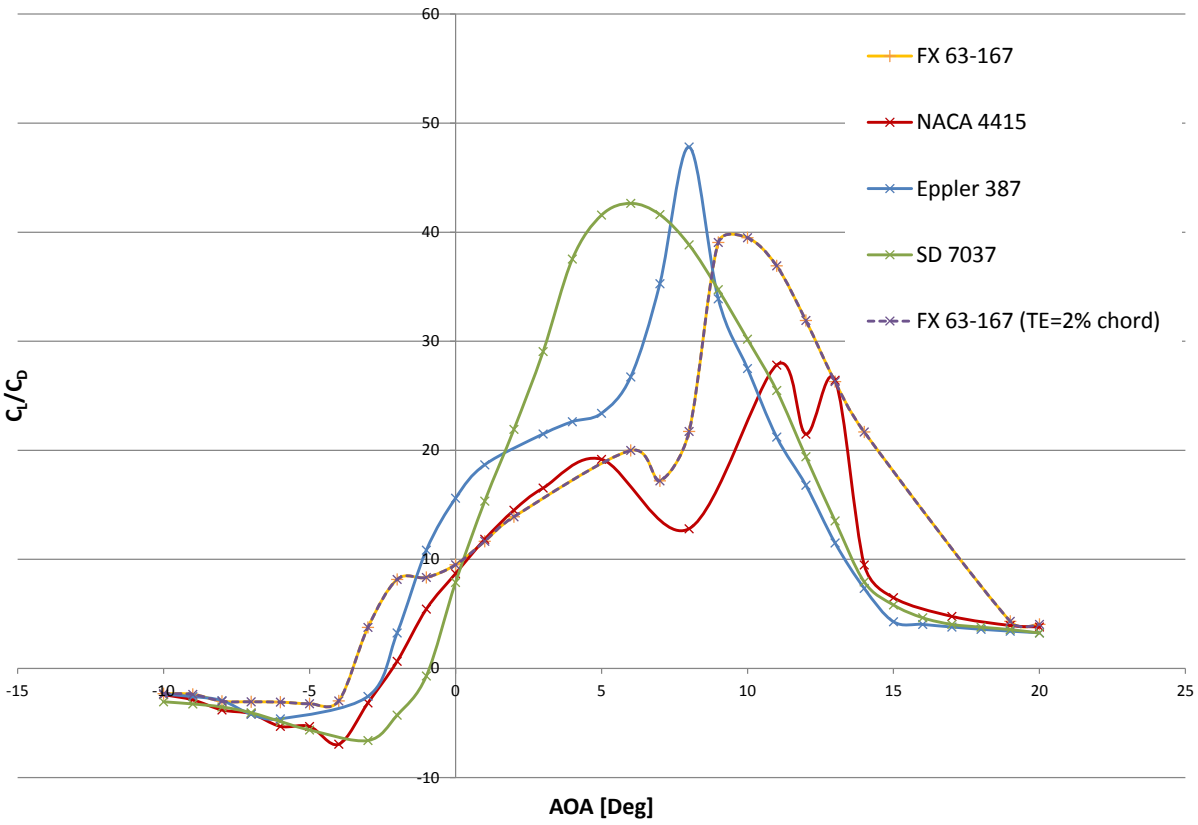

Figure 5.17: $\frac{C_L}{C_D}$ vs.AOA: Suitable Aerofoil Sections: 10km

lift angle which would be detrimental to a glider application.

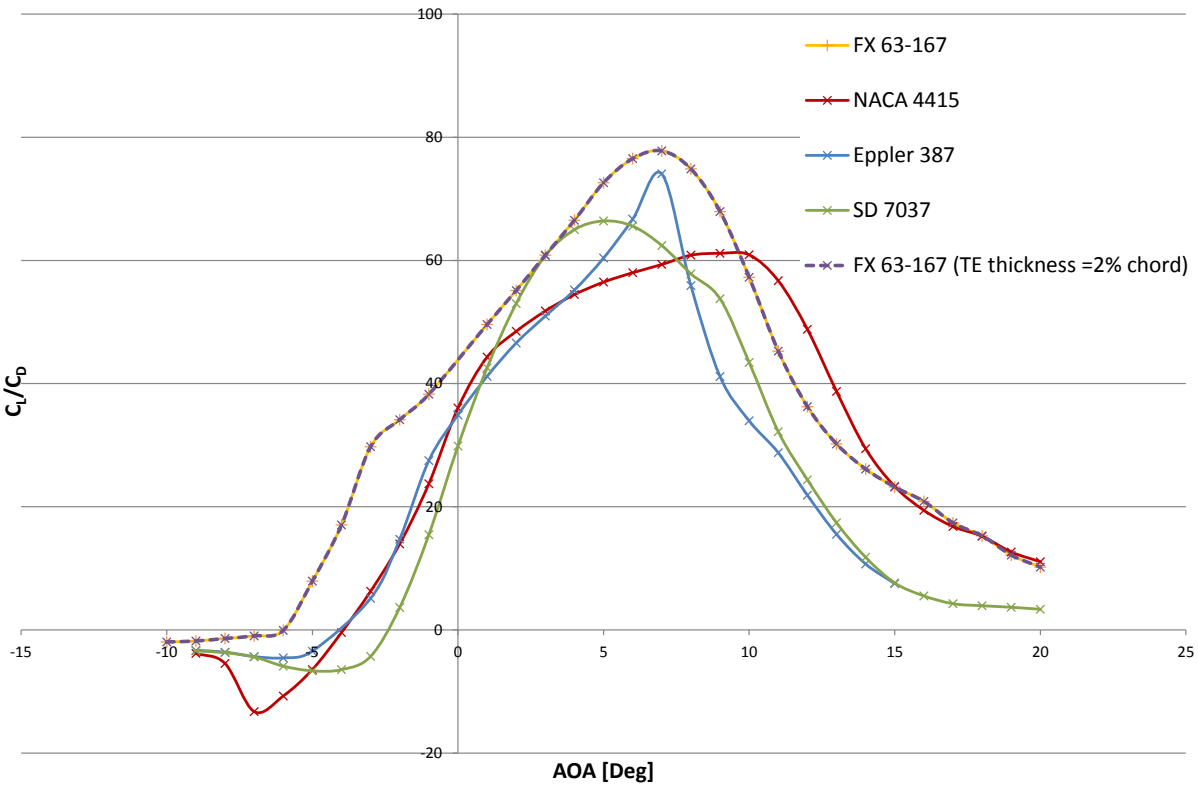

Figure 5.18: $\frac{C_L}{C_D}$ vs.AOA: Suitable Aerofoil Sections: 0km

Wortmann FX 63-137

The Wortmann FX 63-137 is a low Reynolds number aerofoil specifically designed for human powered

flight applications. It has a highly cambered section and an associated high AOA prior to stall. The drop in efficiency upon reaching the stall is less severe that the NACA 4415 section. At negative angles of attack a positive C_L is produced until $-4°$, superior to the other sections tested.

The disadvantage of this section was the very thin tailing edge due to the high degree of camber. Given the most suitable manufacturing method was hot wire cutting this would present a problem due to the accuracy tolerance of $+/-$ $1.5mm$ from the diameter of wire burn. If left unmodified it would have lead to a very easily damaged trailing edge section.

Referring back to the work presented by Selig 2003,[113], it was stated that the FX 63-137 trailing edge could be easily modified with little impact on the aerofoil characteristics. To eliminate the hot wire cutting difficulty the trailing edge was thickened to 2% of the chord length and re-tested. As shown in fig. 5.17 and fig. 5.18, that the additional trailing edge thickness had an effect smaller than could be quantified using XFLR5 as no significant variation in aerofoil performance was seen.

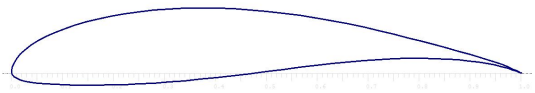

Figure 5.19: Aerofoil Selection: FX 63-137: Standard

Figure 5.20: Aerofoil Selection: FX 63-137: Modified

Selig Donovan 7037

The Selig series of aerofoils are, like the Wortmann series, designed especially for low Reynolds number applications. The SD7037 has been used in numerous home built UAVs, most notably on the RQ-11, American hand launched UAV [109]. The low Reynolds number efficiency is higher at low angles of attack than the NACA 4415 and FX-63-137 at $10km$ however, the loss in efficiency from the onset of stall is noticeable at angles as low as $5°$ and the zero lift angle is only $-1°$. The maximum thickness is 9.2% of the chord which, for a $200mm$ chord has additional implications on the structural design of the wing spars.

Eppler 387

It is seen from Figure 5.17 that of the aerofoils tested at $10km$ it provides the highest aerodynamic efficiency at $8°$. However, above $8°$ the aerofoil stalls suddenly and there is a significant loss in C_L/C_D indicating a rapid loss in lift. At $9°$ AOA this falls below the lift generated by the FX63-137 and above 11 degrees falls below the efficiency of the NACA 4415. The low stall angle is due to the thin aerofoil profile with a maximum thickness of only 9.1%. The sudden loss of lift is not suitable for use in this application as it would place additional sampling rate and method of stall prediction requirements on the autopilot.

Figure 5.21: Aerofoil Selection: Selig Donovan 7037

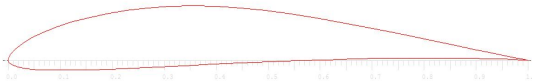

Figure 5.22: Aerofoil Selection: Eppler 387

Summary

The FX 63-137 aerofoil displayed the optimum characteristics for the glider wing section as it was able to sustain a high aerodynamic efficiency over a large range of Reynolds numbers. The main drawback of this section was the thin trailing edge thickness on the standard profile. As shown above this can be resolved with little effect on the overall aerodynamic performance by modifying the tailing edge thickness to be 2% of the chord length [$4mm$], hence making it suitable for hot wire cutting, fig. 5.20.

5.6.2 Wing Sizing

Tight weight restrictions and manufacturing limitations imposed meant Styrofoam hot wire cut wings were the most suitable. Building on work from GDP 16 in 2012 [47] and personal communications with Phil Herring it was clear that including a tapered wing section would significantly increase the manufacturing time and brought a high risk of additional complications, due to uncertain wire cutting tolerances. The potential issues for hot wire cutting a tapered wing were due to the differential tip and root motor speed. The variable motor speed leads to non uniform amount of foam burnt by the wire along the span. Further, the required wing length would be at the top limit of the wire cutter and would likely have to be manufactured in multiple sections.

Due to these limitations combined with, the high demand for hot wire cutting and the short time frame between UAV design and the wind tunnel testing dates the decision was made to compromise the aerodynamic efficiency of a complex, elliptical or tapered profile for a simplistic rectangular wing.

From a conceptual design mass build up it was determined that the glider and payload total mass would be $2.24kg$. To achieve level flight just above sea level the lift required from the wing would be,

$$L = W = mg = 21.98N_{[2.d.p]} \tag{5.10}$$

Using the 2D aerofoil section C_L found from XFLR5 a 3D approximation could be found using the relationship,

$$C_{L_{3D}} = 0.9C_{L_{2D}}cos\Lambda = 1.053 \tag{5.11}$$

Where the 3D C_L being 90% of the 2D value was to approximate the non finite characteristics around the wing tips [84]. This initial value of C_L was taken from the 2D profile section tests and once the wing geometry was complete the $C_{L_{3D}}$ was calculated directly from XFLR5 using the vortex lattice method [VLM] and later validated with CFD and wind tunnel data.

$$L = \frac{1}{2}\rho u_\infty^2 b\bar{c}C_{L_{3D}} \tag{5.12}$$

Where, $u_\infty = 10ms^{-1}$, $\rho = 1.225kgm^{-3}$ and $\bar{c} = 0.2m$. Rearranging for the required span gave,

$$b = \frac{2L}{\rho u_\infty^2 b\bar{c}C_{L_{3D}}} = 1.706\ m \tag{5.13}$$

Due to the unknown magnitude of lift produced by the fuselage it was assumed to be negligible and that the wing area used above was the net wing area and hence the glider would have a net wing span of 1.7m [13]. A variation of span and chord combinations were tested in XFLR5. Those most suitable had

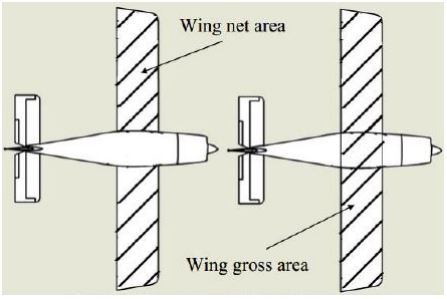

Figure 5.23: Wing Sizing:Net & Gross Wing Area

a chord of $0.2m$ and variations of semi span consisting of $0.75m$, $0.75m$ with $0.1m$ wing tip inclined at $10°$ and $0.85m$. The lift produced from each design configuration was normalised by the aircraft weight.

A window of $+/-5\%$ of the initial design target was marked onto the chart with the window extended over the range of sensible installation angles $0 \circ to + 5°$. The result produced a small window of suitable design configurations as shown in fig. 5.24. It can be seen from fig. 5.24 that the semi span of 0.75m with an additional 0.1m tip inclined at 10° was within $+/-1\%$ of the design target for an installation angle of 3 degrees.

Aspect Ratio

Ideally, from an aerodynamic perspective, the wings would have an infinite aspect ratio to reduce the pressure losses associated with wing tip vortices. This is not practical in reality due to the structural implications however, a high aspect ratio will help to maximise the gliders $\frac{L}{D}$. Using the $1.7m$ span and $0.2m$ chord an aspect ratio of 8.5 was compared to historical guidance and deemed suitable [104].

Sweep

Sweep is to used to reduce shock and associated drag losses from transonic and supersonic flows. Due to the estimated glider Mach number being in the region of 0.03 sweep will not be included.

Taper

Taper helps to reduce the induced drag however due to the limitations previously mentioned from hot wire cutting it has not been considered for the current wing planform. Ideally an elliptical planform wing would be used as it can reduce the drag by approximately 7% compared to a standard un-tapered rectangular wing section. Although not possible to cut an elliptic wing on the wire cutting a taper ratio of $\lambda = 0.45$ would provide a near elliptical loading distribution [104].

Twist

Wing twist can be used to modify the span-wise lift distribution to be close to an elliptic profile. Incorporating twist into a foam hot wire cut wing would be difficult to achieve on the small hot wire cutter and was not considered.

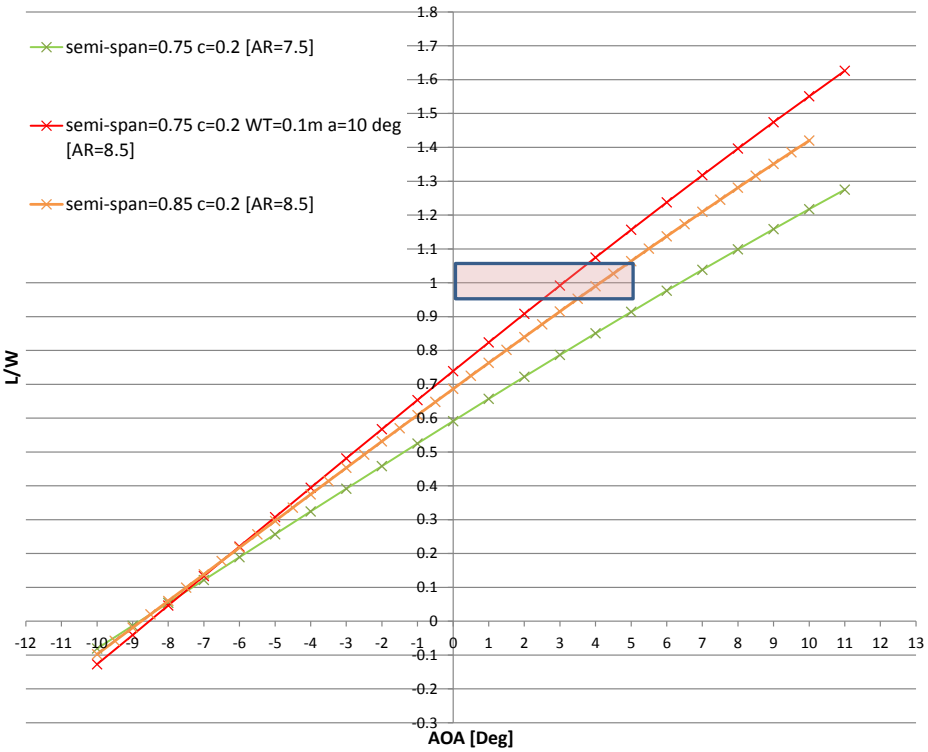

Figure 5.24: Wing Sizing: $\frac{L}{W}$ vs AOA

5.6.3 Wing Tip Analysis

As shown in fig. 5.24 it was found that adding $0.1m$ wing tips angled at ten degrees to the $0.75m$ semi span improved the lift distribution thus improved the $\frac{L}{W}$ and from fig. 5.25 marginally increased the

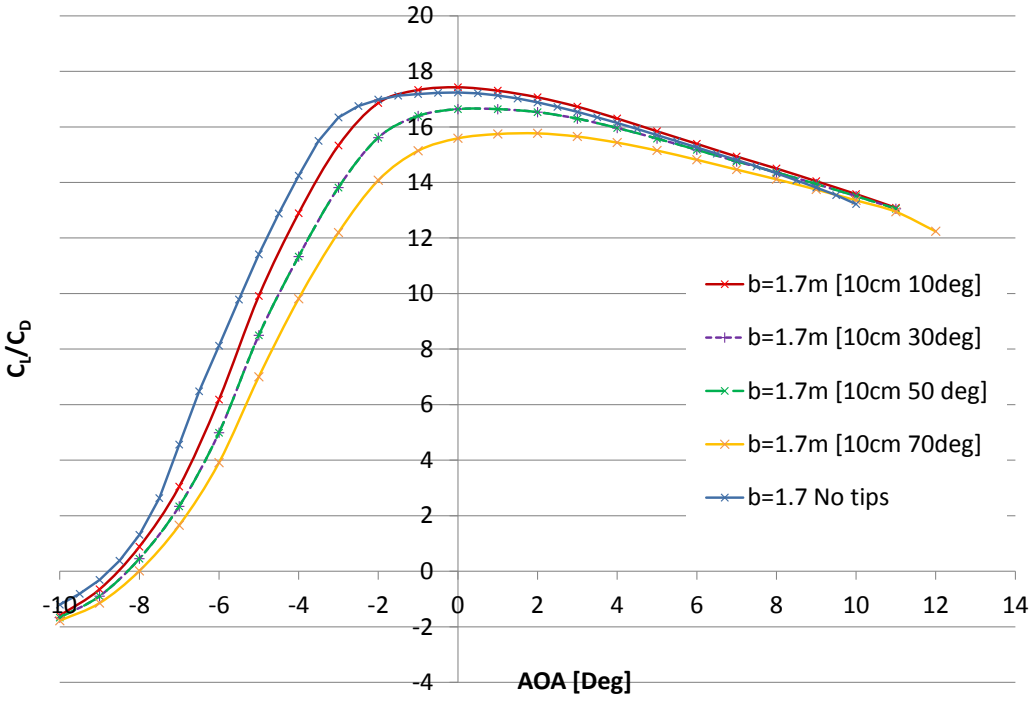

Figure 5.25: Wing Sizing: $\frac{C_L}{C_D}$ vs AOA

aerodynamic efficiency. This seemed counter intuitive considering the vertical lift force would become a component $L \cos 10$ over the inclined section instead of L of a flat wing equivalent.

A second XLFR5 model was created using Helmholtz lifting line theory and compared to the Vortice Lattice Method (VLM). Both methods showed a marginal increase in lift from the addition of the small wing tips. Additionally, the small wing tips added a 2° effective dihedral providing a small contribution to lateral roll stability [24].

The main disadvantage of using wing tips was the complexity added to the manufacturing. The tip and wing sections were designed so that both would be cut at 5° then glued together so that the trailing edge sections would be flush. Cutting a diagonal taper into the end of the wing & tip was difficult to accurately achieve. The difficulties stemmed from the approximate $1.5mm$ wire burn diameter and difficulty of accurately positioning the wire because of its tendency to "jump" roughly $1mm$ when heat was applied. The result of this meant the fit of wing tip and wing was not as flush as initially envisaged and therefore the marginal advantages shown in XFLR5 would be diminished further.

If the tip section was angled up by any more than 10° the induced drag would decrease as expected and so too would the lift produced from the tip section. Therefore, the overall efficiency would decrease. Due to the time constraints between design, manufacturing and wind tunnel testing the decision was taken to include the tips until further Fluent CFD analysis had been completed to validate the XFLR5 data.

With the manufacturing complications as well as fabrication issues, glueing the wing tips into place neatly, it was concluded that the current wing tips do not provide a large enough improvement in efficiency for the current manufacturing method. It is suggested that the improvement in aerodynamic efficiency could be gained from a tapered final wing section combined with the use of end plates.

5.6.4 Wing Position

A high wing configuration was selected as it offered a number of advantages to the low, mid or shoulder wing alternatives. Firstly a high wing separated the wing and structural wing-box away from the payload resulting in a simplified and lightweight design. Secondly a high wing provides lateral stability which, given the small wing tip sections and lack of significant dihedral or roll control was required.

A high wing configuration enhances the glider lateral stability through producing a positive effective dihedral. During slide-slip the lift force, normal to the wing, has a component acting vertically [$Lcos\phi$] which produces a restoring moment [$Lacos(\phi)$] acting about the glider centre of gravity. Where, a is the distance between aerodynamic centre and centre of gravity. Additionally the skin friction from the wing top surface produces a restoring moment due to the moment-arm from centre of gravity,$F_s b$. Finally the fuselage interacts with the span-wise flow during side-slip and increases the AOA of the wing on the side-slip side and reduces the AOA on the opposing wing producing a further contribution to the net restoring moment [61].

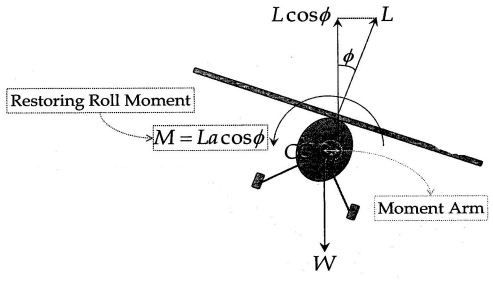

Figure 5.26: Wing Position: High Wing 1 [61]

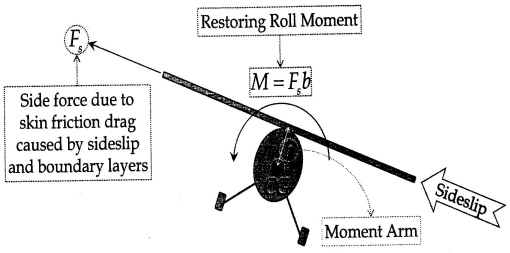

Figure 5.27: Wing Position: High Wing 2 [61]

Wing Installation Angle

It is recommended that the wing installation angle should be between $2-5°$. From fig. 5.24 it was shown that the glider design target of level flight at $10ms^{-1}$ could be met with a wing installation angle of 3° relative to the fuselage top surface [104].

5.6.5 Software

The early conceptual design and optimisation of the wing section and planform was completed using XFLR5. XFLR5 uses the well known and validated 2D XFOIL code and includes additional theoretical 3D methods such as, the vortex lattice method or lifting line theory. At the early stage of design and optimisation XLFR5 offered a number of advantages over a commercial CFD package such as Fluent or Star CCM+. The main advantage was the simplicity of use and low computational demand. XFLR5 requires much the same initial boundary conditions as an XFOIL model and the 3D models use interpolation of the 2D data. Unlike a commercial CFD code the solutions can be computed very quickly enabling testing of multiple geometrical configurations in a relatively short time frame. The results taken from XFLR5 were later validated against a Fluent CFD study seesection 5.12.

5.7 Wing Structural Analysis - Robert Gillman

5.7.1 Method and Assumptions

The following section describes the design of the wing structural geometry and wing spar sizing. In this analysis the structural and aerodynamic reference frames were assumed to be fixed with AOA. Therefore, any drag contribution to bending moment (M_{xx}) was neglected, additionally the wing was assumed to have zero span-wise aerodynamic twist from root to tip.

The span-wise loading profile was a non linear lift distribution given by an approximate coefficient of lift variation calculated from the Schrenk method [41]. The lifting force was integrated using multiple iterations of trapezium integration over a small interval to give the shear force, bending moment and deflection distributions. The wing carbon spars were modelled as fixed cantilever beams clamped by the fuselage wing-box. The effect of the plywood and foam was difficult to accurately quantify and it was assumed they did not contribute to the wing structural rigidity for a distance of $0.1m$ from the root. Meanwhile the carbon spars, due to the symmetric loading, were assumed to be fixed at the join with the wing-box. A loading factor $[n]$ of 2 and a structural safety factor $[S_f]$ of 1.5 was used to provide a conservative estimation for initial spar sizing.

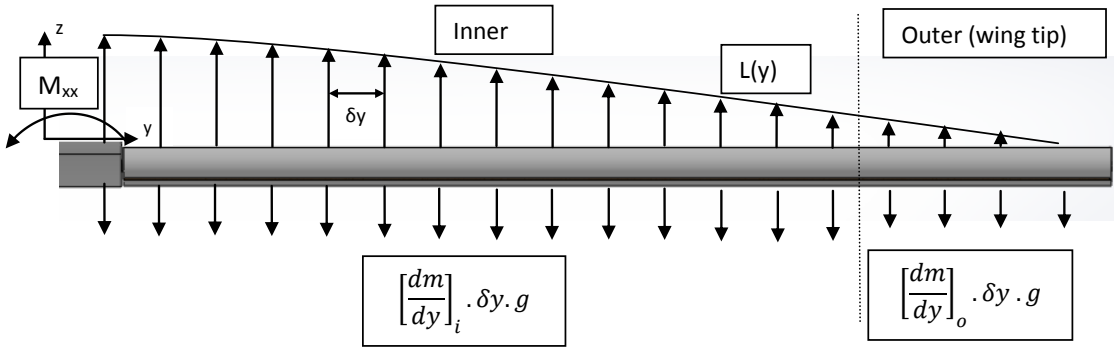

Figure 5.28: Wing loading diagram

5.7.2 Schrenk Method

The span-wise lift distribution of the rectangular planform was approximated using Schrenk's method, which assumes the loading distribution is the average of the rectangular planform shape and the lift distribution of an elliptic profile of the same area [41]. Once the local lift coefficient had been found, across the aerofoil span, the shear force and bending moment distributions were calculated over spatial increments, δy, from tip to root [41]. The equivalent elliptic loading profile was given by,

$$C(y) = \frac{4S}{\Pi b}\sqrt{1 - (\frac{2y}{b})^2} \tag{5.14}$$

S=wing area, b= net wing span, y=Distance from wing root.
The elliptic profile was multiplied by the average wing C_L, where $C_L \approx 1.0$ The equivalent variation in C_L for a rectangular wing is given by the average of the chord and the equivalent elliptic lift distribution profile,$C(y)$ all normalised by the chord.

$$C_{L_{equiv}} = \frac{C(y) + c}{2\bar{c}} \tag{5.15}$$

The aerodynamic loading acting the over the incremental length $\delta y = 10mm$ was calculated using the equivalent lift coefficient $C_{L_{equiv}}$, the average across the element such that:

$$C_{L_{eq\bar{u}iv}} = \frac{C_{L_{equiv}A} + C_{L_{equiv}B}}{2} \tag{5.16}$$

Using the local lift coefficient, the lift acting at the centre of each incremental element was computed. From the lift at the centre of each element the shear force and bending moment distribution along the semi span were found using trapezium integration and suitable boundary conditions, as given below.

$$S_{a[i+1]} = S_{a[i]} + \delta L_{[i+1]} \tag{5.17}$$

For the structural calculations the total system mass estimation was revised to be approximately $m_T = 2.35kg$, an increase of 5% on the initial estimate. As previously mentioned a loading factor of $n = 2$ and a structural safety factor of 1.5 were applied giving a total lifting force on each wing of:

$$L_w = \frac{m_T g n}{2} = 24.525N \tag{5.18}$$

In a similar manner to the shear force the aerodynamic bending moment across the wing was calculated with boundary conditions of zero shear force and bending moment at the wing tip. $S_{a[0]} = 0$ and $M_{xx_a[0]} = 0$.

$$M_{xx_a[i+1]} = M_{xx_a[i]} + \frac{S_{a[i+1]} + S_{a[i]}}{2}\delta y \tag{5.19}$$

To improve the bending moment estimation the inertia relief, bending moment due to the wing weight, was given as M_{xx_m} and calculated using an identical method to above. The difference in mass per unit length of the inside and outside wing sections was because the main wing spars did not run through the wing tip section. This was due to the additional manufacturing complications and mass from including a change in direction of the main wing spars [47].

$$[\frac{dm}{dy}]_i = 0.244kgm^{-1} \qquad [\frac{dm}{dy}]_o = 0.138kgm^{-1}$$

The total and ultimate bending moment along the wing semi span is shown in fig. 5.29 and was given by,

$$M_{xx_T} = M_{xx_a} - M_{xx_m} \tag{5.20}$$

$$M_{xx_{ULT}} = S_F * M_{xx_{total}} \tag{5.21}$$

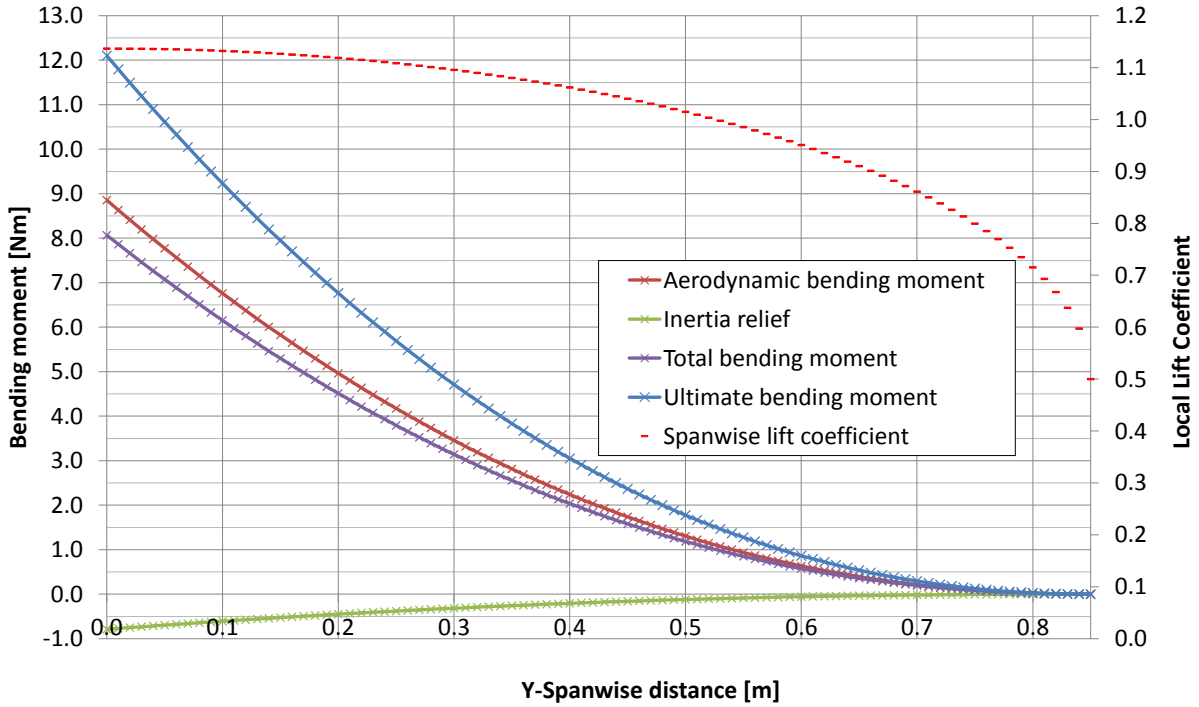

Figure 5.29: C_L & Wing Bending moment [M_{xx}] vs. distance from the wing root.

Maximum Stress

In order to calculate the maximum stress; the wing spar shape, position and material were required. Due to the hot wire cutting requirements for the wing spar holes combined with the highly cambered aerofoil shape the wing was manufactured in two separate sections. The sections were then joined together post wire-cutting using "Deluxe" speed epoxy. The wing spars consisted of a plywood spar of thickness $2.5mm$

positioned at the aerodynamic centre, $0.25\bar{c}$ and two carbon wing spars equidistant from the wooden spar to reduce aerodynamic twisting and distribute the load across the fuselage wing box, thus the use of two carbon spars enabled a thinner more aerodynamic wing box. The plywood spar performed two roles, firstly increasing the flexural rigidity along the wing span and secondly providing a suitable glueing contact for the wing tip.

From GDP 16 a merit index was completed for balsa, aluminium and carbon spars and due to the similar application with the current UAV this was revisited with the conclusion of carbon spars offering a high strength, low mass solution at a high but not unaffordable cost.

Due to a tight manufacturing time frame and difficulties in manufacturing custom carbon fibre parts to a suitable specification the decision was made to use a COTS carbon spar. The ideal carbon spar would have a helical filament wound lay up to resist bending, however it was difficult to find a supplier for a length less than $5m$, with the required external diameter, that would be able to offer a suitable order turn around. The largest supplier of suitable carbon fibre products was "Easy Composites" where both pultruded and roll-wrapped tubes were available.

For sizing the wing spars the maximum stress was computed in each spar for the current application and compared to the manufactures specification [41], see fig. 5.31 and fig. 5.32.

$$\sigma_y = \frac{z_{max} M_{xx}}{I_{xx}} \tag{5.22}$$

Where

$$I_{xx} = \frac{\pi(D_o^4 - D_i^4)}{64} \tag{5.23}$$

The $8mm$ external diameter pultruded tubes were two thirds the price of the roll wrapped alternatives however weren't able to provide suitable flexural strength due to the unidirectional nature of the fibre lay up, as shown by fig. 5.31 [7].

Roll wrapped tubes offered a more suitable but not ideal alternative due to fibres running along the tube length as well as around the circumference, thus providing a superior performance for use as a wing spar where the loading is unlikely to be acting exactly in compression or tension. The smallest diameter of roll wrapped tube available form Easy composites was $10mm$ external diameter. Additionally, the supplier to Easy composites was only interested in manufacturing a custom $8mm$ external tube for a minimum order of $50m$ costing $\approx$ £500.

In summary the compromise was made for the more expensive, $10mm$ external diameter, roll wrapped tube due to the superior strength from its multi directional fibres, lightweight construction and quick availability.

5.7.3 Deflection

To find the wing deflection firstly the slope needs to be calculated. Opposite to the shear force and bending moment calculations, the slope and deflection were integrated from root to tip. Suitable boundary conditions of no slope or deflection were applied at the wing root, $\theta_{i=0} = 0$ and $v_{i=0} = 0$ respectively.

It was assumed that the carbon rods were both clamped to the fuselage wing-box, due to previous condition for symmetric loading. The foam and plywood spars were not modelled as clamped to the wing box and instead assumed to only start distributing load after a span-wise distance of $0.1m$ from the wing root. Additionally, the carbon spars were modelled as only spanning $0.75m$ of the wing which was influenced by the associated manufacturing implications mentioned previously. These assumptions were implemented through multiple integrations of the separate wing components over a specified range,

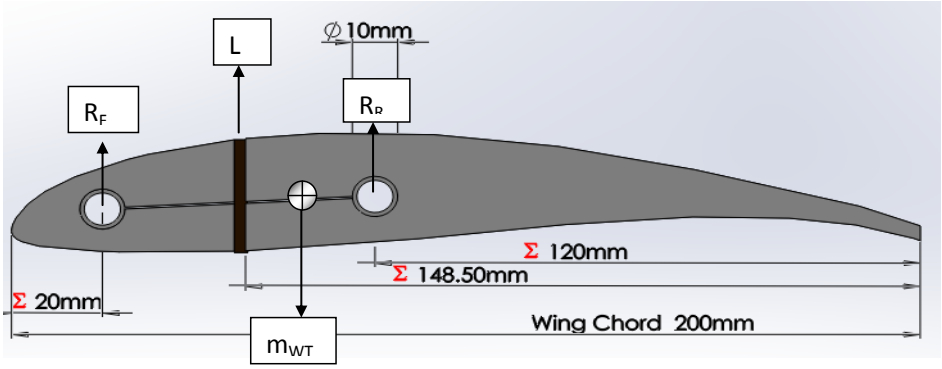

Figure 5.30: Wing cross section

8mm spar			
Outer Diameter	8.00E-03	m	
Inner Diameter	6.00E-03	m	
Position of max stress	4.00E-03	m	
Ixx	1.37E-10	m^4	
Pultruded Spar			
	Stress		**% UFS**
One spar	3.52E+08	Nm^-2	234.78%
Two spars equidistant from Xac	1.76E+08	Nm^-2	117.39%
Two spars [0.2c&0.6c)	2.80E+08	Nm^-2	186.93%
Roll wrapped tube			
	Stress		**% UFS**
One spar	3.52E+08	Nm^-2	61.78%
Two spars equi distance from Xac	1.76E+08	Nm^-2	30.89%
Two spars [0.2c&0.6c)	2.80E+08	Nm^-2	49.19%

Figure 5.31: Wing spar analysis: $8mm$ External diameter

10mm spar			
Outer Diameter	1.00E-02	m	
Inner Diameter	8.00E-03	m	
Position of max stress	5.00E-03	m	
Ixx	2.90E-10	m^4	
Pultruded Spar			
	Stress		**% UFS**
One spar	2.09E+08	Nm^-2	139.18%
Two spars equi distance from Xac	1.04E+08	Nm^-2	69.59%
Two spars [0.2c&0.6c)	1.66E+08	Nm^-2	110.81%
Roll wrapped tube			
	Stress		**% UFS**
One spar	2.09E+08	Nm^-2	36.63%
Two spars equidistant from Xac	1.04E+08	Nm^-2	18.31%
Two spars [0.2c&0.6c)	1.66E+08	Nm^-2	29.16%

Figure 5.32: Wing spar analysis: $10mm$ External diameter

as shown by eq. (5.27). The slope was then integrated from root to tip to calculate the magnitude of deflection along the wing.

$$M(y) = EI_{xx}\frac{d^2v}{dy^2} \tag{5.24}$$

$$\frac{dv}{dy} = \int \frac{Mydx}{EI_{xx}} \tag{5.25}$$

$$v = \int \frac{dv}{dx}dx \tag{5.26}$$

Where,

$$\frac{dv}{dx} = \int_{0.00}^{0.75} \frac{M_{xx}}{EI_{xx}} + \int_{0.01}^{0.85} \frac{M_{xx}}{EI_{xx}} + \int_{0.01}^{0.85} \frac{M_{xx}}{EI_{xx}} \tag{5.27}$$

In order to quantify the benefit of the plywood spar the calculations were done with and without the spar included. It is shown in fig. 5.33 that the addition of the plywood spar reduced the deflection of the wing by approximately half, at a distance of $0.62m$ from the root. The reduction in wing deflection due to the plywood spar was greater at the wing tip where the deflection was reduced from $36mm$ to $9.5mm$. Due to the unknown limit of deflection prior to permanent damage to the foam wing structure the plywood spar remained part of the wing structure for the wind tunnel testing. To provide a validation

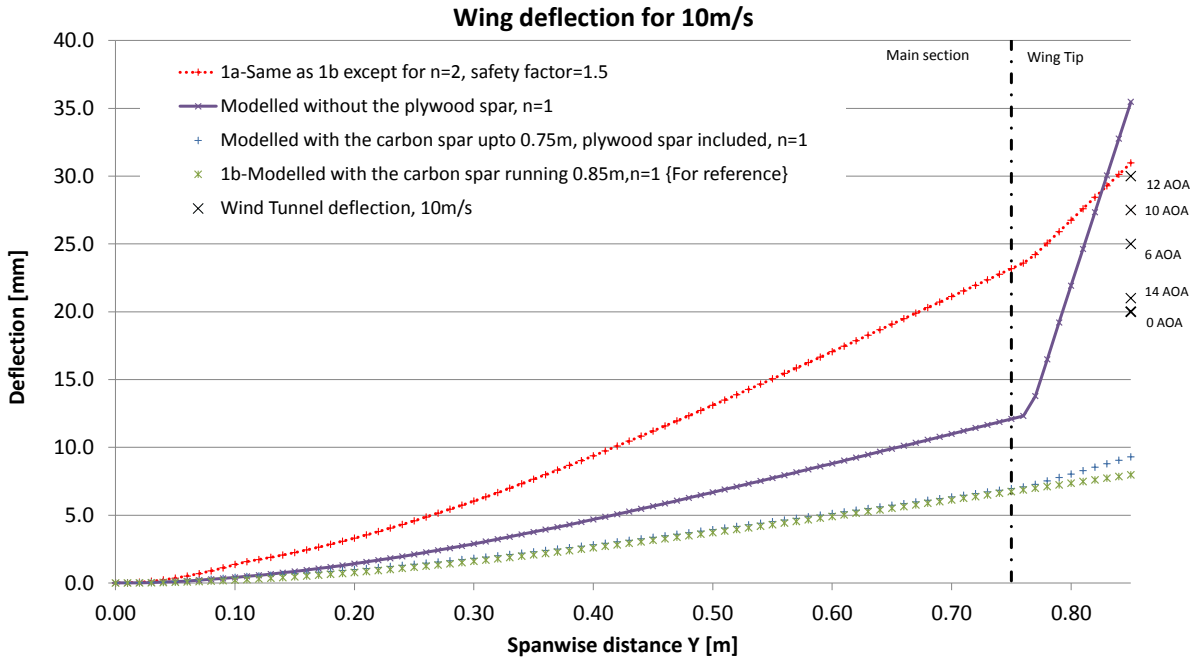

Figure 5.33: Wing theoretical and wind tunnel measured deflection

to the theoretical calculations the tip deflection was measured, in a simplistic manner, during the wind tunnel testing over a range of velocities and angles of attack. Taking into account the approach used to measure the deflection with the wind tunnel running at $10ms^{-1}$, the results were only accurate to the nearest $2.5mm$. It was found that the tip deflection was approximately three times the magnitude of the deflection from the theoretical calculations. The likely contributors to this error included the assumed wing loading profile from the Schrenk approximation, the limited accuracy of the trapezium integration and the unverified foam properties. Personal communication with "Hampshire Insulation", the Styrofoam supplier, highlighted concerns that the foam structural properties quoted by the manufacture were dependent on the exact manufacturing conditions and storage environment since.

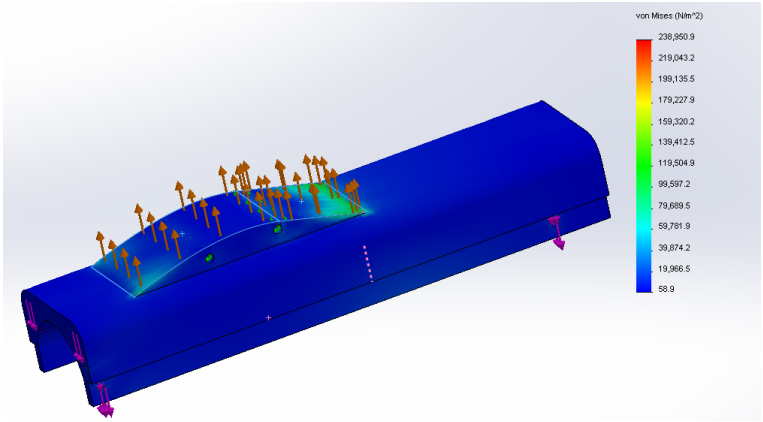

Figure 5.34: Upper fuselage stress analysis

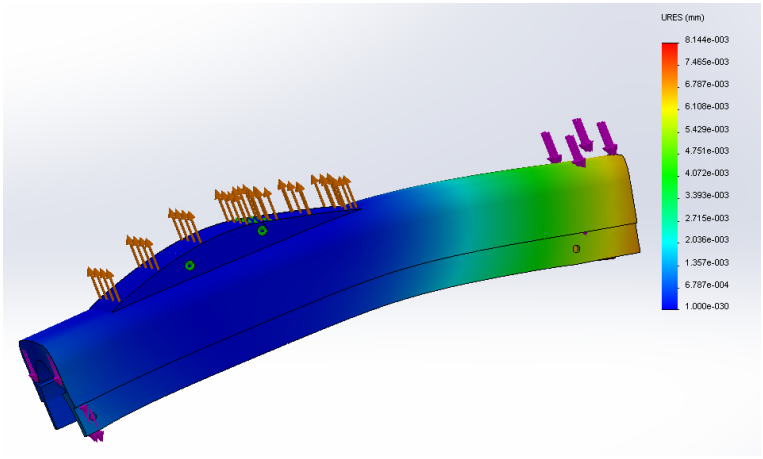

Figure 5.35: Upper fuselage displacement analysis

In summary it was found by including the plywood spar, the main wing and tip deflections were significantly reduced. Due to the unknown and questionable foam structural properties the decision was taken to keep the plywood spar in place until further analysis into the Styrofoam properties had been completed. Additionally, it should be noted that the current analysis was completed to meet the tight wind tunnel deadline and the assumption of $0.1m$ prior to the plywood spar or Styrofoam contributing to the flexural rigidity were estimated. Further wing structural optimisation was completed using an Abaqus FEA section 5.8.4.

5.8 Finite Element Analysis - Kai Xi Tan

5.8.1 Fuselage Finite Element Analysis

Upper Fuselage

The finite element analysis (FEA) was set up by putting fixtures at the holes of the wing-box. This is because during flight, the wings are the main contributors towards the total lift of the glider. Thus, the wing spars apply load to the fuselage during flight. A uniformly distributed lift force of $33N$ was placed on the surface of the wing-box. This is because all the lift by the wing are transferred to the wing-box which pulls the fuselage up. Furthermore, a total force of $34.95N$ acting downwards on the four holes on the fuselage was placed to simulate the total weight of the bottom fuselage section. Finally, a downward force of $2.46N$ and $0.74N$ was placed at the front and back groove of the fuselage to simulate the weight of the electronics and front and back release mechanism. All the acting forces are given a safety factor of 1.5.

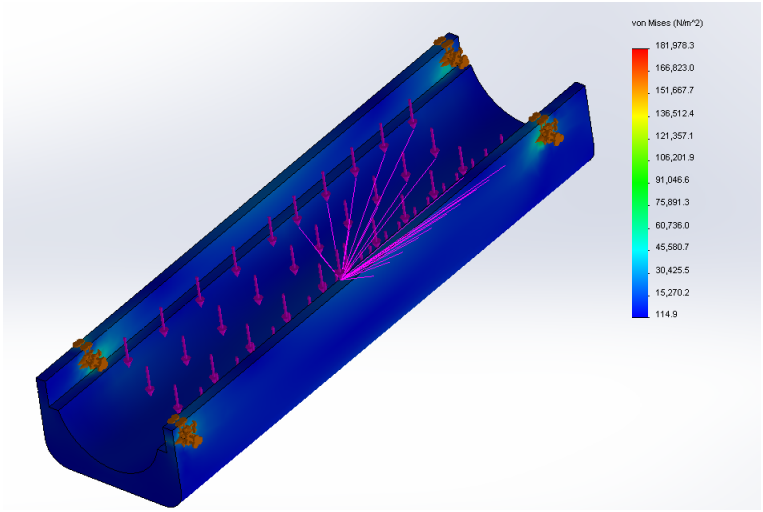

Figure 5.36: Bottom fuselage stress analysis

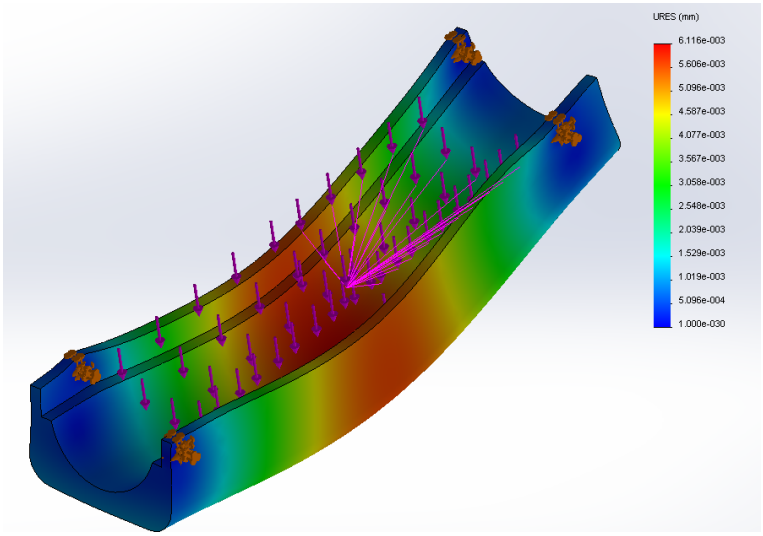

Figure 5.37: Bottom fuselage displacement analysis

The simulation was run and the results are shown in Figure 5.34 and 5.35. Based on the results, the maximum stress that will act on the fuselage is $2.38 \times 10^5 Pa$, which is significantly below the yield point ($5.0 \times 10^5 Pa$). Furthermore, the maximum stress was only acting at the connecting joints between the wing box and the upper fuselage which shows that the wing box would rip of first before the holes fail if failure was to occur. The maximum displacement that is predicted to occur is small and thus insignificant.

Bottom Fuselage

The FEA analysis was set up by putting fixtures at the four holes of the bottom fuselage. This is because the bottom fuselage will only be held in place by the spars that connects the upper fuselage to the bottom fuselage. The loads were placed on the surface of the fuselage which simulates the payloads that are placed in the glider and given a safety factor of 1.5. The loads are as follows:

- A uniform load of $5.09N$ at the drifter section to simulate the weight of the drifter
- A uniform load of $2.17N$ at the drogue section to simulate the weight of the drogue
- A point load of $2.94N$ at position $605mm$ from front of nose-cone to simulate the weight of the sink weights of the drogue
- A load of $1.33N$ at the middle to simulate the weight of the bottom section.

The results of the analysis are in Figure 5.36 and Figure 5.37. The maximum stress that will act on the bottom fuselage is estimated to be at $1.81 \times 10^5 Pa$ which significantly below the yield point. Furthermore, the maximum stress acts only at the holes of the bottom fuselage which was expected. The maximum displacement that will happen to the bottom fuselage is also negligible.

5.8.2 Wing-box Finite Element Analysis

The wing-box is a very important component of the glider as severe failure of the wing box results in the wing spars ripping through the wing box. Therefore, FEA was undertaken in order to ensure failure does not occur during flight.

The analysis is done based on a few assumptions. First, the glider is assumed to be in level flight where lift equals to weight and thus both forces are cancelled. Furthermore, it is assumed that the only force acting on the wing-box is the shear force from the wing spars Also, all the shear force from the wing spars that is acting on the wing-box solely acts on the edge of the wing-box holes. The estimated theoretical shear force of the wing spars at the root in the structural calculation of the wing was used for the analysis which was at $20N$.

To create the simulation for the analysis, a fixture was applied to the bottom surface of the wing-box as that is the point where the wing-box is connected to the fuselage. Since lift equals weight, the fuselage should be fixed during flight and so should the wing-box. The wing-box holes were not made circular but a semi-circle combined with a rectangle so that it is possible to place shear forces onto the top edge of the holes and there is no extra materials that will absorb the acting forces. A total shear force of $20N$ is placed acting on all four edges of the two holes of the wing-box. The acting shear force is already given a safety factor of 1.5. The FEA set-up is as shown in Figure 5.38.

A mesh convergence study was done and plotted on a graph. Unfortunately, the plotted graph showed that the study did not result in a converged value but continued to increase rapidly after certain total number of elements. This means that the study was a failure and an accurate estimate is unattainable.

There are a few reasons why the mesh convergence study failed and FEA does not simulate real life situation:

- The analysis was an overestimation as the total shear force at the root will not solely act on the edge of the wing-box holes.
- Having all the shear force acting only on the edge of the holes might not be an accurate way of performing the analysis as small mesh results in a small area taking too much of the loading.
- The foam properties are unpredictable due to its high compressibility and non-linear properties.

Due to the failure of the mesh convergence study, a physical experiment was done to verify the breaking point of the wing box.

5.8.3 Wing-box Physical Testing

The experiment was set up by cutting a block of foam that has the same thickness as the wing-box. A hole $1cm$ above the bottom of the block is then drilled through. The foam is then clamped at the top and placed at certain distance above the ground. A carbon rod goes through the hole with equal lengths sticking out at both ends. A rope is tied and secured near the tips of the rod. Weights are then added to the ropes. This is to simulate the bending of the wing spars due to the lift produced. The weights on the ropes are increased every iteration by $1kg$ each side and checked to see if there are any notable changes occurring at the edges of the hole on the foam each time. A similar example of how the experiment was set up is shown in Figure 5.39 but with only one spar and one hole instead.

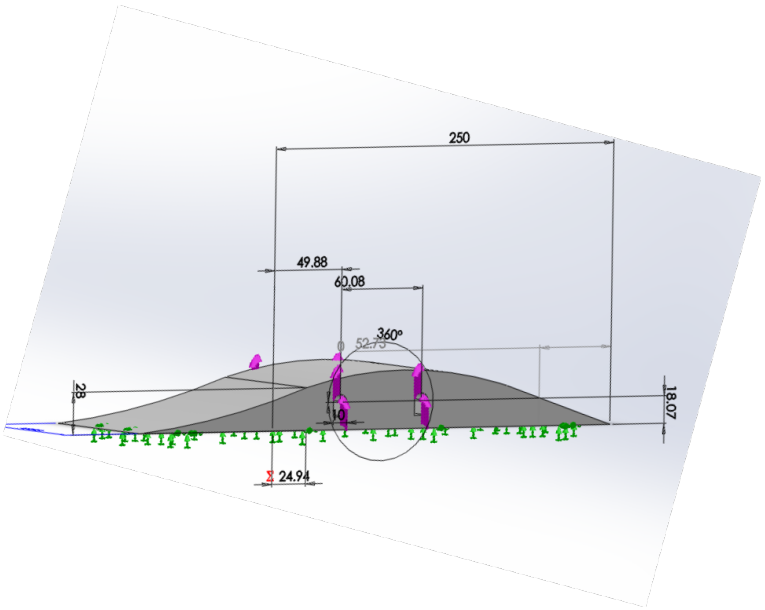

Figure 5.38: Wing-box FEA set-up

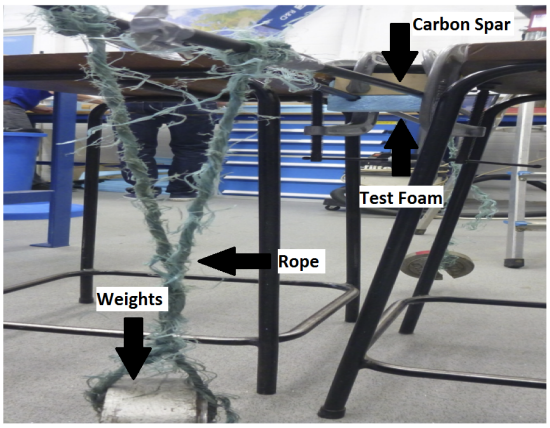

Figure 5.39: Physical experiment set up

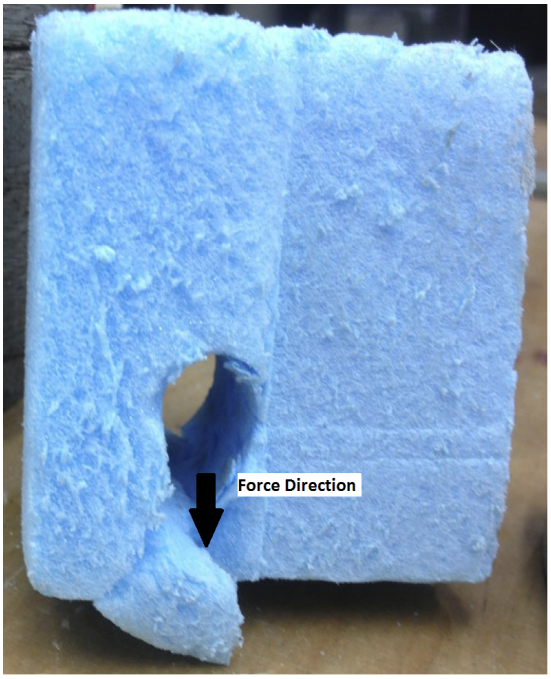

Figure 5.40: Failure of the foam test specimen

The experiment was repeated but with the hole at $1.7cm$ above the bottom which was the minimum distance between the holes and the top of the wing-box. The results of the experiment is shown in Table 5.3

Table 5.3: Wing-box experiment results

Distance between surface and hole	Yield point (kg)	Breaking point (kg)
1	8	16
1.7	14	28*

*Expected breaking point as wing-box did not fail during experiment

The biggest assumption for the experiment is that all the lift will act at the tips of the wing spars like a point mass beam bending. By doing so, the results will be an overestimation, for in reality, the lift is distributed throughout the wing which produces less deflection at the tips and thus lower shear force at the root of the spars. However, if the wing-box does not fail with the overestimation, then it can be safe to say that failure will not occur.

Based on the results, even after the foam has started to yield, it still requires double the load before the foam will undergo severe failure as shown in Figure 5.40. The hole in the foam slowly started to get bigger after the yield point. Finally, the rod finally rips through the foam when ultimate failure occurred. From the results of the experiment, for the $1cm$ case, the foam only started to yield at a total of $8kg$ of weights which is significantly higher than the design requirement which was only $2.25kg$ of lift. In conclusion, the designed wing-box is not expected to fail even if the glider experiences $2.5g$ forces but might start to yield slightly. Moreover, it was decided to stick with the $1.7cm$ distance as an extra precaution to eliminate the possibility of failure during flight as it does not result in significantly increase glider weight.

5.8.4 Wing Finite Element Analysis - Muhammad Anas Abd Bari

To validate the structural performance of the wing and also the roll wrapped carbon tube, the FEA of both structures is then simulated by using a software knows as Abaqus CAE using value derived from material research in following table:

Materials	Density, ρ (kgm^{-3})	Young's Modulus,E(Pa)	Poisson's Ratio,ν
Carbon Rod	1600	$70.0x10^9$	0.1
Styrofoam	30	$1.6\ x10^7$	0.0

Figure 5.41: Material Properties for FEA[30, 123]

5.8.5 Geometry

Few modification has been made to the wing section for Abaqus simulation. Originally, there are a rectangular slot in span-wise direction in the middle of the wing. However, when importing the wing model from Solidworks in IGS format, this model has been considered as a complex geometry hence Abaqus found a few errors that cannot been repaired. Due to this reason, this slot has been removed and only left with the holes for the carbon tube as shown in figure 5.42. Due to its simple geometry, nothing has been changed for the carbon tube model.

Boundary Conditions
The first boundary condition is that the root of both carbon tubes are pinned. Secondly, only the bottom surface of the tubes are in contact with the wing's hole. This to make sure that when load is applied to the lower surface of the wing, the load will be transmitted along the carbon tube. The distribute load was

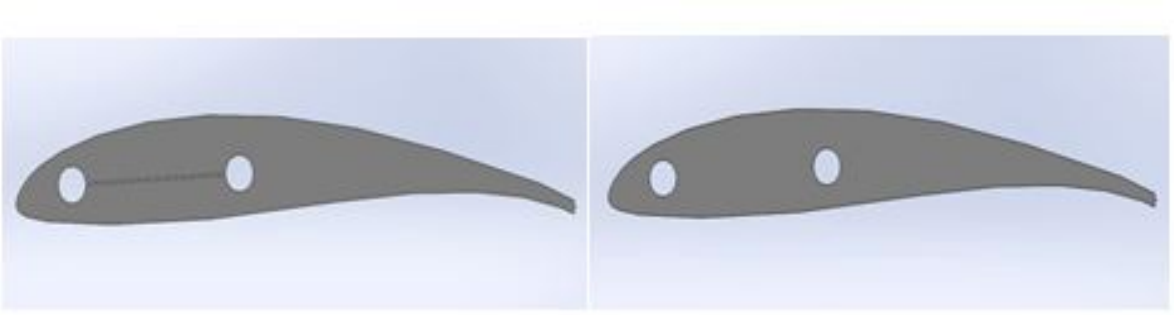

Figure 5.42: Left:Initial wing geometry(with slot) and Right:Wing geometry for Abaqus (without slot)

applied using Shrenk's method, the same magnitude of load has been distributed in span-wise direction about the quarter-chord of the wing by using a polynomial equation gained from Schrenk's Method in which it plotted the lift coefficient values in span-wise direction (see graph in Shrenk's Method section). This equations is: $-40.34x^6+90.86x^5-77.61x^4+30.71x^3-6.05x^2 + 0.40x + 1.13$

Results

Academic Teaching License for Abaqus limits the number of mesh to 20000 nodes only. The size of each nodes has been controlled by the Global Seeds. For this wing and carbon tubes assembly, the lowest possible global size is 21mm. The result obtained from this analysis shows that the maximum stress is located at the bottom surface of the carbon rods with value of $1.916x10^{14}$ Pa whereas the maximum deflection is location at the tip of the wing with the value of 1.454^{11} mm upwards from initial position as shown in figures 5.44 and 5.45 .

This is clearly not right as the magnitude is too large. The main reason behind this outcome is due to unit conversion in Abaqus. By comparing these results with the had calculations, it was found that the maximum stress is bigger by order of magnitude 10^6 and 10^{10} for maximum deflection, therefore correction is required as shown in following table.

Global size	Number of element (per spar)	Number of Elements (wing)	Total Elements	Maximum Stress, Pa	Correction
150	50	2774	2874	6.891E+13	6.891E+06
125	60	2653	2773	7.124E+13	7.124E+06
100	80	3411	3571	9.179E+13	9.179E+06
75	110	4169	4389	5.302E+14	5.302E+07
50	96	6443	6635	2.262E+14	2.262E+07
40	160	7959	8279	1.705E+14	1.705E+07
30	216	10612	11044	1.854E+14	1.854E+07
25	256	12886	13398	1.968E+14	1.968E+07
24	272	13265	13809	1.964E+14	1.964E+07
23	280	14023	14583	1.869E+14	1.869E+07
22	296	14781	15373	2.054E+14	2.054E+07
21	304	15160	15768	1.916E+14	1.916E+07

Figure 5.43: Number of mesh elements and maximum stress for every global size

Mesh Convergence Study

The result has been validated by plotting maximum stress graph. Theoretically, convergence result should be obtained as the mesh getting finer. All the maximum stress values obtained for each global mesh size. The lowest possible global size is $21mm$ whereas the maximum possible is $150mm$. It means that, the lower the value, the greater number of mesh elements hence the finer the mesh is.

From the graph in figure 5.46, it has been noticed that the graph did converge as the number of mesh elements increase. This behaviour validates the results obtained from this analysis.

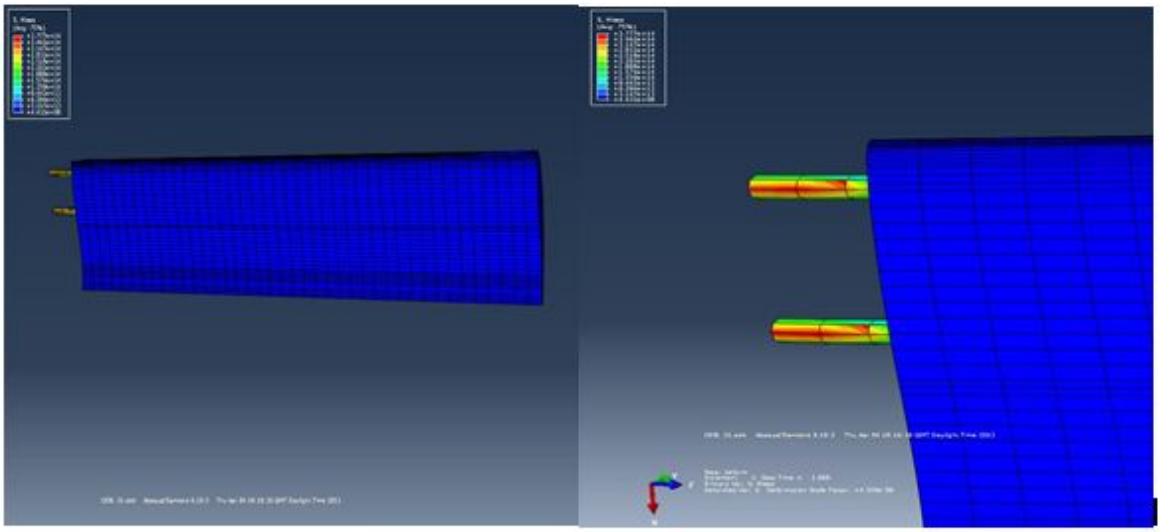

Figure 5.44: Location of maximum stress

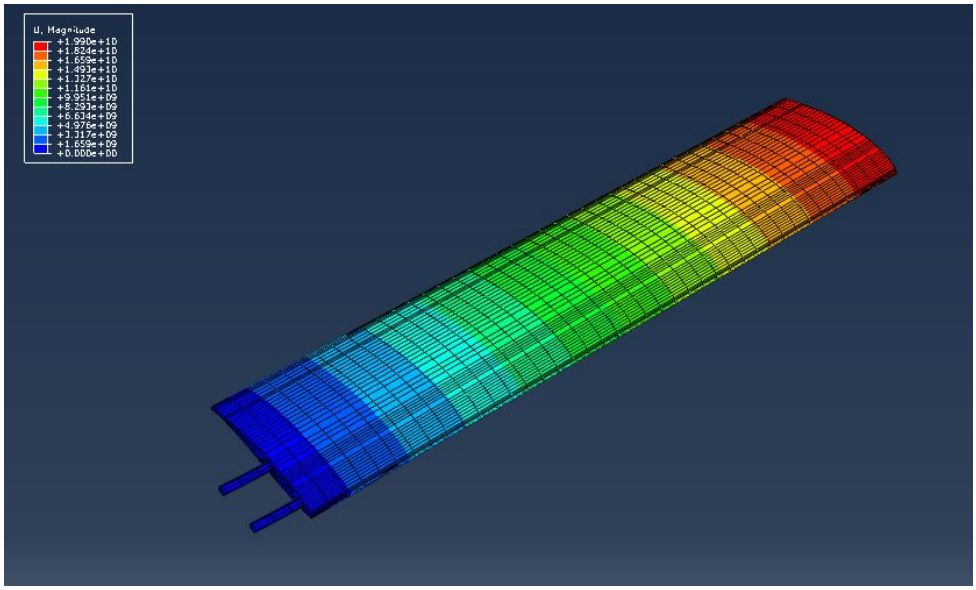

Figure 5.45: Maximum deflection at the wing tip

Comparison Between Beam Bending Theory and Abaqus

The simulation for Abaqus has been conducted for the wing with two carbon tubes. Therefore the results obtained should be compared between the same case for hand calculations. Unfortunately, due to limitation of he teaching licences, it is unlikely to get the value of bending moment from Abaqus, hence only two parameters can be compared which are the maximum stress and also maximum deflection for both cases.

From figure 5.47 it is clearly shown that there are discrepancies between these values. However, these values are and small therefore acceptable. It is most important to know that the structure does not fail from the Abaqus simulation since both the maximum stresses do not exceed the compressive strength value of the carbon tube which is $5.71 \text{x} 10^8$. Also due to its small discrepancy this comparison indicates that both methods did agree to each other and hence validate the structural strength of the wing.

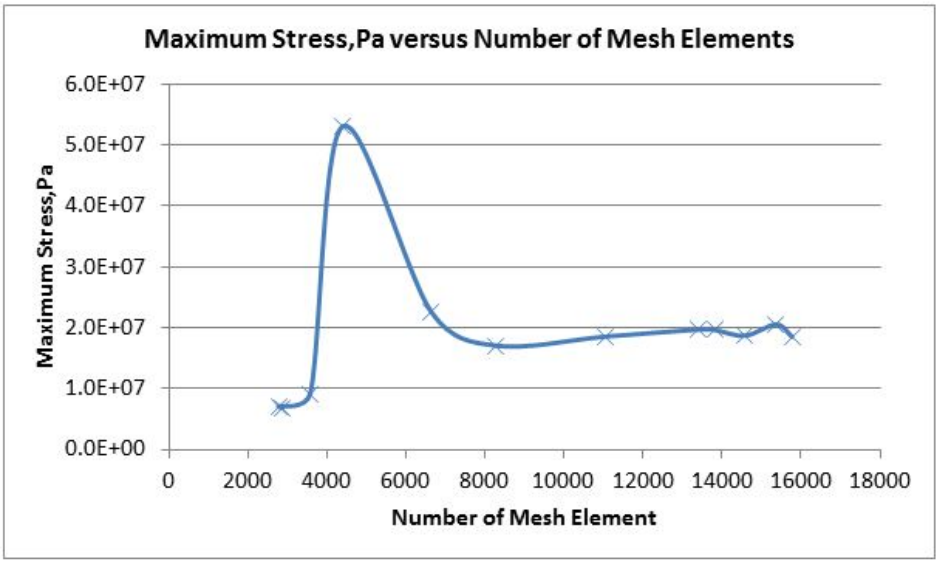

Figure 5.46: Graph of maximum stress versus number of mesh elements

	Beam Bending Theory	Abaqus	Discrepancy ,%
Maximum Stress,Nm^{-2}	$1.04x10^{8}$	$1.92x10^{7}$	81.58
Maximum Deflection, mm	12.32	14.54	16.10

Figure 5.47: Results comparison

5.9 Tail Configuration - Nathan Lao

Although tails can be regarded as small wings, they are usually designed to operate at only a fraction of their lift potential, compared to wings where they are designed to withstand a substantial lifting force.

The tail provides stability and trim to the aircraft by counteracting moments created by other parts of the aircraft, such as the wing. It does this by allowing the lifting force to act through the tail moment arm about the centre of gravity. The horizontal tail allows a restoring moment to balance the pitching moment created by the wing. The vertical tail is usually symmetric as to not create any aerodynamic yawing moments which may cause the aircraft to become unbalanced in flight.

Control is also provided by the tail and is important in determining the handling qualities and capabilities of the aircraft. The control surfaces, elevators and rudder, allow controllability of the aircraft to manoeuvre appropriately in different flight scenarios, such as spin recovery. The size of the tail is also an important factor in determining the control authority.

5.9.1 Tail Arrangement

Having reviewed the possible tail arrangements, as discussed in section 3.2, it was decided to implement a conventional tail configuration. There are several reasons for this; firstly the conventional tail arrangement provides adequate stability and control at the lightest weight [104], which for the objectives set, provide suitable performance and aircraft characteristics. Secondly, due to the available manufacturing facilities, the conventional arrangement introduces less complexity in the manufacturing stages.

Furthermore, the positioning of the horizontal tail with respect to the tail is crucial in defining the stall characteristics of the aircraft. If the horizontal tail is positioned so that when the wing is stalled, the

horizontal tail has no pitch authority due to being blanketed by the wake of the wing, thus stall recovery will be more difficult.

Therefore, the horizontal tail has been positioned so that it is below the chord-wise centreline of the wing to avoid this problem. Figure 5.48 illustrates the solution to avoid this problem.

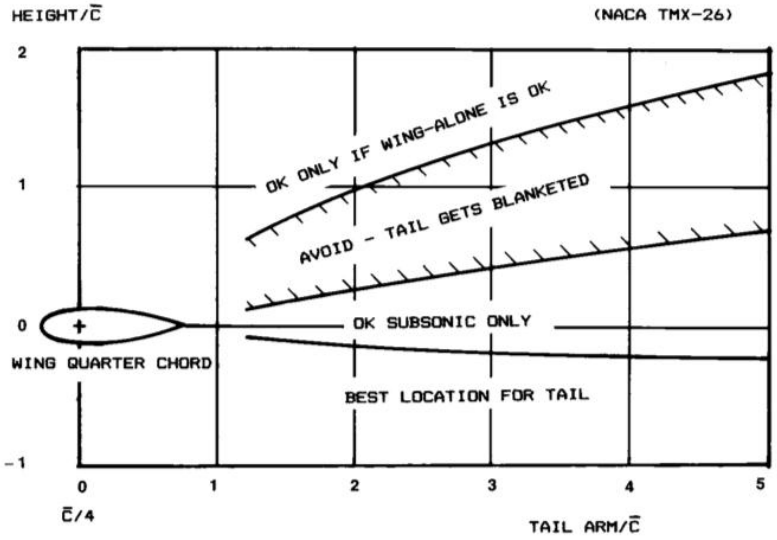

Figure 5.48: Horizontal Tail Positioning [104]

Having the horizontal tail in this position and in a conventional arrangement can cause blanketing of the vertical tail and the rudder. This is not desirable for the reason of reduced spin recovery; when an aircraft is in a spin, it requires adequate rudder control in order to reduce the sideslip angle and stop the rotation of the aircraft. Therefore, the vertical tail has been positioned so that the leading edge is vertically aligned with the horizontal tail leading edge. As the selected vertical tail chord is smaller than the horizontal tail chord, this allows the top half of the rudder to be unblanketed.

5.9.2 Constraints on Tail Characteristics

Due to manufacturing facilities available and cost, there were a few constraints on the tail configuration that needed to be considered.

Tail taper would have allowed for reduced induced drag on the horizontal tail, as well as a reduction in weight, however this could not be fabricated accurately and so was omitted from the design.

Leading edge sweep on the horizontal tail would allow the tail to stall after the wing and allow a straight hinge line for the elevators, which normally have the left and right sides connected to reduce flutter tendencies [104]. However, implementing a sweep on the horizontal tail was not possible, due to complexity and time.

Therefore, due to the above constraints, the horizontal and vertical tail planforms are both rectangular. This was an adequate design as it would still provide the required performance and reduces manufacturing complications, thus saves project time and cost.

5.9.3 Tail Aerofoil Selection

The selection of the aerofoil for the horizontal and vertical tail sections required consideration of several factors. As tail surfaces are required mainly for control, stability and trim, it was decided to have a symmetrical aerofoil section, as this would avoid aerodynamic forces which could disturb the static longitudinal stability of the aircraft. Also, it is necessary for the aerofoil section of the tail to have a

smaller thickness ratio than the wing to help maintain the critical Mach number of the tail above that of the wing [2]; this is to allow controllability of the tail surfaces when the wing develops shock waves past its critical Mach number. A thinner aerofoil section would also allow a saving in weight as well as reduced aerodynamic forces. Furthermore, for simplicity in manufacturing, a symmetrical aerofoil would require a less complicated manufacturing process.

Three NACA 4-digit aerofoil sections were considered for the selection of the tail, whilst considering that tail spars would need to be implemented into the aerofoil sections, thus the aerofoils should be thick enough to accommodate spars whilst being as thin as possible, as mentioned above, and produce the required aerodynamic performance to balance the aircraft. The NACA 0008, NACA 0012 and NACA 0014 aerofoil sections were considered.

XFLR5 was used to analyse each aerofoils characteristics using the inbuilt XFoil direct and inverse analysis capabilities. The analysis was run at a freestream velocity of 10 m/s, a Mach number of 0.03 and a Reynolds number of approximately 137,000; with an angle of attack range from -10 degrees to 15 degrees. Figure 5.49 was obtained from this analysis.

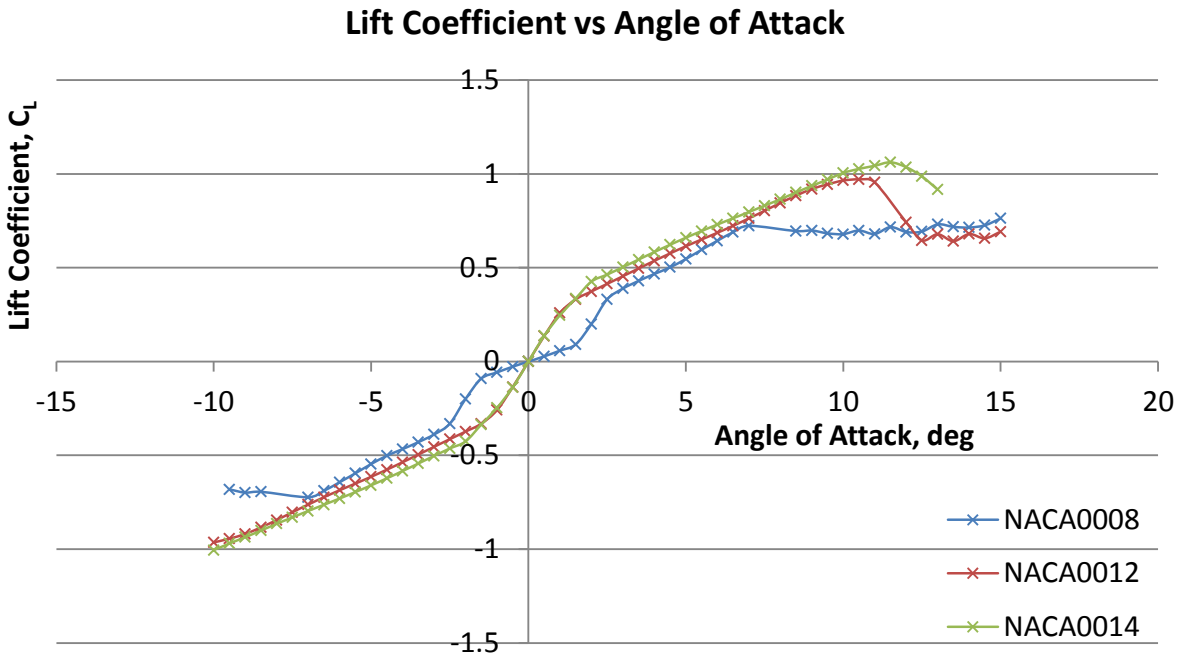

Figure 5.49: Tail Aerofoil Selection, XFLR Analysis

From this analysis it was decided that the NACA 0012 section would be used for the tail. The NACA 0012 section shows a higher stalling angle than the NACA 0008 section, which allows the aircraft to fly at higher AOA without stalling the tail. The NACA 0014 section showed very similar characteristics to the NACA 0012 section, having a slightly larger stall angle; however, it is a thicker section and thus will be heavier, providing excessive thickness for tail spars. The NACA 0012 aerofoil provides a desirable lift curve slope whilst having adequate thickness to accommodate tail spars.

5.9.4 Horizontal Tail

For the sizing of the horizontal tail, a historical approach has been used to estimate the initial size [104]. The horizontal tail volume coefficient C_{HT} is an estimation based on the mean chord of the wing c_W, the wing planform area S_W, the moment arm from the horizontal tail quarter chord to the wing quarter

chord L_{HT}, the horizontal tail planform area S_{HT}.

$$C_{HT} = \frac{L_{HT} S_{HT}}{c_W S_W} \tag{5.28}$$

This equation can be rearranged to calculate the horizontal tail area.

$$S_{HT} = \frac{C_{HT} c_W S_W}{L_{HT}} \tag{5.29}$$

To obtain the value for the horizontal tail volume coefficient C_{HT}, a typical value was taken from averages based upon data of similar classed aircraft. The typical value for sailplanes and homebuilt aircraft is 0.50 [104], where it was assumed the designed glider falls within this category.

The moment arm could be determined, as the wing position and length of the fuselage had been decided. Therefore, with a wing chord of $0.2m$, a wing area of $0.34m^2$ and a moment arm of $0.438m$, the horizontal tail area was calculated to be $0.077m^2$.

The horizontal tail chord was decided to be $0.15m$ and from this the span of the horizontal tail was calculated to be $0.52m$. However, including the width of the fuselage, $0.16m$, taking into account the tail section of the fuselage tapers off, variable hot-wire cutting tolerances and manufacturing simplicity, the horizontal tail was sized to be $0.75m$. This then yielded an aspect ratio of five.

An installation angle of zero degrees was decided upon due to the already complex procedure for manufacturing the fuselage tail section caused by the multiple number of cuts to achieve the desired design.

5.9.5 Vertical Tail

For the sizing of the vertical tail, a similar approach has been used to estimate the initial size. For the vertical tail, the wing yawing moments to be countered are most directly related to wing span and therefore the vertical tail volume coefficient C_{VT} is an estimation based on the wing span b_w, the wing planform area S_W, the moment arm from the vertical tail quarter chord to the wing quarter chord L_{VT}, the vertical tail planform area S_{VT}.

$$C_{VT} = \frac{L_{VT} S_{VT}}{b_W S_W} [104] \tag{5.30}$$

This equation can be rearranged to calculate the vertical tail area.

$$S_{VT} = \frac{C_{VT} b_W S_W}{L_{VT}} \tag{5.31}$$

The value for the vertical tail volume coefficient C_{VT} was taken the same way as the horizontal tail volume coefficient, a typical average value was taken between sailplanes and homebuilt aircraft to be 0.02 [104].

Once again, the moment arm was determined from the SolidWorks model, and was found to be $0.427m$. Performing the above calculations with the wing span of $1.70m$, the area of the vertical tail resulted in $0.026m^2$.

The vertical tail chord was decided to be $0.12m$ which then yielded the vertical tail length to be $0.223m$. However, taking into account manufacturing tolerances from the hot-wire diameter, this was rounded up to $0.23m$. The assumption was made that the vertical tail effectiveness from the fuselage wake at the base of the vertical tail was negligible. This then yielded an aspect ratio of approximately two.

The installation angle of the vertical tail was set to zero degrees as it is not desirable to have aerodynamic loads on the tail which would destabilise the lateral stability of the glider whilst in flight.

5.9.6 Structural Considerations

As the tail surfaces are not designed to operate at their maximum lifting capabilities, and thus should not see significant aerodynamic loads; the spars for the tail surfaces were chosen to be carbon pultruded spars with an outer diameter of $4mm$, where they would be implemented from tip to tip of the horizontal tail and from tip of the vertical tail to an extension length past the other tip. The vertical tail spars extend beyond the full length of the vertical tail so that it can be securely positioned into the top of the fuselage tail section. This would provide sufficient structural rigidity, whilst having a reduced weight advantage over larger diameter spars. The addition of spars in the tail surfaces also help reduce the flutter seen by the tail surfaces at higher velocities.

5.9.7 Control Surface Sizing

Control surfaces are required to allow an aircraft to manoeuvre and control its attitude. On the tail, elevators provide pitch control of the aircraft and the rudder provides yawing authority to the aircraft.

There are no definitive calculations to determine the exact dimensions of the se control surfaces, however, an optimisation process must be implemented in order to obtain the desired control surface effectiveness. Therefore, initial sizing of these control surfaces are estimated based on typical percentage values of aircraft.

The elevators and rudder normally span to about 90% of the horizontal and vertical tail, respectively [104]. Further to this, the chord lengths of the elevators and the rudder has been taken to be 30% of the chord lengths of the horizontal and vertical tail, respectively, where typical values range from $25 - 50\%$ [104].

Using the above guidelines, the elevator span is $0.45m$ in total, however, this was reduced to $0.4m$ due to the constraint of splitting the elevators because the horizontal tail is built into the tail section fuselage; this then yields two elevators, each having a span of $0.2m$. The chord of the elevators yielded $0.045m$.

The rudder span was sized to be $0.2m$ with a chord of $0.036m$.

Flutter is a potentially destructive vibrational disturbance initiated by aerodynamic forces on the control surface. Flutter tendencies can be reduced by using mass balancing and aerodynamic balancing, where mass balancing requires additional weight to be placed forward of the control surface hinge-line and aerodynamic balancing requires part of the control surface to be forward of the hinge-line [66]. Reducing flutter tendencies on both the elevators and rudders would have been desirable; however, due to the complexity in the fabrication of such methods and the relatively low velocities at which the designed glider will achieve, these did not seem to be efficient use of project resources.

5.9.8 Review of Tail Sizings

After the wind tunnel testing of the glider model, the horizontal tail spars were increased in outer diameter from 4mm to 6mm carbon fibre pultruded spars. This was due to the visual observation of the whole horizontal tail fluttering at the higher velocities of testing. The increase in spar diameter reinforced the structural rigidity of the tail and allowed an increase in effectiveness of the elevators.

Optimisation of the control surfaces, elevators and the rudder, would also have been desirable, however, due to time constraints and availability of manufacturing facilities, the control surfaces were not optimised but still produced adequate effectiveness.

5.10 Theoretical Drag Prediction - Nathan Lao

5.10.1 Introduction to Drag

Drag is an important parameter which determines the performance of the aircraft. Total drag depends on different forms of drag; the main contributions are from profile, lift-induced and wave drag. Profile drag consists of form drag and skin friction drag; form drag arises from the size and shape of the aircraft and skin friction drag is produced from the friction of the wetted aircraft skin area and the fluid passing over it. Lift-induced drag arises from the wing tip vortices that are developed; they develop because of the difference in pressure between the upper and lower surfaces of a wing that is operating at a positive lift. As pressure is a continuous function, the pressures must become equal at the wing tips; therefore the tendency for particles in the surrounding flow is to spill around from the lower wing surface around the wing tip and to the upper surface (from the region of high pressure to the region of low pressure) so that the pressure becomes equal above and below the wing [122] as shown in Figure 5.50. These vortices produce an opposing downforce across the wing and thus reduce effectiveness of the wing.

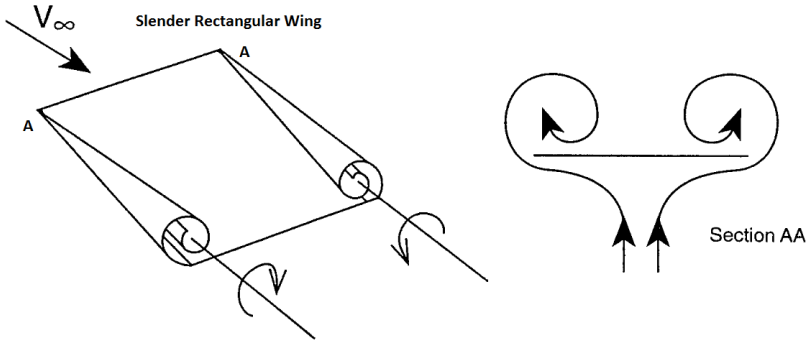

Figure 5.50: Diagram of vortices on a slender rectangular wing [60]

Wave drag is caused from the formation of shock waves on the body of the aircraft, though usually associated with supersonic flight, shock waves can occur at lower speeds where local flow accelerates due to the aircraft geometry.

5.10.2 Theoretical Prediction

Calculating the theoretical value of the designed glider drag coefficient will allow the comparison to values produced from the CFD simulations and the wind tunnel results of the scale model. The final glider characteristic can then be estimated to allow any further optimisation considerations or alternatives.

The total drag coefficient (C_D) equation is a product of the profile (C_{D0}), induced (C_{Di}) and wave drag (C_{DW}).

$$C_D = C_{D0} + C_{Di} + C_{DW} \tag{5.32}$$

Starting with the profile drag of the designed glider, the profile drag of the glider has been split into three sections, fuselage profile drag, wing profile drag and tail profile drag. The following equation defines profile drag, [84], where C_f is the skin friction coefficient, F is the component shape factor, Q is the interference factor, S_{wet} is the component wetted area and S_{ref} is the reference area:

$$C_{D0} = C_f.F.Q\left(\frac{S_{wet}}{S_{ref}}\right) \tag{5.33}$$

The designed glider has been split into three sections, the fuselage, the wing and the tail sections. Due to the surface roughness of the glider material, it has been assumed that there is turbulent flow over the entire glider, thus the Prandtl-Schlichting equation for turbulence over a flat plate has been used to approximate the skin friction coefficient over the three glider sections. The equation uses the Mach number, which for the glider at $10m/s$ at sea level is 0.03, and a cut-off Reynolds number. The cut-off Reynolds number is used to ensure that the skin friction coefficient is not over-predicted and is a function of the characteristic length, l, and the skin roughness value, k.

$$\begin{aligned} R_{e_{cutoff}} &= 38.21\left(\frac{l}{k}\right)^{1.0533} \\ C_f &= \frac{0.455}{(logRe_c)^{2.58}}(1+0.144M^2)^{0.65}[84] \end{aligned} \tag{5.34}$$

The skin roughness value has been taken as 1.7×10^{-6}, as it is the most similar material to the glider with an obtainable value, smooth moulded composite.

The shape factor for each section has been calculated based on equations 5.35[84]:

$$\begin{aligned} F_{fuselage} &= 1 + \frac{2.2}{\lambda^{1.5}} - \frac{0.9}{\lambda^3} \\ \lambda &= \frac{l}{d} \\ F_{wingtail} &= (F^* - 1)\cos^2\Lambda_{0.5c} + 1 \\ F^*_{wing} &= 1 + 3.3\left(\frac{t}{c}\right) - 0.008\left(\frac{t}{c}\right)^2 + 27\left(\frac{t}{c}\right)^3 \\ F^*_{tail} &= 1 + 3.52\left(\frac{t}{c}\right) \end{aligned} \tag{5.35}$$

The interference factor has been approximated, where there are small or no fillets on each section.

Totalling the profile drag values from each section yields a total profile drag of $C_{D0} = 1.54 \times 10^{-2}$.

The induced drag was estimated using the following equation $C_{Di} = \frac{C_L^2}{\pi AR_e}$ [16], where AR is the wing aspect ratio, e is the Oswald span efficiency and C_L is the coefficient of lift.

The C_L value of 0.947 was obtained from the XFLR5 data of the 3D wing at an angle of incidence of three degrees, the installation angle of the wing. Using the following equation to calculate the Oswald span efficiency, $e = 1.78(1 - 0.045 \times AR^{0.68}) - 0.64$ [84], the induced drag can be estimated to be 5.36:

$$C_{Di} = \frac{0.947^2}{\pi \times 8.48 \times 0.797} = 4.22 \times 10^{-2} \tag{5.36}$$

The wave drag has been taken as 5.0×10^{-4} [84] as it has been assumed that the glider will not fly above the drag divergence Mach number, where shock formations affect the drag on the aircraft. The drag divergence Mach number usually initiates from transonic speeds, where the glider has been designed for a Mach number of 0.29 in steady, level flight.

Totalling these components of drag coefficients yields a total drag coefficient of 5.82×10^{-2} at an AOA of 0 degrees with a freestream velocity of $10ms^{-1}$ and sea level conditions.

5.11 Longitudinal Stability - Robert Gillman

The following section describes the pre wind-tunnel analysis completed to ensure longitudinal stability. For the glider to be stable it had to return to its equilibrium trim condition after a disturbance with no applied control inputs. To achieve longitudinal stability the neutral point is required to be located behind the glider centre of gravity, when the glider experiences a disturbance, resulting in an increased AOA, the glider produced a restoring pitching moment, nose down, about the centre of gravity. The gradient of pitching moment coefficient about the centre of gravity with respect to AOA was required to be negative such that,

$$\frac{\partial C_m}{\partial \alpha} = C_{m\alpha} < 0 \tag{5.37}$$

During the analysis the wing position along the fuselage and internal payload configuration were varied to establish the optimal configuration. The neutral point distance from the wing aerodynamic centre,

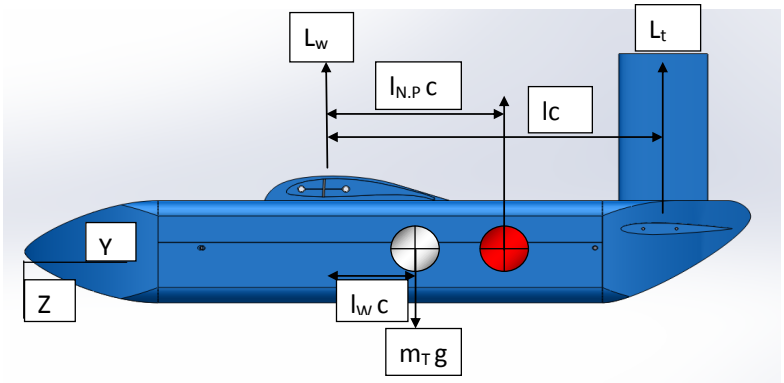

Figure 5.51: Neutral point reference dimensions

$l_{n.p}c$, was found using a moment balance taken about an arbitrary assumed neutral point position, fig. 5.51. It was assumed that any additional lift produced by the fuselage was negligible and additionally $C_{Mow} + C_{Mot}$ did not vary with respect to AOA.

$$M_{n.p} = M_{ow} + M_{ot} + cL_w l_{n.p} - cm_T g(l_{n.p} - l_w) - cL_t(l - l_{n.p}) \tag{5.38}$$

Equation (5.38) was simplified using non dimensional coefficients and differentiated with respect to AOA (α). Using the definition of neutral point, fixed position with respect to angle of attack, the equation was rearranged to find distance from the wing aerodynamic centre to neutral point normalised by wing chord, $l_{n.p}$. In order to simplify the equation the overall aircraft lift coefficient was required which was shown to be, [104] and [16];

$$C_L = C_{Lw} + C_{Lt}\frac{S_t}{S} \tag{5.39}$$

Where it is assumed $S_w >> S_t$ such that $S = S_w + S_t \approx S_w$ however, for the current application this assumption is not entirely accurate.

$$\frac{S_w}{S_t} = \frac{0.34}{0.1125} \approx 3 \tag{5.40}$$

Instead the overall aircraft lift coefficient can be written as,

$$C_L = C_{Lw}\frac{S_w}{S_w + S_t} + C_{Lt}\frac{S_t}{S_w + S_t} \tag{5.41}$$

To find the overall aircraft lift curve slope, C_{L_α}, the horizontal tail lift curve slope was required with

respect to glider angle of incidence. To convert between the two reference frames the effective reduction in tail angle from the induced downwash,ϵ, was taken into account.

$$\alpha_t = \alpha + i_t - \epsilon \tag{5.42}$$

$$\frac{\partial \alpha_t}{\partial \alpha} = 1 - \frac{\partial \epsilon}{\partial \alpha} \tag{5.43}$$

Where,

$$\frac{\partial \epsilon}{\partial \alpha} = \frac{C_{Lw_\alpha}}{\Pi e A_R} = 0.207 \tag{5.44}$$

The oswald span efficiency e was, for a rectangular wing section assumed to be [104],

$$e = 1.78(1 - 0.045A_R^{0.68}) - 0.64 \tag{5.45}$$

Prior to wind tunnel testing the values of C_{Lw_α} and $C_{Lt_{\alpha_t}}$ were taken from XFLR5 vortice lattice method models and transformed such that the lift curve slope was with respect to radians.

$$a_t = C_{Lt_\alpha} = C_{Lt_{\alpha t}}(1 - \frac{\partial \epsilon}{\partial \alpha}) \tag{5.46}$$

$$a_w = C_{Lw_\alpha} \tag{5.47}$$

$$a = C_{L_\alpha} = C_{Lw_\alpha}\frac{S_w}{S_w + S_t} + C_{Lt_\alpha}\frac{S_t}{S_w + S_t} \tag{5.48}$$

The original moment balance can be rewritten in a non dimensional form and then differentiated with respect to alpha.

$$C_{Mn.p} = C_{Mow} + C_{Mot} + C_{Lw}l_{n.p} - C_{mg}g(l_{n.p} - l_w) - C_{Lt}(l - l_{n.p})\frac{S_t}{S_w + S_t} \tag{5.49}$$

$$\frac{\partial C_{Mn.p}}{\partial \alpha} = C_{Lw_\alpha}l_{n.p} - C_{Lt_\alpha}(1 - \frac{\partial \epsilon}{\partial \alpha})(l - l_{n.p})\frac{S_t}{S_w + S_t} \tag{5.50}$$

Rearranging for $l_{n.p}$ the neutral point was given as a distance from the wing aerodynamic centre, normalised by the wing chord.

$$l_{n.p} = \frac{a_t(1 - \frac{\partial \epsilon}{\partial \alpha})\frac{S_t}{S_w + S_t}l}{a} \tag{5.51}$$

Hence the normalised static margin can be defined as;

$$\bar{K_n} = l_{n.p} - l_w \tag{5.52}$$

Where the glider is deemed sufficiently stable for a static margin in a region ranging from $5\% < \bar{K_n} < 15\%$,[104][16]. An excel spreadsheet was used to tabulate the moment of each component from the nose of the glider thus enabling a refined glider mass estimation and location of the overall centre of gravity.

Manoeuvre Stability

The analysis above could be extended further to explore the longitudinal stability characteristics during pitching manoeuvres. From theoretical derivations it can be shown that the dynamic stability of a manoeuvre is always larger than that of a level flight case. Therefore by meeting the level flight static margin requirements above the glider will be deemed sufficiently stable [61].

Payload Alterations

Firstly it was found that inserting the drogue in a reverse manner to that shown in fig. 4.34 brought

Estimate [Apr 2013]

Variables	
Wing LE from start of drifter section [m]	0.1
VT LE offset from HT LE [m]	0.05

Component	X-Dim [m]	Mass [kg]	X_local c.g [m]	Moment arm [m]	Moment [Nm]
Fuselage main section	0.600	0.271	0.300	0.480	1.28
Nose Cone	0.180	0.052	0.090	0.090	0.05
Battery + PCB	0.100	0.176	0.050	0.180	0.31
Release Mechanism [Front]	0.075	0.075	0.038	0.218	0.16
Drifter	0.250	0.518	0.146	0.401	2.04
Drogue (Drogue -sink weights)	0.200	0.221	0.100	0.605	1.31
Drogue (Sink weights)	0.010	0.300	0.005	0.710	2.09
Release Mechanism [Rear]	0.075	0.075	0.038	0.743	0.55
Tail section	0.200	0.071	0.100	0.880	0.61
Wing		0.394	0.033	0.388	1.50
Horizontal tail +Elevator		0.049	0.068	0.873	0.42
Vertical tail +Rudder		0.035	0.054	0.884	0.30
Servo (Elevator)		0.007		0.780	0.05
Servo (Rudder)		0.007		0.780	0.05
				Total Moment [Nm]	10.72
				XCG [m] [From Glider nose]	0.485
TOTAL MASS [kg] [Apr 2013]		2.25		NP[m] [From Glider nose]	0.495
ESTIMATED MASS [kg] [Nov 2013]		2.24		Static margin[% chord]	4.87%
Percentage difference		0.47%		Static margin[mm]	9.735

Figure 5.52: Stability chart

Configuration	Static Margin $\%\bar{c}$
Standard	4.87
Reverse drogue	8.20
No payload	31.72

Table 5.4: Wing tunnel payload configurations: static margin

the sink weights closer to the COG and thus gave a larger static margin. This configuration was used throughout the remainder of the project.
During the stability calculations the components of the drifter payload were moved to find the optimal static margin during flight and once the payload has been released. The aim was to ensure the glider would not suddenly stall and thus ensuring a significant distance between the drifter and glider would be obtained once the payload was released.

5.12 Wing Computational Fluid Dynamics - Nathan Lao

Computational Fluid Dynamics (CFD) is the use of numerical simulations and algorithms to predict physical fluid flow behaviour around a body of interest, such as an aircraft wing. It can also be used to study internal fluid flows and heat transfers, such as fluid through a pipe.

It is used here to validate the results obtained from the XFLR5 data of the designed glider wing; this will allow confirmation that the designed wing and its sizing produce the desired lift performance.

As XFLR5 is a free package, it does not offer the same guarantees of robustness, reliability or precision as a commercial software package [8]; therefore carrying out CFD simulations on the designed wing will build confidence into the design.

5.12.1 Software and Domain

The chosen CFD package was FLUENT 14.0, used as part of ANSYS Workbench 14.0, a framework that allows clear, logical steps with ease of use through its integration of powerful process tools. To allow for a faster simulation, half of the wing was simulated, which will still allow the coefficient of lift and drag to be calculated as the forces acting on the wing and the reference planform area is proportional to the full

span. The designed wing has a semi-span of $0.848m$ and a chord of $0.2m$ with a $0.1m$ wing tip dihedral at 10 degrees. The wing geometry was imported into ANSYS Design Modeller from Solidworks, where the domain was created. The geometry was meshed in ANSYS Mesher and the simulation was performed by FLUENT.

The domain created was sufficiently large enough to not interfere with the flow around the wing, whilst not being too big so that the cell count within the mesh is excessively high, thus saving on simulation time. The domain dimensions in relation to the wing chord is shown in Figure 5.53.

Downstream from trailing edge	Upstream from leading edge	Vertically above and below the wing	Spanwise from the wing tip
10 chord lengths	5 chord lengths	6 chord lengths	5 chord lengths

Figure 5.53: Wing CFD domain size

This domain size could possibly have been optimised through a domain sensitivity study, which would allow for a faster simulation run time without compromising the values produced, however, it was not seen as a beneficial use of time and resources to optimise the domain as the above domain provided accurate results and did not interfere with the flow around the wing.

5.12.2 Meshing

Unstructured Mesh

Unstructured meshes normally have an arbitrary connectivity between elements and the element shapes can vary from triangles to tetrahedrals, depending whether the geometry is 2D or 3D. An advantage of unstructured meshes is that they require little user input, as setting control points is not necessary. Unstructured meshes also have the ability to conform onto complex geometries where a structured mesh would struggle or even find it impossible to do so. Furthermore, unstructured meshes are well suited to inexperienced users as they require less user interaction and will still generate a valid mesh [64].The generation of unstructured meshes are commonly measured in hours. As unstructured meshes have arbitrary connectivity with other elements, the requirement for the calculation of the solver's equations is more demanding of computational memory. Thus, the execution times of unstructured meshes are longer than that of structured meshes. Tetrahedral and triangular elements are harder to align in the flow direction which leads to numerical diffusion, a product of numerical error [3].

Structured Mesh

Structured meshes generally have quadrilateral elements in 2D and hexahedral elements in 3D, which are arranged in rectangular patterns called a block. These meshes are usually characterised by regular connectivity, how each element is connected to each other.

Structured meshes allow the user great control in constructing the mesh, as the user can place points and edges where desired. Quadrilateral and hexahedral elements are also efficient at filling space and support high skewness before the solution is significantly affected [64]. As the user is able to control the elements, the mesh is often aligned in the direction of the fluid flow. It is because of these reasons that make structured meshes most desirable for numerical simulations as they require less computational memory and execute faster.

However, on the other hand, a drawback of structured meshes is that the generation of the structured blocks requires time and expertise in laying out the control points for the geometry, where generation of structured meshes are generally measured in days and weeks. [96] also points out that structured meshes can only be used for geometrically simple solution domains.

Chosen Mesh Structure

Harpoon $V3.4b$, an automatic structured meshing tool, was used to create a structured mesh of the domain and wing, however, these meshes turned out to be unstable once simulation had commenced and the solution diverged. This may be because of Harpoon being unstable on the facilities available and thus there was a lack of control in constructing the mesh. Therefore, ANSYS Mesher was utilised to produce an unstructured mesh, where it also allowed greater control on the wall spacing and element sizes.

5.12.3 Turbulence Model

CFD packages, such as, FLUENT and STAR CCM+, solve flow problems by solving the governing equations in an iterative manner, where either a transient solver or a steady state solver is used. The incompressible governing equations solved by these packages are shown by equation (5.53), [130].

$$\begin{aligned} \frac{\delta \rho U_i}{\delta t} + \frac{\delta(\rho U_i U_j)}{\delta x_j} &= -\frac{\delta P}{\delta x_i} + \frac{\delta}{\delta x_j}\left[\mu \tfrac{\delta U_i}{\delta x_j}\right] - \frac{\delta \overline{\rho u_i' u_j'}}{\delta x_j} \\ \frac{\delta U_i}{\delta x_i} &= 0 \end{aligned} \tag{5.53}$$

The governing equations are not closed and so require closure functions and coefficients for the CFD package to solve. The turbulence models are often based on eddy viscosity concepts which relate the Reynolds stresses to the mean velocity gradient. Below are brief overviews of the turbulence models considered.

Spalart-Allmaras Model

The Spalart-Allmaras (S-A) model is a relatively simple one-equation model that solves a transport equation for the kinematic eddy viscosity, equation (5.54) [128]. It includes eight closure coefficients and three closure functions; these are used to solve the Navier-Stokes equations.

$$\frac{\delta \tilde{\nu}}{\delta t} + U_j \frac{\delta \tilde{\nu}}{\delta x_j} = c_{b1}\tilde{S}\tilde{\nu} - c_{w1} f_w \left(\tfrac{\tilde{\nu}}{d}\right)^2 + \frac{1}{\sigma}\frac{\delta}{\delta x_k}\left[(\nu + \tilde{\nu})\tfrac{\delta \tilde{\nu}}{\delta x_k}\right] + \frac{c_{b2}}{\sigma}\frac{\delta \tilde{\nu}}{\delta x_k}\frac{\delta \tilde{\nu}}{\delta x_k} \tag{5.54}$$

The Spalart-Allmaras model was designed specifically for aerospace applications involving wall-bounded flows and has been shown to give good results for boundary layers subjected to adverse pressure gradients [53].

However, the Spalart-Allmaras model is still relatively new, and no proposal has been made regarding its suitability to all types of complex engineering flows. Furthermore, one-equation models are often criticised for their inability to rapidly accommodate changes in length scale, such as might be necessary when the flow changes abruptly from a wall-bounded to a free shear flow. [53]

According to Churchfield and Blaisdell [22], the Spalart-Allmaras turbulence model predicts the mean flow about a wing tip vortex most accurately. Work was also done by Javaherchi [58] on the S-A model, where he concluded that the S-A model produces similar results to the $k-\omega$ model, where the dissipation rate in the $k-\omega$ model is faster than the S-A model.

Standard $k-\omega$ Model

The $k-\omega$ model is a two transport equation model, where it solves for kinetic energy (k) and turbulent frequency (ω).

The $k-\omega$ model in FLUENT incorporates modifications for low Reynolds number effects, compressibility and shear flow spreading [54]. This model performs significantly better under adverse pressure gradient

conditions. The model does not employ damping functions and has straightforward Dirichlet boundary conditions, which leads to significant advantages in numerical stability [76]. Also, this model tends to underpredict the amount of separation for severe adverse pressure gradient flows.

Reasons why this model is chosen over the $k-\epsilon$ model is that it demonstrates better performance for wall-bounded and low Reynolds number flows than the $k-\epsilon$ model. It is more suitable for complex boundary layer flows under adverse pressure gradient and separation, for example, external aerodynamics and turbomachinary [75]. This model can also be used for transitional flows, although it does tend to predict transition rather excessively and earlier than what it would realistically be. Thus, requires a high mesh resolution near the wall, leading to increased computational cost.

$k-\omega$ SST Model

The Shear Stress Transport (SST) is a variant of the standard $k-\omega$ model; it combines the $k-\omega$ model for use near walls and the $k-\epsilon$ model away from walls using a blending function, and also uses a modified eddy viscosity formulation to account for the transport effects of the principle turbulent shear stress [75].

This model offers similar benefits as the standard $k-\omega$ model, but also accounts for the transport of turbulent shear stress and gives accurate predictions of the amount of flow separation under adverse pressure gradients [76]. Menter [76] recommends SST for high accuracy boundary layer simulations.

On the other hand, there are still limitations with this model, where the dependency on wall distance makes it less suitable for free shear flows compared to the standard $k-\omega$ model. Menter [76] suggests that a Reynolds stress model may be more appropriate for flows with sudden changes in strain rate or rotating flows while the SST model may be more appropriate for separated flows.

Chosen Model

The turbulence model used for all simulations has been chosen as the Spalart-Allmaras model; this is for several reasons. Firstly, it is a one equation model, which means that simulation time is reduced in comparison to using a two equation model, such as the $k-\omega$ model. As Javaherchi [58] concluded, the S-A model produces similar results as the $k-\omega$ model. Furthermore, the S-A model was designed specifically for aerospace applications and thus is able to capture wing tip vortices. Therefore, the S-A model was the most appropriate model for the simulation problems and the given time constraint.

5.12.4 Wall Spacing

In order for FLUENT to accurately calculate the flow in and around the wing boundary layer, the wall spacing of the mesh has to be at a sufficient distance away from the wall to capture the flow behaviour in the boundary layer. Having a large wall spacing will result in an inaccurate calculation of the flow and the required lifting or drag forces will not be reliable. Having a very small wall spacing will cause the mesh to be unnecessarily fine and cause a significant increase in simulation time.

The y^+ value is a non-dimensional distance from the wall to the first mesh node. Equation (5.55) defines this parameter, where u_* is the friction velocity, y is the wall spacing required and ν is the kinematic viscosity.

$$y^+ = \frac{u_* y}{\nu} \tag{5.55}$$

There are two main approaches for resolving wall bounded turbulence, near-wall modelling and wall functions. Near-wall modelling fully resolves the flow at the wall, which requires a fine mesh with nodes within the viscous sublayer. Wall functions used by turbulence models use empirical laws, such as the law of the wall, to link the solution variables at the near-wall cells.

Values of y^+ close to 30 are most desirable for wall functions, whereas, a y^+ value of 1 is most desirable

for near-wall modelling [48]. As the S-A model is the chosen turbulence model and the wall function approach will be utilised to resolve the boundary layer flow, a y^+ value of 30 will be used in order to comply with the suggested values for the S-A model [55]and to reduce simulation time, compared to the near-wall approach.

With known quantities of the freestream velocity ($10ms^{-1}$), the freestream density ($1.225kgm^{-3}$), the dynamic viscosity ($1.79 \times 10^{-5}Pa.s$) and the wing reference length ($0.2m$); the desired wing y^+ value of 30, yielded the boundary layer first layer thickness to be $8.948 \times 10^{-4}m$.

5.12.5 Boundary Conditions

Boundary conditions used are important in determining whether the flow behaves as expected within the simulation domain. As this simulation of the wing will be used to validate the data obtained from XFLR5, it has been modelled as a wing in free flight, just as the XFLR5 study simulated. Therefore, the front of the domain has been set as a velocity inlet boundary (blue), the rear of the domain has been set as a pressure outlet boundary (red) and the rest of the domain has been set as symmetry planes (yellow) with the exception of the wing (white), which has been set as a wall boundary. These boundary conditions can be seen in the Figure 5.54.

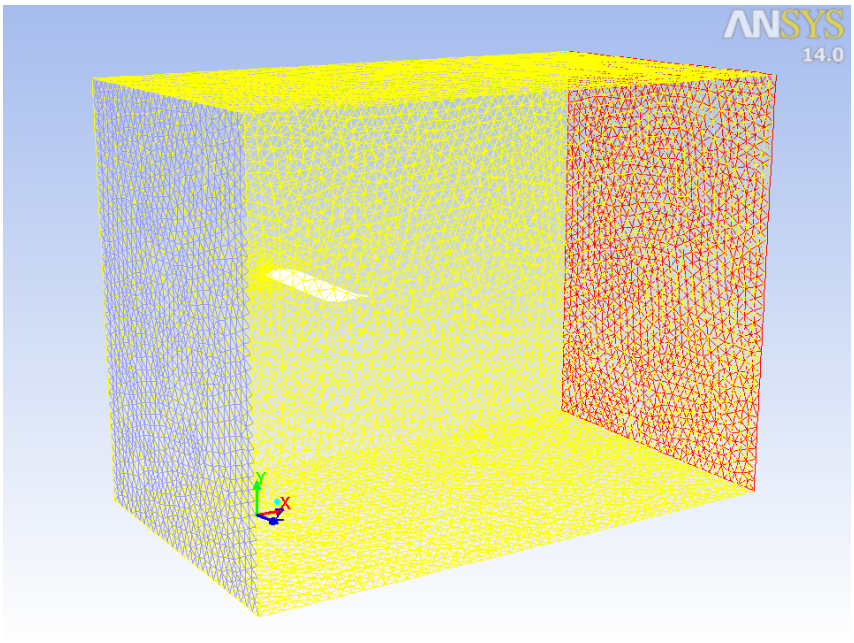

Figure 5.54: Wing mesh boundary conditions

5.12.6 Mesh Sensitivity

A mesh sensitivity study was carried out to obtain a mesh independent result; thus allowing the project to obtain an accurate solution without using significant computational resources. A range of meshes were obtained with a range of 200 thousand to 8 million elements; all meshes within the mesh sensitivity study were run at an angle of incidence of zero degrees.

Mesh Quality

The shape of the elements can have a significant impact on the accuracy of the solution; this includes the skewness and aspect ratio of the elements. Skewness is defined, in the FLUENT manual, as the difference between the shape of the element and the shape of an equilateral element of equivalent volume [56]; and aspect ratio is a measure of the stretching of the element. Both factors can yield inaccurate results and/or destabilise the solution. Mesh quality was measured by the values of maximum element

skewness and aspect ratio, where no meshes exceeded the recommended value of 0.98 for skewness and 100 for aspect ratio [5]. Any meshes that did not satisfy these conditions were discarded.

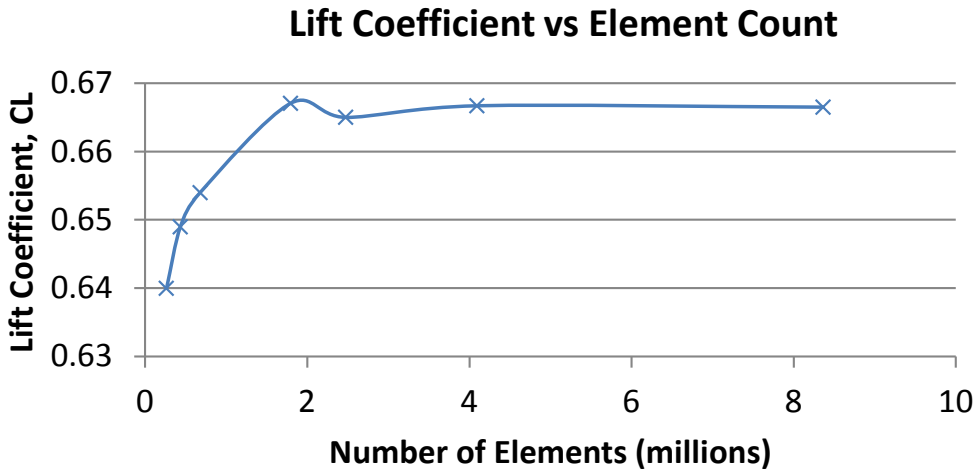

Figure 5.55: Wing mesh sensitivity, lift coefficient

From Figure 5.55, the optimum mesh chosen had $1,796,656$ cells; this is because it contains the least amount of cells to obtain the most accurate results, as defined by Baran [20].

5.12.7 Simulation Setup

All CFD simulations throughout this project have used the 3D double precision version of FLUENT, this is due to the 3D nature of the problem and for the improved accuracy of results. As it has been determined that the designed glider will not experience a Mach number above 0.3, compressibility effects have not been considered and so the pressure based solver was utilised in all simulations.

The wing CFD simulations were run at a freestream velocity of $10ms^{-1}$, sea level conditions and a range of AOA from 0 degrees to 20 degrees.

Discretisation

The segregated algorithm SIMPLEC was used as a converged solution can be obtained more quickly. The PRESTO! pressure interpolation scheme has been used due to the amounts of swirl generated by the tip vortices from the wing and tail.

The discretisation scheme used for the momentum equations was the second order upwind scheme because in this approach, higher order accuracy is achieved through a Taylor series expansion and less numerical diffusion occurs.

Convergence

The convergence criteria set for the iterative method is important in terms of both accuracy and efficiency. For all of the simulations, a convergence criteria of 1×10^{-4} was set on the continuity, and x-, y- and z- components of velocity. This is the recommended criteria given by Xie [130], where a criteria greater than 5×10^{-4} is poor and a criteria of 1×10^{-5} is excellent; the chosen criteria gives a good balance of accuracy and efficiency for the solutions.

Reference Values

The reference values used for the simulations are important in post processing the data and determining the forces on the wing. The wing reference area was taken as its planform area of $0.1696m^2$ and the reference length was the wing chord of $0.2m$; the rest of the reference values were taken as standard sea level measurements, for example, the reference temperature was $288K$.

Wing Results
After each simulation the data was analysed using CFD-Post, part of ANSYS Workbench 14.0. Using this software allowed each case to be analysed visually to ensure that no unexpected flow behaviours occurred. All of the obtained simulation runs produced the expected flow behaviours and vorticity was also visualised from the wing tip.

Figure 5.56 below shows the pressure contours over the wing attached to the symmetry face at an AOA of 3 degrees, the installation angle of the wing, and is as expected. There is a region of low pressure on the top surface of the wing and higher pressure on the lower surface of the wing; with the greatest pressure value being on the leading edge of the wing. The pressure scale shows the pressure difference from the reference pressure of $101,325Pa$.

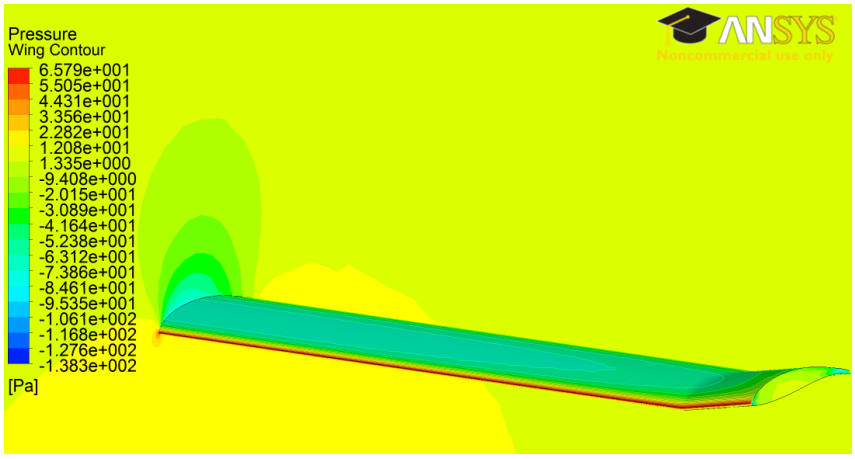

Figure 5.56: Pressure contours over the wing at 3 degrees AOA

Having obtained data from all of the wing simulations, these were compared with the data obtained from the XFLR5 runs to determine whether the designed wing performs as intended and provides the required lifting force.

Figure 5.57 below shows the comparison of the XFLR5 Vortex Lattice Method (VLM) lift coefficient versus AOA graph with the wing CFD. There is a strong correlation between the two curves, which means that the designed wing will provide the desired performance. There is approximately a difference of 2.5% between the gradients of linear sections of XFLR5 and the CFD, where C_{L_α} is 0.08 and 0.082, respectively. The CFD curve also shows the stalling angle of the wing to be around 15 degrees, which agrees with the aerofoils stalling angle, thus proving the CFD simulations is sufficiently accurate to capture the lifting performance of the wing.

Performing the wing CFD study has provided confidence and maturity within the CFD process and solver settings; this is valuable information for the upcoming CFD on the glider.

5.13 Wind Tunnel Testing - Robert Gillman

5.13.1 Aims

The balloon launched Lagrangian drifter wind tunnel testing took place on 25th-26th Feb 2013 in the RJ Mitchell wind tunnel. The aims of the wind tunnel testing session were:

- Prove the initial design condition, sufficient lift for level flight at $10ms^{-1}$, had been satisfied.
- Compare lift and drag results to theoretical estimates and XFLR5 data to gain a better understanding on the accuracy of 3D modelling in XFLR5.
- Establish data for CFD validation to aid from future design changes.

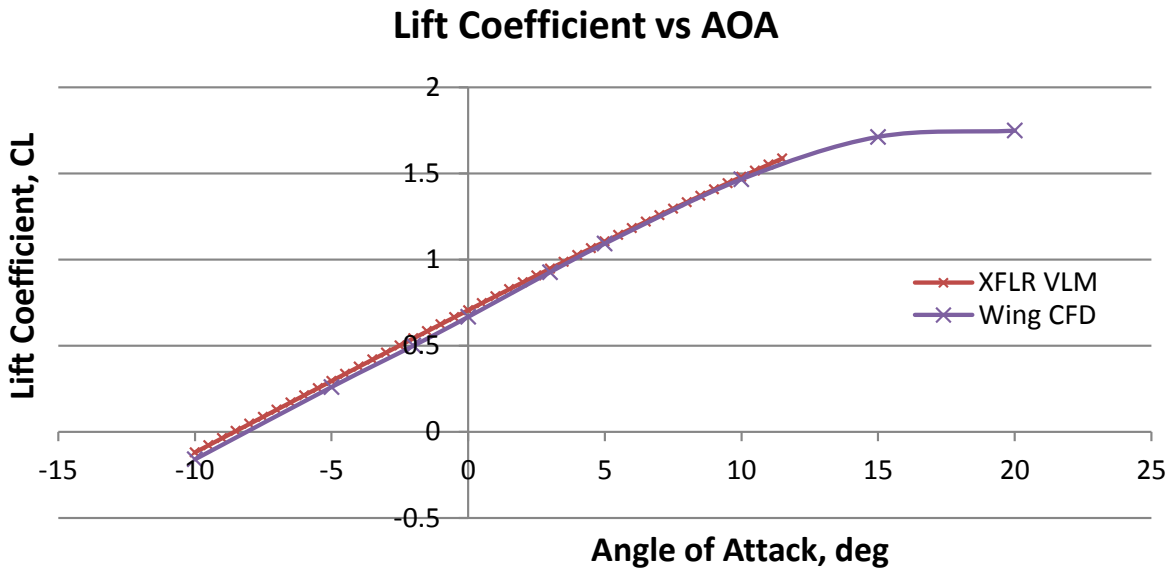

Figure 5.57: Comparison of XFLR5 and the wing CFD lift coefficient versus AOA graph

- Establish coefficients for glider lift and drag for use in the MATLAB flight prediction code.
- Ensure longitudinal and lateral stability prior to flight testing.
- To gain an understanding how the glider will respond once the payload has been released.
- Measure the effectiveness of control surfaces.
- Visually observe the glider structural response to near stall conditions.

5.13.2 Wind Tunnel Mounting

The glider was attached upside down in the wind tunnel from three roof mounted struts. This is common practice for a subsonic model in a roof mounted wind tunnel as it increases the distance between the aerofoil upper surface and the wake interaction from the bluff struts, therefore improving the accuracy of results. The struts were attached to an overhead six component force balance(lift,drag, side force, pitch, yaw and roll), from which the aerodynamics forces and moments were computed.

The attachments from the glider to the main wind tunnel plyons were designed in exactly the same manner as for the "Land" UAV and shall not be repeated here. The mounts allowed one degree of freedom so the Glider could pivot longitudinally about the mounting bolt to simulate pitch changes.

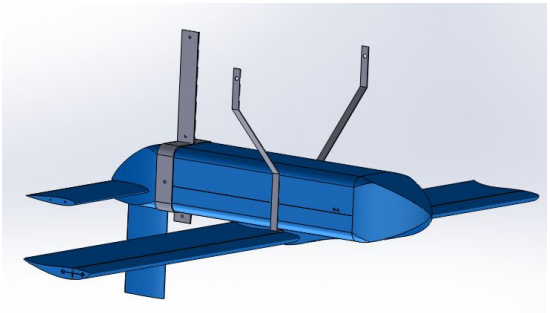

Figure 5.58: Wind Tunnel mount design

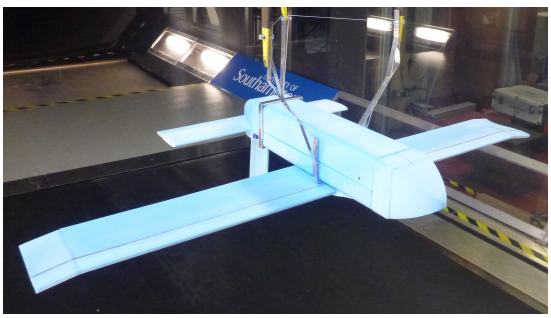

Figure 5.59: Wind Tunnel set up

5.13.3 Interference

Due to the enclosed nature of the wind tunnel it is difficult to truly replicate free flight conditions because of the interference from the wall boundaries and blockage effects from the struts and model. During wind

tunnel testing the aim was to achieve results, as close as feasibly possible, to free flight conditions. In order to achieve this it was ensured the Glider was mounted centrally with significant horizontal and vertical clearance from the wind tunnel boundaries, as shown in fig. 5.60, thus minimising the interference between the wind tunnel boundary layer and glider flow field. Additionally to take into account the interference from the mounting struts a tare was taken with "wind on" of just the Glider mounting mechanisms at each velocity and AOA tested. The "tare" was then subtracted from the raw wind tunnel data. Although this is not the most accurate approach for taking into account the effect of the struts because it neglects any additional downstream effects on the boundary layer it does provide a reasonable time efficient solution.

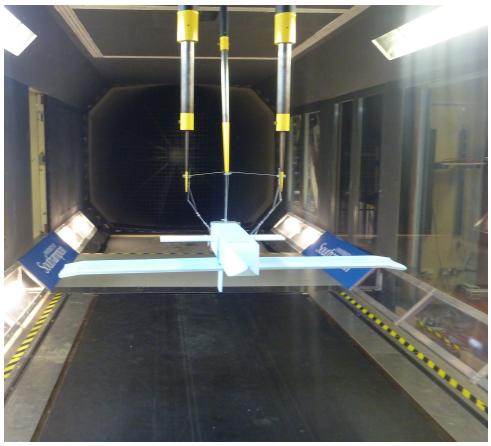

Figure 5.60: Wind Tunnel boundaries

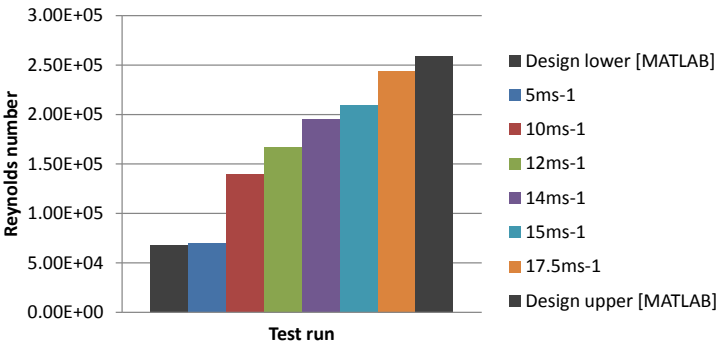

Figure 5.61: Comparison of estimated to wind tunnel Reynolds number

5.13.4 Dynamic Similarity

To establish the true aerodynamic properties its was important to ensure dynamic similarity between the expected free flight conditions and the wind tunnel tests. The dynamic similarity was maintained by ensuring the range of wind tunnel Reynolds numbers was with in the expected upper and lower limits predicted by the MATLAB flight prediction code. In order to calculate the wind tunnel Reynolds number it was assumed the dynamic viscosity remained constant over the testing at $\mu = 1.82e^{-5} Nsm^{-2}$ [28].

5.13.5 Data Processing

As previously mentioned to remove the interference effects the raw wind tunnel data had the tare results subtracted. The forces measured by the overhead balance were relative to the balance system axes and for comparison with XFLR5 and later CFD were converted to the aircraft axes. Although at small AOA the difference between the different co-ordinate systems was negligible at the maximum pitch angle of 20° the small angle approximation became inaccurate.

$$L_{aircraft} = L_{Wt}\cos(\alpha) - D_{Wt}\sin(\alpha) \tag{5.56}$$

$$D_{aircraft} = D_{Wt}\cos(\alpha) + L_{Wt}\sin(\alpha) \tag{5.57}$$

Lift
From the wind tunnel data it was found that the glider was able to produce an average of approximately 21.3N of lift over the two testing days, fig. 5.62. The wing had been designed such that the glider should be able to sustain level flight at this velocity, the required lift to achieve this condition is marked as the design target on the graph below.

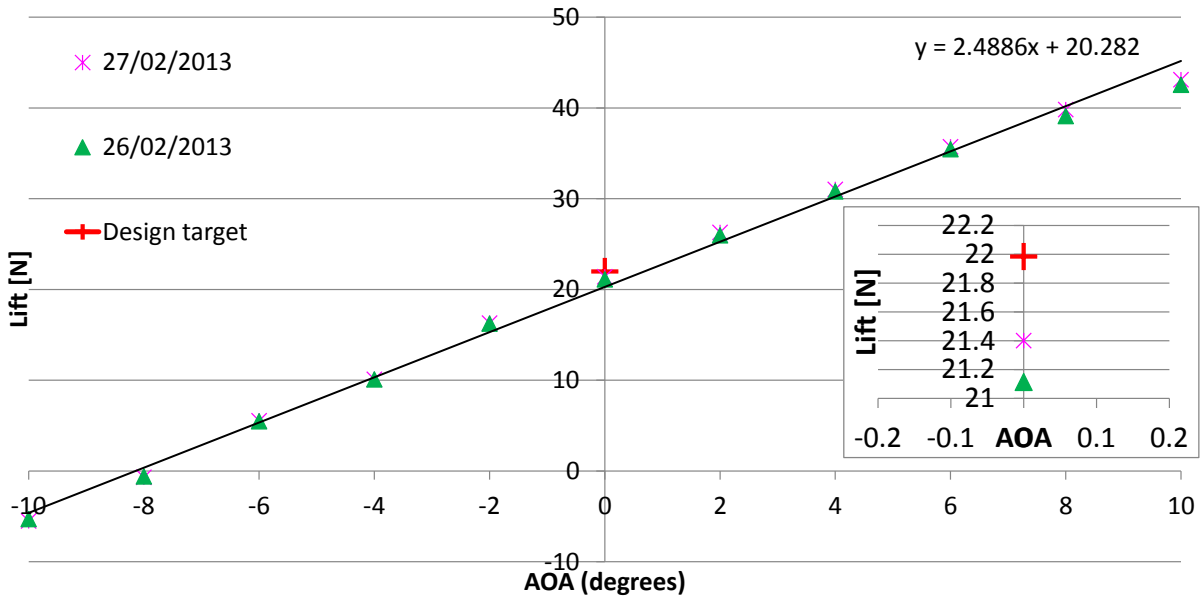

Figure 5.62: Comparison of design and wind tunnel lift.

It was found that the glider performed as expected and produced a maximum difference in lift to the design condition of $0.85N$. Taking into account the fact that the wing sizing was completed using the net wing area, as at the time the fuselage dimensions had not been finalised, a margin of error was expected. Unfortunately no accurate conclusions can be drawn about the lift produced by the fuselage except,that it is roughly equal to the loss in lift from the fuselage-wing boundary layer interactions caused by separating the wing into two sections.

5.13.6 Coefficient of Lift

The coefficient of lift from the wind tunnel testing, about the aircraft axes, was compared to an approximate glider coefficient of lift from XFLR5 3D VLM data and a theoretical prediction using 2D XLFR5 data. The purpose of which was to establish the unknown accuracy of 3D modelling in XFLR5 and confirm no detrimental impact on the wing performance from the thickened trailing edge modification.

The theoretical approach provided a bench line model and used 2D XFLR5 data, from the widely accepted XFOIL code, combined with transforms to 3D.[104],[16]. The transform was applied to both the wing and horizontal tail and then combined, using the equations below, to estimate the overall aircraft coefficient of lift.
The transform used to convert 2D coefficients to 3D was;

$$C_{L_{3D\alpha}} = \frac{C_{L_{2D\alpha}}}{1 + \frac{C_{L_{2D\alpha}}}{\pi A_R}} \tag{5.58}$$

Where $C_{L_{2D\alpha}}$ represents the XFLR5 2D lift curve slope for the relevant section. As the wing has a 3 ° installation angle the XFLR5 lift curve slope was shifted accordingly.

$$C_{Lw} = C_{Lw_o} + C_{Lw_\alpha}(\alpha + \alpha_{0w}) \tag{5.59}$$

The horizontal tail XFLR5 lift coefficient was converted from α_t to α taking into account the induced downwash over the horizontal tail generated by the wing.

$$C_{Lt} = C_{Lt_o} + C_{Lt_\alpha}(\alpha + \alpha_{0t})(1 - \frac{d\epsilon}{d\alpha}) \tag{5.60}$$

XFLR 5 3D VLM	$C_L = 0.0801(\alpha) + 0.7788$
XFLR 5 2D + 3D transform	$C_L = 0.0982(\alpha) + 0.8168$
Wind Tunnel	$C_L = 0.0747(\alpha) + 0.6859$

Where the induced downwash with respect to angle of attack can be approximated by;

$$\frac{\partial \epsilon}{\partial \alpha} \approx \frac{C_{Lw_\alpha}}{\Pi e A_R} \tag{5.61}$$

For a rectangular cross section the Oswald span efficiency e, taken from [104], can be determined from;

$$e = 1.78(1 - 0.045A_R^{0.68}) - 0.64 \tag{5.62}$$

Using a derivation shown previously in section 5.11 a more accurate overall lift equation can be written as;

$$C_L = C_{Lw}\frac{S_w}{S_w + S_t} + C_{Lt}\frac{S_t}{S_w + S_t} \tag{5.63}$$

Substituting in the above equations for C_{Lw} & C_{Lt} yields;

$$C_L = (C_{Lw_o} + C_{Lw_\alpha}(\alpha + 3))\frac{S_w}{S_w + S_t} + (C_{Lt_\alpha}\alpha(1 - \frac{d\epsilon}{d\alpha}))\frac{S_t}{S_w + S_t} \tag{5.64}$$

Where C_{Lt_o} and α_{0t} are both zero due to the horizontal tail being a symmetric NACA 0012 section with no installation angle.
The comparison between the XLFR5 VLM method and the XFLR5 2D data with a 3D transform were found to be reasonably close.

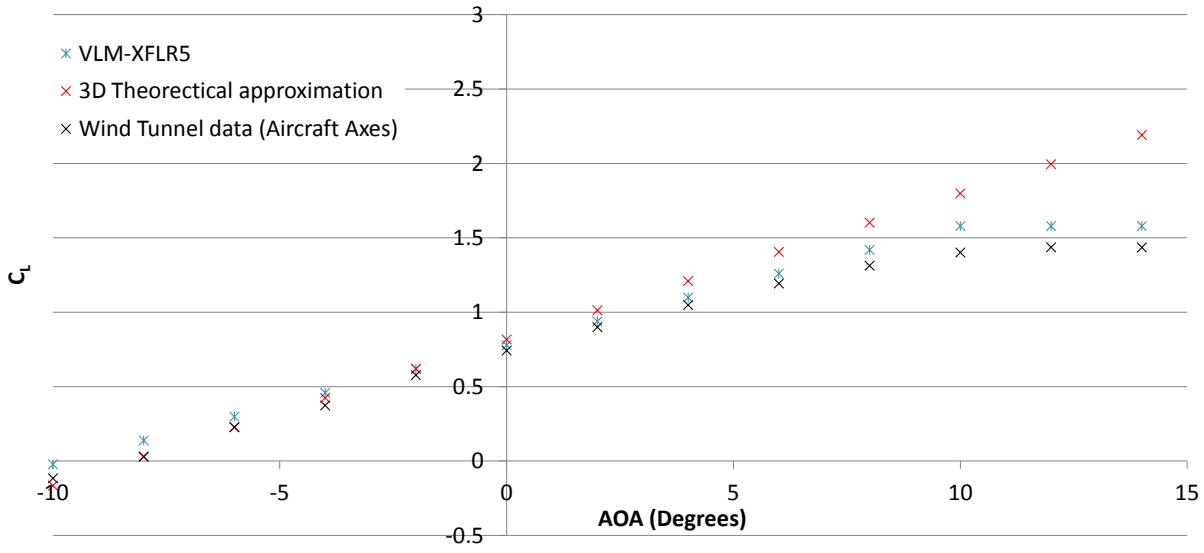

Figure 5.63: Complete glider lift coefficient comparison

It appears from fig. 5.63 that the XFLR5 3D vortice lattice method (VLM) provides an accurate representation to wind tunnel data. However, this is slightly misleading without the previous assumptions being taken into account. The XFLR5 models were run as a single section wing and horizontal tail where the wing section was modelled using net area lifting area and not gross area. Therefore, the analysis for overall lift coefficient assumes no lifting contribution from the fuselage. The XFLR5 VLM and wind tunnel data both show reasonably close correlation to the XFLR5 2D and Raymer transform approach up until the onset of stall at approximately 10°. Above the stall angle the 2D data and theoretical transform approach, as expected, fails to model the separation of the boundary layer. The marginally larger C_{L_α} from the theoretical approach is most likely due to assumptions in Oswald span efficiency which are not

specific for a small UAV.

From fig. 5.63 it is inconclusive for finding the exact magnitude of error from XFLR5 VLM or the contribution of lift from the fuselage alone. However, within the realms of this project it is concluded that XFLR5 provides reasonable data and the custom aerofoil section has shown to be effective both in XFLR5 and during wind tunnel testing. Hence it is concluded that the increased trailing edge thickness has no significant detrimental impact on the aerofoil performance. Further wind tunnel testing could be completed with only the aerofoil wing section to provide further analysis on the accuracy of XFLR5 or with only the fuselage section to establish its aerodynamic properties and enable further optimisation.

5.13.7 Drag

The wind tunnel drag data was compared with a theoretical drag build up derived previously. Due to the difficultly of accurately calculating the coefficient of drag by hand this was only completed for one AOA.

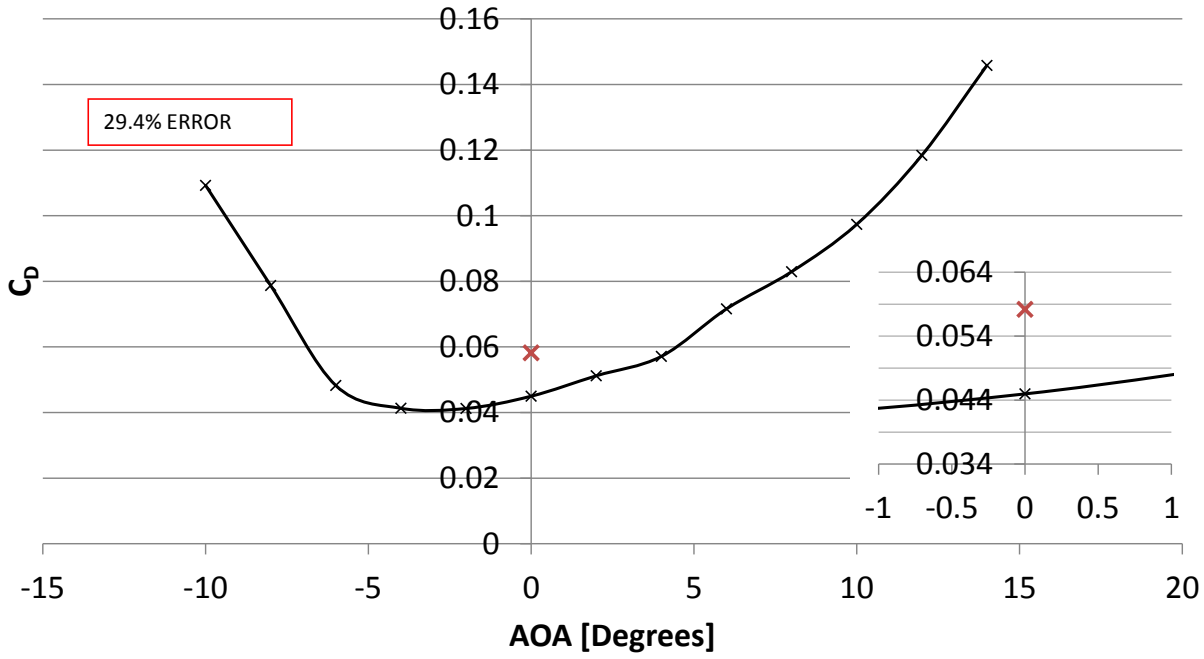

Figure 5.64: Theoretical drag build up vs. Wind Tunnel

Unfortunately the data from the sea tare results at $10ms^{-1}$ suggested the marginally larger struts of similar design to the Land set-up produced close to zero drag. It was found that both struts produced a similar drag at $5ms^{-1}$ yet differed significantly at $10ms^{-1}$ with the sea tare drag decreasing. It is believed this error resulted from the adjustment of the struts after the $5ms^{-1}$ run to re secure the wooden spacers. It was ensured the balance strut was recalibrated however, is believed the error stemmed from a user input into the program during recalibration. Unfortunately this error was only identified after the group had finished their allocated wind tunnel slot.

The wind tunnel was then booked to remeasure the sea $10ms^{-1}$ tare however the wind tunnel set up had changed and required significant time to be reset to the original set-up. Due to the last minute booking, high demand for the wind tunnel and short time slot there wasn't sufficient time for it to be completed. Instead the Land tare data was used as the next best alternative, though doing so added further error into the results it is believed, due to the similar nature of the struts, the error is likely to be relatively small.

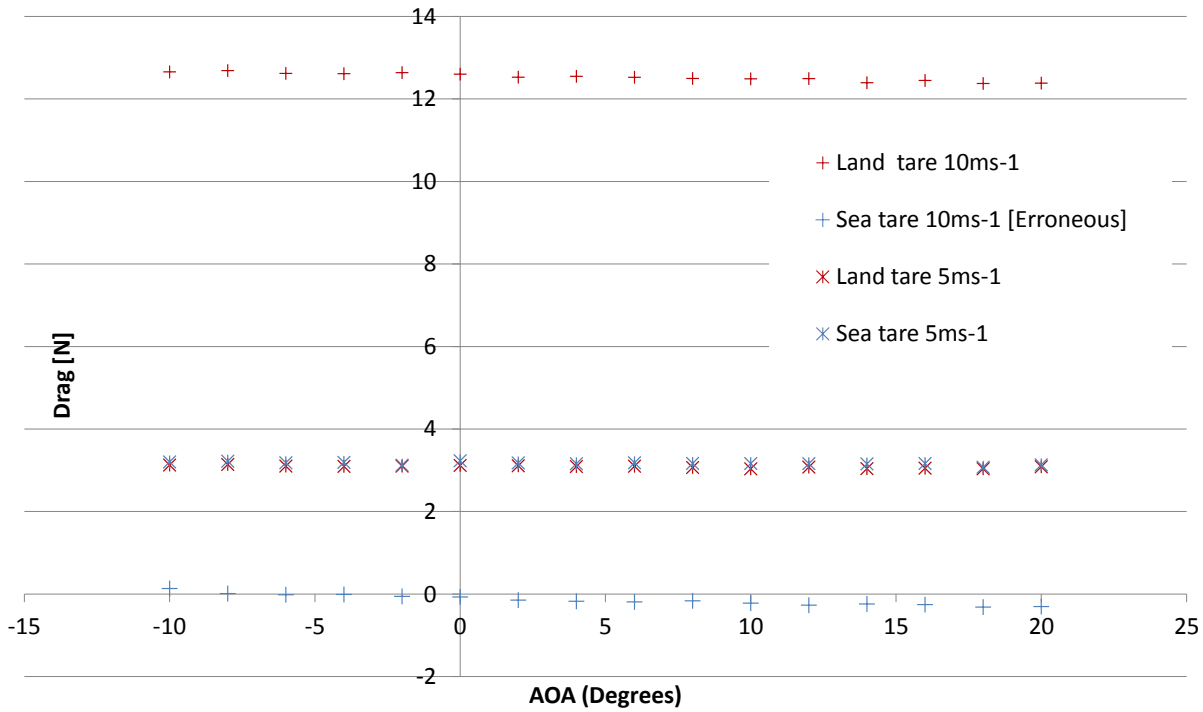

Figure 5.65: Tare data comparison

Given the approximations and limited theoretical data it is difficult to draw conclusions between the theoretical and experimental results. To improve the analysis a complete glider CFD using FLUENT was completed, see section 5.15.

5.13.8 Aerodynamic Efficiency

From wind tunnel testing the maximum aerodynamic efficiency (L/D) was found to be 12.9 at an AOA of 4 degrees. To achieve the initial requirement of a deployment radius of $20km$, the glider would need to maintain a glide angle of approximately negative four degrees, where it will be able to provide an aerodynamic efficiency of two.

Figure 5.66 determines that as long as the autopilot system is able to maintain a glide angle greater than negative six, the glider will produce a net positive lift and thus be able to maintain its forward flight.

Considering, as mentioned above, the use of "Land" tare data for the "Sea" struts, the accuracy of this aerodynamic efficiency is reasonably close to what value was expected, however, the reliability of the exact data is questionable; thus will be confirmed by further testing through CFD studies and flight testing, 5.15.

5.13.9 Longitudinal Stability

Prior to flight testing it was important to ensure the theoretical longitudinal stability calculations, shown previously, matched the glider's physical response. The gliders pitching moment was measured over a range of AOA, velocities and payload configurations. The pitching moment measured during the wind tunnel testing was about the wind tunnel reference datum which is fixed from the balance setup and located at centre height of the tunnel and equidistant between the front and rear struts. From M_{datum}, C_m was calculated using;

$$C_m = \frac{M_{datum}}{qS\bar{c}} \tag{5.65}$$

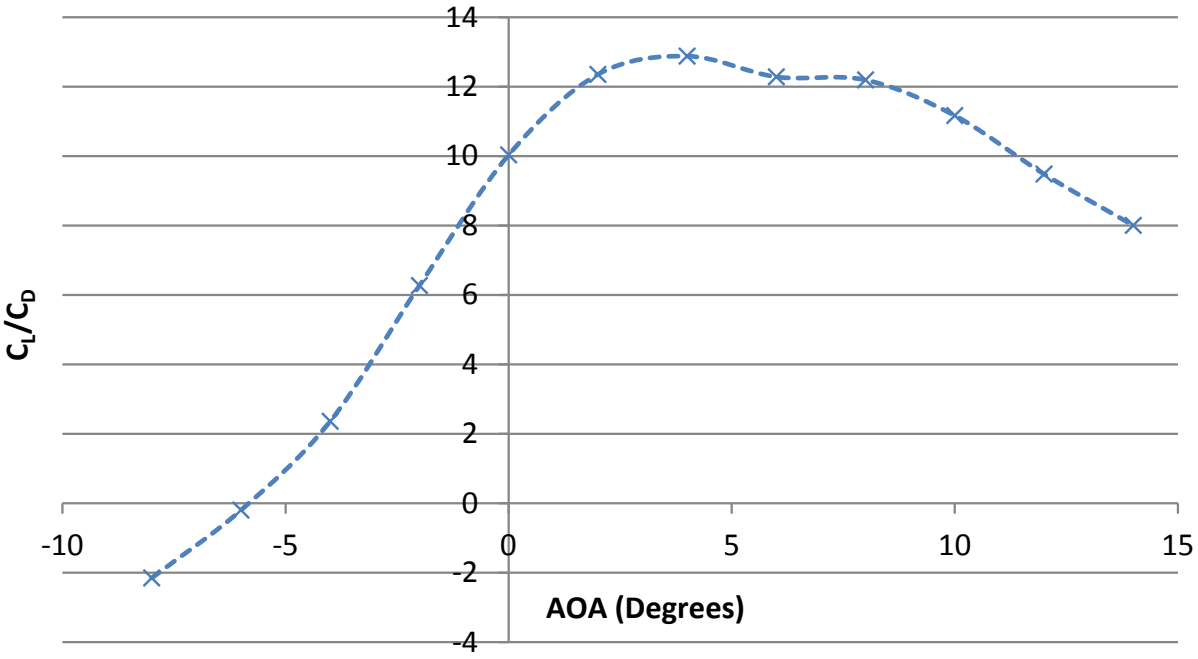

Figure 5.66: Glider aerodynamic efficiency

In order for the glider to exhibit longitudinal stability the pitching moment derivative with respect to angle of attack needs to be negative. When this criteria is satisfied an increase in AOA, either by pilot input or gust, will result in a nose down restoring pitching moment. The magnitude of pitching moment cannot be too large otherwise the glider will not, under the right flight conditions, be able to perform trimmed level glider prior to payload release.

$$\frac{\partial C_m}{\partial \alpha} = C_{m\alpha} < 0 \tag{5.66}$$

From fig. 5.67 the glider is shown to be stable over the range of AOA tested. Due to the difference

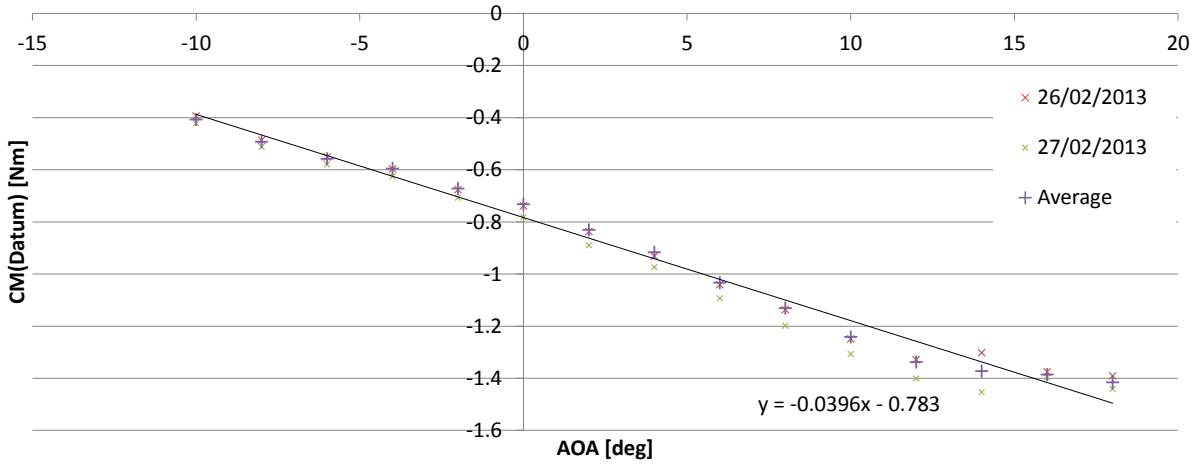

Figure 5.67: Pitching moment vs. AOA

in position of the wind tunnel reference datum and aircraft centre of gravity no comparison of static margin can be drawn between the wind tunnel and the theoretical approximation. Considering that both methods show that the glider produces nose down pitching moment to positive AOA proves the glider to be longitudinally stable.

5.13.10 Lateral Stability

Yawing Moment due to Side-Slip

To determine the glider response to side-slip the overhead balance was displaced by an angle ψ anticlockwise from above with the natural yawing moment response, N, measured. If laterally stable the glider would produce a negative yawing moment for a positive yawing angle such that in real flight conditions the glider will yaw into line with the incoming velocity vector. ψ is the known as the yaw angle and is the angle from the inflow vector to the aircraft centre line. β is the side-slip angle and measured from the glider centre-line to the inflow velocity such that;

$$\psi = -\beta$$

For the glider to exhibit lateral stability then the following must be true.

$$\frac{\partial N}{\partial \beta} > 0 \tag{5.67}$$

The yawing moment can then be in a non dimensional form by;

$$C_n = \frac{N}{qSb} \tag{5.68}$$

Where: N= yawing moment, S=Gross wing area, b=Gross wing span and q is dynamic pressure.

Hence applying the above to the wind tunnel data it can be seen in fig. 5.68 that the glider exhibits lateral stability with respect to side-slip at $10ms^{-1}$.

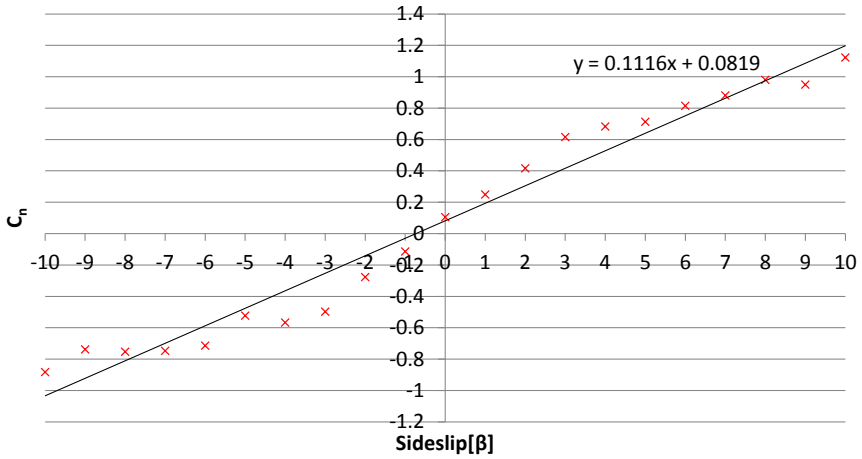

Figure 5.68: Yaw moment v.s.side-slip

Rolling Moment due to Side-Slip

The glider lateral response to side-slip was investigated by measuring the rolling response thus establishing if the gliders 2° effective dihedral, from the wing tips, was sufficient to provide a suitable restoring rolling moment from side-slip [24]. The rolling moment coefficient can be given by,

$$C_l = \frac{L}{qsb} \tag{5.69}$$

L is the rolling moment about X axis, running along the aircraft centre line.
The moment was taken about the reference datum point which is fixed equidistant between the front and rear struts at the centre height of the wind tunnel. The rolling moment due to side-slip definition for

stability was for a negative change in roll moment with respect to side-slip angle.

$$\frac{\partial C_l}{\partial \beta} = C_{l\beta} < 0 \tag{5.70}$$

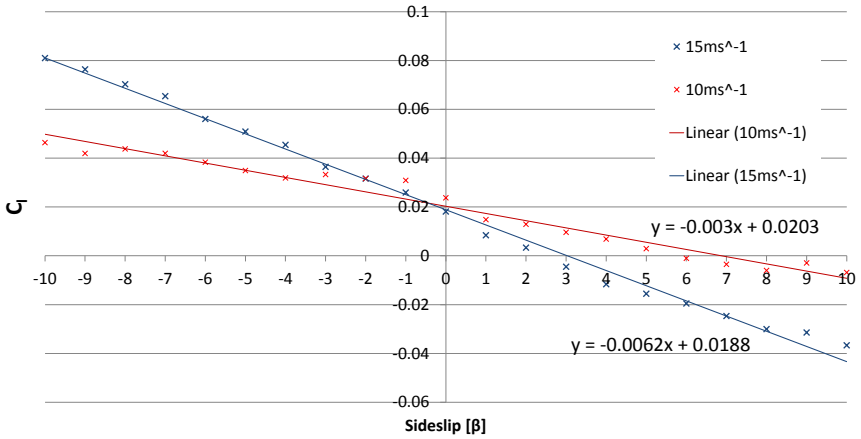

Figure 5.69: Rolling moment vs. sideslip

From fig. 5.69 the glider was found to be stable and showed a small restoring moment due to side-slip at $10ms^{-1}$. As the aircraft velocity was raised the $C_l vs. \beta$ gradient increased as the effective dihedral increased due to the wing deflection.

From an effective static dihedral of 2 deg at $10ms^{-1}$ the dihedral had increased to 3.3 deg at 0 deg AOA and to 5 deg at $15ms^{-1}$ for 0 deg AOA [24].

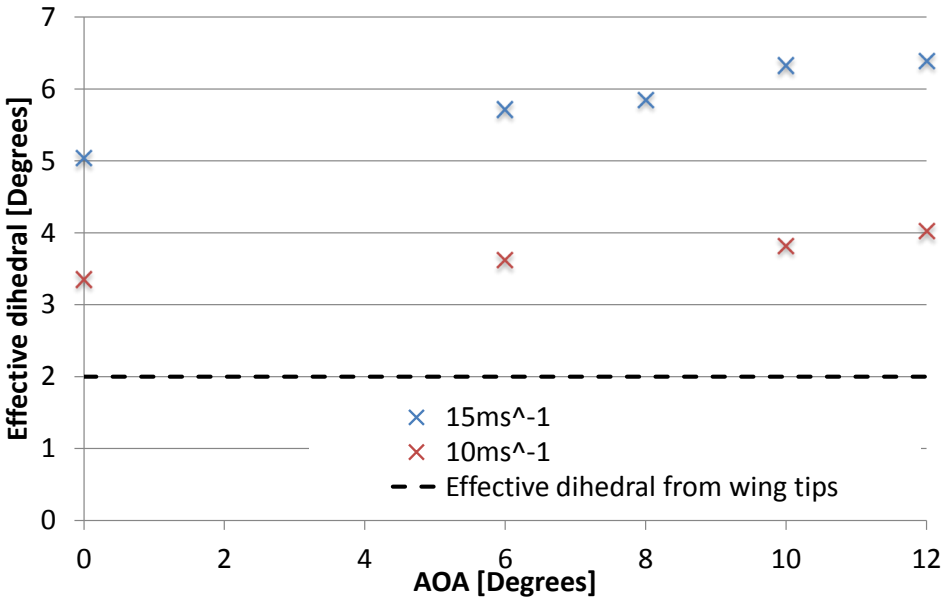

Figure 5.70: Effective wing dihedral from deflection vs. AOA

This was within the historical trends set out in [104] for an un-swept high wing configuration and deemed suitable. Calculating if this is actually sufficient for the current glider application will be established during the flight testing.

5.13.11 Control Surfaces

The control surface sizing had been completed previously using trends in historical data. To ensure this was of suitable magnitude for the current application control surface authority tests were undertaken.

Elevator Effectiveness

The elevator deflection was set by the remote control to only allow a maximum deflection of approximately 30 degrees. $C_{m\delta e}$

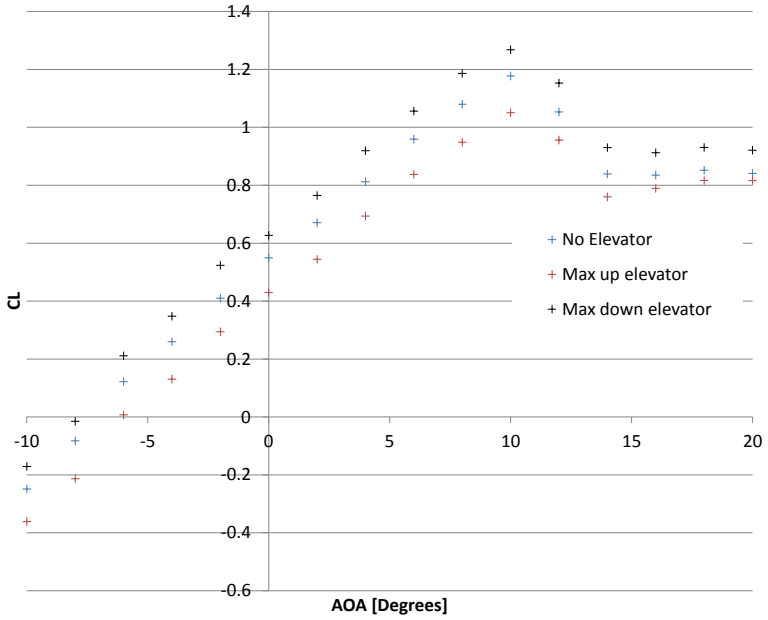

Figure 5.71: Elevator influence on C_L

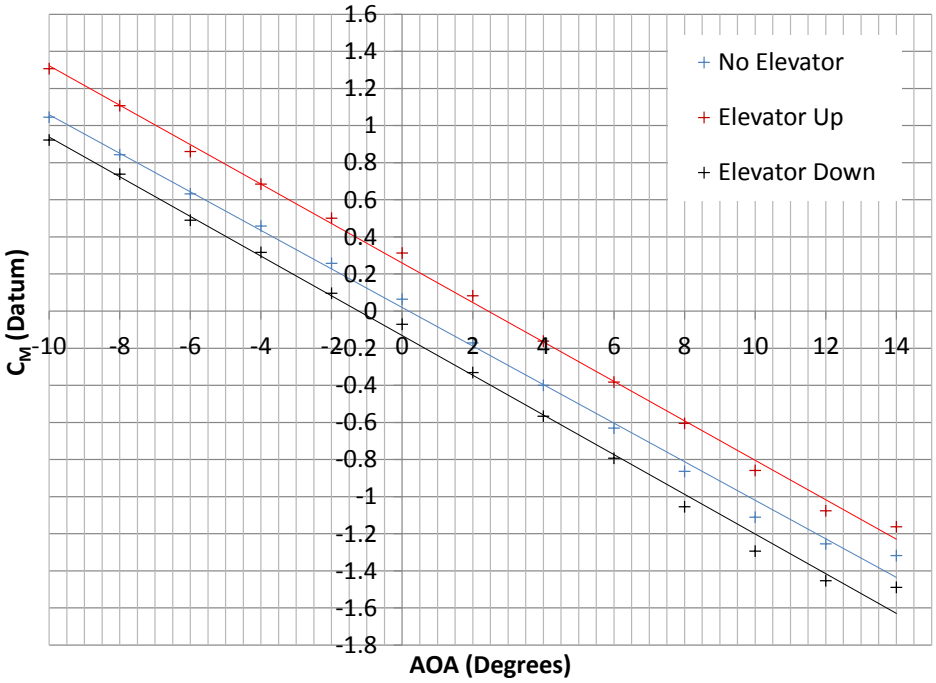

Figure 5.72: C_M vs. AOA [Elevator]

It was seen in fig. 5.69 that theoretically the elevators had sufficient pitch authority to enable the glider to pitch up at two degrees. From the $\frac{L}{D}$ plot it was required that the glider should maintain an AOA larger than -8 deg for optimum efficiency and therefore believed the elevators were suitably sized. This would be confirmed during flight testing. The servos were installed so the control rods went over the

top aerofoil surface of the horizontal tail although this was detrimental to the aerodynamic performance it allowed greater elevator adjustment It can be seen from fig. 5.72 that this control set up led to the pitching moment from an positive elevator (input) being larger than that of the negative elevator input. This is more suitable than the opposite scenario, of mounting the control rods below the horizontal tail, for the given glider application as it enabled greater pitch up authority.

Rudder Effectiveness

It was found that the rudder was able to produce a yawing moment that would be capable of restoring the glider from a side-slip of -17 deg to starboard and -15 deg to port, using extrapolated. Further analysis on the control surface effectiveness was to be completed during flight testing.

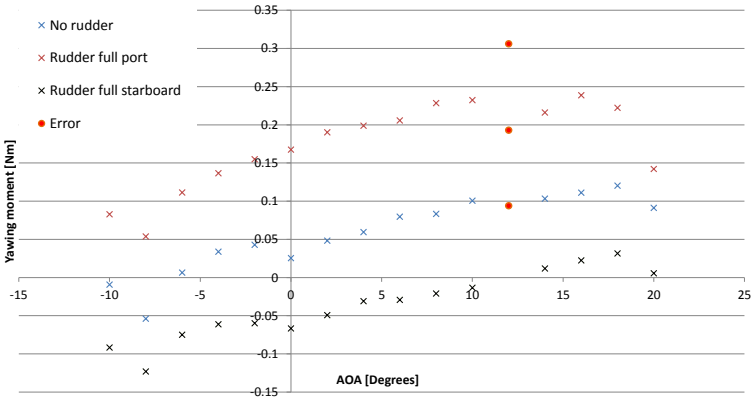

Figure 5.73: Rudder influence on C_n

Additionally visual tests were completed to ensure the structural strength and design of the horizontal and vertical tail sections were adequate as well as the range of deflection sufficient. It was found that the horizontal tail spars were marginally undersized as visible deflection resulted from the elevator torque on the horizontal tail, under full elevator deflection. Significant oscillations were also present close to the stall condition and therefore the horizontal tail spars diameter was increased from four to six millimetres. For the vertical tail section it was concluded an additional hinge was required in the middle of the rudder section to prevent excessive twisting resulting from the servo torque being applied from one end of the control surface.

Finally the control surface tests confirmed the previously selected servos were of sufficient torque to fully deflect the control surface under load over a wide range of velocities and AOA.

5.13.12 Repeatability

In order to achieve accurate results it is important that the tests completed show close long and short term reliability. The short term repeatability was addressed by the wind tunnel data acquisition system taking numerous readings over a 10 second interval and returning the average. In order to ensure longer term repeatability the temperature and atmospheric pressure in the tunnel during the testing duration were recorded. This enabled the variation in density to be calculated assuming the air to act as a perfect gas. To monitor the long term repeatability a standard test run was devised that would be completed after significant breaks or adjustments. The base line test was a 10ms^{-1} standard payload run with no control inputs and completed twice on both days of testing. It is shown in fig. 5.75 that in general the runs show close correlation and the largest difference was the early morning run on the first day of testing. It is believed this was due to a particularly cold morning and once the wind tunnel temperature had warmed up later on a close correlation was seen between the remaining runs.

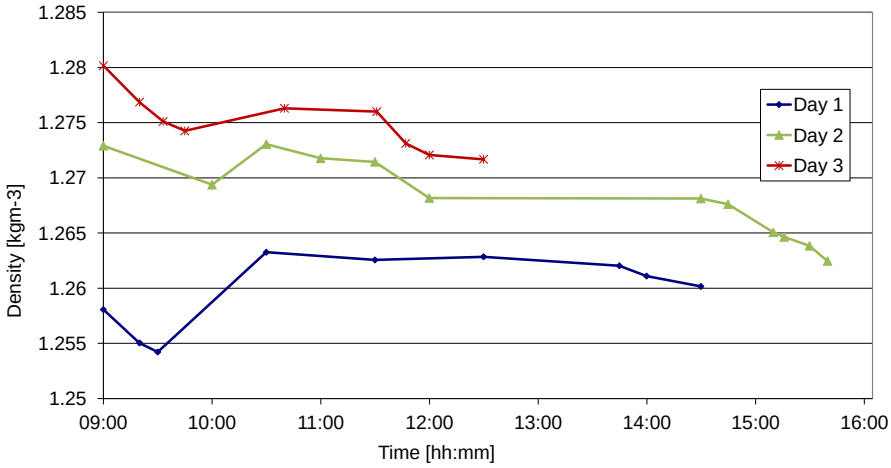

Figure 5.74: Wind Tunnel Testing: Density variation

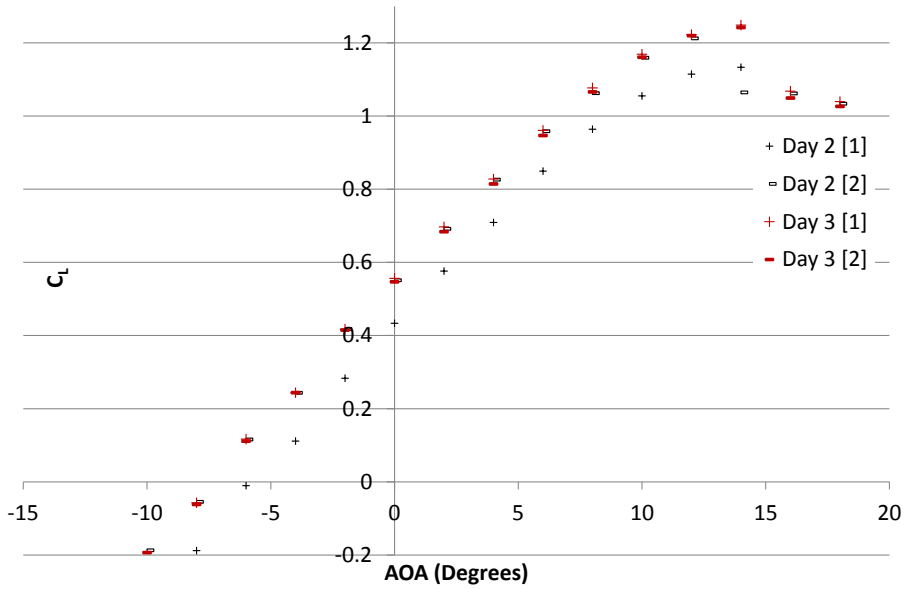

Figure 5.75: Wind Tunnel Testing: C_L repeatability

5.14 Nichrome Wire Balloon Release Mechanism - Raja Yuhanis

The general configuration of a nichrome wire cutter consists of a nichrome wire wrapped around a polymer, which has a low melting point. The nichrome wire is connected to a power source which delivers the required current to heat up the wire; this thermal heating of the nichrome wire will melt it and detach the payload. Therefore, it is suitable to be used as a release mechanism in a deployment system. Nichrome wire is used as it has a high resistivity and good resistance to oxidation at high temperatures. A drawback of using nichrome wire is that it cannot be soldered using a common electrical solder, therefore crocodile clips can be used for a connection to be made between the wire and the power source.

5.14.1 Concept

It was intended to use a nichrome wire cutting mechanism for the balloon cut-down instead of a mechanical release mechanism which was used in the previous year's project (GDP16 2012). This was designed with the aim to produce a small, simple, inexpensive, lightweight and easy to use mechanism. The maximum

voltage supply for this application was $7.2V$ and the maximum current supply was 2 A.

$$I = \frac{V}{R} \tag{5.71}$$

Using equation 5.71, it can be observed that by increasing the resistance of the wire, the voltage required to retain the same amount of current increases. It can be concluded that the longer the wire, the more resistance it has, therefore a larger voltage is required to supply desired current. In this design, the maximum voltage and maximum current was specified, hence the diameter required to break the polymer cable needs to be determined. The wire diameter determined the American Wire Gauge (AWG) value. The melting point of the nylon cable is 216 °C [31], this then requires the nichrome wire to be capable of reaching this temperature.

Power per unit length:

$$\frac{P}{l} = \frac{VI}{l} = \frac{V^2}{Rl} \tag{5.72}$$

$$\text{Resistance per length} = \frac{l\rho}{A} \tag{5.73}$$

Substituting resistance per unit length to the power equation:

$$\frac{P}{l} = \frac{AV^2}{\rho l^2} \tag{5.74}$$

Rearranging the equation to find area [115]

$$A = \frac{Pl\rho}{V^2} \tag{5.75}$$

$$\pi R^2 = \frac{Pl\rho}{V^2} \tag{5.76}$$

$$\rho \approx 1.5 \text{ x } 10^{-6} \tag{5.77}$$

The maximum power is 14.4 watts, and the length designed for the hot wire cut-down is approximately $0.12m$. From equation 5.76, the diameter of the wire was calculated to be $0.25mm$; this lead to an American Wire Gauge (AWG) of 30.

A nichrome wire calculator [92] was utilised to ensure the optimal diameter nichrome wire was used in the production of the balloon cut down release mechanism.

5.14.2 Design

After determining the optimal wire diameter, a first design for the mechanism was developed. The nichrome wire was integrated into the design in a manner where it was fed into an engraved path on the lower mechanism board, see Figure 5.76. The two boards then sandwiched the nichrome wire and the nylon cable together. The two boards were made from $3mm$ thick plywood, where the grooves was made to be $1mm$ deep on each board, ensuring that the nylon cable is not too tightly clamped. Another possible way to manufacture the mechanism boards is by 3D printing them with the designed groove paths integrated, this will produce a higher quality board whilst maintaining the intended purpose. However, this option was not utilised due to the strict time constraints imposed in producing a possible balloon release mechanism in time for testing.

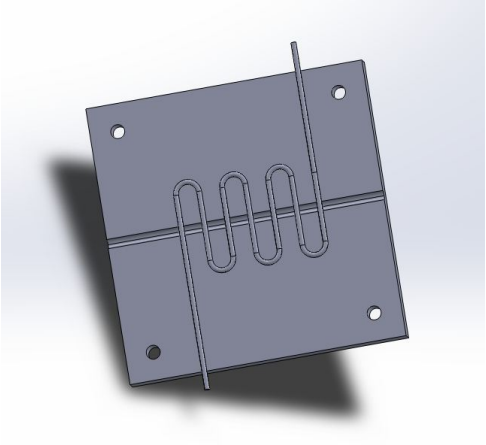

Figure 5.76: Nichrome wire cutdown design

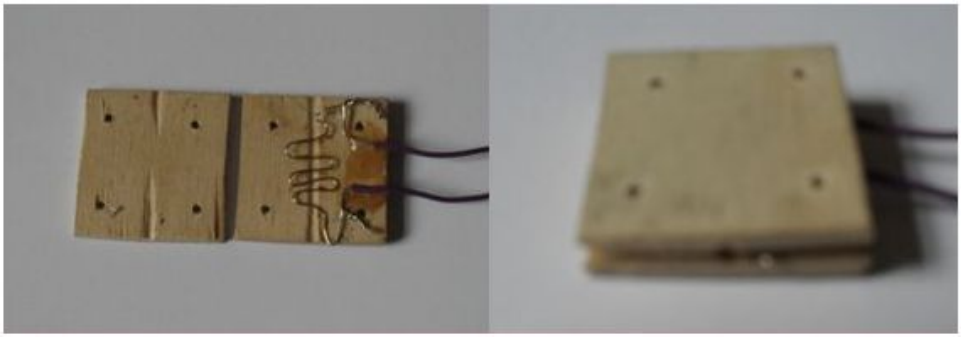

Figure 5.77: Nichrome wire cutdown model

Testing

Testing was completed to obtain the time taken for the nichrome wire to melt the nylon cable. A length of nylon cable was sandwiched between the boards and at each end of the nylon cable, $2N$ weights were attached. Four AA batteries were used as the power source, which was attached to the $0.12m$ nichrome wire via crocodile clips. Time taken for the nichrome wire to melt the nylon cable ranged from 10-15 seconds; this is an acceptable melting time for the purposes of a balloon release.

5.15 Glider Computational Fluid Dynamics - Nathan Lao

Further to the CFD study on the wing (section 5.12), a CFD study of the glider in the R J Mitchell wind tunnel was performed to allow comparison with the wind tunnel data that was obtained. The wind tunnel results provide validation of the CFD results and thus allow further glider optimisations with CFD testing, as the project has limited wind tunnel testing time.

Further to simulating the glider in the R J Mitchell wind tunnel, a CFD study of the glider in a free flight domain was carried out to assess the performance and flow structure around the aircraft. This will also allow comparison of the glider in free flight and the glider in the wind tunnel.

5.15.1 Computing Facilities

The glider studies will use FLUENT 14.0 to perform the numerical simulations. The geometry and meshing will be carried out in ANSYS 14.0 Workbench, using ANSYS DesignModeler and ANSYS Mesher, respectively. This will allow for easy organisation and clear steps in simulating the configurations. ANSYS CFD-Post will be utilised for post-processing of the flow solution. This is the same software packages used during the wing CFD study, thus building in consistency and maturity.

High Performance Computing (HPC)

Due to the nature of the problems being in 3D and having a relatively complex geometry, they required HPC facilities to accommodate the large amount of computing power during setup as well as running the simulations. The University of Southampton iSolutions Linux teaching cluster, Lyceum 2, was utilised as it provided substantially greater computing power and memory than the Windows workstations available, which would have been impractical. Using these facilities, a batch script was written to allow several simulations to be submitted to Lyceum 2 and run autonomously.

5.15.2 Wind Tunnel Glider Computational Fluid Dynamics

Wind Tunnel Domain

For the wind tunnel study, the wind tunnel dimensions were replicated into the CFD domain. This was achieved by measuring the dimensions of the wind tunnel before the wind tunnel tests commenced. An accurate SolidWorks model of the wind tunnel was available for verification also, and the measured dimensions were checked against the SolidWorks model.

The width, height and length of the R J Mitchell wind tunnel were $3.5m$, $2.4m$ and $10.5m$, respectively. However, to reduce the number of elements produced during meshing and the running time of the simulations, half of the wind tunnel domain was modelled along with half of the glider, where the cut was made half way along the z-axis. Therefore the width, height and length of the wind tunnel domain were $1.75m$, $2.4m$ and $10.5m$, respectively. Figure 5.78 shows the modelled half glider inside the half wind tunnel domain. The location of the glider in relation to the wind tunnel is also accurate.

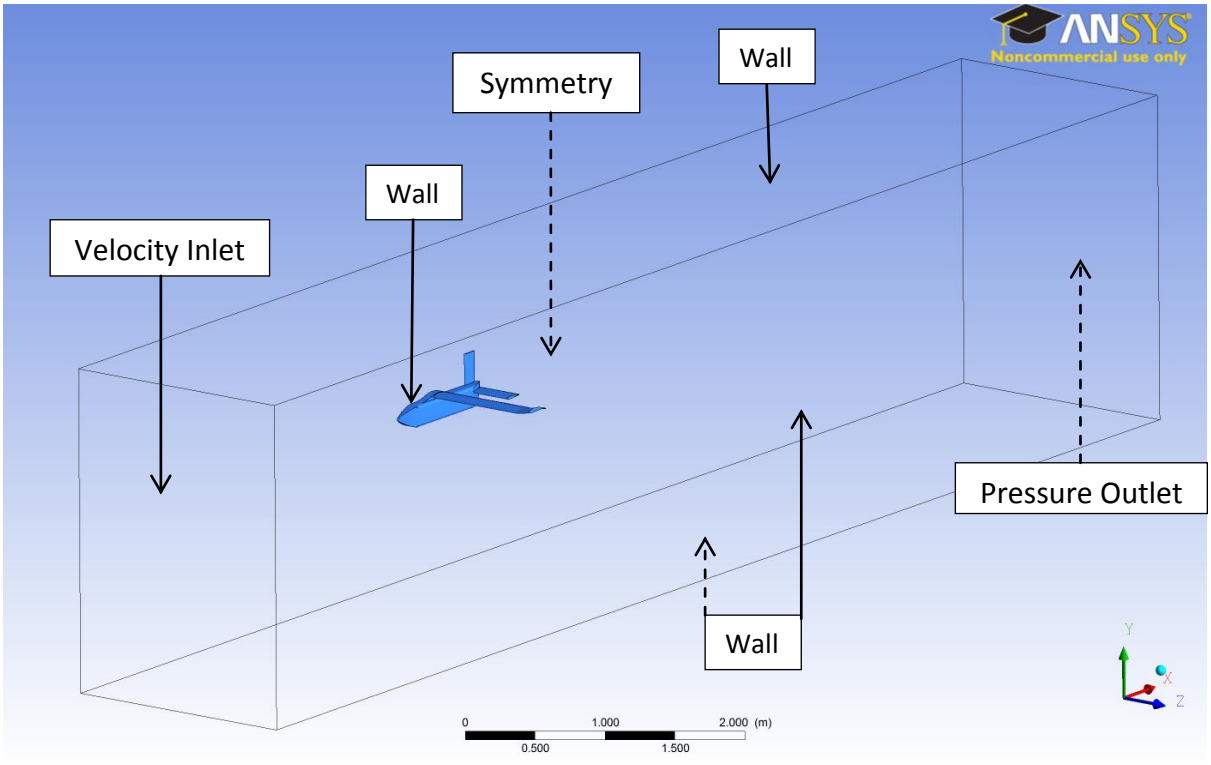

Figure 5.78: R J Mitchell wind tunnel half domain with half glider

Tail Wall Spacing

To accurately capture the flow behaviour in the boundary layer of the tail, the correct y^+ value must be obtained during the meshing of the glider tail. As mentioned in section 5.12.4, large wall spacing will result in inaccuracies calculating the lift and drag forces on the glider, on the other hand, having too small wall spacing will result in an unnecessarily fine mesh, thus increasing simulation time.

Using the same approach as the wing wall spacing, a wall function approach, the y^+ value required is 30.

With known quantities of the freestream velocity ($10ms^{-1}$), the freestream density ($1.225kgm^{-3}$), the dynamic viscosity ($1.79 \times 10^{-5}Pa.s$) and the tail reference length ($0.15m$); the desired wing y^+ value of 30, yielded the boundary layer first layer thickness to be $8.766 \times 10^{-4}m$.

Meshing

Using ANSYS Mesher, unstructured meshes were created for all glider CFD simulations. Due to the increased complexity of the geometry of the glider, meshing can be more demanding; therefore to reduce meshing difficulties, the geometry had to be modified by solidifying glider components, for example, the wing spars had to be removed and the spar holes filled in. However, these modifications did not affect the external glider profile which is crucial in accurately simulating the aerodynamic forces seen by the glider.

Mesh Sensitivity

A mesh sensitivity study was performed for the wind tunnel CFD study to allow for an accurate solution without unnecessary computational resources. The y^+ value on both the wing and the tail were maintained at a value of 30 and element sizings were varied. The meshes ranged from one million elements to 16 million elements; the same mesh quality standards were upheld as the mesh sensitivity of the wing CFD 5.12.6.

Observing the graphs produced from the mesh sensitivity study, Figure 5.79 and Figure 5.80, the mesh which provides adequate lift coefficient accuracy can be taken as the 8 million element mesh, however, as the drag coefficient of the glider is also a value of interest, Figure 5.80 shows that the 11 million element mesh would provide a more accurate solution, similar to a 15 million element mesh. Therefore the chosen wind tunnel domain mesh had $11,346,558$ elements.

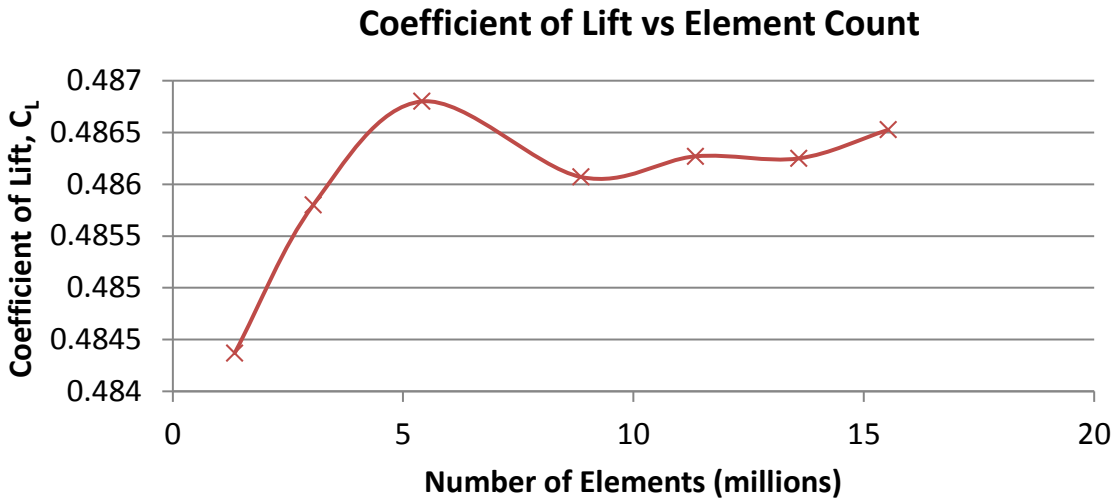

Figure 5.79: C_L vs Element Count, Wind tunnel domain mesh sensitivity

Boundary Conditions

As this study is a simulation of the glider in the R J Mitchell wind tunnel, it has been modelled with the dimensions and characteristics of the wind tunnel. Therefore, the front of the domain has been set as a velocity inlet boundary, the rear of the domain has been set as a pressure outlet boundary and the rest of the domain has been set as a wall with the exception of the plane adjacent to the glider, which has been set as a symmetry plane due to the modelling of half of the domain and glider. Figure 5.78 shows the boundary conditions used for the wind tunnel simulations.

Simulation Setup

The simulation setup for the glider CFD studies were the same as the setup for the wing CFD study,

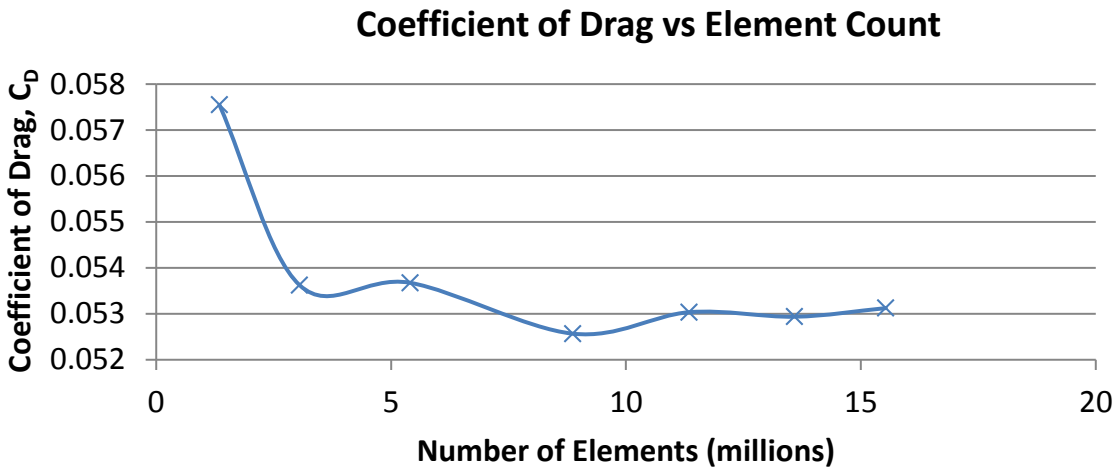

Figure 5.80: C_D vs Element Count, Wind tunnel domain mesh sensitivity

which has been explained in section 5.12.7.

However, the reference values used for the glider CFD studies required modification as they are crucial in obtaining the correct aerodynamic forces on the glider. The glider reference area was taken as its planform area of $0.28745m^2$ and the reference length was the glider length $0.98m$; the rest of the reference values were taken as standard sea level measurements, for example, the reference density was $1.225kgm^{-3}$.

Results

Having run simulations of the glider in the wind tunnel domain for a range of AOA, from -8 degrees to 10 degrees; a comparison of the results can be made between the experimental wind tunnel data and the results from the wind tunnel domain CFD.

Figure 5.81 shows the comparison of the lift coefficient versus AOA curve between the CFD results and the experimental results. There is clearly a strong correlation between the two curves, where it being an approximately 7% difference at 0 degrees AOA between the two lift coefficients. The difference of lift from the CFD results may be caused by the mesh of the glider, which may be too coarse to accurately resolve the exact lifting force on the glider. However, for the purposes of this project and the limited resources available, the results are more than adequate in determining that the CFD model can accurately simulate the lift coefficient on the glider in the R J Mitchell wind tunnel with an acceptable error of approximately 7%.

The comparison of drag coefficients has also been evaluated between CFD and experimental wind tunnel data. It should be mentioned that the drag coefficients calculated from the experimental wind tunnel data were calculated using the "Land" tare results at the same conditions instead of the actual sea glider tare results, this is because erroneous data was obtained from the wind tunnel run as explained in section 5.13.7. Therefore, the data from the powered land system glider mounting struts are the most sensible values obtainable, as the booking of the wind tunnel to re-test the sea tare was not possible before the deadline of the project. The powered land system glider mounting struts are smaller than the mounting struts of the sea glider, which may account for the drag coefficient curve being underestimated.

With this in mind, Figure 5.82 shows the accuracy of the wind tunnel glider CFD has performed reasonably well, as the drag coefficient difference at 0 degrees AOA is approximately 20%; this difference would be smaller if the correct sea glider mounting strut drag values were obtained. The theoretical value calculated for the drag coefficient at 0 degrees AOA was 0.0582, which is a percentage error of approximately 9% from the CFD value at 0 degrees AOA of 0.0532.

Visual inspection of the flow within the domain was performed for each simulation, where there was no

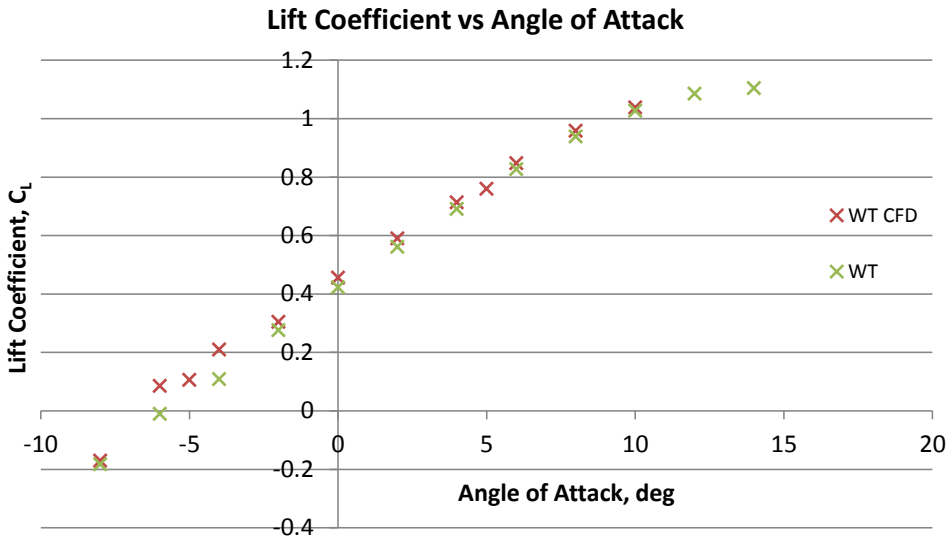

Figure 5.81: Comparison of experimental wind tunnel (WT) and the wind tunnel CFD (WT CFD) lift coefficient versus AOA graph

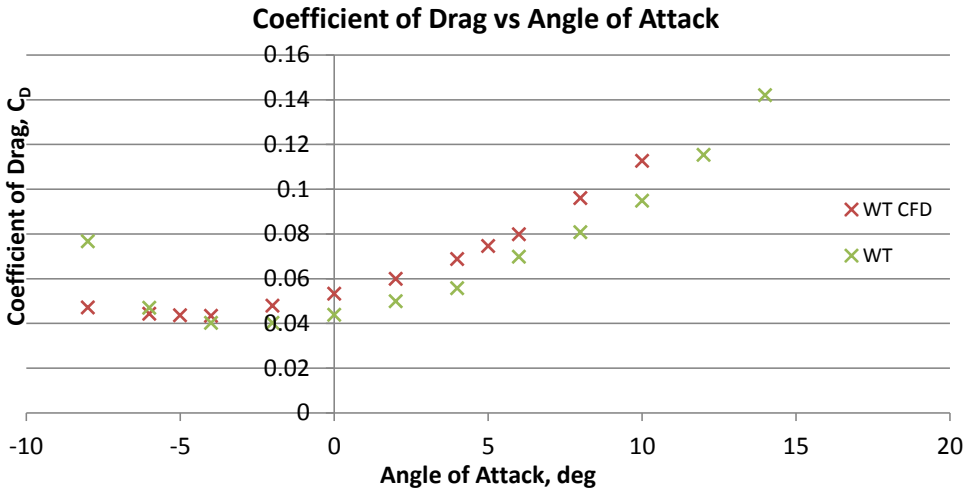

Figure 5.82: Comparison of experimental wind tunnel (WT) and the wind tunnel CFD (WT CFD) drag coefficient versus AOA graph

unexpected flow behaviour observed. Figure 5.83 shows the pressure contours around the glider and on the symmetry plane adjacent to it; the contours are as expected with the greatest increase in pressure being along the leading edge and at the tip of the nose cone. Lower pressure on the upper surfaces and higher pressure on the lower surfaces are observable, where the reference pressure is $101,325Pa$.

This wind tunnel domain glider CFD study has proven that it is capable of simulating the glider within the R J Mitchell wind tunnel to an acceptable standard, producing valuable information on the glider's aerodynamic performance. This allows for further optimisation and maturity of the glider with a reduced overall cost of performing tests in the wind tunnel.

5.15.3 Free Flight Glider Computational Fluid Dynamics

Further to the CFD study of the glider in the R J Mitchell wind tunnel, a free flight CFD study has also been carried out to assess whether the wind tunnel is adequate in obtaining information about how the glider would perform upon deployment and a prediction of the glider performance in level flight at its designed payload deployment conditions; being approximately at sea level with a freestream velocity of $10ms^{-1}$.

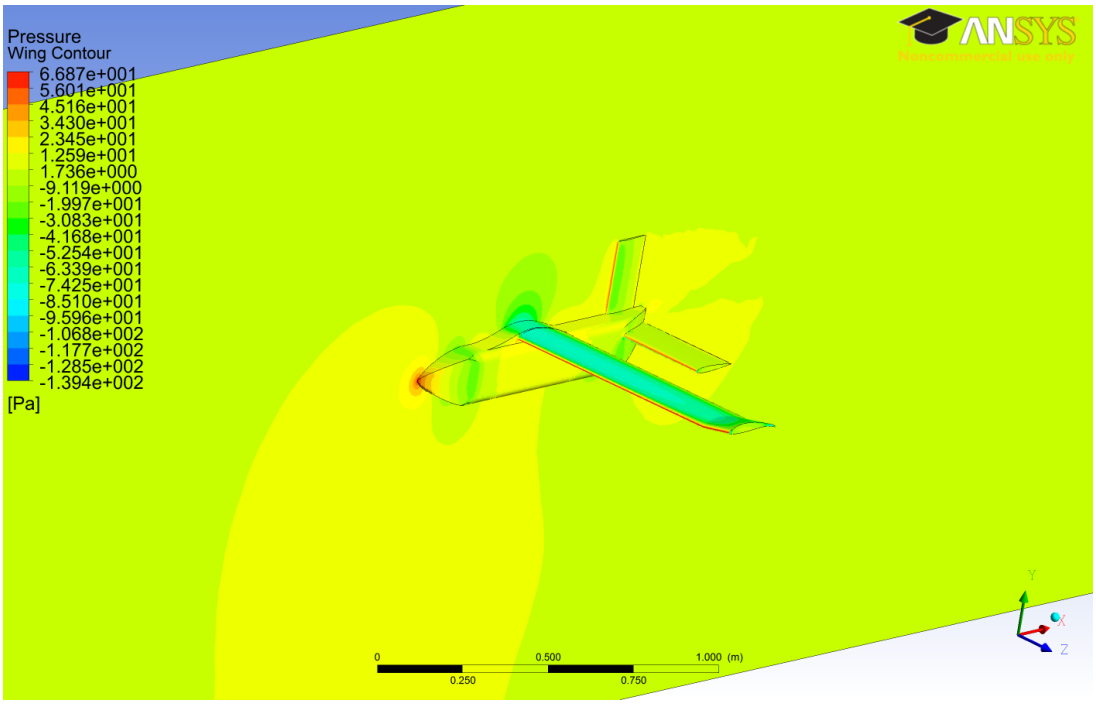

Figure 5.83: Pressure contours on the glider and the adjacent symmetry plane

Free Flight Domain

The free flight domain has to be sufficiently large so as not to interfere with the flow around the glider, which could result in distorted lift and drag forces. However, to reduce meshing and simulation times, there is a requirement to have a small domain. A domain sensitivity study was not carried out as time was limited; however a suitable domain size was chosen which would provide faster simulation times without the domain disturbing the flow around the glider; this was decided by user experience and suggested distances based on glider characteristics.

The free flight domain had the dimensions as shown in Figure 5.84.

Downstream from glider	Upstream from glider	Vertically above and below the glider	Spanwise from the glider wing tip
7 metres	2 metres	3 metres	2 metres

Figure 5.84: Free flight domain dimensions

Meshing

The same meshing techniques were used as the wind tunnel glider CFD; an unstructured mesh was produced with inflation layers which met the required y^+ values to enable the wall function of the Spalart-Allmaras turbulence model.

Due to the very limited time, a mesh sensitivity study was not carried out, but instead similar meshing values were used as that which were used in the wind tunnel CFD study. This obtained a mesh element count of $12,467,220$, which was then inspected with the same mesh quality criterions upheld in the previous CFD studies.

Boundary Conditions

As this study is a simulation of the glider in free flight, the domain has boundary conditions applied to it which would allow no wall interference from the domain boundaries. This is achieved by setting the following conditions on the domain boundaries; the front of the domain has been set as a velocity inlet

boundary (blue), the rear of the domain has been set as a pressure outlet boundary (red) and the rest of the domain has been set as symmetry (yellow) with the exception of the glider, which has been set as a wall boundary condition (green); this is shown in Figure 5.85. The symmetry planes around the domain allow for no interference with the flow associated with the glider; this was then proven during visual post processing of the data, which showed straight streamlines at the outer symmetry plane from the wing tip.

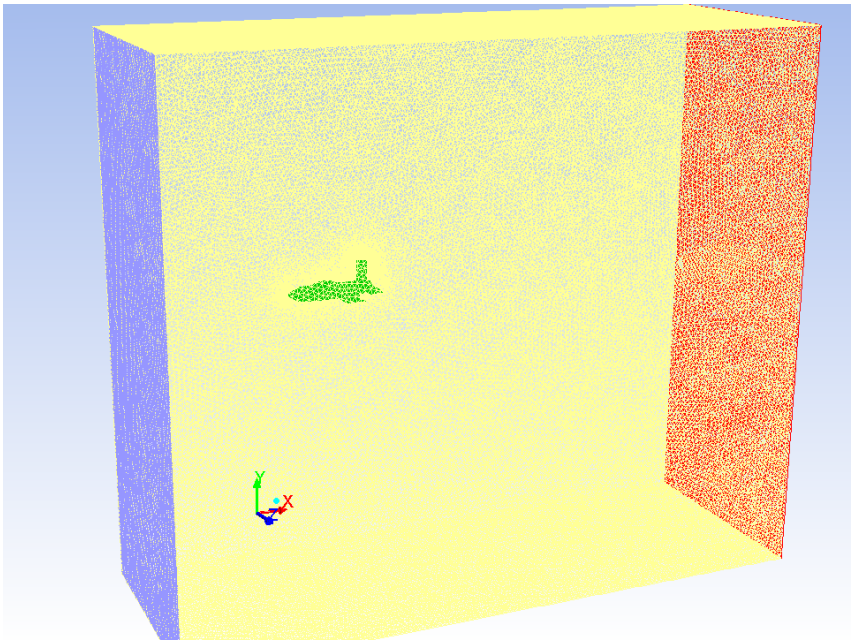

Figure 5.85: Free flight domain with boundary conditions

The simulation setup in FLUENT 14.0 was the same as the wind tunnel glider CFD.

Results

Having run simulations of the glider in the free flight domain for a range of AOA, from -8 degrees to 10 degrees in 2 degree increments; a comparison of the results can be made between the wind tunnel CFD data and the free flight CFD data.

Figure 5.86 shows the comparison of lift coefficient versus AOA between the wind tunnel and free flight CFD simulations; the two curves have a strong positive relationship, where the free flight CFD has a maximum difference of 20% from the wind tunnel CFD curve at -2 degrees. This difference could be accounted for by the difference in meshes, where the local element size can vary around the glider and thus resolve the forces differently at different AOA. Notwithstanding, the general percentage error is small and acceptable, approximately 10%, therefore it can be determined that the wind tunnel CFD is sufficiently accurate to estimate the lifting force of the glider in free flight.

Figure 5.87 shows the comparison of the drag coefficient with AOA curve of the two CFD studies. There is a good match between the two curves where there is a maximum difference of 5% at 10 degrees AOA and an average percentage error of less than 1% over the whole range of AOA. This shows that the wind tunnel domain does not affect the drag values on the glider significantly and so can also be used further in the testing process to estimate free flight performance at design conditions, neglecting external influences, such as, gusts.

Figure 5.88 shows the pressure contours on the glider in free flight at 0 degrees AOA and the vortices that are formed on the wing tip, tail tip and rear of the fuselage. The wing tip vortex is the largest and strongest of the three, as expected, which affects the amount of downwash seen by the wing. This effect can be attenuated by passive flow control, such as, larger angled wing tips or active flow control which is

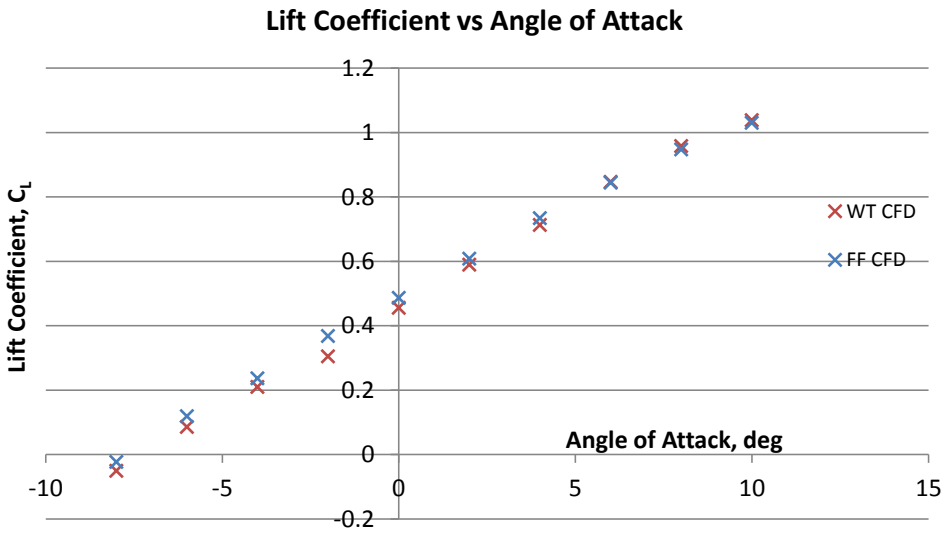

Figure 5.86: Comparison of wind tunnel CFD (WT CFD) and the free flight CFD (FF CFD) lift coefficient versus AOA graph

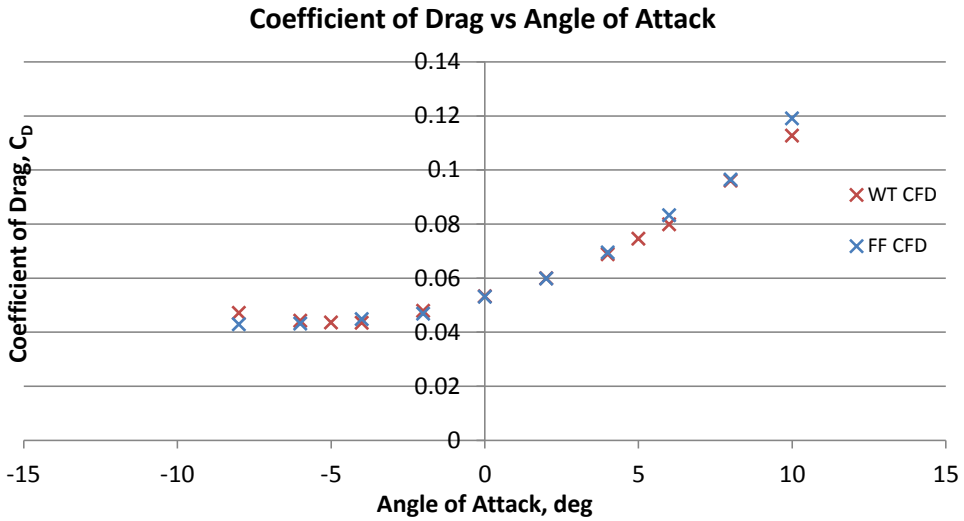

Figure 5.87: Comparison of wind tunnel CFD (WT CFD) and the free flight CFD (FF CFD) drag coefficient versus AOA graph

more complex to implement, for example, suction or blowing at the wing tip.

Overall, the free flight study has shown that the testing within the wind tunnel provides an acceptable estimate of the free flight aerodynamic performance of the glider. It has also given an approximate performance of the glider at its design release conditions.

5.15.4 Limitations of Computational Fluid Dynamics

Using CFD to further optimise the glider design, it has to be stated that there are limitations of using CFD as a numerical model of the current study. Where the CFD solution relies upon the physical model on which it is based, it will inherently contain inaccuracies as real world processes cannot be modelled exactly. Geometry modelling errors may also occur in the creation of the geometry of the problem. There will also be numerical errors introduced into the solution, which comes about from solving the governing equations on a computer. The round-off error is the numerical error introduced after a repetitive number of calculations in which a computer is constantly rounding numbers to some significant figure [15]. Discretisation error is the difference between the exact analytical solution of the governing partial differential equations and the solution of the difference equation. The discretisation

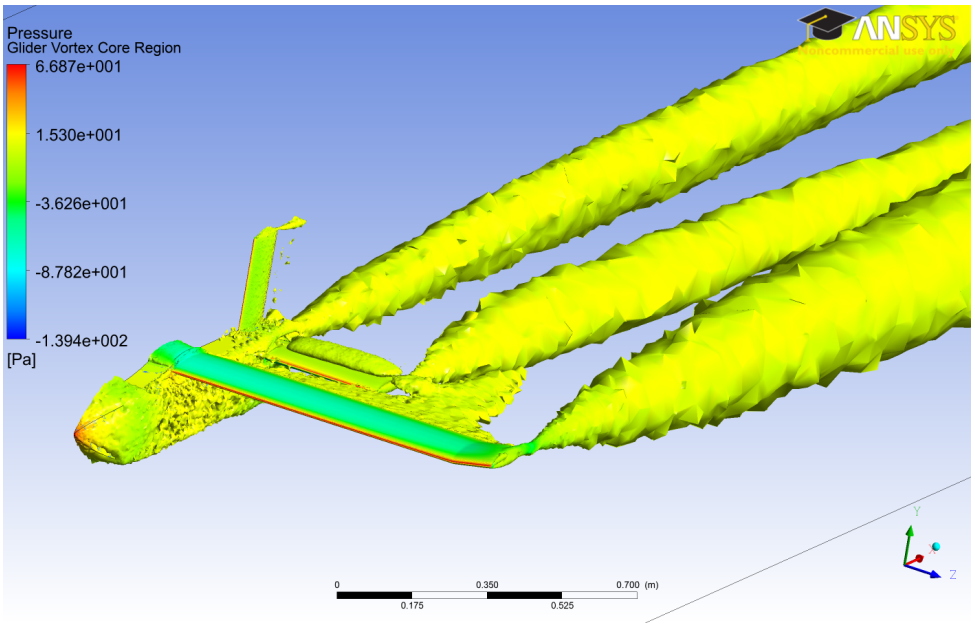

Figure 5.88: Glider in free flight with pressure contours and vortices

error is dependent on the mesh quality, as a mesh becomes more refined the solution would become less sensitive to the grid spacings.

Although experimental wind tunnel testing is the most accurate way of obtaining information of the aerodynamic performance of the glider without flight testing, it can be much more costly and impractical due to the requirement of fabricating a model glider and the use of the wind tunnel; therefore, the CFD studies performed are of great value to the project as it will allow further testing without the incurred costs of wind tunnel testing due to the working solution of the wind tunnel simulation which has been validated.

The accuracy of the current studies have proven to be sufficient in estimating aerodynamic performance, however, for improved accuracy, a two-equation turbulence model and a $y+$ value of 1 could be used, which would fully resolve the boundary layer accurately and thus be able to simulate the turbulence near the walls more accurately, allowing more reliable lift and drag values to be obtained.

6 Electronics - Benjamin James Oxley

6.1 Electronic Design

Electronics are a vital part of the construction and operation of both gliders and the ocean drifter as they determine how it is controlled in flight, how data is relayed and are necessary to make the system autonomous. The powered glider requires an autopilot system, telemetry and motor control to improve it for further use, this requires the selection of suitable batteries, power control and selection and programming of an autopilot system.

6.1.1 Sea Glider Systems Diagram

The ocean glider requires a complex system of electronics in order to ensure reliable function throughout all parts of the flight, this is summarised in the figure below (Figure 6.1). All parts of the system must be capable of intercommunication and compatibility in order to make the system work reliably. In addition, due to the requirement to work over long periods whilst floating, it must be possible to power each component separately and for the system to enter a low power state for much of the time spent floating. A short list of requirements was drafted to aid the design process:

- Antennas must situated be above water level
  This is due to the much higher level of attenuation in water compared with air, after being submerged by as little as 5mm it may not be possible to sustain communication with satellites.
- All control surfaces controllable from within the waterproofed vessel.
  To reduce the complexity of electronics and the protection of delicate and expensive components for testing, all major electronic systems must be contained within the waterproofed drifter.
- Drifter pot to be stable in the water for transmission to satellites.
  For successful communication with satellites via Iridium the drifter must stay relatively stable in the water and be upright so as to keep the antenna pointing in the right direction.
- All external connections to be waterproofed to IPX8 standard (submersion to 1m for extended periods of time).
  Due to the large durations of time spent in the water, it is imperative that the system is completely waterproof, even when submerged, and remains so for long periods of time.
- Buoy to have an internal diameter of at least 60mm to accommodate all internal electronics minimum dimensions.

6.1.2 Remote Control Equipment

For testing an manual flight a remote control (RC) system is required in order to control the flight surfaces of the aircraft, actuate release mechanisms and set the autopilot mode. The systems are developed with Spektrum 2.4GHz remote control equipment, although this system allows for quick interchanging of equipment and switching of airframes it could be changed for another system. The system needs to be at least 5-channel in order to control the elevators, rudder, throttle and flight mode for manual control. In addition, channels may be required for the balloon release mechanism, pitch control (if used in elevon mode) and the fuselage release mechanism for the sea system.
The particular system used is a Spektrum DX8s transmitter and AR9000 receiver with a TM1000 telemetry module. The AR9000 is bound to the DX8s using a bind cable (ground connected to signal) which is inserted into the bind socket of the receiver (also the telemetry socket) and may require the telemetry

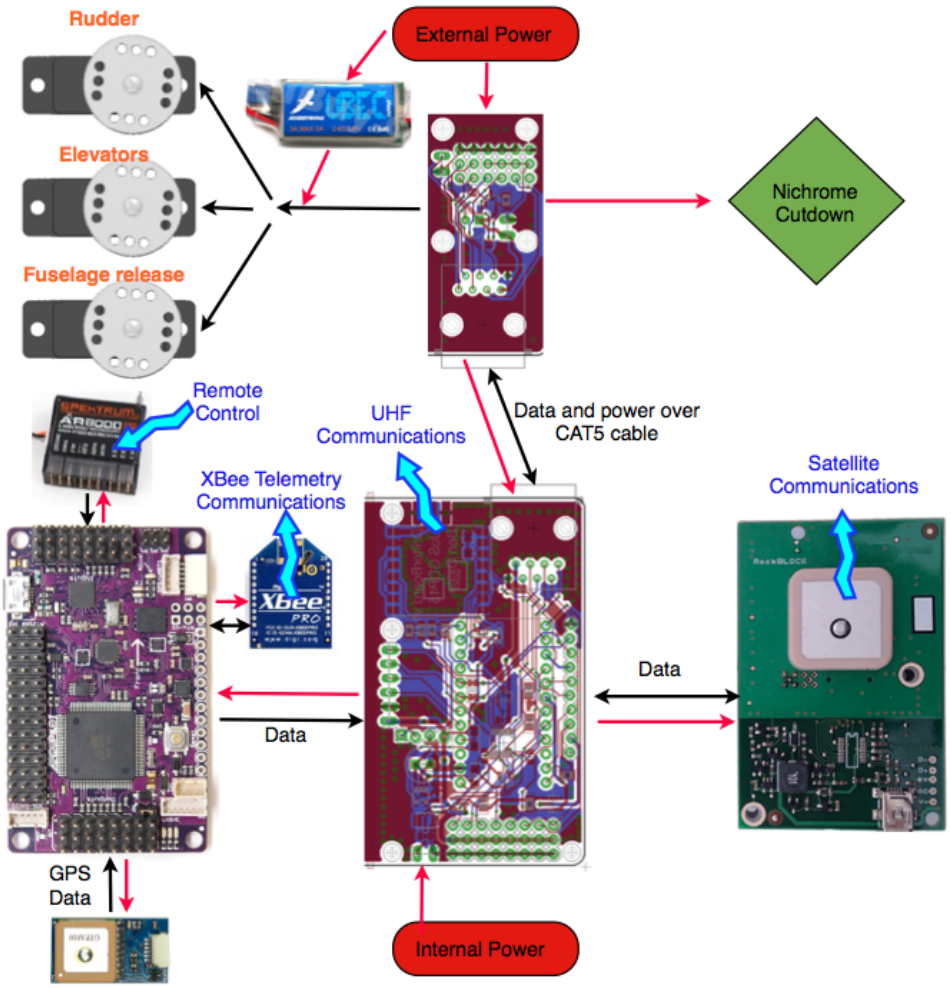

Figure 6.1: A simple diagram of the layout and interconnections of the Ocean Glider

module to be unplugged to do this. Once the receiver is turned on (with the bind plug in) we then want to turn on the transmitter, holding down the bind button on the top of the transmitter whilst turning on.

Each system however, requires at least a 7-channel controller as it requires elevators, rudder, fuselage release, towing release and mode switching. As none of the flight control channels can have auxiliary functions on them, we require 4 channels for stick controls and 3 for the auxiliary functions outlined above. An AR8000 or 9000 module is suitable for this function. Both Planes can be bound to the same controller but cannot be controlled at the same time.

Component Wiring

Connections between components are made with standard servo leads. For the RC receiver to Ardupilot connections male-male servo leads are required. The servos are connected with extension leads to reach the back of the plane. In addition, the two elevator servos are connected with a Y-lead splitter so that they both receive the same input signal from the elevator output. One servo has had it's internal wiring modified so that it actuates in the opposite direction for the same input signal. This means that identical elevator deflections are experienced on each side and remove the need for a servo reverser.

Fail Safes

The Spektrum receiver has inbuilt fail safes in case of loss of signal with the transmitter. As we want the Ardupilot to handle any loss of signal, we need to ensure that the fail safe values are correct and safe on the receiver. Most importantly for safety, especially during testing, the throttle fail safe must be as low as possible in the event of signal loss.

The Electronic Speed Controller (ESC) also requires the timing mode may need to be changed to match

the motor otherwise there will be issues with reaction speeds of the motor to spinning up and braking.

6.1.3 Sea Glider System Mounting and Interconnects

The system has to be designed to be slid directly into the buoy in one piece so that it is easy to construct, test and operate. The mount is designed to be as lightweight as possible whilst ensuring that the electronics are secure and accessible. This has been achieved by creating a multi-layered mounting system which can be reconfigured to match the dimensions of components (fig. 6.3).
Due to cutting constraints, the material used is 3mm perspex, this is an extremely rigid and shatter resistant material which provides good impact resistance for the drifter upon impact with the water. In addition, perspex can be heated and bent to provide some of the more complex shapes achieved on the mount. A thinner perspex could be used to make the mount lighter and easier to manufacture. The plates are laser-cut and designed to be as easy as possible to mount extra components on. Weight has been removed wherever possible and cut-outs have been added to route wiring through.
The cut pieces are mounted on a skeleton of M4 nylon stud with spacers to produce a lightweight and easily reconfigurable design. The whole mount then slides into the drifter pot and is packed out with foam around the outside for temperature control and impact resistance. A switch is mounted on the top level so that the system can be easily turned on without disassembly. However, the antennas for both the Iridium modem and the GPS have to be mounted at an angle in order to fit them through the neck of the cylinder but also to allow for reliable operation both in flight and when in the water. Antennas do not have an even radiation pattern, which means that when tilted at an angle the gain of the antennas to satellites directly above them is less. The antennas have a reasonable radiation pattern for transmission and should have a nominal gain of +2dBi (against the nominal value of +3dBi when mounted at 0 degrees) as is shown in Figure 6.2. Due to good line of sight with satellites from the sea, reception of messages should be reasonably simple and reliable, even when transmitting in heavy weather. This assumption also stands for the GPS antenna which is of the same design (patch antenna) and similar frequency.

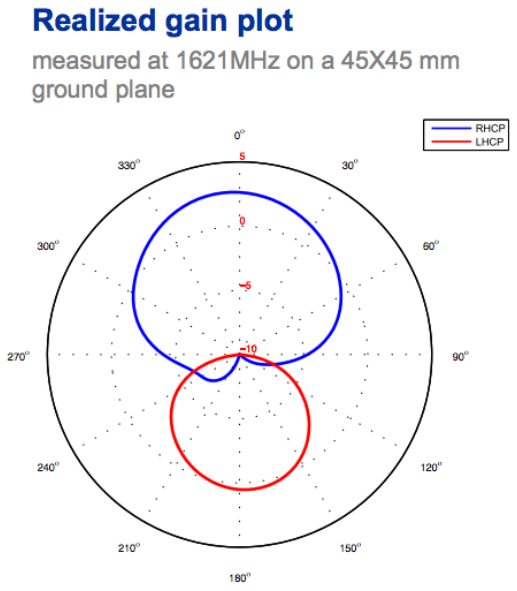

Figure 6.2: Radiation pattern for the 1621MHz patch antenna used on the RockBlock Modem [72]

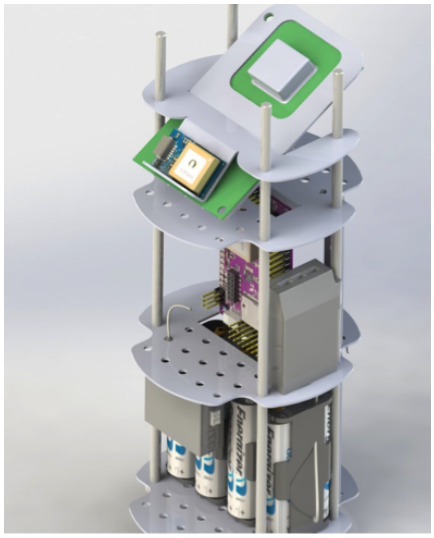

Figure 6.3: The mounting system for all parts of the seabourne electronics system

To keep the system stable, the centre of gravity of the load is designed to be mounted as low as possible

such that when floating in the water it stays the right way up. However, as the Iridium modem is required to be placed at the top, to keep the antenna in a suitable position for transmission, the weight of this component is in the wrong place to move the centre of gravity downwards. Ballasting in the drogue or the bottom of the cylinder is necessary to reduce the centre of gravity. Initially the centre of gravity was calculated using real masses for components in Solidworks and the correct densities for materials. The real masses used for components, this data was fed into the design of the UAV and for calculating the stability in the water of the vessel. The centre of gravity of the drifter from the lid is 146mm, this is approximately 50% of the drifter height and will not be stable without the drogue acting on it. To improve this, the Iridum antenna could be mounted on a coaxial cable and the main circuitry placed at the bottom of the drifter. In this case, a different design of antenna could be used for better reception [73]. However, this would mean a major redesign of components and breaking the loaned rockblock modem board which cannot be done for the purpose of this test.
Lightweight cables and single pin connectors are used to go between the Ardupilot and the daughter board for communicating telemetry and servo positions.

Elevons
By changing the settings on the Spektrum controller, it is possible to drive the elevators on the plane like elevons, this gives some roll authority. If the Ardupilot is also set up correctly, it can also control the craft using elevons but with the current version of the Arduplane software (2.70) it cannot concurrently use a rudder. For this project, where manoeuvrability is not a high priority, the system can run with just elevators and a rudder.

6.1.4 Sensors

A payload of sensors may be mounted in the lower tray section and directly connected the daugtherboard which handles some data storage and relay for the system. A good option for sensors on this payload would be to use thick-film printed sensors as they are extremely lightweight and could be adapted to measure many elements of sea conditions on a single chip including salinity, temperature, diluted oxygen and carbon dioxide.

6.2 Power Systems

	Launch	Flight	Drift	Flight Total	Drift Total	Grand Total
Duration (Hours)	4	2	168	2	168	170
	Time awake in seconds			Energy consumption in Joules		
Arduino Pro Mini Awake	14400	7200	10080	1080000	504000	1584000
Arduino Pro Mini Sleep Mode	0	0	594720	0	2973600	2973600
Ardupilot GPS aquire	120	0	20160	72000	12096000	12168000
Ardupilot active	14280	7200	10080	8592000	4032000	12624000
Rockblock Modem Charge USB	0	0	30240	0	13608000	13608000
Rockblock Modem Idle	0	0	3360	0	1008000	1008000
Servo actuate	0	720	0	1296000	0	1296000
Servo hold	14400	6480	0	1252800	0	1252800
			Total energy used (Joules)	12292800	34221600	46514400 J
			Total energy before voltage regulators	15223281.7	42379690.4	57602972.1 J
			Total energy in milliamp-seconds (mAs)	2537213.62	7063281.734	9600495.36 mAs
			Total energy in milliamp-hour (mAh)	704.781562	1962.022704	2666.80427 mAh
			Duration possible at sea on one set (4) batteries (Weeks)		1.529034294	Weeks

Figure 6.4: A breakdown of all of the power consuming components and endurance for drifting

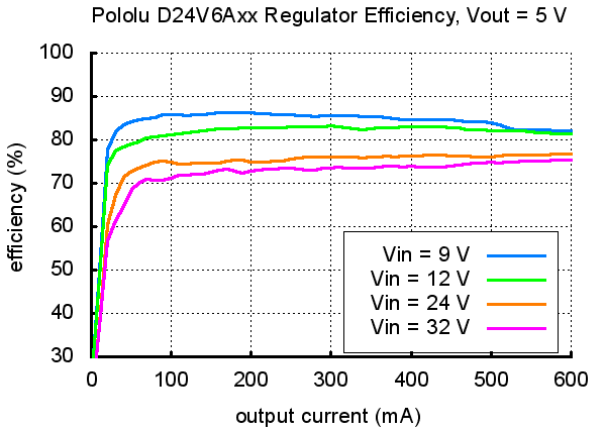

Figure 6.5: Efficiency of combined switching regulator and LDO combined

The secondary board has been designed to handle the complex power requirements of the equipment used. The intention is to ensure that all equipment runs off the external batteries during flight in order to extend the maximum run time of the drifter once it is in the water. In order to do this an "ideal diode" type MOSFET switching chip (LTC4353) has been used that can switch between power supplies in order to keep the circuitry functioning [65]. This is then fed into voltage regulators. Most of the electronics runs off a switched mode step-down regulator which has a higher efficiency than a normal linear regulator. This is because it acts like a voltage transformer using inductance to create a modified voltage output. A linear regulator essentially “wastes" the excess voltage in order to maintain a regulated voltage supply and hence is less efficient and becomes even more so the higher the supply voltage. However, at low current draw (typically <10mA) switched mode regulators become extremely inefficient (fig. 6.5) and so a linear regulator powers the Arduino processor to maintain an efficient regulated voltage whilst the rest of the electronics is turned off (in sleep mode). The switched mode regulator supplies a current to the rest of the circuitry which is higher current. A pre-built 0.6A circuit is used which attaches to the board via a 4-pin header. This can be switched on and off in order to turn off all attached equipment during sleep mode. However during testing it was found that this was not sufficient to maintain a 5v output supply at 0.6A with a 7.6v input. This causes problems with the receiver and Ardupilot telemetry transmissions and as a result a more efficient 2A switched-mode voltage regulator was used for some of the rest of the testing process.

6.2.1 LTC4353 Circuit Design

The power switching module needs to be able to switch to the internal battery supply if and when the voltage on the main supply drops below 5.5v (enough for our regulators to regulate it down to 5v). This is the same behaviour as when the primary battery becomes unplugged (when being released from the glider). As the EN2 pin on the LTC4353 is triggered for 0.6v or below we need a voltage divider of roughly 9.1 times which equates to a ratio of R1 to R2 of 8.1. We can use a 100k and 12k to give 0.589v out at 5.5V. LEDs have been put on the outputs to show which supply is powering the system for testing but should not be soldered up for real use as they will increase power consumption. Large capacitors are placed on the outputs in order to stop a voltage drop during supply changes. Testing shows that voltage output remains basically constant regardless of the input and when the external power supply is unplugged the system remains fully powered up and continues to function normally. This shows how successful this design has been and means that we can effectively power the whole system during flight from the external supply so as not to affect our endurance whilst being used as a drifter once deployed.

6.2.2 Servos

The servos are powered directly from the battery eliminator circuit, separate to the main autopilot electronics. These are high current and the BEC ensures that the servos do not overload the on-board voltage regulator. This is possible as long as the ground and signal lines which control the position of the servo are also connected, through the ethernet cable, to the internal circuitry of the daughter board PCB.

6.3 Autopilot Design

6.3.1 Autopilot Selection

There are many openly available autopilot systems on the market available at low cost to the consumer. In addition it is possible to build bespoke systems and implement open-source code for control which allows for a great deal of flexibility in design, cost and operational conditions. Due to time constraints, it was necessary to choose a pre-made autopilot system which, in addition, had to be cheap enough to be implemented for both airframes. The Ardupilot system was chosen as it is the most heavily supported and documented system at the time of writing which was compatible with all aspects of our design brief and with open-source code that could be modified to meet operational requirements.
To reduce cost during further development it may be possible to design an all-in-one board which acted as a complete telemetry, satellite and autopilot solution for the system. If the design was to be implemented for commercial use this would be necessary in order to reduce system cost and increase reliability by eliminating system component interconnects. Producing a bespoke PCB system also has the advantage of reducing system weight. Commercial off-the-shelf systems usually cost too much for application here and would stop the design from being compact and disposable and an alternative to current means of drifter deployment [114].

6.3.2 Ardupilot Mega 2.5

The Ardupilot is an Open-source autopilot system that is capable of being applied to a variety of land and air vehicles. Choosing a pre-developed autopilot system de-risks some of the development issues by using a highly tested and proven system to control the safety critical components of flight. It was decided to the daughter board, a separate second processor, to check that the Ardupilot system is running reliably and to handle external transmission via Ultra High Frequency (UHF) radio and UHF to satellite communications. This board checks for a communication from the Ardupilot containing any applicable data such as GPS position and sensor data.

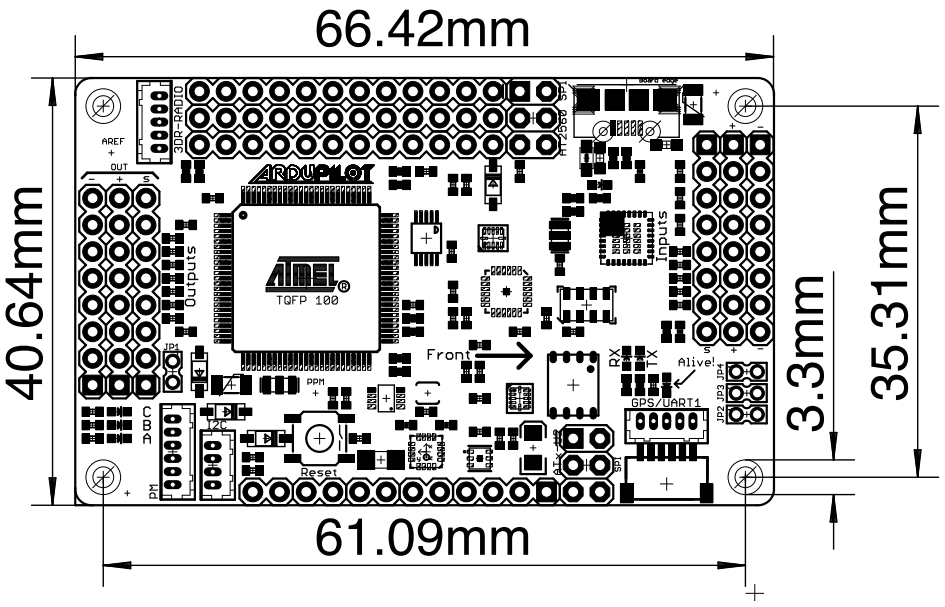

Figure 6.6: The ArduPilot 2.5 with dimensions

The glider uses the newest version of the Ardupilot available at the time of writing, Ardupilot Mega V2.5 which has on board an Atmel ATMEGA2560 [19], GPS [50], accelerometer [57], magnetometer, gyroscope and barometric pressure sensor [74]. An additional daughter-board handles long range communications and “watchdog" system (anti-software crash) for the Ardupilot and is controlled by an Arduino mini. This listens to the telemetry data output from the Ardupilot over the Xbee wireless telemetry link before it is transmitted. It decodes the MAVLink packets that are transmitted to get all relevant position and attitude data from the autopilot that is then used to send long-range messages over both the VHF and Iridium communications modules. The drifter system is designed to be powered by Energiser Lithium Ultimate batteries as they have an extremely high energy density, long shelf life and high efficiency in all realistic temperatures [40].

Airspeed Sensing
In addition to the on-board sensors of the glider, a differential pressure sensor is used with a pitot static/dynamic tube in order to gauge airspeed directly to aid the autopilot in flight.

Telemetry
The Ardupilot is connected via 2.4Ghz Xbee Pro modules to the computer which allows for a 2-way real time telemetry link, allowing for new autopilot commands to be sent, positions and sensor data to be relayed back to the ground station. In addition parameters can be changed in flight to adjust way-points and flight-paths but also update PID values whilst in the air.

Ardupilot Mission Planner
The Ardupilot mission planner for Windows is much better and more usable than the OS X/Linux equivalent which is quite buggy. The OS X variant does, however support multiple flying systems in the air at once, something not possible in the Windows program.
All PID values can be set within the program, flight paths set and directly uploaded to the flight system. In addition, the telemetry from the Xbee telemetry link is downloadable directly into the mission planner so that the glider can be monitored in real time.

6.3.3 PID Values

PID controllers are used both for direction decisions and their modification alters the flight path. It is especially important in controlling how the plane turns around corners and how quickly it attempts to turn. The Ardupilot comes with the settings already configured for a small plane but seeing as this glider

does not have roll control via ailerons the PID values have to be changed to use the rudder more for direction changing. Although PID values are given for some standard craft these are not right for the larger, less responsive airframe used so we require larger values for proportional control in order to make the reaction rates acceptable.
The Ardupilot uses two PID controllers for most surfaces, the navigation control loop decides on the rate and angle at which to bank for a turn whilst the servo PID controls how quickly to move the control surfaces (and how much) to achieve this angle. Due to the quick response of the control surfaces, little derivative control is required and the control loops are mainly based around proportional and integral control. As the PID controls are designed to be generic to any airframe, tuning them using theory is difficult. Instead gradual application and static testing helps to decide on these values. Rolling and pitching the aircraft whilst in stabilise mode allows the user to see how control surfaces are deflected to keep the craft stable. It is suggested that the aircraft is tested in successively more autonomous modes to ensure control. The aircraft is first tested in stabilise mode, then fly-by-wire and then fully autonomous flight.

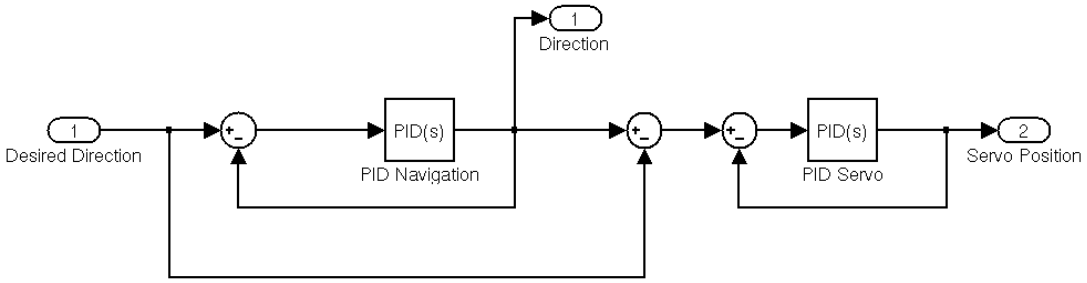

Figure 6.7: Approximate setup of Ardupilot simulated PID loops

6.4 Daughter Board

The daughter board is based around an Arduino Pro Mini 3.3v processor board which uses an Atmel ATMEGA382 processor. This is capable of being reprogrammed in an adaptation of C++ to handle all of the processing requirements of the daughter board in addition to being able to read sensor data and communicate with other systems.

6.4.1 Operation Scheme

The operational procedures of the board is outlined in Figure 6.8. The system regularly checks it's altitude and ensures that in the case of loss of GPS signal the system will attempt to release the plane. However, as GPS is required in order to allow the glider to function correctly, this is left as a last resort. Code has been modified on the Ardupilot to pass data to the daughter processor handling radio transmissions. In addition, the daughter processor has been coded to handle all data transmissions and control power to the Ardupilot system. A MOSFET allows the power to be completely isolated from the Ardupilot and Iridium modem and then turned on with almost no extra power loss as MOSFET have an on-state resistance in the milliohms range .

Exterior connections to servos will need some form of waterproof connection in order to ensure that there is no water ingress. In addition, these plugs must detach with minimal force in order to ensure that the drifter successfully detaches from the glider. Waterproofed connectors or cable glands are necessary in order to breakout the servo connections from the main buoy casing whilst keeping integrity. Waterproof

connectors were experimented with but mostly these connectors are only waterproof whilst connected, making them unusable for this design [25, 83, 67].

6.4.2 Daughter Board Design and Manufacture

The PCB designed is a 2-layer board, 1.6mm thick FR4 with a silkscreen and solder resist layer. The total produced board size is 66x64mm but the internal board is only actually 66x38mm. PCBs were designed using Cadsoft's Eagle electronic design package.

The first step in this process is to design a schematic, showing the connections between components and defining component types and values. This is then checked using internal electrical rule checks to ensure that the schematic is correct. Some custom components "footprints" were designed for integrated circuits where these were not available in current libraries. The components are then placed onto a board design manually taking into account RF interference shielding, optimal track lengths (the shorter the better) and where areas unbroken ground planes would be beneficial for the design. Ground planes are especially beneficial under high frequency and RF components such as the switch-mode voltage regulator and UHF communications system. Sockets were selected for easy and secure connections to other components. The schematic for the entire daughter-board layout is shown in fig. F.1.
Next, the board is routed automatically to place a initial layout of tracks to connect components. Once this is done, this is manually modified in order to make tracks as thick as possible where they may require high currents (especially the nichrome cut-down line). Tracks are also modified to remove inefficient

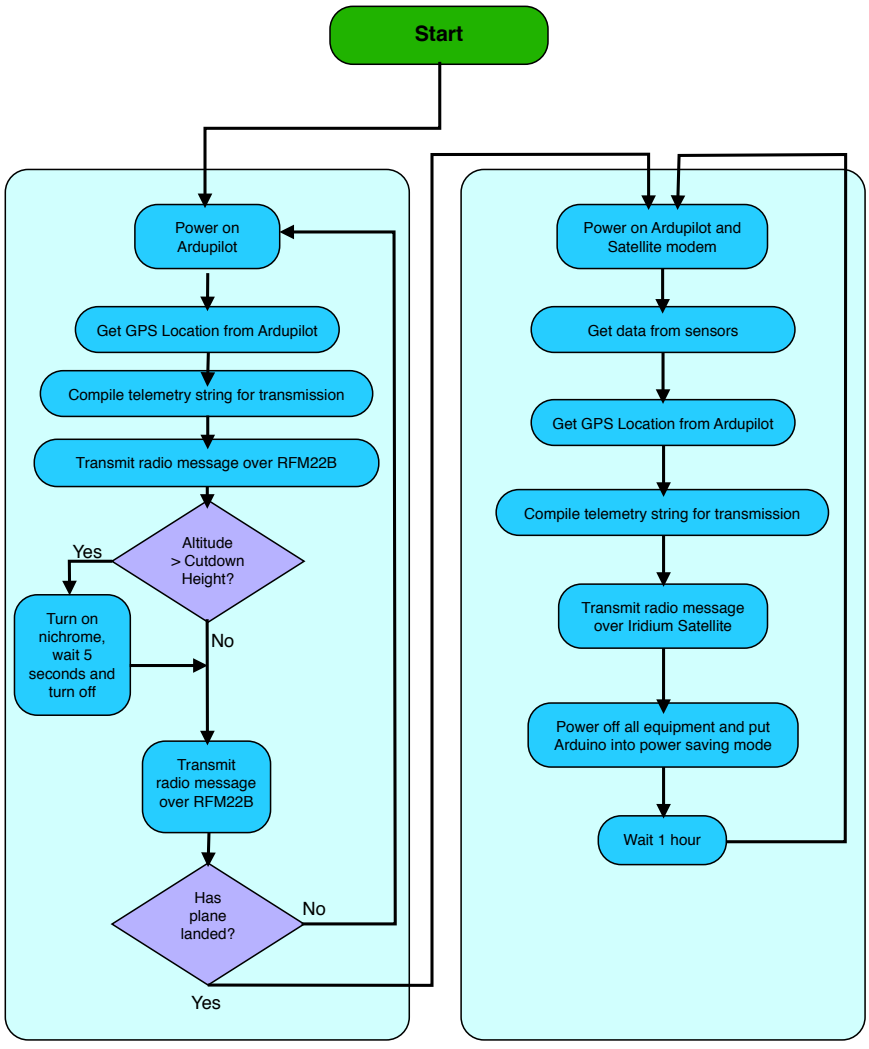

Figure 6.8: Flowchart to explain the basic operation of the Arduino control board

routing (this happens a lot with auto-routing) and where the auto-router is unable to route all tracks on the board, these are completed manually. It is usually not difficult to route tracks, even if the auto-router is not able to do so.
The PCB design is then checked using the manufacturers design rules which define the minimum track sizes, drill sizes etc. Usually tracks and drill holes need to be moved in order to meet all design rule checks. Once this is complete, Gerber files are created using a CAM file. The Gerber files are used by the manufacturer to directly produce the boards. These boards were created in one piece (daughter board and external adaptor) to reduce production costs, the exterior adapter is then cut off from the main board. Manufacturing the board with a fast turnaround is possible but considerably more expensive. In small batches of 10 the total cost of manufacture is £71.75. For slower turnaround this cost is approximately halved, making the boards £3 each. Parts purchased for constructing boards have to be bought in quantities of 100 and so although the total electronics costs are approximately £100, the cost per board is £4. Once manufactured, the board can be hand-soldered using a precision soldering iron and solder paste or reflow soldered in a reflow oven. The board has been designed with all of the components on one side which considerably reduces the difficulty of manufacturing in a reflow oven.

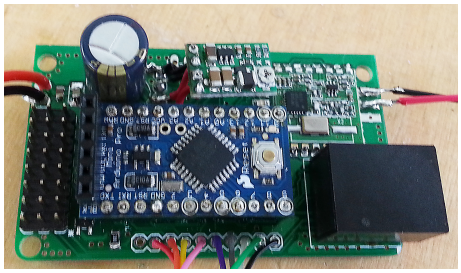

Figure 6.9: The completed daughter board.

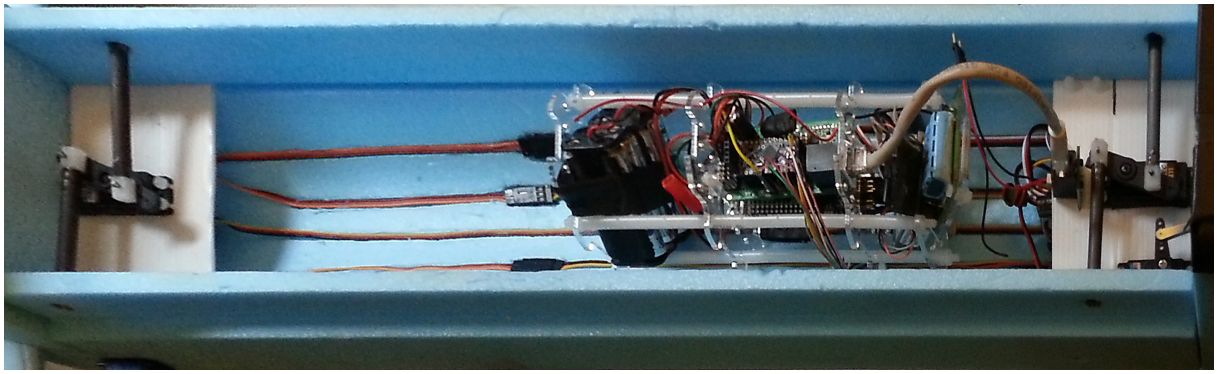

Figure 6.10: The completed system in the glider without the buoy cylinder

6.4.3 Programming

The Arduino code, written in a modified version of C++. To create a system with MAVLink, NMEA (GPS protocol) and other functions, modified libraries have been created to handle processing of incoming signals and communication with external systems such as the Iridium mode and Ardupilot communications and control. These are imported into the main code and called to update systems and send messages. The Arduino also monitors it's own core temperature (with an accuracy of ±2 deg Celsius. This can be used as an extra sensor to corroborate other sensor data without adding extra weight or complexity to the system [1].

[1] The code for the project is available on the accompanying CD or from `www.github.com/ben-oxley/ArduGliderIridium`

6.4.4 External Adapter

The external adapter for the board breaks out the internal connectors to normal servo connections and allows the servos to be powered off of a BEC which is high enough current to supply all of the servos. The board also has a system for using a nichrome wire cut-down mechanism from a balloon or towing plane. This has an advantage over a traditional cut-down mechanism of using no power whilst in flight and weighing only 10% of a mechanical release. However, for testing a traditional mechanical cut-down was used as it allowed faster turnaround of the plane from landing to the next launch.

Decoupling capacitors are used to reduce radio frequency (RF) noise and voltage regulator noise on the 5v and 3v lines. This helps to regulate stable functioning of the microprocessors that are sensitive to this interference.

Cut-down Mechanism
There are several compatible ways of controlling a cut-down with the supplied electronics. The micro controller can either power a MOSFET attached to a suitable cut-down mechanism such as a nichrome wire or solenoid. Or, using the data channels connected to the Arduino, a pulse width modulation signal can be created to control a servo position to move a servo based towing mechanism. For high starting current mechanisms such as the nichrome wire, a large capacitor has been included, this supplies the some of the current while the wire heats up to it's lower resistance.

6.5 Communications

6.5.1 Iridium Modem

The Iridium 9602 modem is a short-burst data modem for the Iridum network, it allows the uplink and downlink of short messages to web servers. This can act as a long range means of communication whilst in the water. This is chosen as a mechanism of telemetry relay as at low altitudes, the distance that the low power UHF (434MHz) radio is able to transmit over is severely reduced (from $750km$ to several hundred meters). To make the design process easier, a RockBlock Modem adapter has been used. This allows direct serial communication from the Arduino whilst taking care of power and antenna concerns. The RockBlock service also provides a internet service for receiving messages. The Iridium modem uses a 9-wire interconnect and a serial communications protocol over a 3.3v UART which can be connected directly to the Arduino Mini to send commands. It also has a set of extra output signals that signal when the system has messages available for download and when it is ready to send messages. In addition there is also a way to put the system into sleep mode which is a low power mode where the system will use a maximum of 0.2mA. However, as we are looking to conserve as much energy as possible whilst floating the whole of this system is not powered when it is not required via a MOSFET on the power handling board. As Iridum messages are charged per character and there is a maximum length of message for Short Burst Data (SBD) communications it is important to only transmit necessary information over the Iridium satellites. We use the same format as UHF communications to transmit our messages with a checksum at the end to ensure validity of the data. A CRC16 cyclic redundancy check is used as this is an easily computable checksum that is much more reliable than XOR (as XOR checksums only require an even number of bits to be flipped and the checksum will not be useful). Floating point variables are converted into strings via a simple section of code which is much smaller than the floating point conversion library. The message contains the transmission number, time, GPS position and sensor data within a 60 byte string.

6.5.2 UHF Communications

The UHF communications module is a RFM22B, this has been selected as it is a heavily tested and documented module that is extremely lightweight and compatible with the 3.3v Arduino system. It has a selectable output frequency which helps to avoid frequency clashes on launches and is compatible with receiving data as well as transmitting. In later projects an uplink to the balloon may be useful. It is coded to transmit Radioteletype (RTTY) sentences which are decodable over large distances (until the system is below the horizon) as long as suitable receiving equipment is used.

A simple antenna is used for the radio so that it can be packed efficiently into the casing, a dipole whip antenna is attached directly to the board and arranged to as straight as possible to give a good radiation pattern. This can be modified by carefully wrapping around the drifter to form a helical antenna. A helical antenna is circularly polarised which means it is less susceptible to fading of the signal whilst turning and has a more even radiation pattern around it [127].

Whilst in the air, free space path loss allows us to receive transmissions from a great distance:

$$FSPL(dB) = 10log_{10}((\frac{4\pi}{c}df)^2) \tag{6.1}$$

$$FSPL(dB) = 20log_{10}(\frac{4\pi \times 434e6}{2.9979e8}) + 20Log_{10}(d) \tag{6.2}$$

At a distance of 660km (the distance of the horizon at the maximum flight altitude of 34km) the attenuation of the signal is 141dB. Although the signals transmitted are limited to 10mW (in the 434Mhz ISM Band), previous experiments have shown it is easily possible to decode transmissions using this scheme over this distance with an amateur radio receiver and a yagi antenna [17].

6.6 Testing

Continual testing of the electronics took place through it's development as parts were connected together and their function determined. This continual testing identifies problems and issues with the system design and allows for changes to take place before flight. However, some sections are more difficult or unsafe to test in this manner and so several different testing procedures were used in order to aid development.

Wind Tunnel Testing

The wind tunnel was used as an opportunity to test the remote control and propulsion systems for both craft. Throttled control was used with the propulsion system and data was relayed back via the telemetry link to the computer for monitoring and testing of the link stability. This proved the controllability of the aircraft from the remote control system and highlighted some ease of use problems such as turning on the plane when closed.

Hardware-in-the-Loop Testing

The Ardupilot has the ability to be tested as a hardware-in-the-loop system where a simulation can be run through X-Plane flight simulator and the data fed to the Ardupilot. With a suitable plane model, it is possible to test the reactions and function of the plane to a programmed flight path. This proved the function of the autopilot in theory and linked with the physical testing of the response of the control surfaces when in stabilise mode, helps to guarantee the correct function of the system in full autopilot flight.

6.7 Electronics Flight Testing

6.7.1 Powered Glider Testing

The powered glider worked well during manual flight, was highly responsive and stable once ballasted. However, the motor timing is not set up correctly and as a result, reduction from full throttle to idle is slow and difficult to control, this will require fixing for autopilot flight. To fix this issue an ESC programming card needs to be purchased. The autopilot is suffering from issues with voltage regulation during flight which causes crashes and unreliability. A higher voltage battery supply is recommended or a higher quality separate BEC circuit which has a lower drop-out voltage (the lowest input voltage at which the system can longer sustain the target output voltage).

6.7.2 Oceanographic Glider Testing

The electronics in the glider worked well during flight, providing a reliable test-bed and and easy system for turning on. However for calibrating and power control, external switches for controlling the entire system would be very useful, this would mean the whole system could be constructed ready for launch beforehand and turned on at site, ready to launch.

6.8 Further Work

The project needs further development in order to make it reliable and safe for extended use. It is recommended that the batteries are upgraded to 3s 11.1v lithium polymer cells. In addition, it is necessary to buy a higher quality BEC to supply the Ardupilot to protect it against crashing. However, in addition to this, the higher voltage supply will need better capacitors (16 or 20v rating). Voltage regulators will also need to be upgraded so that they are capable of regulating a higher voltage supply. This should eliminate some of the reliability issues in the design whilst using switching regulators should mean the efficiency of the system remains similar. More work needs to be done to place antennas so that telemetry links are reliable.
The sea system needs more drifting testing in order to establish its reliability and endurance in cold water over long periods of time.
Other items of electronic design that require modification include:

- Large smoothing capacitors should go on regulated side of regulator.
- The RockBlock modem can be relocated almost exclusively to analog pins, freeing up digital PWM pins for servo control.
- The Ethernet connection can be optimised to make best use of port now that all connections in and out are known, more servo connections directly from the Arduino would be useful.
- An easy and integrated way of monitoring some servo signals from the Ardupilot would allow for greater functionality.
- Jumpers for led operation to reduce power consumption for long duration operation.
- External power switches for easy operation and resetting of electronic equipment would make testing and operation significantly easier.

7 | Flight Testing - Benjamin James Oxley

Flight testing took place on the 25th of March, 2013 at Draycott Aerodrome with test pilot Paul Heckles. Mean temperature for the day was $1°C$, a sea level pressure of 1014.81 hPa and a wind speed of 25 km/h with a gust speed up to 44 km/h. Before flight testing began, a detailed flight plan was constructed in order to ensure all the desired information was gathered during test flying. This included flight plans, manoeuvres and testing of pre-defined autopilot routes.

7.1 Pre-Flight Issues

There were some issues with the Celsius tow plane used as it needed some repairs since it's previous use. Additionally the fuel needed to be removed and replaced as it had gone off from sitting for a year. In addition it had a broken undercarriage both front and rear. The horizontal stabiliser was loose and the fuel inlet port should have been clamped fully shut for flight by plugging it completely. The glow plug was also burnt out and stopped the plane from starting.
Once these problems were fixed the plane flew well and was powerful enough to launch the powered glider. The plane was difficult to fly with the powered glider and release mechanism attached. This helps to confirm that attaching the larger glider in a similar manner would not have worked well.

The pilot suggested a few issues with the powered glider that were modified to meet flight criteria. For remote control flight it is necessary to design the craft such that the centre of gravity lies under the centre of pressure of the wing. This meant it was necessary to ballast the front of the nose with approximately 100g to move the COG forwards. This worked well and the plane was still able to fly well and climb quickly.
Additionally, some of the flight surfaces should have been modified and strengthened in order reduce movement in the output due to loose connections. Push rods should be fabricated using z-bend pliers which are designed for the job of making these push-rods as this reduces sliding. The control horns should be aligned such that the push rod hole is aligned with the hinge so as to give equal rotational output in both directions for the linear input.

The glider required less modifications to be ready for flight but needed a heavy re-arrangement of components in order to meet the remote control flight requirements. Additionally 100g was stuck to the nose to bring the COG under the wing. The rudder was also loose and was glued in for security. The mechanical release mechanism for towing the plane worked well and was much more useful than a nichrome cut-down as it allowed for a quick turnaround of the system from landing to launch due to it's simplicity and direct compatibility with the remote control system. The test pilot also suggested that any towing system should be releasable from both ends (the tow plane and the glider) for safety. The glider has very little polyhedral in comparison to the powered glider, the pilot commented that the glider was slightly less stable as a result of this. At low speeds, this is expected as most of the dihedral comes from wing deflection at nominal flying speeds.

Figure 7.1: Powered glider mounted on Celsius

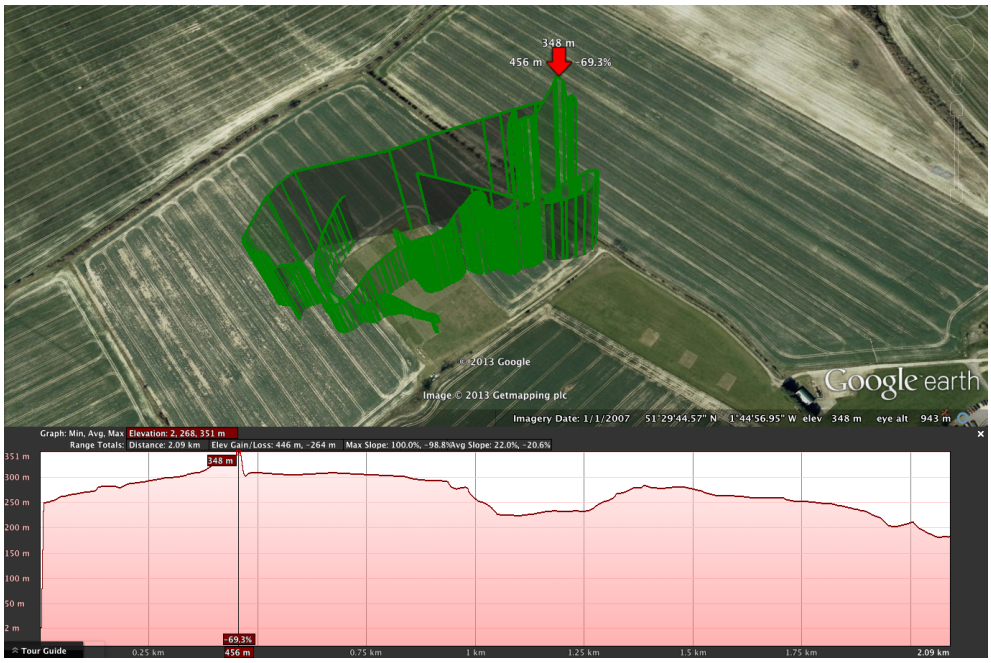

Figure 7.2: Google Earth graph of flight altitude and path

7.2 Flight Tests

7.2.1 Powered Glider Test One

The glider was taken up to release height on the large Celcius plane and released at an altitude of 187m where it dove momentarily to pick up speed and then levelled out. A set of manoeuvres were undertaken to establish controllability and flight speed. The plane released well and was stable in flight, it was still a little unstable and pulled up too easily. On the second flight more weight (30g) was added to the nose in order to increase stability. The plane was capable of climbing in flight which suggests that catapult launching will be probable. Analysis of the telemetry showed that prior to release, the Ardupilot reset in mid-air. This suggests some issues with power causing a reset. The latest firmware version was 2.68 and was then upgraded to 2.70 after flight testing to determine if this version of the firmware was the issue.

Figure 7.3: Powered glider coming in to land

The flight took 3 minutes, 7 seconds and consumed 1890mAh of charge as indicated by the battery charger when recharging the battery afterwards.

7.2.2 Powered Glider Test Two

Flight two was undertaken directly after the first test, the autopilot was reprogrammed with a set of way points around the airfield that would demonstrate way point following, craft manoeuvrability and in-air way point control. The glider was release and fell into a flat spin as the Ardupilot reset. It then re-initialised mid-air and recovered for a few seconds before crashing again. The glider again fell into a flat spin and crashed at low velocity. It is likely that there is an issue with the ESC used, a higher quality ESC and separate BEC or separate power supply for the servos and Ardupilot may be worthwhile and as more weight is needed in the nose for ballast, a separate power supply could be added here. Total time for both flights is 3 minutes, 23 seconds. Approximately 80% of the time, the motor was on and when charging the battery back to full charge, 1890mAh of charge was absorbed. This is in line with the approximate rate of discharge calculated. However, if the plane was to fly at it's slowest level speed then this may be extended to approximately 15 minutes flight time.

7.2.3 Glider Flights Summary

We were unable achieve glider tow launch for the sea plane as the test pilot deemed that the pilots were not skilled enough to do a glider tow and so an effective winch launch was devised. A set of launches were done using this method and it was flown into the wind and released from the towing mechanism. Although it only reached a maximum height of 20m (approximately) it was possible to roughly test the system and check control surfaces and glider ratio. The glider was slightly damaged on one hand launch where it collided with the ground and cracked the wing-box partially. The glide ratio seemed acceptable from visual inspection but requires some corroboration with telemetry.

7.2.4 Further Work

Most of the further work required on the airframes is discussed in chapter 8 but as a direct result of flight testing the following issues were identified and discussed:

- The centre of gravity requires modifying for further flight tests.
  On both planes the centre of gravity was too far back for model scale flight, for further flight testing the planes will either need redesigning or ballasting to bring the centre of gravity forwards.

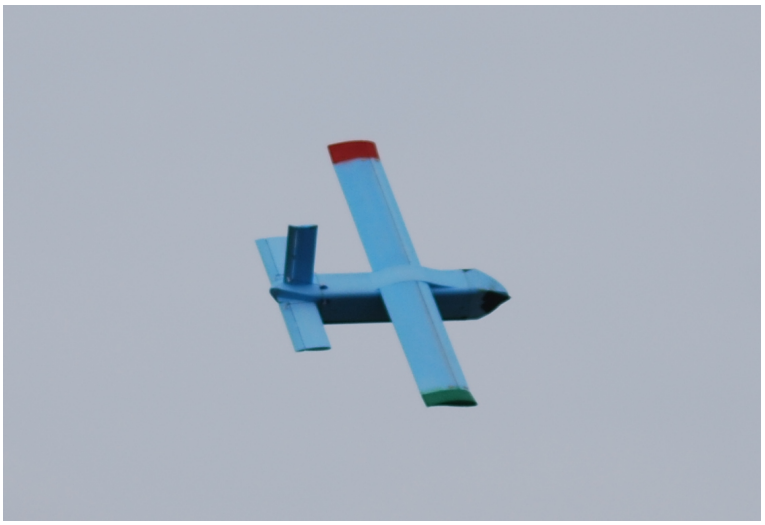

Figure 7.4: Glider in flight

- Designing a Removable Nose
  A removable nose or an easier way of priming the release mechanism would make set-up and launch faster for the drifter deployment glider.
- Modification of the autopilot system.
  Due to the electronics issues outlined above it was not possible to test the functionality of the autopilot system. For future testing, the reliability of the autopilot needs establishing.
- Waterproofing of the buoy cylinder
  For water testing the drifter needs properly sealing with silicon sealant to ensure water tightness. As it is likely to be in the water for multiple days it is imperative that the cylinder is completely watertight and also completely free from humidity internally.
- Nylon inserts in fuselage release
  The fuselage release mechanism damages the edges of the holes from continuous and repeated use, nylon inserts should be used (as they are self-lubricating) to protect the release mechanism holes and distribute the load to the foam.
- External power switches
  For safety and calibration, an external power switch would make operation of the powered glider safer and easier. The same is true of the drifter deployment glider, however this will inherently need two external switches (one for each battery).
- Elevator modifications
  The elevators need modification to reduce "play" in the controls and ensure the system is responsive and controllable.

8 | Conclusions and Further Work

8.1 Conclusions

During the course of this project a large amount of work has been undertaken to modify the GDP 16 (2012) UAV into a powered glider, in order to extend its range or endurance, dependent on the mission requirement.

In addition, a complex balloon launched Lagrangian ocean drifter has been developed. The development of this system included the design and manufacture of a drogue-buoy pair, a suitable means for transporting the drifter from the balloon to the ocean and electronics development to enable efficient sub-system integration. To meet the requirement of a suitable means of drifter deployment an unmanned aerial glider was developed from concept to flight test.

8.1.1 Powered Glider

The previous year's GDP 16 glider has been successfully redesigned into a powered glider to enable it to climb for testing purposes and have significantly extended the range. An additional outcome of this is the ability to extensively loiter and survey aerial sites during glide and then continue on to another defined way-point.
Flight testing highlighted issues with electronics reliability that need to be addressed before further testing is undertaken. However, from the flight testing completed to date it can be concluded that the glider is stable, albeit with ballast to meet the pilot's requirements. It is also easy to fly and requires minimal changes to be launched from a high altitude balloon. The added elevators performed sufficiently and enable suitable pitch control.
Testing, including wind tunnel testing, and simulation through MatLab allowed for the comparison of physical tests and theoretical calculations which were shown to have satisfactory correlation.
Fabrication of new components and redesign of the nose and tail sections has resulted in an improved design, built on a solid initial foundation. This system offers a more compact and low cost alternative to commercial products and could act as a good base for further atmospheric research.
Although the Celcius aircraft and associated piggyback mechanism provide a suitable test-bed, the fact that the glider has been shown to climb in its current configuration means that it could easily be launched from a catapult mechanism.

8.1.2 Balloon Launched Lagrangian Drifter

The design of a balloon launched Lagrangian ocean drifter has presented a low cost alternative solution to the current SVP Lagrangian drifter design and method of deployment.

Drifter
The drifter system has undergone a lot of development to become fully operational and reliable. The optimisation techniques developed allowed for prioritisation between interdependent characteristics and have resulted in a low cost and compact final design. However, in further analysis some of the assumptions could be replaced by further hydrodynamic stability considerations which would act to obtain a more reliable design considering the harsh operating conditions expected.

The current iteration of the buoy is unstable when uncoupled from its drogue, which limits its potential use as both a subsurface and surface drifter. Further development could improve the watertight seal, buoy robustness and provide a more efficient weight distribution, improving the stability through the

consideration of non conventional shapes. The potential for the drifter to be used for both surface and subsurface applications may wish to be considered, as it would improve the potential commercial suitability of such a system.

Drogue
The design of the drogue constituted a disproportionate amount of project time and resources considering the limited depth of analysis and testing that has been completed to reach the current configuration. The drogue design, by water tank testing, was shown to deploy reliably and quickly with a sink weight of $300g$ attached to the bottom. Additionally, the drogue has an approximate packing ratio of 20:1 and thus enables the whole drifter system to be delivered by an aerodynamically efficient glider.

The drogue design comprised of a number of strong assumptions, from which it is believed the current system would provide a suitable water following capability, albeit with a higher slip velocity than a current SVP Lagrangian drifter. The main reasons for this are the competing system requirements, such as, high drogue mass during drifting with a low mass during flight in order to reduce the required size and hence improve the efficiency of the glider. Unfortunately due to the lack of suitable skills within the group, combined with the number of higher priority project requirements and the limited capabilities of the University water tank, no drogue slip velocity tests were completed.

Drifter Deployment Glider
Wind tunnel testing, CFD studies, and, structural calculations and FE analysis have been completed during the design process, which enabled successful flight testing to be completed.

Although not all planned flight tests were performed for a multitude of reasons including, weather conditions, availability of suitable pilots and the desired method of glider launch, the limited flight testing proved to be useful. From pilot feedback during testing a number of additional issues were identified which will require careful redesign and development as discussed further in section 8.2.

The complex requirement for suitable subsystem integration led to the design, development and manufacturing of a custom made PCB and a suitable method of power regulation. The custom electronics enabled the in-flight power source to be mounted externally to the surface buoy, ultimately reducing the size of the overall system, due to the interdependence of design variables. The lack of group members with suitable skills to develop the complex electronics resulted in a high reliance on one group member.

The deployment glider has shown to reliably deploy its payload over a range of angles of attack. The glider is ideally suited as a disposable deployment solution and most of the valuable components are the electronics which are kept safely within the drifter, significantly decreasing the cost, should the drifter be recovered.

Furthermore, a nichrome wire balloon release mechanism has been developed for use with the glider to enable a lightweight, low cost and disposable solution for balloon release. Although, testing in a laboratory environment has successfully been completed, further testing for confidence in reliability is required prior to balloon launched flight tests.

The process of concept development and iterative refinement of concepts has produced a successful design capable of meeting the demanding project aims and objectives. Ideally, it would be worthwhile to further optimise the fuselage, wing and release mechanism designs in order to drive down the glider size, cost and manufacturing time. A compact lightweight disposable UAV for oceanographic means has been developed. Without much further work a novel, lightweight surface drifter could be developed by neglecting the requirement for a drogue.

8.2 Recommendations

The following section addresses the key recommendations for future development of both the powered glider and balloon launched Lagrangian drifter UAVs. The recommendations are formed from a combination of uncompleted objectives, group experience and test pilot feedback.

8.2.1 Powered Glider

Catapult launching

As previously mentioned, catapult launching formed a viable alternative to piggyback launching, however to enable the propeller to clear the gantry of the catapult, the propeller sizing analysis would need to be revisited. Should the propeller sizing be altered then further analysis from either, piggyback launch flight tests or wind tunnel tests would be required for confirmation of the gliders ability to climb. An alternative approach would be to modify the catapult gantry.

Motor response lag

The ESC timing is believed to be incorrectly set-up for the motor used and this results in a sluggish change in throttle response to propeller RPM. This can be rectified by purchasing a ESC programming card, changing and testing the timing.

New pitot tube for airspeed

As a new fuselage is required for further testing due to the damage sustained on the second flight test, it would possible to easily replace the current pitot tube with a combined pitot-static tube, which could be placed in the nose and more easily calibrated. This is less likely to be damaged upon impact than mounting the pitot tube on the fuselage upper surface.

Foam properties

During this project it was difficult to source the original foam used in GDP 16, 2012 for the glider manufacturing. It is believed the 30g/l EPP quoted as the final foam choice is incorrect, using a sample of the original foam and consulting the expertise of Hampshire Insulation it was determined that the closest equivalent was an 18g/l EPP. However, this alternative foam was more brittle than the original. It is suggested that a lower density foam is sourced from a wider range of suppliers to reduce the risk of brittle failure on impact, such as landing. Additionally, it should be noted that the wire burn diameter of the $18g/l$ foam was approximately $0.5mm$ less than the original. Therefore careful modification of the fuselage dimensions was required for an accurate sliding fuselage. This becomes increasing difficult with the use of multiple foam properties. Having said this, individual components could benefit from the use of a variety of foams dependent on the component application. The limiting factor for this would be the minimum bulk order of specific foams and the allocated time for manufacture.

8.2.2 Balloon Launched Lagrangian Drifter

Improved control surfaces and linkages

The test pilot deemed the control surfaces to have too much "play" in their motion and structurally inadequate for long term use. The surfaces should be re-designed to reduce movement by mounting the control horns more securely. A suggested method is to laminate the region of control horn contact with a thin plywood and ensuring they align with the rotational axis of the hinge. Additionally for manufacturing the control rods the use of z-bend pliers would be advantageous to bending the rods by hand, doing this would help to reduce the play in the control surface mechanism.

Meet model aircraft requirements for COG

Although the design process followed a commonly used process for determining optimal COG, both aircraft were deemed unsuitable to fly. For remote control aircraft it is a general requirement that the COG

is placed at the aerodynamic centre of the wing. This would be difficult to accomplish for this aircraft due to the mass of the drogue. Should the drogue be redesigned so that the mass could be situated closer to the nose section of the aircraft during flight, it may be possible to bring the COG closer to the aerodynamic centre of the wing. An additional method to bring the centre of gravity forwards could be to design a hollow tail section for the aircraft. However, as the density of the foam is low, the mass saved is unlikely to change the COG considerably.

Create nylon inserts for the release holes

Even though the release mechanism was designed so that the carbon release pins move parallel inside the holes, the foam is damaged on the edges after a number of releases due to the inherent difficulty in aligning the fuselage sections precisely. To prevent further damage, Nylon inserts could be placed inside the holes, which would also act to reduce the coefficient of friction.

An improved manufacturing and packing method for the drogue

Ideally, the drogue should be sown around circular metal rings but during manufacturing it was noted that the stiffeners are not all evenly circular. It would be beneficial to undertake further research and analysis into drogue design.

Analysis of drogue slip velocity & catenary

A full scale drogue test is required to obtain the true water following properties of the drogue. The analysis completed with in this report was constricted in scope by the assumptions that had to be made due to the complexity of the problem. Additionally it would be advantageous to investigate the effect of the subsurface current profile on the drogue catenary and thus quantify the critical current speed and required drogue ballast to remain in a suitable orientation.

Flight testing release mechanism

For the balloon launched Glider to be flight tested via a glider tow, the current release mechanism would be required to be releasable from both ends (from the glider and the towing plane). Additionally, the attachment for the towing mechanism should be moved to a point about the COG of the aircraft. If a bigger RC plane can be used, then the piggyback attachment developed for the powered glider can be used but has to be redesigned to fit on the new wing profile and to accommodate the wider fuselage.

Implement roll control

The current limitations of the deployment glider are the lack of roll control as ailerons have not been included. It has been shown that as the airspeed increases the wing deflection, as expected, increases. Therefore, the effective dihedral and lateral stability increase. However, as found during flight testing, although the glider is designed to be launched from an altitude of $10km$ where roll control could be negated, it would be advantageous to include some roll control for further flight testing. The additional control would act to prevent damage to the glider and increase the range of weather conditions suitable for launch. Instead of adding ailerons to the current design it is believed the use of elevons controlled separately by the Ardupilot would be the most suitable, low cost and lightweight solution.

Complete further drifter tests in water

It would be extremely beneficial to physically test the drifter in an open sea environment, where it can be left to drift for multiple weeks and upload its position via the telemetry link. This would validate the buoy's capabilities and inform the changes that would need to be made for the next version of the design.

Design and build of a new buoy shape

The current cylinder design is marginally stable when the drogue is attached, however, when the currents reduce the tension on the connecting line the cylinder will no longer be stable and will sit flat on the water. A tapered cone design would be a more optimal shape where the main ballast would sit in the thinner part of the buoy. This would make for a much more stable design. Such a cylinder could be produced easily to be fitted to the electronics and plane system by 3D printing the casing and coating with glass fibre for strength and water resistance.

8.2.3 Additional recommendations

Finite element analysis

The FEA undertaken has encountered problems in converging and modelling realistic results. The theoretical calculations have provided the best estimation of beam bending in the wind spars. If a full FE analysis for the wings, spars and wing-box as a system could be successfully modelled in-depth then a more optimal, lighter system could be designed by focusing reinforcement on the high-stress regions. Use of better non-linear foam material models would also be essential in properly understanding the stresses present in the current design.

MatLab flight prediction

To further expand on the results of the MatLab simulation, wind tunnel testing results could be fitted, using a suitable method to a polynomial function. This could then act as a lookup table in order more accurately model the C_L vs α curve. Additionally, for high altitude flights, a simple logic system could be developed to help model the behaviour of the autopilot system. With further work the MatLab tool could be used to aid the design process from to choose the optimal flight profiles for range or endurance.

8.2.4 Future Applications

In addition to basic oceanographic surface measurements such low cost, easily deployable buoys may have other uses. Such a suggested use is an application in oil spill monitoring as the ease of rapid deployment and lows cost would allow the buoys to monitor the position and range of spreading oil.

The system could also be modified to act as a reliable surface current drifter where there would be no requirement for a drogue.

A | Powered Glider Gantt Chart

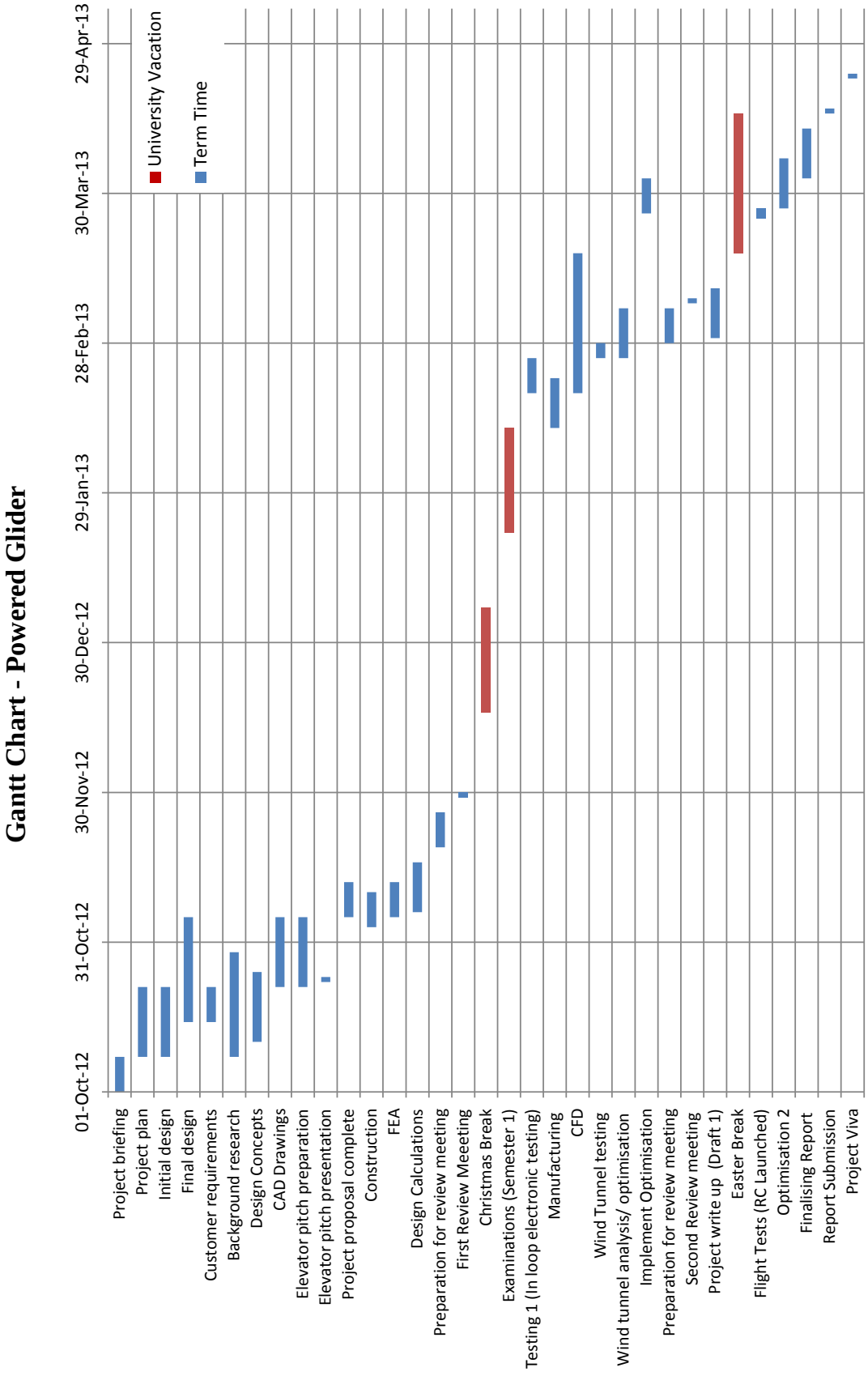

Figure A.1: Powered Glider Gantt Chart

B | Balloon Launched Lagrangian Drifter Gantt Chart

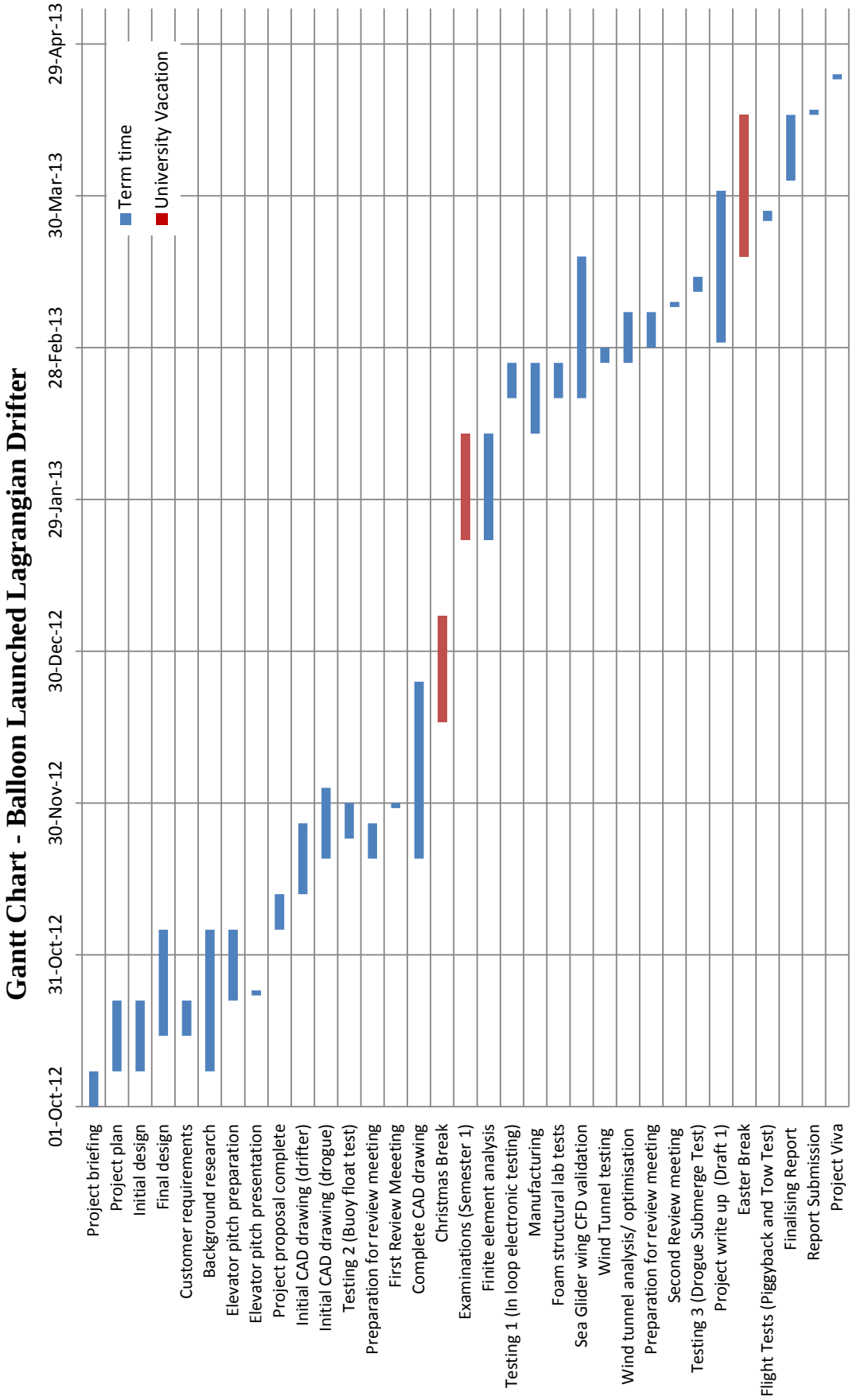

Figure B.1: Balloon Launched Lagrangian Drifter Gantt Chart

C | Criticality Matrix

	Failure	Effects	Precautions	Severity (0-10)	Probability (1-10)	Detection (1-10)	Risk Priority Number
Motor Mount	Motor mount fails structually due to fatigue, creep, etc.	Motor falls off, propeller may damage aircraft, aircraft able to glide depending on damage	Constantly check for any cracks that may have started to form on the motor mount	5	8	6	240
	Motor mount plate melts from motor overheating	Toxic gas released, damage to motor mount plate, propeller thrust angle changes, adverse effects on aircraft	Make sure that the motor is not overworked and is not touching the mount plate	3	1	7.5	22.5
	Motor mount dislodges from aircraft due to propeller exerting force if hitting ground	Severe damage to aircraft and components, loss of propulsion system	Stop running the motor when the aircarft is a meter above ground	7	2.5	0.1	1.75
	Motor mount screw comes loose due to vibration	Motor mount plate falls off, propeller may damage aircraft, aircraft able to glide depending on damage	Check whether the screws are loose before and after every flight	4	2	8	64
Motor and Propeller	Propeller fails to deploy	Aircraft glides, loss of propulsion generation, motor remains on thus wasting battery	Do ground testing to check if propeller folds out, put lubricant to ease deployment	2	3.33	8	53.28
	Loss of motor power	Loss of propulsion generation, aircraft able to glide	Check that the battery is fully charged before flight, check if the connections between power source and motor is secure	1	3.5	4	14
	Motor overheats	Damages motor mount plate, could cause fire, release of toxic gas	Make sure the autopilot does not overwork the motor, take note if steam is coming out of the motor	6	2	5	60
	Motor screws come loose due to vibration	Motor falls off, propeller may damage aircraft, aircraft able to glide depending on damage	Check whether the screws are loose before and after every flight	4	2	8	64
	Propeller off failure from motor shaft	Propeller may damage aircraft and/or personnel, loss of propulsion generation, aircraft able to glide depending on damage	Check whether the propeller is mounted onto the motor shaft correctly and securely	6	3.5	7	147
Tailplane	One elevator servo fails	Aircraft may spiral if one servo position is different from the failed servo, longitudinal stability affected	Check whether the servos are working correctly before everyflight	7	1	7	49
	Servo linkage breaks	Aircraft loses pitch authority, adverse affects on aircraft due to elevator flapping	Check the linkages are secure before flight	8	4	8	256
	Servo dislodges elevator due to overpower	Aircraft loses pitch authority, adverse affects on aircraft due to elevator removal	Check whether the servos are working correctly before everyflight	8	0.5	8	32
Electronicsw	Loss of power to electronics	Loss of power to propulsion generation, loss of power to control surfaces, aircraft able to glide	Check that the battery is fully charged before flight, check if the connections between power source and electronics are secure	1	1	4	4
	Autopilot malfunction	Aircraft flight disturbed and flight path may become arbitrary/unpredictable, may require manual control	Make autopilot to do self testing	5	2	5	50
	Battery Explodes	Catastrophic failure to aircraft	Prevent battery from exposure to high temperatures	10	0.1	0.1	0.1

Figure C.1: Criticality matrix

D Stability Calculations

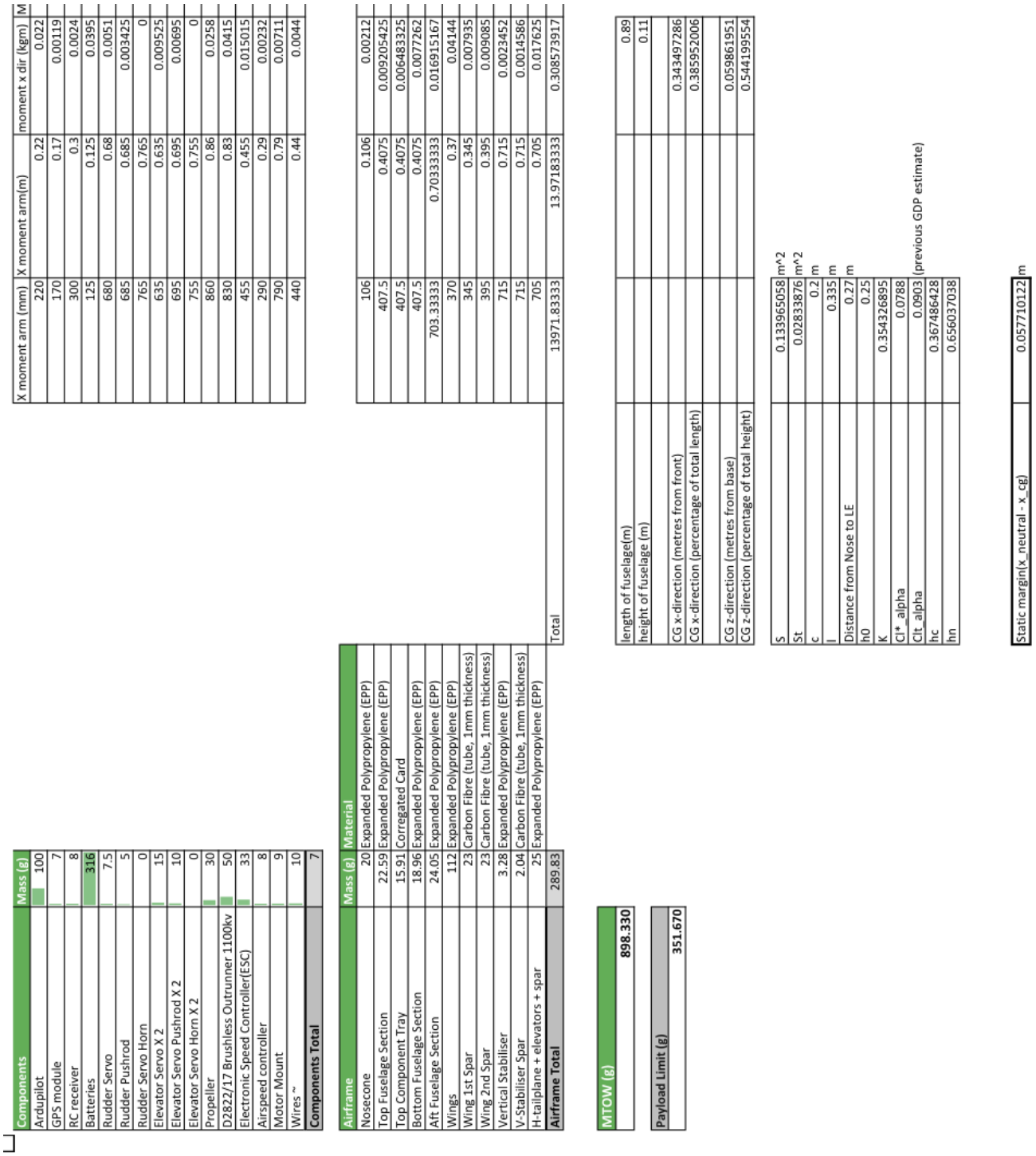

Components	Mass (g)
Ardupilot	100
GPS module	7
RC receiver	8
Batteries	316
Rudder Servo	7.5
Rudder Pushrod	5
Rudder Servo Horn	0
Elevator Servo X 2	15
Elevator Servo Pushrod X 2	10
Elevator Servo Horn X 2	0
Propeller	30
D2822/17 Brushless Outrunner 1100kv	50
Electronic Speed Controller(ESC)	33
Airspeed controller	8
Motor Mount	9
Wires ~	10
Components Total	7

Airframe	Mass (g)	Material
Nosecone	20	Expanded Polypropylene (EPP)
Top Fuselage Section	22.59	Expanded Polypropylene (EPP)
Top Component Tray	15.91	Corregated Card
Bottom Fuselage Section	18.96	Expanded Polypropylene (EPP)
Aft Fuselage Section	24.05	Expanded Polypropylene (EPP)
Wings	112	Expanded Polypropylene (EPP)
Wing 1st Spar	23	Carbon Fibre (tube, 1mm thickness)
Wing 2nd Spar	23	Carbon Fibre (tube, 1mm thickness)
Vertical Stabiliser	3.28	Expanded Polypropylene (EPP)
V-Stabiliser Spar	2.04	Carbon Fibre (tube, 1mm thickness)
H-tailplane + elevators + spar	25	Expanded Polypropylene (EPP)
Airframe Total	289.83	

MTOW (g)
898.330

Payload Limit (g)
351.670

X moment arm (mm)	X moment arm(m)	moment x dir (kgm)	M
220	0.22	0.022	
170	0.17	0.00119	
300	0.3	0.0024	
125	0.125	0.0395	
680	0.68	0.0051	
685	0.685	0.003425	
765	0.765	0	
635	0.635	0.009525	
695	0.695	0.00695	
755	0.755	0	
860	0.86	0.0258	
830	0.83	0.0415	
455	0.455	0.015015	
290	0.29	0.00232	
790	0.79	0.00711	
440	0.44	0.0044	

106	0.106	0.00212	
407.5	0.4075	0.009205425	
407.5	0.4075	0.006483325	
407.5	0.4075	0.0077262	
703.33333	0.70333333	0.016915167	
370	0.37	0.04144	
345	0.345	0.007935	
395	0.395	0.009085	
715	0.715	0.0023452	
715	0.715	0.0014586	
705	0.705	0.017625	
Total	13971.83333	13.97183333	0.308573917

length of fuselage(m)		0.89
height of fuselage (m)		0.11
CG x-direction (metres from front)		0.343497286
CG x-direction (percentage of total length)		0.385952006
CG z-direction (metres from base)		0.059861951
CG z-direction (percentage of total height)		0.544199554

S	0.133965058	m^2
St	0.02833876	m^2
c	0.2	m
l	0.335	m
Distance from Nose to LE	0.27	m
h0	0.25	
K	0.354326895	
Cl*_alpha	0.0788	
Clt_alpha	0.0903	(previous GDP estimate)
hc	0.367486428	
hn	0.656037038	

Static margin(x_neutral - x_cg)	0.057710122	m

Figure D.1: Stability table

E | Pareto Front Optimisation of Glider Dimensions

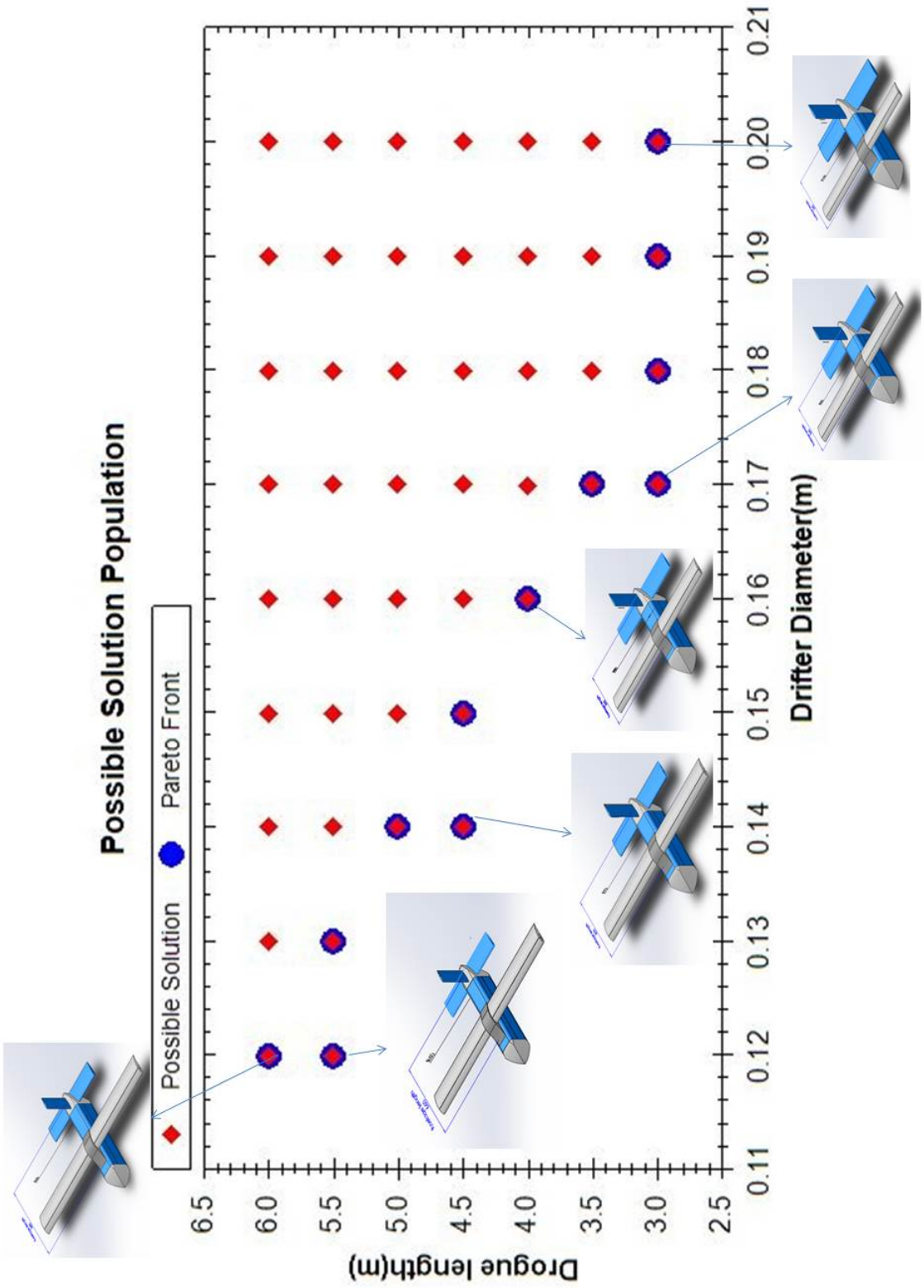

Figure E.1: Pareto front with respective glider dimension

F | Electronics Schematics

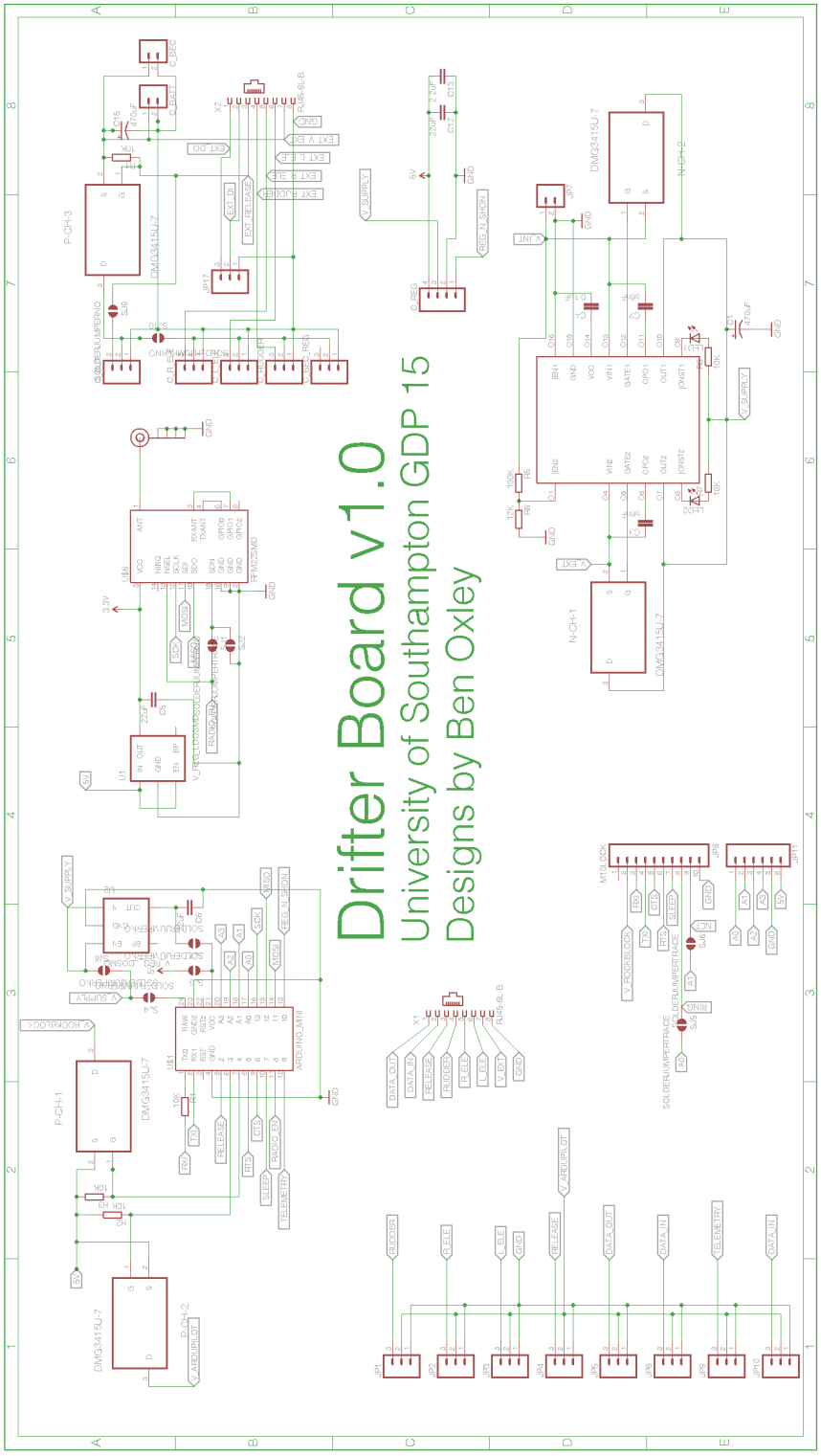

Figure F.1: The schematic for the power systems board

G | Bibliography

[1] "Drag Coefficient." [Online]. Available: http://www.engineeringtoolbox.com/drag-coefficient-d_627.html

[2] (1999) Wing and tail plane design. Scribd. [Online]. Available: http://www.scribd.com/doc/50227650/Wing-and-Tailplane-Design-08-05.

[3] (2007) Structured vs unstructured mesh. CFD Node. [Online]. Available: http://www.cfdnode.com/topics-disp.php?topNo=07

[4] (2008) Introducing pareto front evaluation as a concept for objective evaluation of inverse planning and delivery techniques). European Society for Therapeutic Radiology. [Online]. Available: http://www.medicalnewstoday.com/releases/122378.php

[5] (2009) Fluent 12.0 getting started guide. ANSYS Inc. [Online]. Available: www1.ansys.com/customer/content/documentation/.../fluent/flgs.pdf

[6] "Warrior (Aero-Marine) - Gull UAV - Introduction," 2011.

[7] "Easy Composites," 2012. [Online]. Available: http://www.easycomposites.co.uk/

[8] (2012) Xflr5 disclaimer. [Online]. Available: http://www.xflr5.com/xflr5.htm

[9] (2013) A sample atmosphere table (si units). Public Domain Aeronautical Software (PDAS). [Online]. Available: http://www.pdas.com/m1.html

[10] About.com. (2013) General properties of steels. [Online]. Available: http://metals.about.com/od/properties/a/General-Properties-Of-Steels.htm

[11] Airliners.net. Advantages of a t-tail vs a conventional tail. [Online]. Available: http://www.airliners.net/aviation-forums/tech_ops/read.main/138595/

[12] Alibaba.com. (2012) High quality plastic 3d printer filament. [Online]. Available: http://esun.en.alibaba.com/product/375819931-213475262/high_quality_plastic_filament_3D_printer_PLA_ABS_PVA_welding_rods.html

[13] A. P. Analysis, "Chapter 3 Drag Force and Drag Coefficient," vol. 2, pp. 1–41, 2009.

[14] C. Anderson. (2013) Inverted v-tail advantages. [Online]. Available: http://diydrones.com/profiles/blogs/inverted-vtail-advantages

[15] J. D. Anderson, *Computational Fluid Dynamics: The Basics with Applications*. McGraw-Hill, 1995.

[16] ——, *Fundamentals of Aerodynamics*. McGraw Hill, 2007.

[17] APEX, D. Saul, and P. Patel, "Launch 1 | ApexHAB," 2011. [Online]. Available: http://www.apexhab.org/alpha/launch-1/

[18] M. F. Ashby, *Materials Selection in Mechanical Design*. Butterworth-Heinemann, 2004.

[19] Atmel, "8-bit Atmel Microcontroller with 64K/128K/256K Bytes In-System Programmable Flash ATmega640 / V ATmega1280 / V ATmega1281 / V ATmega2560 / V ATmega2561 / V," Tech. Rep., 2012. [Online]. Available: http://www.atmel.com/Images/doc2549.pdf

[20] O. U. Baran, *Control Methodologies in Unstructured Hexahedral Grid Generation*. Vrije Universteit Brussel, 2005.

[21] A. biz Ltd. (2010) Air tractor at401b olney. [Online]. Available: http://www.us.all.biz/air-tractor-at401b-g9495

[22] M. J. C. . G. A. Blaisdell, "Numerical simulations of a wingtip vortex in the near field," *Journal of Aircraft*, pp. 230–243, 2009.

[23] F. Bormann. (2006) Borjet aeromodels. [Online]. Available: http://www.borjet.de/

[24] M. Brungard, "Equilavent Dihedral Calculator." [Online]. Available: www.charlesriverrc.org/articles/design/eda1.xls

[25] Bulgin, "Ethernet Buccaneer Âő," pp. 43–48, 2013.

[26] CAA (Safety Regulation Group), "CAP 393 Air Navigation : The Order and the Regulations."

[27] ——, "CAP 722 Unmanned Aircraft System Operations in UK Airspace âĂŞ Guidance."

[28] J. Calvert and R. Farrar, *An Engineering Data Book*, 3rd ed. Palgrave Macmillan, 2008.

[29] Codecogs. (2004) Cantilever beam. [Online]. Available: http://www.codecogs.com/users/23287/Cantilever-Beams-101.png

[30] P. Composites. (2012) Mechanical properties of carbon fibre composite materials, fibre / epoxy resin. [Online]. Available: http://www.performance-composites.com/carbonfibre/mechanicalproperties_2.asp

[31] D. Corp. (2010) Plastic properties of nylon (polyamide). [Online]. Available: www.dynalabcorp.com/technical_info_nylon.asp

[32] CPRegier. (2013) Material selection. [Online]. Available: http://develop3d.com/images/lightbox_images/Modulus_density_chart_LB.jpg

[33] Dassault Systèmes, "Creating a Coupled Eulerian- Âŋ Lagrangian Model."

[34] ——, "Abaqus Technology Brief Water Landing of Space Flight Re-entry Vehicles Using Abaqus / Explicit," pp. 1–4, 2011.

[35] S. Database. (2013) Futaba s3114m - micro high-torque servo w/micro plug. [Online]. Available: http://www.servodatabase.com/servo/futaba/s3114m

[36] Dimension. (2013) 1200es 3d printer series. [Online]. Available: http://www.dimensionprinting.com/3d-printers/printing-productspecs1200series.aspx

[37] ——. (2013) Faqs. [Online]. Available: http://www.dimensionprinting.com/3d-printers/3d-printing-faq.aspx

[38] M. Drela, "Low-Reynolds-Number Airfoil Design for the M.I.T. Daedalus Prototype- A Case Study," *Journal of Aircraft*, vol. 25, no. 8, pp. 724–732, Aug. 1988. [Online]. Available: http://arc.aiaa.org/doi/abs/10.2514/3.45650

[39] E. Y. Eagles. (2013) Velocity aircraft velocity. [Online]. Available: http://www.youngeagles.org/photos/gallery.asp?action=viewimage&categoryid=17&text=&imageid=1124&box=&shownew=

[40] Energizer, "Energizer L91 - Ultimate Lithium," pp. 1–2, 2009. [Online]. Available: http://data.energizer.com/PDFs/l91.pdf

[41] P. Engineering, "Wing Spanwise Lift Distribution:Schrenk Approximation," 2001. [Online]. Available: http://www.lightaircraftassociation.co.uk/2010/Engineering/Design/schrenkapproximation.pdf

[42] A. G. et.al., *Lagrangian Analysis and Prediction of Coastal and Ocean Dynamics*. Cambridge University Press, 2007.

[43] EzineMark. (2013) The advantages of modern foam cutting methods. [Online]. Available: http://foam.ezinemark.com/the-advantages-of-modern-foam-cutting-methods-31de222ce7f.html

[44] F. Foam. (2012) Epp or eps: Which foam is best? [Online]. Available: https://www.flyingfoam.com/content/eps-or-epp-which-foam-best

[45] Fortus. (2012) Ppsf. [Online]. Available: http://www.stratasys.com/materials/fdm/~/media/Main/Secure/Material%20Specs%20MS/Fortus-Material-Specs/Fortus-MS-PPSF-01-13-web.ashx

[46] E.-T. A. E. Forum. (2005) Engine locations. [Online]. Available: http://www.eng-tips.com/viewthread.cfm?qid=140936

[47] GDP16, *Balloon Launched Glider*. University of Southampton, 2012.

[48] A. Gerasimov, "Modelling turbulent flows," *FLUENT*, 2006.

[49] R. Geyer, "Field Calibration of Mixed Layer Drifters," *American Meteorlogical Society*, vol. 6, pp. 333–342, 1988. [Online]. Available: http://journals.ametsoc.org/doi/pdf/10.1175/1520-0426(1989)006%3C0333%3AFCOMLD%3E2.0.CO%3B2

[50] GlobalTop Technology Inc., "FGPMMOPA6H GPS Standalone Module Data Sheet," pp. 1–37, 2011.

[51] P. Gyre, “SVP Price List,” no. 760, pp. 0–1, 2012.

[52] HomebuiltAirplane.com. (2013) Single versus twin tail. [Online]. Available: http://www.homebuiltairplanes.com/forums/aircraft-design-aerodynamics-new-technology/3515-single-versus-twin-tail.html

[53] F. Inc, *10.2.4 The Spalart-Allmaras Model.* Lebabnon, 2003.

[54] ——, *10.2.8 The Standard k-ÏĽ model.* Lebabnon, 2003.

[55] ——, *10.9.3 Near-Wall Mesh Guidelines for the Spalart-Allmaras Model.* Lebabnon, 2003.

[56] ——, *6.2.2 Mesh Quality.* Lebabnon, 2003.

[57] InvenSense, “MPU-6000 and MPU-6050 Product Specification,” pp. 1–54, 2012.

[58] T. Javaherchi, *Review of Spalart-Allamras Turbulence Model and its Modifications.* Northwest National Marine Renewable Energy Center, 2010.

[59] D. Johnson, R. Sotcker, D. Byrne, R. Head, J. Imberger, and C. Pattiaratchi, “A Compact , Low-cost GPS Drifter for Use in the Oceanic Nearshore Zone , Lakes and Estuaries,” *Journal of Atmospheric and Oceanic Technology*, 2000.

[60] J. Katz, *Race Car Aerodynamics: Designing for Speed.* Bentley Publishers, 2006.

[61] D. Kim, J, “SESA 2009: Mechanics of Flight,” in *Mechanics of Flight*, University of Southampton, 2010, p. Lecture Notes.

[62] E. T. K.J Rawson, *Basic Ship Theory.* Butterworth-Heinemann, 2001.

[63] L. A. Laboratory, “Effect on stability and control of a pusher propeller behind conventional tail surfaces as determined by tests of a powered model in free-flight tunnel,” 1943.

[64] Q. F. Lee, *CFD Grid Generation Methods.* ChmlTech Ltd, 2005.

[65] Linear Technology Corporation, “LTC4353 - Dual Low Voltage Ideal Diode Controller,” pp. 1–16, 2012.

[66] D. D. Liu, “Aerodynamic and mass balance effects on control surface flutter,” *Flutter Prevention Handbook: A Preliminary Collection*, pp. 1–24, 1996.

[67] LTW, “LTW Waterproof Serial Socket,” 2003.

[68] R. Lumpkin and M. Pazos, “Measuring surface currents with Surface Velocity Program drifters : the instrument , its data , and some recent results,” National Oceanographic and Atmospheric Administration, Tech. Rep., 2005.

[69] Marlin-Yug-LTD, “SVP / RTC Mini Lagrangian Drifter,” p. 540450, 2009.

[70] ——, “SVP-B / RTC Lagrangian Drifter,” p. 540450, 2009. [Online]. Available: http://marlin-yug.com/productfile/SVP-B.pdf

[71] ——, “SVP Surface Lagrangian Drifter,” no. January, p. 540450, 2009.

[72] Maxtena, “Iridium Patch Antenna.” [Online]. Available: http://www.m2mconnectivity.com.au/sites/default/files/brochures/mpad254-1621.pdf

[73] ——, “Iridium Certified Antenna,” 2012.

[74] Measurement Specialties, “MS5611-01BA01 MS5611-01BA01 Barometric Pressure Sensor,” pp. 1–20, 2012.

[75] F. Menter, “Zonal two equation k-ÏĽ turbulence models for aerodynamic flows.” *AIAA Paper*, pp. 93–2906, 1993.

[76] ——, “Two-equation eddy-viscosity turbulence models for engineering applications,” *AIAA Paper*, pp. 1598–1605, 1994.

[77] R. Miles, Melhado.J, and E. Hughes, “Air-launched Expendable Micro-sized Wave Buoy,” *MTS-0-933957-28-9*, pp. 1867–1871, 1867.

[78] N. Minebea. (2010) Brushless dc motors. [Online]. Available: http://www.nmbtc.com/brushless-dc-motors/why-brushless-motors.html

[79] S. Mittal, “Prediction of Hysteresis Associated with the Static Stall of an Airfoil,” no. August 1999, 2000.

[80] T. T. Mk. Volume 1 principles of flight. [Online]. Available: http://www.scribd.com/doc/45224522/Complete-Aircraft-Aerodynamics

[81] E. Monahan, "Trends in Drogue Design," Department of Atmospheric and Oceanic science, University of Michigan, Tech. Rep., 1972.

[82] M. Mowlem and E. Waugh, "An Unmanned Aerial Vehicle For Oceanographic Application," Ph.D. dissertation, University of Southampton.

[83] Multicomp, "Multicomp STP Jack," 2012.

[84] S. Newman, *A Handbook of Aircraft Design.* University of Southampton, 2010.

[85] P. P. Niiler and C. Martin, "Global Drifter Programme Barometer Drifter Design Reference Global Drifter Programme Barometer Drifter Design Reference," no. 4, 2009.

[86] D. Nolan. (2009) Top 6 new very light jets. [Online]. Available: http://www.popularmechanics.com/science/space/4216980

[87] S. U. D. of Aeronautics and Astronautics. (1999) Engine placement. [Online]. Available: http://adg.stanford.edu/aa241/propulsion/engineplacement.html

[88] U. of Illinois. (2004) Materials selection and design. [Online]. Available: http://web.mse.uiuc.edu/courses/mse406/handouts/chX_selection.pdf

[89] T. U. of Iowa. (2013) Stability of a floating body. [Online]. Available: http://www.engineering.uiowa.edu/fluidslab/pdfs/57-020/stability.pdf

[90] M. I. of Technology. (2005) Materials and shape selection. [Online]. Available: http://ocw.mit.edu/courses/materials-science-and-engineering/3-080-economic-environmental-issues-in-materials-selection-fall-2005/lecture-notes/lec_ms2.pdf

[91] N. P. on Technology Enhanced Learning. (2010) Stability of floating bodies in fluid. [Online]. Available: http://nptel.iitm.ac.in/courses/Webcourse-contents/IIT-KANPUR/FLUID-MECHANICS/lecture-5/5-7_stability_floating_fluid.htm

[92] J. Online. (2010) Nichrome wire application calculator. [Online]. Available: http://www.jacobs-online.biz/nichrome/NichromeCalc.html

[93] PAR. (2012) Polycarbonate - plastic sheet. [Online]. Available: http://www.par-group.co.uk/UserDocs/Polycarbonate-Plastic-Sheet.pdf

[94] S. Part. (2012) Polyjet rapid prototyping. [Online]. Available: http://www.speedpart.de/eigene_dateien/pdf/dez2009/materialdatenblaetter-polyjet-neu.pdf

[95] M. Pazos, "All You Wanted To Know About Drifters," 2006.

[96] J. H. F. . M. Peric, *Computational Methods for Fluid Dynamics*, 3rd ed. Springer, 2002.

[97] A. M. Place. Rockwell commander 112 and 114.

[98] Plasticpedia. (2013) Rotational moulding. [Online]. Available: http://www.bpf.co.uk/Plastipedia/Processes/Rotational_Moulding.aspx

[99] C. Plastics. (2012) Polypropylene. [Online]. Available: http://www.copeplastics.com/polypropylene.html

[100] D. Plastics. (2012) Typical physical properties of moulded foams. [Online]. Available: http://www.dssmith-foamproducts.com/download/Materials-Matrix.pdf

[101] P.-M. Poulain, R. Gerin, E. Mauri, and R. Pennel, "Wind Effects on Drogued and Undrogued Drifters in the Eastern Mediterranean," *Journal of Atmospheric and Oceanic Technology*, vol. 26, no. 6, pp. 1144–1156, June 2009. [Online]. Available: http://journals.ametsoc.org/doi/abs/10.1175/2008JTECHO618.1

[102] A. Propellers. (1999) Apc suggested rpm limits. [Online]. Available: http://www.apcprop.com/v/html/rpm_limits.html

[103] S. Randall, "Balloon Data - Randomsolutions.co.uk," 2010. [Online]. Available: http://ukhas.org.uk/guides:balloon_data

[104] D. P. Raymer, *Aircraft Design: A Conceptual Approach.* American Institute of Aeronautics and Astronautics Inc. AIAA., 1999.

[105] RCfoam. (2012) Magic mount lightflight. [Online]. Available: http://www.rcfoam.com/product_info.php?cPath=152&products_id=908&osCsid=ceb3972dfdc38be52775808ec332fbb3

[106] ——. (2012) Plywood motor mount. [Online]. Available: http://www.rcfoam.com/product_info.php?cPath=152&products_id=933&osCsid=ceb3972dfdc38be52775808ec332fbb3

[107] RCGroups. Advantages/disadvantages of a v-tail versus regular rudder/elevator setup. [Online]. Available: http://www.rcgroups.com/forums/showthread.php?t=1342419

[108] N. A. Rotorwerks. (2010) Tractor engine advantages. [Online]. Available: http://pitbullrotorcraft.com/links/gyrolink.html

[109] R. Rq-b, "Raven rq-11b," p. 2187.

[110] M. Sadraey, *Aircraft Design: A Systems Engineering Approach*. Wiley Publications, 2012.

[111] C. Sailcloth. (2006) Fibermax stabilised nylon. [Online]. Available: http://www.challengesailcloth.com/nylon/fibermax.pdf

[112] F. Scientific. (2013) Bottle wide neck cylindrical 2l. [Online]. Available: https://webshop.fishersci.com/insight2_uk/getProduct.do?productCode=10648335&resultSetPosition=11

[113] M. S. Selig and T. O. Rto, "Low Reynolds Number Airfoil Design Lecture Notes VKI Lecture Series Various Approaches to Airfoil Design," no. November, pp. 24–28, 2003.

[114] Sky Circuits, "Sky Circuits Autopilot Systems," 2009.

[115] S. Srivastava. (2013) Properties of nichrome wire. [Online]. Available: http://www.buzzle.com/articles/properties-of-nichrome-wire.html

[116] M. J. Starink. (2012) Microstructural engineering for transport applications, chapter 1 (online lecture notes). [Online]. Available: https://blackboard.soton.ac.uk/bbcswebdav/pid-1740520-dt-content-rid-774740_1/courses/SESG6007-14388-12-13/META%28MJS2012%29%20Ch1.pdf

[117] Stratasys. (2012) Absplus. [Online]. Available: http://www.dimensionprinting.ru/Download/ABSplus.pdf

[118] T. Surface, V. Program, P. Gyre, N. Gps, N. American, G. D. Program, O. Drifting, B. Cooperation, and T. Argos, "SVP Lagrangian Drifter surface float drogue type :."

[119] P. Systems. (2012) Hdpe thermoplastic. [Online]. Available: http://tiefziehen.com/en/HDPE/

[120] ——. (2012) Ldpe thermoplastic. [Online]. Available: http://tiefziehen.com/en/LDPE/

[121] ——. (2012) Pmma thermoplastic. [Online]. Available: http://tiefziehen.com/en/PMMA/

[122] T. A. Talay, *Introduction to the Aerodynamics of Flight*. Scientific and Technical Information Office, National Aeronautics and Space Administration, 1975.

[123] TheEngineeringToolbox. (2012) Elastic properties and young modulus for some materials. [Online]. Available: http://www.engineeringtoolbox.com/young-modulus-d_417.html

[124] E. Toolbox. (2010) International standard atmosphere. [Online]. Available: http://www.engineeringtoolbox.com/international-standard-atmosphere-d_985.html

[125] Transpressnz. (2011) Saab 340. [Online]. Available: http://transpressnz.blogspot.co.uk/2011/12/saab-340.html

[126] B. University. (2013) Is lithium-ion the ideal battery? [Online]. Available: http://batteryuniversity.com/learn/article/is_lithium_ion_the_ideal_battery

[127] J. Voogt, "Antenna Types and Applications," 2002.

[128] D. C. Wilcox, *Turbulence Modelling for CFD*. DCW Industries, 1994.

[129] J. WU, "Sea surface drift currents induced by wind waves.pdf," *American Meteorlogical Society*, pp. 1441–1451, 1983.

[130] Z. T. Xie, *Applications of CFD: Lecture Slides*. University of Southampton, 2010.

[131] R. J. R. Zhiyong Cai, *Wood Handbook, Chapter 12: Mechanical Properties of Wood-Based Composite Materials*. General Technical Report FPL-GTR-190, 2010.